FACULTY OF SCIENCE
UNIVERSITY OF COPENHAGEN

Ph.D. Thesis
Christo Buizert

The influence of firn air transport processes and radiocarbon production on gas records from polar firn and ice

Academic supervisor:
Prof. Thomas Blunier

Submitted 21/10/2011

CENTRE FOR ICE AND CLIMATE

Abstract

Air bubbles found in polar ice cores preserve a record of past atmospheric composition up to 800 kyr back in time. The composition of the bubbles is not identical to the ancient atmosphere, as it is influenced by processes prior to trapping, within the ice sheet itself, and during sampling and storage. Understanding of these processes is essential for a correct interpretation of ice core gas records. In this work we focus on transport processes in the porous firn layer prior to bubble trapping, and in situ cosmogenic radiocarbon (^{14}C) production in ice.

First, we present a review of firn air studies. We describe the firn air sampling process, the relevant physical characteristics of firn, the different mechanisms of air transport, and the effects of firn air transport on gas records.

Second, we present a characterization of the firn air transport properties of the NEEM deep drilling site in Northern Greenland (77.45° N 51.06° W). The depth-diffusivity relationship needs to be reconstructed using reference tracers of known atmospheric history. We present a novel method of characterizing the firn transport using ten tracers simultaneously, thus constraining the effective diffusivity better than the commonly used single-tracer method would. A comparison between two replicate boreholes drilled 64 m apart shows differences in measured mixing ratio profiles that exceed the experimental error, which we attribute to lateral inhomogeneities in firn stratigraphy. We find evidence that diffusivity does not vanish completely in the lock-in zone, as is commonly assumed. Six state-of-the-art firn air transport models are tuned to the NEEM site; all models successfully reproduce the data within a 1σ Gaussian distribution. We present the first intercomparison study of firn air models, where we introduce diagnostic scenarios designed to probe specific aspects of the model physics. Our results show that there are major differences in the way the models handle advective transport, and that diffusive fractionation of isotopes in the firn is poorly constrained by the models.

Third, we describe an empirical method to calculate the magnitude of diffusive fractionation (DF) of isotopes in the ice core record. Our method 1) requires little computational effort, 2) uses only commonly available ice core data, 3) does not require knowledge of the (unknown) true atmospheric history, and 4) is arguably more accurate than a full modeling study. The method consists of an analytical expression for the DF in combination with a parameterization of gas age at the lock-in depth based on five modern firn air sites. We test the accuracy and dynamic response of our method by comparing it to a firn air transport model for two modern, well-characterized firn air sites. We find an excellent agreement on timescales relevant for ice core data ($\geq$ 100 years). We apply our method to CH_4, CO_2 and N_2O mixing ratios found in ice cores, and find that $\delta^{13}C$–CH_4 is the only trace gas isotopic signal for which the diffusive correction should always be applied during transitions. We apply the DF correction to published $\delta^{13}C$–CH_4 records over the last glacial termination and the 8.2 kyr event. In both cases the DF correction exceeds the analytical precision of the data during abrupt transitions. We argue that the corrected time series are more consistent than the uncorrected ones. We show that our method has an uncertainty of around 15% in the case thermal fractionation-corrected $\delta^{15}N$–N_2 data is used, and around 20% when uncorrected $\delta^{15}N$–N_2 data is used. We argue that our empirical method is more accurate than the alternative of a full modeling study.

Fourth, we describe in detail the development of the CIC firn air model. We derive expressions for the air velocity in the open porosity, the bubble trapping rate, and for the pressurization of closed bubbles due to firn compaction. We test these equations for NEEM and South Pole, and find they predict the total air content accurately within 3%. We give a complete mathematical description of trace gas mass transfer in the open porosity, and its numerical implementation using the Crank-Nicolson method. We present a new way to reconstruct the effective diffusivity profile with depth. We show how mixing ratios in the closed porosity can be calculated, and show how the trapping process broadens the age distribution. We find the additional broadening due to trapping to be negligible at NEEM, because of its high accumulation and relatively long lock-in zone. At South pole there is significant broadening due to the lower accumulation rate and short lock-in zone.

Fifth, we combine cosmic ray scaling and production estimates with a 2-D ice flow line model to study cosmogenic ^{14}C production at the Taylor Glacier blue ice area, Antarctica. We find that 1) ^{14}C production by thermal neutron capture in air bubbles is negligible, 2) including ice flow patterns caused by basal topography can lead to surface ^{14}C activities that differ by up to 25% from activities calculated using an ablation-only approximation, which is used in all prior work, and 3) at high ablation margin sites, solar variability modulates the strength of the dominant spallogenic production by 10%. We introduce two methods to parameterize vertical strain rates in modeling ice flow, and assess which method is more reliable for Taylor Glacier. Finally, we present a sensitivity study from which we conclude that uncertainties in published cosmogenic production rates are the largest source of potential error. The results presented here can inform ongoing and future ^{14}C and ice flow studies at ice margin sites, including important paleoclimatic applications such as the reconstruction of paleoatmospheric ^{14}C content of methane.

Resumé

Luftbobler fanget i polare iskerner giver en optegnelse af fortidens atmosfæriske sammensætning op til 800.000 år tilbage i tiden. Sammensætningen af gassen i boblerne er ikke identisk med fortidens atmosfære, da den bliver påvirket af processer forud for formationen af boblerne, i isen, og senere ved prøvetagning og opbevaring. Forståelse af disse processer er afgørende for fortolkning af iskernes gas optegnelser. I dette studie fokusere vi på transport processerne i den porøse firn før formationen af boblerne, og in situ kosmogonisk kulstof (^{14}C) produktion i is.

Først præsenterer vi en gennemgang af firn luft undersøgelser. Vi beskriver prøvetagning af firn luf, de relevante fysiske egenskaber ved firn, de forskellige former for lufttransport, og virkningerne af firn lufttransport på gas optegnelser i iskerner.

For det andet, præsentere vi en karakteristik af firn lufttransport egenskaber af NEEM dybe borested i det nordlige Grønland (77,45° N 51,06° W). Dybde-diffusivitet forhold skal rekonstrueres ved hjælp af sporstoffers kendte atmosfærisk historie. Vi præsenterer en ny metode til at karakterisere firn transport ved hjælp af ti sporstoffer samtidigt, og dermed bestemme den effektive diffusivitet bedre end den almindeligt anvendte sporing af et enkelt sporestof. En sammenligning mellem to replikere boringer, boret 64 m fra hinanden, viser forskelle i målt mixing-ratio profiler, forskellen overstiger den eksperimentelle fejl, dette tilskriver vi lateral uensartetheder i firn stratigrafi. Vi finder, at diffusivitet ikke forsvinde fuldstændig i lock-in zone, som normalt antages. Seks state-of-the-art firn lufttransport modeller er tunet til NEEM stedet; alle modeller gengive data inden for en 1σ Gauss distribution. Vi præsenterer det første sammenligningsprogrammer for undersøgelse af firn luft-modeller, hvor vi indføre diagnostiske scenarier designet til at sonde specifikke aspekter af den modelleret fysik. Vores resultater viser, at der er store forskelle i den måde modelleren håndterer advective transport, og den diffusive fraktionering af isotoper i firn er dårligt bestem af modellerne.

For det tredje, beskriver vi en empirisk metode til at beregne størrelsen af diffusive fraktionering (DF) af isotoper i iskerne optegnelser. Vores metode 1) kræver lille beregningsmæssige indsats, 2) bruger tilgængelige iskerne data, 3) kræver ikke kendskab til den (ukendte) sande atmosfærisk historie, og 4) er mere nøjagtig end en fuld modellering studier. Metoden består af et analytisk udtryk for DF i kombination med en parameterisering af gas alder ved lock-in dybden baseret på fem moderne firn luft sites. Vi tester nøjagtighed og dynamisk respons af vores metode ved at sammenligne den med en firn lufttransport model for to moderne, velkarakteriseret firn luft sites. Vi finder en god sammenhæng på tidsskala relevante for iskernedata ($\geq$ 100 år). Vi anvender vores metode til CH_4, CO_2 og N_2O blandingsforhold fundet i iskerner, og finder, at δ^{13}C–CH_4 er den eneste sporgas isotopiske signal, hvor man er nødt til at bruge diffusive korrektion under transitioner. Vi anvender DF korrektion på offentliggjort δ^{13}C–CH_4 optegnelser over transitionen fra sidste istid og 8200 års begivenhed. I begge tilfælde overstiger DF korrektionen den analytiske præcision af data under de bratte transitioner. Vi hævder, at den korrigerede tidsserier er mere konsekvent end de ikke-korrigerede. Vi viser, at vores metode har en usikkerhed på omkring 15% i ved termiske fraktioner korrigeret δ^{15}N–N_2 data, og omkring 20%, ved ikke-korrigerede δ^{15}N–N_2 data. Vi argumenterer for, at vores empiriske metode er mere præcis end den alternative fuld modellering studie.

For det fjerde, en detaljeret beskrivelse af udviklingen af CIC firn luften model bliver givet. Vi udlede udtryk for lufthastigheden i den åbne firn, boblen formationen, og for trykket i lukkede bobler på grund af firn komprimering. Vi tester modellen på NEEM og South Pole, og finde den forudsige præcist det samlede luft indhold inden for 3%. Vi giver en komplet matematisk beskrivelse af sporgas massetransport i det åbne firn, og dens numeriske implementering ved hjælp af Crank-Nicolson metoden. Vi præsenterer en ny måde at rekonstruere den effektive diffusivitet profil med dybde. Vi viser, hvordan blandingsforhold i lukket firn kan beregnes, og viser, hvordan boble formations processen gør aldersfordeling større. Vi finder en forøgelse på grund af boble formationen er ubetydelig ved NEEM, på grund af den høje akkumulation og lange lock-in zone. På sydpol er der en betydelig forøgelse på grund af den lavere akkumulation og den korte lock-in zone.

For det femte, kombinerer vi den kosmiske stråling skalering og et produktion skøn med en 2-D is-flyde model for at studere kosmiske ^{14}C produktionen på Taylorgletsjeren blå is-området, Antarktis. Vi finder, 1) ^{14}C produktion af termisk neutron capture i luftbobler er ubetydelig, 2) is-flydning forårsaget af basal topografi kan føre til overflade ^{14}C aktiviteter, der varierer med op til 25% fra aktiviteter beregnet med en ablation-only tilnærmelse, som anvendes i alle tidligere studier, og 3) ved høje ablation sites, sol variation ændre styrken af den dominerende produktions mekanisme med 10%. Vi introducerer to metoder til at parametrisere lodret strain rats i is flyde modellering, og vurdere hvilken metode er mest pålidelig for Taylor Glacier. Til sidst præsenterer vi en følsomhedsanalyse, hvorfra vi konkludere, at usikkerheder i de offentliggjorte kosmisk c produktions rater er den største kilde til potentielle fejl kilde. De resultater, der præsenteres her, kan hjælpe igangværende og fremtidige ^{14}C - is flydnings studier ved isranden, herunder vigtige palæoklimatiske applikationer, såsom genskabelsen af det palæoatmosfærisk indhold af ^{14}C i metan.

Preface

Copenhagen, October 2011

This thesis has been submitted to the Faculty of Science, University of Copenhagen, in partial fulfillment of the requirements for the degree of Doctor of Philosophy. The bulk of the work was carried out at the Center for Ice and Climate, Niels Bohr Institute, under the supervision of Prof. Thomas Blunier. This work owes much to his continued support and the freedom he gave me in letting me work on topics of my own choosing. Through the CIC I met many wonderful colleagues and friends; I will thank them more thoroughly at the end of this thesis.

During my studies I had the pleasure of spending five months at the The Institute of Arctic and Alpine Research, University of Colorado, Boulder CO, USA. I am very grateful to Vasillii Petrenko, Bruce Vaughn and James White for their hospitality and support. This visit led to a very fruitful and continuing collaboration, to which chapter 6 of this thesis is testimony. The connection with Boulder has enriched my life in many ways.

In the summer of 2009 I spent near four weeks on Greenland as part of the NEEM deep drilling project; an experience that initializes one into the world of ice coring more deeply than other academic endeavors ever could. Through the NEEM gas consortium I had the privilege of working closely with many great scientist: Jeff Severinghaus, Patricia Martinerie, Vas Petrenko, Cathy Trudinger (the 'firn gang'), and David Etheridge.

Nothing is more changeable than a PhD topic, and one would be hard-pressed to recognize this thesis as the outcome of the original project description I applied for in May 2008. Some would blame this on my constellation – Gemini. I blame it on the Mass Spectrometer.

Christo Buizert

Contents

1

Introduction and Motivation

Air bubbles found in polar ice cores preserve a record of past atmospheric composition. This natural archive has been used to reconstruct the atmospheric evolution up to 800 kyr back in time (Jouzel et al., 2007). The three major greenhouse gases, CO_2, CH_4 and N_2O, show variations both on the orbital timescale of glacial cycles (Loulergue et al., 2008; Petit et al., 1999; Schilt et al., 2010a) as well as on the millennial timescale of abrupt Dansgaard-Oeschger (DO) events (Brook et al., 1996; Schilt et al., 2010b; Ahn et al., 2008). Greenhouse gas concentrations first of all control the radiative surface forcing of the atmosphere; the observed synchronicity with temperature reconstructions implying an amplifying role to climatic variations on orbital timescales. Second of all, their atmospheric mixing ratio and isotopic composition reflect interactions between the different parts of the climate system, such as biosphere, ocean and atmospheric circulation. Trace gases should therefore also be thought of as complex climatic proxies, containing valuable information on the anatomy of past climate change.

Also non-trace gas atmospheric constituents contain valuable (climatic) information, where attention has focused mainly, though not exclusively, on their stable isotopic composition. For example, the deviation of $\delta^{18}O$–O_2 from seawater (the Dole effect) reflects the monsoon intensity (Severinghaus et al., 2009), the Kr/N_2 ratio is a proxy for past mean ocean temperatures (Headly and Severinghaus, 2007), and the evolution of $\delta^{40}Ar$ constrains the degassing rate of ^{40}Ar from the Earth's crust (Bender et al., 2008).

Much work has also been devoted to the atmospheric radiocarbon (^{14}C) abundance, in particular for CO_2. Initial studies mostly focused on the potential for radiocarbon dating of ice samples (e.g. Fireman and Norris, 1982; Andree et al., 1984); more recently the ^{14}C abundance of CH_4 has been used for paleoclimatic reconstructions of the (^{14}C-free) marine clathrate contribution to the methane budget over the last glacial termination (Petrenko et al., 2009).

The composition of air bubbles in polar ice samples is not identical to that of the ancient atmosphere which the bubbles represent. There are a number of processes by which the gas composition is altered. First, the air is affected by the transport through the 40-120 m thick porous firn layer, only at the bottom of which the air is permanently occluded in the ice. The firn layer changes the composition through gravitational separation (Craig et al., 1988), thermal fractionation (Severinghaus et al., 2001), smoothing through diffusion and bubble trapping (Spahni et al., 2003), diffusive isotopic fractionation (Trudinger et al., 1997, this thesis) and molecular size fractionation at bubble closure (Huber et al., 2006). Second, within the ice sheet or glacier itself there is the possibility of in situ production. CO_2 measurements done on Greenland ice show anomalous concentration spikes that have been attributed to in situ production from either organic material or carbonate reactions (Tschumi and Stauffer, 2000; Guzman et al., 2007). Also for N_2O production artifacts are observed whenever the dust level exceeds a critical threshold; the artifacts have been attributed to bacterial production at subfreezing temperatures (Miteva et al., 2007). Cosmic rays produce ^{14}C within the ice itself, mainly through fast neutron spallation of abundant ^{16}O atoms (Lal et al., 1990). The resulting ^{14}C can end up as either $^{14}CO_2$, ^{14}CO or $^{14}CH_4$ (Petrenko et al., 2009). Third, during post-coring storage of ice samples, diffusion through microcracks and through the ice itself can alter the gas composition (Kobashi et al., 2008). This effect is only relevant for small diameter molecules, such as H_2, He, O_2 and Ar.

Understanding of all the effects that can alter the gas composition of an ice core sample are essential for a correct interpretation of the data. In most cases these effects are a nuisance, as they require a correction be made (which introduces additional uncertainty). In several cases, however, these deviations from the atmospheric signal provide additional information that can be interpreted as a (climate) proxy. Thermal fractionation signals in $\delta^{15}N{-}N_2$ and $\delta^{40}Ar$ are now routinely used to estimate the magnitude of temperature variations over Greenland (Severinghaus and Brook, 1999); the magnitude of the close-off fractionation $\delta O_2/N_2$ has been interpreted as a local summer insolation proxy, allowing orbital tuning of ice core chronologies (Bender, 2002; Kawamura et al., 2007); it situ cosmogenic ^{14}C can be used to estimate past accumulation rates in ice cores, and ablation rates at margin sites and blue-ice areas (Lal et al., 1990, 2000).

In this thesis we will investigate some of the effects that influence the gas composition in polar ice and firn samples in detail. In chapter 2 we present a review of gas transport in the porous firn layer, and all the different processes that affect the gas composition in ice cores. Chapter 3 presents a characterisation of the firn air transport at the NEEM deep drilling site in Northern Greenland, as well as the first intercomparison study of firn air models. Chapter 4 investigates in detail the mechanism of diffusive isotopic fractionation in the firn, which has received little attention in the literature so far. In chapter 5 we describe the development of a new 1-D numerical firn air transport model, the CIC model. Finally in chapter 6 we describe the effect of in situ cosmogenic ^{14}C production on gas records from the Taylor Glacier blue-ice area in Antarctica.

References

Ahn, J., Headly, M., Wahlen, M., Brook, E. J., Mayewski, P. A., and Taylor, K. C. (2008). Co2 diffusion in polar ice: observations from naturally formed co2 spikes in the siple dome (antarctica) ice core. *J. Glaciol.*, 54(187):685–695. ISI Document Delivery No.: 374XF Times Cited: 2 Cited Reference Count: 49 Ahn, Jinho Headly, Melissa Wahlen, Martin Brook, Edward J. Mayewski, Paul A. Taylor, Kendrick C.

Andree, M., Moor, E., Beer, J., Oeschger, H., Stauffer, B., Bonani, G., Hofmann, H., Morenzoni, E., Nessi, M., Suter, M., and Wolfli, W. (1984). C-14 dating of polar ice. *Nucl. Instrum. Meth. B* , 5(2):385–388.

Bender, M. L. (2002). Orbital tuning chronology for the vostok climate record supported by trapped gas composition. *Earth Planet Sc. Lett.*, 204(1-2):275–289. ISI Document Delivery No.: 619LJ Times Cited: 24 Cited Reference Count: 57.

Bender, M. L., Barnett, B., Dreyfus, G., Jouzel, J., and Porcelli, D. (2008). The contemporary degassing rate of Ar-40 from the solid Earth. *Proc. Natl. Acad. Sci. U. S. A.*, 105(24):8232–8237.

Brook, E. J., Sowers, T., and Orchardo, J. (1996). Rapid variations in atmospheric methane concentration during the past 110,000 years. *Science*, 273(5278):1087–1091.

Craig, H., Horibe, Y., and Sowers, T. (1988). Gravitational separation of gases and isotopes in polar ice caps. *Science*, 242(4886):1675–1678.

Fireman, E. and Norris, T. (1982). Ages and composition of gas trapped in Allan-Hills and Byrd core ice. *Earth Planet. Sc. Lett.*, 60(3):339–350.

Guzman, M. I., Hoffmann, M. R., and Colussi, A. J. (2007). Photolysis of pyruvic acid in ice: Possible relevance to co and co$_2$ ice core record anomalies. *J. Geophys. Res.-Atm*, 112(D10):10.

Headly, M. A. and Severinghaus, J. P. (2007). A method to measure Kr/N-2 ratios in air bubbles trapped in ice cores and its application in reconstructing past mean ocean temperature. *J. Geophys. Res.-Atmos.*, 112(D19).

Huber, C., Beyerle, U., Leuenberger, M., Schwander, J., Kipfer, R., Spahni, R., Severinghaus, J. P., and Weiler, K. (2006). Evidence for molecular size dependent gas fractionation in firn air derived from noble gases, oxygen, and nitrogen measurements. *Earth Planet Sc. Lett.*, 243(1-2):61–73.

Jouzel, J., Masson-Delmotte, V., Cattani, O., Dreyfus, G., Falourd, S., Hoffmann, G., Minster, B., Nouet, J., Barnola, J. M., Chappellaz, J., Fischer, H., Gallet, J. C., Johnsen, S., Leuenberger, M., Loulergue, L., Luethi, D., Oerter, H., Parrenin, F., Raisbeck, G., Raynaud, D., Schilt, A., Schwander, J., Selmo, E., Souchez, R., Spahni, R., Stauffer, B., Steffensen, J. P., Stenni, B., Stocker, T. F., Tison, J. L., Werner, M., and Wolff, E. W. (2007). Orbital and millennial antarctic climate variability over the past 800,000 years. *Science*, 317(5839):793–796. ISI Document Delivery No.: 198JN Times Cited: 27 Cited Reference Count: 39 Jouzel, J. Masson-Delmotte, V. Cattani, O. Dreyfus, G. Falourd, S. Hoffmann, G. Minster, B. Nouet, J. Barnola, J. M. Chappellaz, J. Fischer, H. Gallet, J. C. Johnsen, S. Leuenberger, M. Loulergue, L. Luethi, D. Oerter, H. Parrenin, F. Raisbeck, G. Raynaud, D. Schilt, A. Schwander, J. Selmo, E. Souchez, R. Spahni, R. Stauffer, B. Steffensen, J. P. Stenni, B. Stocker, T. F. Tison, J. L. Werner, M. Wolff, E. W.

Kawamura, K., Parrenin, F., Lisiecki, L., Uemura, R., Vimeux, F., Severinghaus, J. P., Hutterli, M. A., Nakazawa, T., Aoki, S., Jouzel, J., Raymo, M. E., Matsumoto, K., Nakata, H., Motoyama, H., Fujita, S., Goto-Azuma, K., Fujii, Y., and Watanabe, O. (2007). Northern hemisphere forcing of climatic cycles in antarctica over the past 360,000 years. *Nature*, 448(7156):912–U4.

Kobashi, T., Severinghaus, J. P., and Kawamura, K. (2008). Argon and nitrogen isotopes of trapped air in the gisp2 ice core during the holocene epoch (0-11,500 b.p.): Methodology and implications for gas loss processes. *Geochim. Cosmochim. Ac.*, 72(19):4675–4686. doi: DOI: 10.1016/j.gca.2008.07.006.

Lal, D., Jull, A. J. T., Burr, G. S., and Donahue, D. J. (2000). On the characteristics of cosmogenic in situ c-14 in some gisp2 holocene and late glacial ice samples. *Nucl. Instrum. Meth. B*, 172:623–631.

Lal, D., Jull, A. J. T., Donahue, D. J., Burtner, D., and Nishiizumi, K. (1990). Polar ice ablation rates measured using in-situ cosmogenic c-14. *Nature*, 346(6282):350–352.

Loulergue, L., Schilt, A., Spahni, R., Masson-Delmotte, V., Blunier, T., Lemieux, B., Barnola, J. M., Raynaud, D., Stocker, T. F., and Chappellaz, J. (2008). Orbital and millennial-scale features of atmospheric CH_4 over the past 800,000 years. *Nature*, 453(7193):383–386.

Miteva, V., Sowers, T., and Brenchley, J. (2007). Production of n2o by ammonia oxidizing bacteria at subfreezing temperatures as a model for assessing the n2o anomalies in the vostok ice core. *Geomicrobiology Journal*, 24(5):451–459. Miteva, Vanya Sowers, Todd Brenchley, Jean.

Petit, J. R., Jouzel, J., Raynaud, D., Barkov, N. I., Barnola, J. M., Basile, I., Bender, M., Chappellaz, J., Davis, M., Delaygue, G., Delmotte, M., Kotlyakov, V. M., Legrand, M., Lipenkov, V. Y., Lorius, C., Pepin, L., Ritz, C., Saltzman, E., and Stievenard, M. (1999). Climate and atmospheric history of the past 420,000 years from the vostok ice core, antarctica. *Nature*, 399(6735):429–436. ISI Document Delivery No.: 202TH Times Cited: 1329 Cited Reference Count: 52.

Petrenko, V. V., Smith, A. M., Brook, E. J., Lowe, D., Riedel, K., Brailsford, G., Hua, Q., Schaefer, H., Reeh, N., Weiss, R. F., Etheridge, D., and Severinghaus, J. P. (2009). (ch4)-c-14 measurements in greenland ice: Investigating last glacial termination ch4 sources. *Science*, 324(5926):506–508. ISI Document Delivery No.: 436JU Times Cited: 1 Cited Reference Count: 29 Petrenko, Vasilii V. Smith, Andrew M. Brook, Edward J. Lowe, Dave Riedel, Katja Brailsford, Gordon Hua, Quan Schaefer, Hinrich Reeh, Niels Weiss, Ray F. Etheridge, David Severinghaus, Jeffrey P.

Schilt, A., Baumgartner, M., Blunier, T., Schwander, J., Spahni, R., Fischer, H., and Stocker, T. F. (2010a). Glacialial–interglacial and millennial-scale variations in the atmospheric nitrous oxide concentration during the last 800,000 years. *Quaternary Science Reviews*, 29(1-2):182 – 192.

Schilt, A., Baumgartner, M., Schwander, J., Buiron, D., Capron, E., Chappellaz, J., Loulergue, L., Schuepbach, S., Spahni, R., Fischer, H., and Stocker, T. F. (2010b). Atmospheric nitrous oxide during the last 140,000 years. *Earth Planet. Sci. Lett.*, 300(1-2):33–43.

Severinghaus, J. P., Beaudette, R., Headly, M. A., Taylor, K., and Brook, E. J. (2009). Oxygen-18 of O_2 Records the Impact of Abrupt Climate Change on the Terrestrial Biosphere. *Science*, 324(5933):1431–1434.

Severinghaus, J. P. and Brook, E. J. (1999). Abrupt climate change at the end of the last glacial period inferred from trapped air in polar ice. *Science*, 286(5441):930–934.

Severinghaus, J. P., Grachev, A., and Battle, M. (2001). Thermal fractionation of air in polar firn by seasonal temperature gradients. *Geochem. Geophy. Geosy.*, 2.

Spahni, R., Schwander, J., Flückiger, J., Stauffer, B., Chappellaz, J., and Raynaud, D. (2003). The attenuation of fast atmospheric ch_4 variations recorded in polar ice cores. *Geophys. Res. Lett.*, 30(11):1571.

Trudinger, C. M., Enting, I. G., Etheridge, D. M., Francey, R. J., Levchenko, V. A., Steele, L. P., Raynaud, D., and Arnaud, L. (1997). Modeling air movement and bubble trapping in firn. *J. Geophys. Res.-Atm*, 102(D6):6747–6763.

Tschumi, J. and Stauffer, B. (2000). Reconstructing past atmospheric CO_2 concentration based on ice-core analyses: open questions due to in situ production of CO_2 in the ice. *J. Glaciol.*, 46(152):45–53.

2

Overview of firn air studies

C. Buizert[1]

2.1 Introduction

Firn is the intermediate stage between snow and glacial ice, which constitutes the upper 40–120 m of the accumulation zone of ice sheets. Within the firn a vast network of interconnected pores exists, which exchanges air with the overlying atmosphere. At the bottom of the firn column, air is permanently trapped within the ice matrix, storing an atmospheric sample from the time of pore closure. In this way air bubbles in glacial ice have been used to reconstruct changes in atmospheric composition up to 800 kyr back in time (Loulergue et al., 2008; Lüthi et al., 2008; Petit et al., 1999).

If one thinks of glacial ice as a flask for storing samples of ancient atmosphere, then the firn is the valve that gradually closes the flask. But far from an ideal valve, the firn alters the composition of air as it travels downwards, through e.g. gravitational separation (Craig et al., 1988; Schwander, 1989), diffusive smoothing (Spahni et al., 2003) and thermal fractionation (Severinghaus et al., 2001). An understanding of firn air transport processes is therefore essential for interpretation of ice core gas records. Continued exchange with the atmosphere furthermore keeps firn air at the firn-ice transition younger than the surrounding ice, resulting in an age difference age between glacial ice and the air bubbles it contains (Schwander and Stauffer, 1984).

The firn itself also acts as an archive of old air, preserving a continuous record of atmospheric composition up to a century back in time (Kaspers et al., 2004). Sampling of firn air allows to reconstruct the recent atmospheric history of many trace gas species and their isotopic composition.

---

[1] This is an invited chapter, to be published as section 19.25 in the Encyclopedia of Quaternary Sciences, 2^{nd} edition; Editor-in-chief: S.A. Elias; Elsevier Science.

2.2 Firn air sampling

2.2.1 Firn air sampling device

The primary means of studying firn transport is by sampling of firn air (Schwander et al., 1993). The principle is illustrated in Fig. 2.1a. The firn air sampling device (FASD) is lowered into a borehole drilled to the desired sampling depth. By inflating the bladder, firn air is isolated from the overlying atmosphere. The borehole is then purged from contamination by pumping on the purge- and sampling lines. CO_2 mixing ratios are monitored on the air flow to assess whether the hole has been sufficiently purged. A baffle plate (Fig. 2.1b) is often used to separate the purge- and sampling lines. The purge flow has a higher risk of being contaminated by air

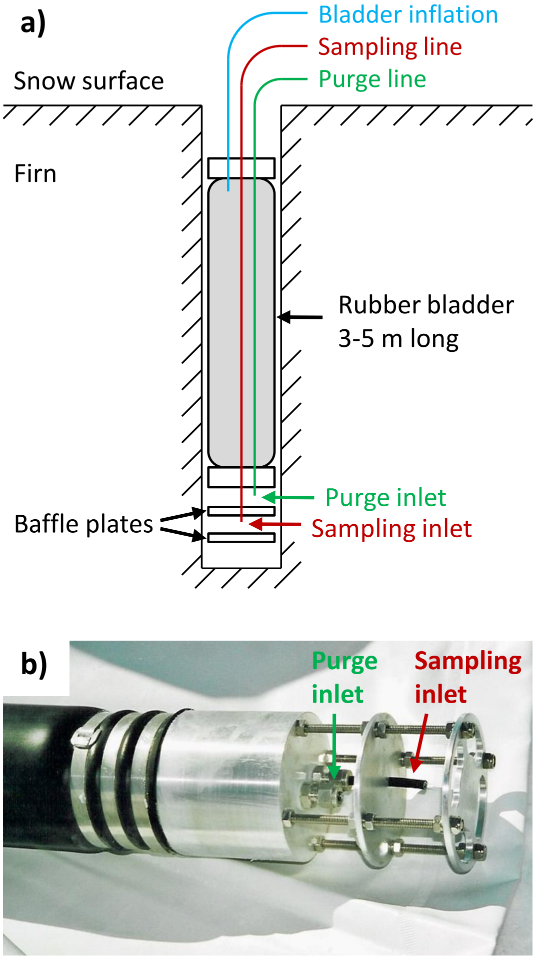

Figure 2.1: **a)** *The principle of firn air sampling (not to scale). The FASD is suspended in the borehole from a steel cable.* **b)** *Sampling head of the University of Bern FASD. Photograph courtesy of Jakob Schwander.*

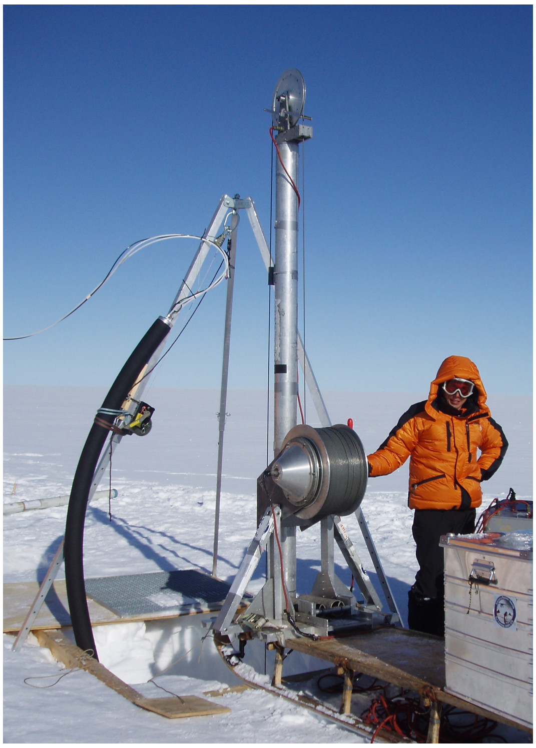

Figure 2.2: Firn air sampling at NEEM, Northern Greenland, July 2009. Vasilli Petrenko with the University of Copenhagen shallow electro-mechanical drill (3 inch core) and the CSIRO FASD bladder assembly. Photograph courtesy of Anne Solgaard.

leaking past the bladder, and is discarded. Air from the sampling line is collected in flasks, which are shipped to the laboratory for analysis.

In the deep firn, density layering causes air to flow preferentially in the horizontal plane during sampling. Sturrock et al. (2002) observed that the mixing ratios of CH_4, CO_2, N_2O, H_2 and CO do not change systematically with time or air volume extracted during sampling at each level. They interpret this as evidence that the air from each sampling depth originates from a narrow horizontal firn layer, rather than from regions significantly above or below the FASD inlet. In shallow strata with higher permeability, the collection region is presumably closer to a sphere or ellipsoid.

At several sites, air sampled from the deepest firn strata was found to be slightly depleted in heavy gases and isotopologues such as δKr/N_2, δXe/N_2, $\delta^{15}N_2$ and δ^{40}Ar (Severinghaus and Battle, 2006). The authors interpret this as a mass-dependent collection artifact caused by the large pressure gradients that the sampling procedure induces in these low permeability layers.

Table 2.1: Overview of firn air sampling sites and characteristics.

Site	Location		Altitude (m a.s.l.)	p (hPa)	T (°C)	A (cm ice yr^{-1})	CZ depth (m)	z_{cod} (m)	Year(s) sampled	Main reference
Northern hemisphere										
Devon Isl.	75.3°N	82.1°W	1929	792^{a}	-23	30	$\sim 0^{b}$	59	1998	FIRETRACC, Clark et al. (2007)
NEEM	77.4°N	51.1°W	2484	745	-28.9	22	4	78	2008, 2009	Buizert et al. (2011)
NGRIP	75.1°N	42.3°W	2917	691	-31.1	19	1–2^{c}	78	2001^{d}	CRYOSTAT, Kawamura et al. (2006)
Summit	72.6°N	38.4°W	3214	665	-31.4	23	$\sim 0^{b}$	80	1989, 2006	Schwander et al. (1993), Witrant et al. (2011)
Southern hemisphere										
Berkner Isl.	79.6°S	45.7°W	900	895^{f}	-26	13	$<2^{c}$	64	2003	CRYOSTAT
DE08-2	66.7°S	113.2°E	1250	850	-19	120	0^{b}	85	1993	Etheridge et al. (1996)
DML^{g}	77.0°S	10.5°W	2176	757^{f}	-39	7	$<5^{c}$	74	1998	FIRETRACC
Dome C	75.1°S	123.4°E	3233	658^{f}	-54	3.2 (2.7^{c})	2^{c}	100	1999	FIRETRACC
Dome Fuji	77.3°S	39.7°E	3810	600	-57.3	2.8 (2.3^{c})	9	104	1998	Kawamura et al. (2006)
DSSW20K	66.8°S	112.6°E	1200	850	-21	16	4	52	1998	Trudinger (2001)
H72	69.2°S	41.1°E	1241	857	-20.3	33	2	65	1998	Kawamura et al. (2006)
Megadunes	80.8°S	124.5°E	2880	677	-49	$\sim 0^{h}$	23	68	2004	Severinghaus et al. (2010)
Siple Dome	81.7°S	148.8°W	620	940	-25.4	13	$<2^{b}$	57	1996,1998	Severinghaus et al. (2001)
South Pole	90.0°S		2840	681	-51	8	$<2^{b}$	123	1995–2008^{j}	Severinghaus et al. (2001)
Vostok	78.5°S	106.8°E	3471	632	-56	2.4	13^{b}	100	1996	Fabre et al. (2000)
WAIS-D	79.5°S	112.1°W	1766	799^{f}	-31	22	3	76.5	2005	Battle et al. (2011)
YM85	71.6°S	40.6°E	2246	730	-34	17	14^{k}	68	2002	Kawamura et al. (2006)

Unless indicated otherwise, values can be found in the main reference, or references therein (last column)

[a] Huber et al. (2006)

[b] Severinghaus et al. (2010)

[c] Landais et al. (2006)

[d] There were two separate NGRIP firn air campaigns in 2001 (J. Schwander, personal communication, 2011).

[f] Calculated from the altitude using the pressure-altitude relationship over Antarctica from Stone (2000).

[g] Also referred to as BAS depot (Landais et al., 2006). Note that the location differs from that of the EDML ice core.

[h] The long term average accumulation estimate is 2.5 cm ice yr^{-1}. Sampling was done during an accumulation hiatus.

[j] Firn air was sampled in 1995, 1998, 2001 and 2008.

[k] High wind speeds at this site cause the unusually thick CZ.

2.2.2 Overview of firn sampling sites

Firn air has been sampled from sites on both hemispheres, covering a wide range of climatic conditions. Table 2.1 gives an overview of sampling sites. The Law Dome DE08-2 site is characterised by a very high accumulation rate, which allows for reconstructing atmospheric variations with high temporal resolution. At sites on the Antarctic plateau (Dome C, Dome Fuji, Megadunes, Vostok), on the other hand, the oldest air can be found.

2.3 Physical firn structure and transport properties

2.3.1 Firn density and porosity

Polar firn is a porous medium that is densified gradually under the weight of overlying precipitation, until its density ρ approaches the pure ice density ρ_{ice} of around 920 $\text{kg}\,\text{m}^{-3}$. The interstitial space between ice crystals is referred to as the porosity s, which is defined as the volume fraction not occupied by ice, or $s = 1 - \rho/\rho_{\text{ice}}$. It can be divided into open (s_{op}) and closed (s_{cl}) porosity; the former refers to pores that are still connected to the overlying atmosphere, whereas the latter refers to pores that have already been closed-off. Owing to firn densification the porosity decreases with depth, and air is gradually occluded in bubbles. At Siple station, Schwander and Stauffer (1984) found that 80% of the bubble volume is formed in the density range $795 < \rho < 830$ kg m^{-3}. The average density ($\overline{\rho_{\text{co}}}$) at which the bubbles are closed-off is found in this interval. This mean close-off density was found to be independent of accumulation rate, and is mostly a function of the site temperature (Martinerie et al., 1992, 1994):

$$\overline{\rho_{\text{co}}} = \left(\frac{1}{\rho_{\text{ice}}} + 6.95 \cdot 10^{-7} T - 4.3 \cdot 10^{-5} \right)^{-1} \tag{2.1}$$

where T is the mean annual site temperature in K. The mean close-off density in Eq. (2.1) was determined by total air content measurements in mature ice. It is defined through the porosity which, at the atmospheric pressure of the site, matches the measured air content. Apart from temperature, the close-off density (and thereby the total air content) is also influenced by wind strength (Martinerie et al., 1994) and insolation (Raynaud et al., 2007).

A second useful definition is the full close-off depth z_{cod} (with corresponding ρ_{cod}), which is the depth where all air is occluded ($s_{\text{op}} = 0$). The full close-off is deeper than the mean close-off depth of Eq. (2.1). The deepest point at which firn air can be sampled in the field is around z_{cod}.

Several s_{cl} parameterizations exist. Schwander (1989) gives the following empirical relation based on measurements of bubble volume in ice samples from Siple station, Antarctica:

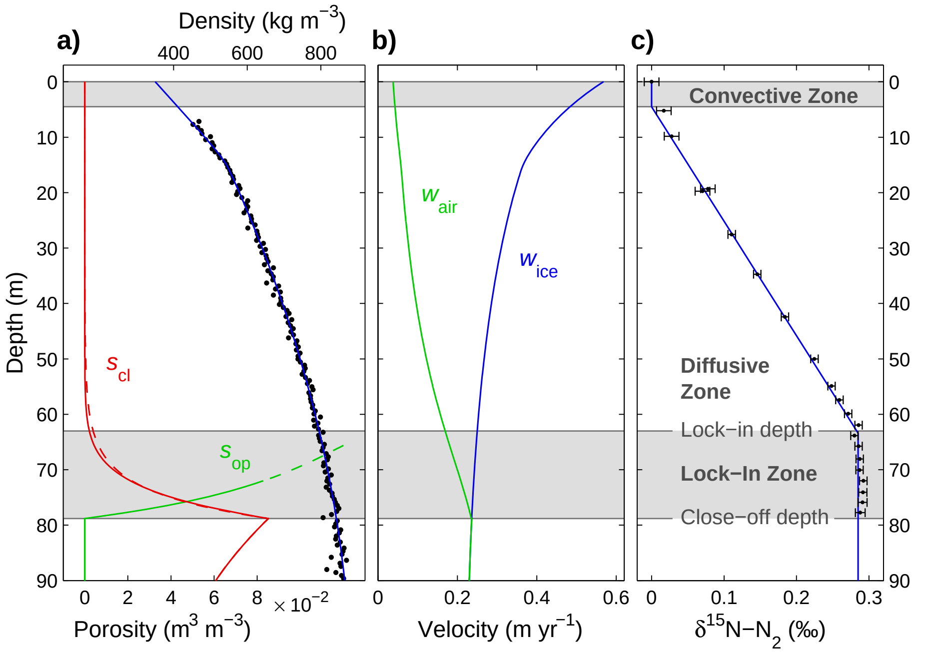

Figure 2.3: Firn characteristics at NEEM. **a)** *Firn density and porosity using the parameterizations of Schwander (1989) (solid line) and Goujon et al. (2003) (dashed line).* **b)** *Downward velocity of firn layers (w_{ice}) and of air in the open porosity w_{air}) calculated using Eq. (2.4).* **c)** *Zonal division based on gravitational enrichment of δ^{15}N-N$_2$. Data are corrected for thermal fractionation.*

$$s_{\text{cl}} = \begin{cases} s \exp\left[75(\rho/\rho_{\text{cod}} - 1)\right] & \text{for} \quad \rho \leq \rho_{\text{cod}} \\ s & \text{for} \quad \rho > \rho_{\text{cod}} \end{cases} \tag{2.2}$$

It must be noted that measurements of bubble volume tend to underestimate closed porosity, as pores can be re-opened by sample cutting. (Severinghaus and Battle, 2006) adapted Eq. (2.2) for Summit, Greenland, to have a more gradual close-off.

An alternative parameterization is given by Goujon et al. (2003), based on density and total air content measurements from three Greenland and Antarctic sites:

$$s_{\text{cl}} = 0.37 s \left(\frac{s}{\overline{s_{\text{co}}}}\right)^{-7.6} \tag{2.3}$$

where $\overline{s_{\text{co}}}$ is the mean close-off porosity $\overline{s_{\text{co}}} = 1 - \overline{\rho_{\text{co}}}/\rho_{\text{ice}}$. Equation (2.3) is designed to be consistent with Eq. (2.1), and indicates that 37 % of the porosity is closed for $\overline{\rho_{\text{co}}}$. Both parameterizations are shown in Figure 2.3a.

2.3.2 Open porosity air flow and transport properties

In the firn-ice transition air bubbles are trapped and advected downwards with the ice. Conservation of mass demands an air flow in the open pores to replace the air thus removed. Assuming the firn to be in steady state with respect to accumulation and densification, the downward velocity of air in the open pores can be derived from the porosity ratio and mass conservation (Buizert et al., 2011):

$$w_{\text{air}} = \frac{A\rho_{\text{ice}}}{s^*_{\text{op}}p_0}\left(\frac{s_{\text{cl}}(z_{\text{COD}})p_{\text{cl}}(z_{\text{COD}})}{\rho_{\text{COD}}} - \frac{s_{\text{cl}}(z)p_{\text{cl}}(z)}{\rho(z)}\right) \tag{2.4}$$

where A is the accumulation rate in $\mathrm{m\,yr^{-}1}$ ice equivalent, s^*_{op} the effective open porosity $s^*_{\text{op}} = s_{\text{op}}\exp(M_{\text{air}}gz/RT)$, p_0 the barometric pressure, $p_{\text{cl}}(z)$ the enhanced pressure in closed bubbles due to firn compaction, M_{air} the molar mass of air in $\mathrm{kg\,mol^{-1}}$, g the gravitational acceleration and R the molar gas constant. The result is plotted in Figure 2.3b, together with the downward velocity of the ice layers $w_{\text{ice}} = A\rho_{\text{ice}}/\rho$. The ice layers descend faster than the air does; i.e. the air in the open porosity is moving upwards relative to the ice matrix. This back flow is due to compression of open pores by the firn densification process (Rommelaere et al., 1997).

Pore geometry and connectivity dictate the firn air transport properties. Gas diffusivity and permeability in firn samples have been determined using direct measurements (Albert et al., 2000; Fabre et al., 2000; Schwander et al., 1988), and by modeling of gas transport in reconstructed pore geometries (Courville et al., 2011; Freitag et al., 2002). However, gas diffusivities determined on individual firn samples do not represent the transport properties of the firn as a whole (Fabre et al., 2000), showing that the lateral dimensions of the diffusive path exceed that of a typical firn sample.

2.3.3 Density layering

Polar firn is a layered medium that exhibits large density variations around the mean caused by seasonal changes in climatic conditions and precipitation density, as well as wind and insolation features that are preserved in the densification process. As high-density layers reach the close-off density first, they can form impermeable layers that inhibit vertical gas transport (Martinerie et al., 1992). Such sealing layers are often invoked to explain the presence of a non-diffusive zone, or lock-in zone (LIZ) just above the bubble close-off depth (Battle et al., 1996; Landais et al., 2006). Firn air can be pumped from the LIZ, meaning a large (laterally) connected open porosity still exists in the low density layers.

The high density sealing layers have been linked to winter precipitation through measurements of water stable isotopes (Martinerie et al., 1992). Recent studies of firn microstructure indicate a density cross-over around 600-650 $\mathrm{kg\,m^{-3}}$, suggesting that high density LIZ layers originate as low density layers at the surface (Freitag et al., 2004). Boreholes separated by as little as 65 m were found to have different firn air transport properties caused by lateral variability in the firn stratigraphy (Buizert et al., 2011).

Although the dense layers impede vertical transport, they do not completely seal off the air below. The air content implied by such fully sealing layers is incompatible with measurements in mature ice. Furthermore, at many sites firn air transport models require finite gas diffusivity in the LIZ to reproduce the measured mixing ratios of trace gases (Severinghaus et al., 2010; Witrant et al., 2011). The back flow of air due to pore compression can be facilitated by (micro) cracks and channels in the dense layers.

2.4 Trace gas transport in the firn

2.4.1 Zonal description of transport

The firn column is commonly divided into three zones, based on the gravitational isotopic enrichment of molecular nitrogen with depth (Sowers et al., 1992). The zones correspond to different modes of firn air transport, as depicted in Fig. 2.3c. The convective zone (CZ) refers to the upper few meters of the firn column which are vigorously ventilated. The air in the CZ is essentially of current atmospheric composition, and consequently it has the same δ^{15}N-N$_2$ as the atmosphere (which is zero by definition). Below the CZ we find the diffusive zone (DZ), where mass transfer is dominated by molecular diffusion. In diffusive equilibrium gravitational separation gives enrichment in heavy isotopes with depth, as is evident from the presented δ^{15}N-N$_2$ measurements. The lock-in depth is defined as the depth at which gravitational enrichment stops. Continued pore compaction leads to a decreasing effective diffusivity with depth; the lock-in depth corresponds to the point where diffusivity becomes effectively zero. At this depth the air gets isolated from the atmosphere, and therefore the lock-in depth determines the age in mature ice. Below the lock-in depth we find the lock-in zone (LIZ), or non-diffusive zone, where advection with the ice matrix dominates the transport. Since advection does not discriminate between isotopologues, gravitational separation does not occur in the LIZ. The existence of the LIZ has been linked to the formation of high density sealing layers that inhibit vertical diffusion (section 2.3.3).

2.4.2 Overview of mass transfer mechanisms

2.4.2.1 Diffusion

Spatial variations in gas concentration or partial pressure lead to isobaric mass transfer along the gradient, from regions of higher to lower concentration. In porous media, such as polar firn or unsaturated soil, two types of diffusion should be considered. Knudsen diffusion occurs when the pore diameter is sufficiently small, or pressure sufficiently low, and molecules collide predominately with the walls rather than with other gas molecules. The second type is molecular diffusion, which represents the opposite regime of predominantly inter-molecular collisions. In polar firn the molecular free mean path of $\lambda \sim$100 nm is about four orders of magnitude smaller than typical pore sizes of $\sim$1 mm (Freitag et al., 2004; Kipfstuhl et al., 2009). Consequently, firn air diffusion is of the molecular type. In soils, particle and pore sizes are generally much smaller and Knudsen diffusion cannot always be neglected. Fick's law is commonly used to describe molecular diffusion in firn. The validity of this approach has been questioned in the case of soil diffusion (Thorstenson and Pollock, 1989), in particular for studies of soil respiration (Freijer and Leffelaar, 1996). When modeling trace gas transport Fick's law provides a good approximation; it is not suited to describe transport of main components of air such as O_2.

The effective diffusivity of gas X in the open porosity is given by (Dullien, 1975):

$$D_X = s_{\mathrm{op}} \frac{D_X^0}{\tau} = s_{\mathrm{op}} \gamma_X \frac{D_{\mathrm{CO_2}}^0}{\tau} \tag{2.5}$$

where D_X^0 is the free-air molecular diffusion coefficient for gas X at the pressure and temperature of the site, τ is the tortuosity of the pore geometry and $\gamma_X = D_X / D_{\mathrm{CO_2}}$ is the diffusivity of gas X relative to that of CO_2. Recommended values for γ_X, as well as a review of D_X^0 measurements and their temperature dependence are given in Appendix A. Although parameterizations of τ as a function of s_{op} do exist (Schwander et al., 1988), diffusivities measured on firn samples do not represent the diffusive behaviour of the entire firn (Fabre et al., 2000). Best results are obtained when $\tau(z)$ is reconstructed site-specifically using measurements of reference tracers (section 2.5.1).

Diffusive transport leads to a separation of the gas mixture by gravity, resulting in a gradual enrichment in both heavy molecules and isotopologues with depth. In diffusive equilibrium the enrichment relative to the atmosphere is given in delta notation by:

$$\delta_{\mathrm{grav}} = \left[\exp\left(\frac{gz\Delta M}{RT} \right) - 1 \right] \cdot 10^3‰ \cong \frac{gz\Delta M}{RT} \cdot 10^3‰ \tag{2.6}$$

where ΔM can be the molar mass deviation from air in $\mathrm{kg\,mol^{-1}}$ ($\Delta M = M_X - M_{\mathrm{air}}$), or the mass difference between two isotopologues when considering isotopic enrichment. Macroscopic transport processes, such as convection and advection, can locally drive the air column out of diffusive equilibrium, reducing the gravitational separation below the equilibrium slope given by Eq. (2.6).

Temperature gradients in the firn also lead to diffusive separation of the gas mixture. Thermal diffusion results in seasonal isotope fractionation in the firn in response to the annual temperature cycle (Severinghaus et al., 2001; Weiler et al., 2009), as well as isotope excursions in the ice core record during abrupt climate

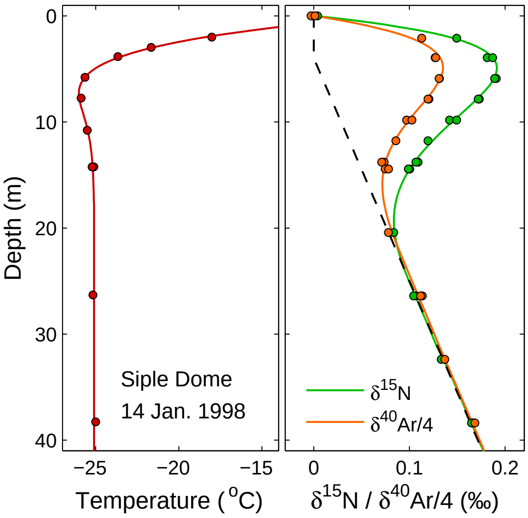

Figure 2.4: Thermal fractionation by seasonal temperature gradients in the upper firn. Data are from Severinghaus et al. (2001); temperature measurements and firn air sampling were both done on 14 January 1998 at Siple Dome, Antarctica. Solid curves are a guide to the eye; the dashed line gives the equilibrium gravitational slope of Equation (2.6). The $\delta^{40}Ar/^{36}Ar$ data have been divided by 4 to show the gravitational enrichment per unit mass difference.

changes (section 2.6.2). Thermal diffusion can be described as the tendency of heavier molecules to preferentially diffuse towards colder regions. This is illustrated in Figure 2.4 for firn air sampled at Siple Dome, Antarctica. The seasonal temperature minimum around 5 m depth leads to a local enrichment in heavy isotopologues of N_2 and Ar.

2.4.2.2 Convection

In the firn air literature convection is used as a generic term for processes that ventilate the upper firn, such as wind pumping (Colbeck, 1989), pressure variations due to seasonality and synoptic scale weather systems (Waddington and Cunningham, 1996), and convective flow driven by (seasonal) temperature gradients. Ventilation affects ice core and firn gas records, as well as post-depositional processes of volatile chemical species. The CZ is typically 1-15 m deep (Kawamura et al., 2006; Landais et al., 2006); an unusually thick CZ of 23 m was observed at the Megadunes site in central Antarctica, caused by a combination of strong winds and an accumulation hiatus giving rise to deep vertical cracks that act as conduits for air exchange (Severinghaus et al., 2010). CZ thicknesses are listed in Table 2.1. Typically, deep convective zones are found at sites with low accumulation rates (e.g. Vostok) or high wind speeds (e.g. YM85). A clear negative correlation between accumulation rate and estimated CZ thickness was found along the EPICA Dome C deep ice core (Dreyfus et al., 2010).

The CZ thickness can be determined empirically using the barometric line fitting method (Bender et al., 1994), in which the barometric slope is fit to isotopic data in the lower DZ, where the gravitational separation is undisturbed by temperature gradients and ventilation. The intercept with the depth-axis gives the CZ thickness, as shown in Figures 2.3c and 2.4.

In numerical modeling of firn air transport, convection can be included in several ways. The most rudimentary way is to use the bottom of the CZ as the upper boundary, and assume the air above to be of atmospheric composition. A more advanced approach is to include an eddy diffusion term that equally affects all gases and isotopologues (Kawamura et al., 2006):

$$D_{\mathrm{eddy}}(z) = D^0_{\mathrm{eddy}} \exp\left(-\frac{z}{H}\right) \tag{2.7}$$

where D^0_{eddy} is the eddy diffusivity at the surface and H is a characteristic depth scale. The eddy diffusion terms prevents gravitational separation by overwhelming molecular diffusion.

2.4.2.3 Advection

The bulk motion of air in the open porosity (section 2.3.2) gives rise to downward advective mass transfer of trace gases. Firn air models deal with advection in different ways. It can be included by dividing the firn column into boxes of equal air content, and shuffling them downwards after a given time interval has elapsed (Schwander et al., 1993). An advantage of this approach is that it minimizes numerical diffusion artifacts. Alternatively, advection can be included as a continuous flux using a calculated air velocity in the open pores (Rommelaere et al., 1997; Sugawara et al., 2003). A third approach is to work in a Lagrangian reference frame that moves downwards with descending ice layers (Trudinger et al., 1997). It must be noted that this approach overestimates the advective transport, unless the backflow due to pore compaction is explicitly taken into account.

2.4.2.4 Dispersive mixing

Equation (2.4) describes the average air velocity; in reality a non-uniform velocity distribution exists between air expelled upwards by pore compaction, and air in isolated pockets which is advected downwards at the velocity of descending ice layers. Furthermore, atmospheric pressure variations and firn densification induce pressure gradients in the firn, which force viscous air flow. All these macroscopic flow patterns lead to dispersive mixing throughout the firn column, although it is overwhelmed by molecular diffusion in the DZ. Soil air studies have shown that viscous flow from atmospheric pressure fluctuations can induce mixing down to tens of meters, and that the dispersive flux can exceed the diffusive one (Massmann and Farrier, 1992). Firn air models do not explicitly include these flow patterns, and dispersive mixing

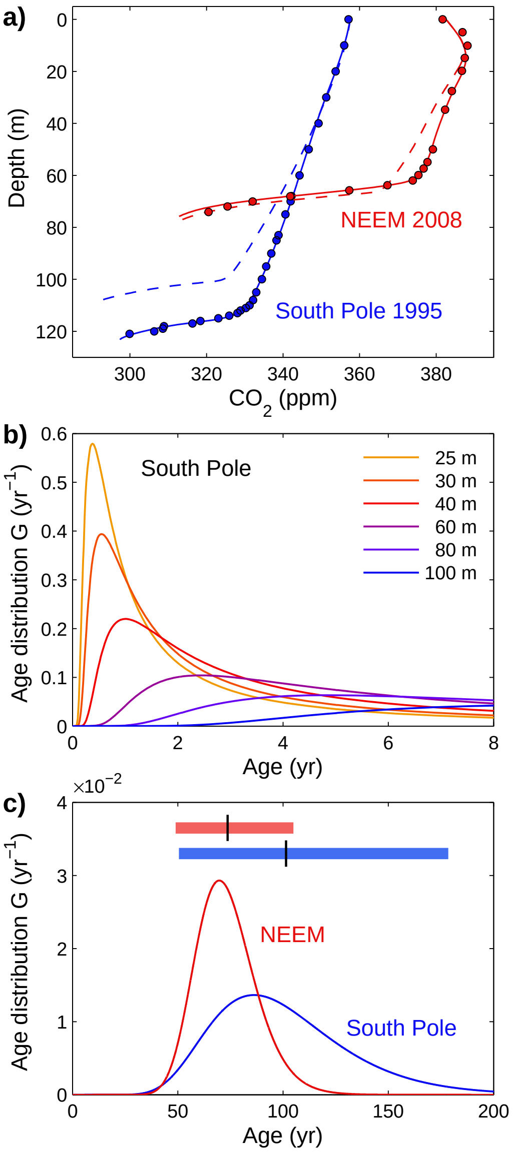

Figure 2.5: **a)** *Tuning procedure for transport modeling. Dashed lines show model solutions using the diffusivity parameterization of Schwander et al. (1988); solid lines show the optimized fit using CO_2 as a reference tracer. The northern hemisphere CO_2 seasonal cycle is clearly visible in the upper firn at NEEM.* **b)** *CO_2 age distributions for selected depths at South Pole.* **c)** *Comparison of NEEM and South Pole age distributions at the close-off depth (78 and 122 m, respectively). Top bars show the 95% age interval and mean CO_2 age.*

is mostly neglected. Some studies include dispersion phenomenologically through an eddy diffusion term in the deepest firn (Buizert et al., 2011; Severinghaus et al., 2010).

2.5 Dating of firn air and reconstructing recent atmospheric composition

2.5.1 Reconstructing the effective diffusivity

Numerical firn air transport models are essential for dating and interpretation of firn air records. The largest uncertainty in the transport description is how the effective diffusivity of gases changes with depth (Eq. 2.5). Best results are obtained when the diffusivity profile is reconstructed through an inverse method (Rommelaere et al., 1997; Trudinger et al., 1997). The method consists of forcing a firn air model with a reference tracer of know atmospheric history (usually CO_2 or CH_4), and optimizing the fit to the measurements through adjusting the diffusivity profile. The procedure is illustrated in Figure 2.5a for South Pole (SPO) and NEEM. The dashed line shows the modeled CO_2 mixing ratio using the tortuosity parameterization of (Schwander et al., 1988). The solid lines show the fit to the data after the optimization procedure.

Several studies have used multiple reference tracers simultaneously to improve the diffusivity reconstruction (Buizert et al., 2011; Trudinger et al., 2002).

2.5.2 Age distribution

Firn air does not have a single age, but is a mixture of air with different ages. Figure 2.5b shows for SPO how the CO2 age distribution $G(z, t)$ progresses with depth. The mean age $\Gamma(z)$ of the gas mixture (first moment of the distribution) increases with depth, as the gases need time to be transported into the firn. Diffusion broadens the distribution with depth. Figure 2.5c compares age distributions at the bottom of the firn column for NEEM and SPO. The latter has a longer firn column and low accumulation rate, resulting in older air at the bottom of the firn as well as a wider distribution.

The gas age distribution, which is different for each gas, provides a complete description of the firn transport properties. Age distributions can be calculated by forcing a numerical firn air transport model at the atmospheric boundary with a rectangular pulse of short duration. Alternatively, they have been inferred experimentally by measuring the spread of the $\Delta^{14}C$-CO_2 “bomb spike” caused by atmospheric testing of thermonuclear weapons, which peaks in the early to mid 1960s (Levchenko et al., 1996).

The gradual nature of the trapping process further broadens the age distribution. Air bubbles found at a single depth have not all been formed at the same time, and represent a mixture of ages. Within the LIZ, where the majority of bubbles form, gas diffusivities are small and air in the open pores is advected downwards at nearly the same velocity as the ice (Figure 2.3b). Consequently the broadening due to trapping is small compared to the diffusive broadening described above (Blunier and Schwander, 2000).

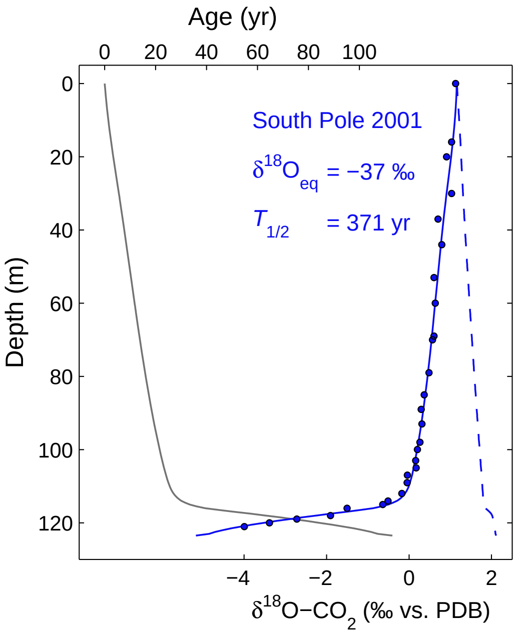

Figure 2.6: Oxygen exchange between CO_2 and firn results in ^{18}O depletion with depth (lower axis). The dashed line shows the expected $\delta^{18}O$ signal in the absence of exchange; the solid line gives the best fit to the data based on the modeled ages (grey curve, upper axis) and the parameters listed. The reaction half-time $t_{1/2}$ is the only parameter which is tuned in the data fitting.

2.5.3 Firn air dating with δ^{18}O of CO_2

An alternative firn air dating method based on the isotopic composition of CO_2 has been presented by Clark et al. (2007). Atmospheric δ^{18}O-CO_2 is relatively stable over time (Allison and Francey, 2007). Within the firn, atomic oxygen exchange with water molecules gradually alters the oxygen isotopic composition of CO_2, until equilibrium with the strongly depleted δ^{18}O of glacial ice is reached (Siegenthaler et al., 1988). This principle is illustrated in Figure 2.6 for SPO firn.

Depending on the site temperature, the time required for the magnitude of the exchange to reach half its final magnitude ($t_{1/2}$) ranges from tens to hundreds of years depending on temperature (Assonov et al., 2005). Knowing the rate of O-exchange, the amount of time the CO_2 has been in contact with the ice (i.e. the age) can be calculated. The main advantage of the technique is its applicability to warm sites with summer melt layers that complicate conventional dating. The drawback is that $t_{1/2}$ and the equilibrium fractionation must be well known. Clark et al. (2007) solve this issue by using the Δ^{14}C-CO_2 signal, which peaks around 1963, as an absolute age marker to calibrate $t_{1/2}$.

2.5.4 Reconstructing recent atmospheric composition

The firn air itself preserves a continuous record of atmospheric composition which can be sampled to reconstruct trace gas mixing ratios and isotopes for the recent atmosphere. Each firn air sample represents a mixture of gas ages, and consequently mixing ratios measured in the firn cannot be directly mapped onto a timescale.

Once the firn air transport is well characterized using reference tracers, the forward diffusive problem is well described by the modeled age distribution alone. Subsequently the most probable atmospheric history of a trace gas of interest can be reconstructed from firn air measurements through an inverse method (Rommelaere et al., 1997; Sugawara et al., 2003; Trudinger et al., 2002). For a more rudimentary dating, mixing ratios of a trace gas of interest can also be directly compared to reference gas measurements at identical sampling depths (Montzka et al., 2004).

Firn air has thus been used to reconstruct the recent atmospheric mixing ratios and/or isotopic composition of e.g. carbon dioxide (e.g. Etheridge et al., 1996), methane (e.g. Bräunlich et al., 2001), ethane (Aydin et al., 2011), nitrous oxide (e.g. Ishijima et al., 2007), carbon monoxide (Assonov et al., 2007), several halocarbons (e.g. Butler et al., 1999; Sturges et al., 2001a) and carbonyl sulfide (e.g. Sturges et al., 2001b).

2.6 Effects of firn air transport on ice core and firn gas records

The firn layer complicates the interpretation of ice core records, as it alters the atmospheric composition prior to bubble closure. At the same time the peculiarities of firn air transport give rise to additional signals which can be used for dating and climate reconstruction. In this section we discuss the consequences of firn air transport for the interpretation of ice core and firn air records.

2.6.1 Delta age and gravitational fractionation

Continued exchange with the atmosphere keeps firn air at the lock-in depth younger than the surrounding ice, resulting in an age difference Δage between glacial ice and the air bubbles it contains (Schwander and Stauffer, 1984). This is arguably the most important artifact of the firn layer. Accurate Δage estimates are pivotal in investigating the relative timing of abrupt changes in temperature and greenhouse gas concentrations (Barnola et al., 1991; Fischer et al., 1999), inter-hemispheric synchronization of ice core records (Blunier and Brook, 2001; Morgan et al., 2002) and deriving consistent ice core timescales (Lemieux-Dudon et al., 2010). Figure 2.7 shows age estimates as a function of accumulation rate and temperature, assuming stationary conditions. The figure also indicates modern day conditions of several firn

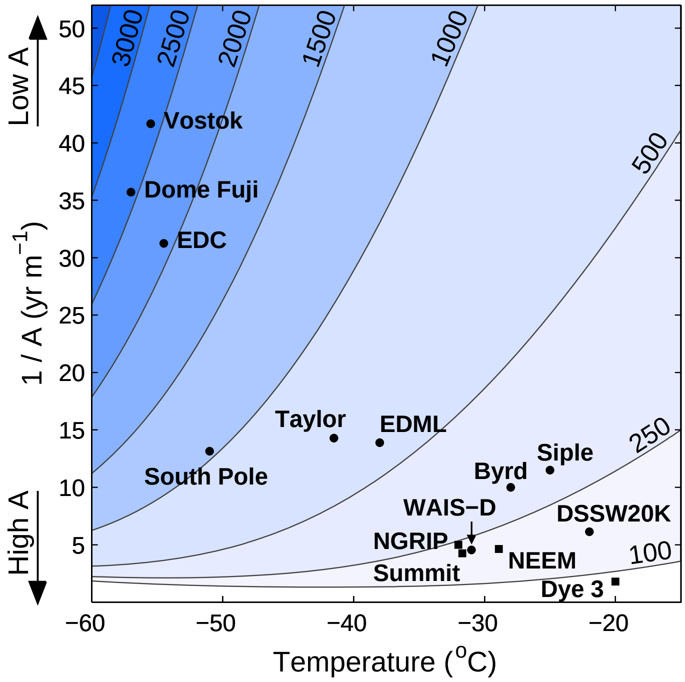

Figure 2.7: Contour plot of age estimates as a function of temperature and inverse accumulation rate (i.e. the number of annual layers per meter ice). Indicated are modern day conditions of several ice coring sites. Density profiles were calculated using the steady state Herron-Langway model (Herron and Langway, 1980). Following Blunier and Schwander (2000), we assume gas lock-in at a density of 14 kg m^{-3} below the mean close-off density of Eq. (2.1). The age of the air was parameterized following Schwander et al. (1997).

sampling and ice coring sites.

The Δage is fixed at the lock-in depth, where gas diffusion effectively ceases and the stagnant air is advected downwards with the ice. The modern day Δage can be estimated with an accuracy of a few years for sites that are well characterized using reference tracers; the largest uncertainty being the fraction of bubbles formed above the lock-in depth. To estimate Δage back in time, a combination of several methods can be used. First, past changes in lock-in depth can be estimated from accumulation and temperature variations, using firn densification models (Barnola et al., 1991; Goujon et al., 2003). Second, climatic changes recorded in both the gas record and in precipitation stable isotopes allow determination of Δdepth (Figure 2.8), which in turn constrains Δage (Caillon et al., 2001, 2003; Severinghaus et al., 1998). Third, records of e.g. CH_4 or δ^{18}O-O_2 from other, well dated ice cores, can be used for synchronization of chronologies (Capron et al., 2010; Loulergue et al., 2007).

The lock-in depth calculated by densification models can be compared to measurements of the gravitational enrichment in δ^{15}N-N$_2$, which records the diffusive column length. Note that the diffusive column length does not directly give the lock-in depth, as the thickness of the CZ is unknown. Models predict a deeper lock-in depth during colder glacial conditions, implying a larger δ^{15}N-N$_2$. This is indeed observed in Greenland ice cores (Schwander et al., 1997). Antarctic ice cores (with the exception of the coastal Byrd site) show a pronounced model-data mismatch with lower δ^{15}N-N$_2$ (i.e. shorter diffusive column) during glacial conditions (Landais et al., 2006). An increased CZ thickness is often invoked to explain the mismatch, where the Megadunes site, with an unusually thick convective zone of > 23 m, could provide a modern analog for central Antarctic glacial conditions (Severinghaus et al., 2010).

Measurements of gravitational enrichment in δ^{15}N-N$_2$ are also used to correct gas records for the effect of gravity.

2.6.2 Thermal fractionation and gas thermometry

Thermal diffusion causes isotopic fractionation in the presence of temperature gradients (section 2.4.2.1). Seasonal temperature variations and the associated isotope effect occur only in the upper firn (Figure 2.4). They could potentially affect the deep firn (and thereby the ice core record) through seasonality in transport properties, such as convective mixing and temperature dependent diffusion coefficients. No evidence for such rectifier effects was found (Severinghaus et al., 2001); seasonal thermal fractionation should have little or no impact on the ice core record.

Climate-induced changes in mean annual surface temperature, on the other hand, can cause isotopic signals in the ice core record if the temperature change is sufficiently large and rapid. This principle is illustrated in Fig 2.8 for the GISP2 core in central Greenland. Abrupt warming events during the last deglaciation are accompanied by positive δ^{15}N and δ^{40}Ar excursions as the deep, colder firn gets enriched in heavy isotopes relative to the warmer surface. As the temperature sensitivity of δ^{15}N and δ^{40}Ar/4 is different, the signals can be used in combination to infer the amplitude of the temperature change (Landais et al., 2004; Leuenberger et al., 1999; Severinghaus and Brook, 1999). The excursions furthermore provide clear time markers in the gas record that can be used to determine Δage more accurately than densification models allow. The method does not work well for Antarctica where temperature changes are more gradual.

2.6.3 Molecular size fractionation at close-off

Within the LIZ a systematic enrichment is observed for gas species with a small molecular diameter, such as He, Ar, Ne and O$_2$ (Huber et al., 2006; Severinghaus and Battle, 2006). This has been explained by the preferential exclusion of these species from closing bubbles, causing them to accumulate in the open porosity. Closed bubbles are pressurized through continued firn compaction, which increases gas partial

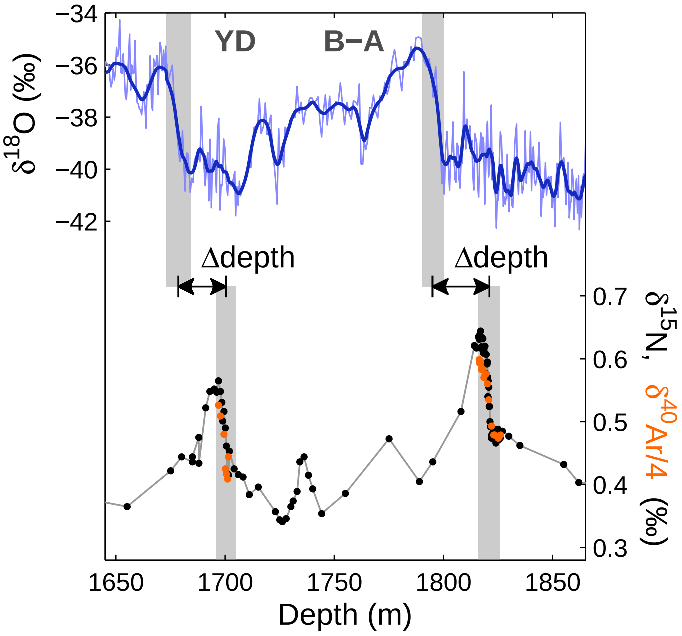

Figure 2.8: GISP2 oxygen isotopes of precipitation with 200-yr running average (upper curve, left axis) and transient thermal fractionation signals in N_2 and Ar caused by rapid warming over Greenland (lower data, right axis). Data from (Severinghaus et al., 1998) and (Severinghaus and Brook, 1999). The depth difference between the observed warming in the ice and gas records constrains Δage.

pressures in the bubbles relative to the open porosity. This gradient drives selective permeation of gas through the ice lattice. Huber et al. (2006) find a strong dependence of the fractionation magnitude on the collision diameter of the molecule, suggesting a critical size of 3.6 Å. Recently Battle et al. (2011) reported that the O_2 excluded from the closing bubbles is isotopically depleted in δ^{18}O-O_2, showing the permeation through the ice lattice to be mass dependent. The mechanisms causing close-off fractionation are similar to those responsible for post-coring gas loss during ice sample storage (Bender et al., 1995).

The close-off fractionation is shown in Figure 2.9 for SPO firn. The enrichment is strongest in the LIZ where the vast majority of bubbles are occluded, and the low effective diffusivity prevents diffusion of the signal. Note that a gradient exists in the DZ, indicative of an upward diffusive gas flux. Hereby some O_2 (Ne) is lost to the atmosphere, leading to a correspondingly depleted $\delta O_2/N_2$ ($\delta Ne/N_2$) in gas bubbles.

It has been found that $\delta O_2/N_2$ can be used as a local summer insolation proxy, allowing orbital tuning of ice core chronologies (Bender, 2002; Kawamura et al.,

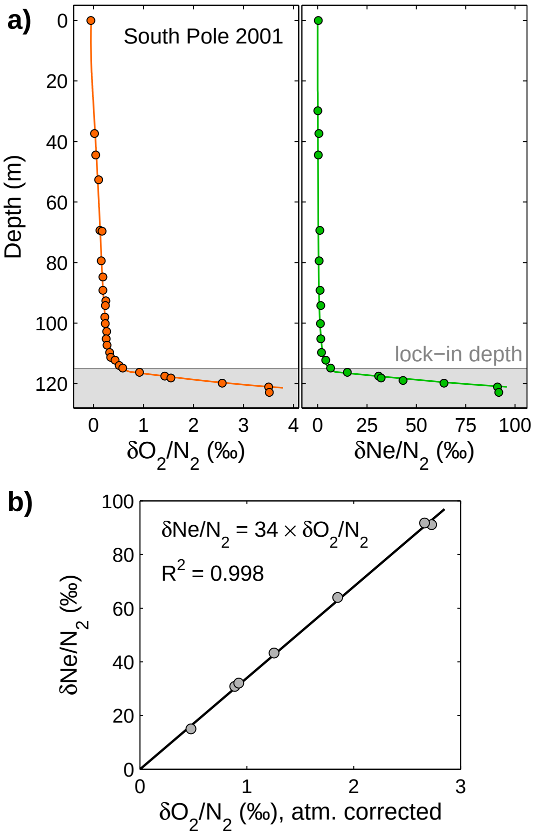

Figure 2.9: Molecular size fractionation during bubble close-off, data and model output are from Severinghaus and Battle (2006). **a)** *Enrichment in O_2 and Ne vs. N_2, expressed in delta notation using the modern atmosphere as the reference. Data are corrected for the effect of gravity. Note the slope in the DZ, indicative of a diffusive upward flux.* **b)** *After $\delta O_2/N_2$ has been corrected for the atmospheric trend (mostly due to anthropogenic influence), there is a linear relation between $\delta Ne/N_2$ and $\delta O_2/N_2$, indicating their preferential expulsion from closing bubbles occurs with a constant ratio.*

2007). This is thought to be controlled by a chain of events. Summer insolation influences physical properties of surface ice grains, which in time will determine physical properties of deep firn strata after densification and metamorphism. Bender (2002) suggested that physical properties of grains near the firn-ice transition directly influence the magnitude of the O_2/N_2 fractionation. More recently, Fujita et al. (2009) proposed a model in which deep firn air transport is modulated, thus controlling the amount of O_2 lost to the atmosphere. Note that, though measured in the gas phase, $\delta O_2/N_2$ dating constrains the ice age and not the gas age.

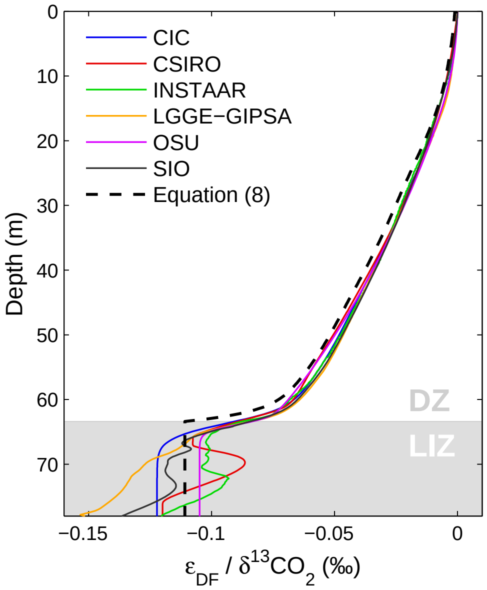

Figure 2.10: Isotopic diffusive fractionation in the NEEM firn for a hypothetical atmospheric CO_2 *scenario. See Buizert et al. (2011) for details and model acronyms.*

2.6.4 Isotopic diffusive fractionation

A secular variation in the atmospheric mixing ratio of a gas species results in isotopic fractionation in the firn, even in the absence of a changing atmospheric isotopic composition (Trudinger et al., 1997). As an example, consider a rise in atmospheric CO_2. The lighter $^{12}CO_2$ isotopologue diffuses faster into the firn than $^{13}CO_2$, giving rise to isotopic depletion with depth. This diffusive fractionation $\varepsilon_{\mathrm{DF}}$ can be approximated by

$$\varepsilon_{\mathrm{DF}} = \begin{cases} \frac{k}{C}\left(\frac{D_i}{D_j} - 1\right)\Gamma(z) & \text{for} \quad z \le z_{\mathrm{lid}} \\ \varepsilon_{\mathrm{DF}}(z_{\mathrm{lid}}) & \text{for} \quad z > z_{\mathrm{lid}} \end{cases} \tag{2.8}$$

where C is the atmospheric mixing ratio (ppm), k the rate of increase (ppm yr^{-1}), D_i (D_j) the diffusion coefficient of the minor (major) isotopologue, $\Gamma(z)$ the mean gas age (yr), and z_{lid} the lock-in depth.

Figure 2.10 shows the diffusive fractionation calculated with Eq. (2.8) and six numerical firn air models for a hypothetical exponential CO_2 increase of $k/C = 2.5 \cdot 10^{-3}$ (equivalent to $k = 1$ ppm yr^{-1} at $C = 400$ ppm), while keeping $\delta^{13}CO_2$ fixed at 0 ‰. Within the DZ, the profiles agree well. Within the LIZ the model solutions diverge, as the models use different parameterizations of LIZ transport. More work is needed to elucidate the nature of LIZ transport, and thereby the true magnitude of the diffusive fractionation.

Firn air and ice core records need to be corrected for the effect of diffusive fractionation, although often the effect will be small. Some corrections for the recent anthropogenic increase found in literature are 0.1 ‰for $\delta^{13}CO_2$ at Law Dome (Francey et al., 1999) and 1.2 ‰for $\delta^{13}CH_4$ at WAIS-Divide (Mischler et al., 2009). The effect is larger for CH_4 as the relative mass difference between the isotopologues, and thereby the ratio of diffusivities, is larger.

2.6.5 Smoothing by diffusion and bubble trapping

The firn causes smoothing of the atmospheric signal, limiting the temporal resolution at which atmospheric variations are recorded in the ice. One can think of the firn as a low-pass filter to the atmospheric signal; high frequency variations, such as the annual cycles of trace gases, are not preserved. Spahni et al. (2003) studied the attenuation of the rapid CH_4 excursion associated with the 8.2 kyr event, and found it to be attenuated by about 13% in the GRIP core, and 44% in the EPICA Dome C core. The low accumulation rate and deeper lock-in depth at the latter site are responsible for the stronger attenuation.

By taking the Fourier transform of the age distribution, we can evaluate how atmospheric variations at different time scales are attenuated by the firn column (Figure 2.11). As the bubble trapping occurs predominately throughout the LIZ, the age distribution halfway the LIZ is taken as a measure of the signal recorded in the air bubbles. Additional smoothing by the trapping process is not accounted for. Atmospheric variations on time scales of several hundreds of years or longer are recorded with their full amplitude; variations faster than ∼50 years are attenuated so strongly they cannot be observed within the measurement noise. Variations at intermediate time scales (such as the aforementioned 8.2 kyr event) are recorded with reduced amplitude. In theory, the true atmospheric history could be reconstructed from high resolution records with deconvolution techniques also used for water stable isotope records (Johnsen, 1977).

2.7 Summary

Firn air studies are important for interpretation of ice core gas records and reconstructing recent atmospheric variations. Following $\delta^{15}N$-N_2 gravitational enrichment, the firn column is divided in the convective, diffusive and lock-in zones, where gas transport is dominated by surface ventilation, diffusion and advection, respectively. Transport properties are determined by pore geometry and connectivity, as well as density layering. Diffusivity measurements on finite samples do not represent the entire firn, and diffusivity needs to be reconstructed using reference tracers. Gravitational separation, Δage, diffusive smoothing and diffusive isotopic fractionation are firn effects that need to be considered when interpreting ice core records. Thermal fractionation and close-off fractionation give rise to new proxies that can be used

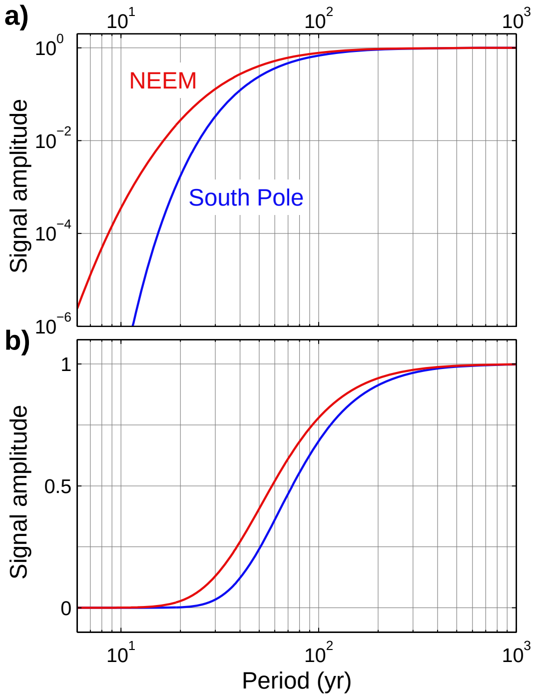

Figure 2.11: Bode plot of the firn transfer function on **a)** *a log-log scale and* **b)** *a semi-log scale, obtained by fast Fourier transform (FFT) of the modeled* CO_2 *age distributions halfway the LIZ. The transmitted signal amplitude is plotted as a function of the period of the oscillation (*$P = 1/f$ *with* f *the frequency in* yr^{-1}*).*

for temperature reconstruction and dating.

2.8 References

Albert, M. R., Schultz, E. F., and Perron, F. E. J. (2000). Snow and firn permeability at siple dome, antarctica. *Ann. Glaciol.*, 31:353–356.

Allison, C. E. and Francey, R. J. (2007). Verifying southern hemisphere trends in atmospheric carbon dioxide stable isotopes. *J. Geophys. Res.-Atm*, 112(D21):27. ISI Document Delivery No.: 228CQ Times Cited: 5 Cited Reference Count: 62 Allison, C. E. Francey, R. J.

Assonov, S. S., Brenninkmeijer, C. A. M., and Jockel, P. (2005). The o-18 isotope exchange rate between firn air co_2 and the firn matrix at three antarctic sites. *J. Geophys. Res.-Atm*, 110(D18):15.

Assonov, S. S., Brenninkmeijer, C. A. M., Jockel, P. J., Mulvaney, R., Bernard, S., and Chappellaz, J. (2007). Evidence for a co increase in the sh during the 20th century based on firn air samples from berkner island, antarctica. *Atmos. Chem. Phys.*, 7:295–308.

Aydin, M., Verhulst, K. R., Saltzman, E. S., Battle, M. O., Montzka, S. A., Blake, D. R., Tang, Q., and Prather, M. J. (2011). Recent decreases in fossil-fuel emissions of ethane and methane derived from firn air. *Nature*, 476(7359):198–201.

Barnola, J. M., Pimienta, P., Raynaud, D., and Korotkevich, Y. S. (1991). Co2-climate relationship as deduced from the vostok ice core - a reexamination based on new measurements and on a reevaluation of the air dating. *Tellus B*, 43(2):83–90. ISI Document Delivery No.: FG714 Times Cited: 119 Cited Reference Count: 0.

Battle, M., Bender, M., Sowers, T., Tans, P. P., Butler, J. H., Elkins, J. W., Ellis, J. T., Conway, T., Zhang, N., Lang, P., and Clarket, A. D. (1996). Atmospheric gas concentrations over the past century measured in air from firn at the south pole. *Nature*, 383(6597):231–235.

Battle, M. O., Severinghaus, J. P., Sofen, E. D., Plotkin, D., Orsi, A. J., Aydin, M., Montzka, S. A., Sowers, T., and Tans, P. P. (2011). Controls on the movement and composition of firn air at the west antarctic ice sheet divide. *Atmos. Chem. Phys. Discuss.*, 11(6):18633–18675.

Bender, M., Sowers, T., and Lipenkov, V. (1995). On the concentrations of o-2, n-2, and ar in trapped gases from ice cores. *J. Geophys. Res.-Atm*, 100(D9):18651–18660. ISI Document Delivery No.: RV887 Times Cited: 23 Cited Reference Count: 32.

Bender, M. L. (2002). Orbital tuning chronology for the vostok climate record supported by trapped gas composition. *Earth Planet Sc. Lett.*, 204(1-2):275–289. ISI Document Delivery No.: 619LJ Times Cited: 24 Cited Reference Count: 57.

Bender, M. L., Sowers, T., Barnola, J., M, and Chappellaz, J. (1994). Changes in the o2/n2 ratio of the atmosphere during recent decades reflected in the composition of air in the firn at vostok station, antarctica. *Geophys. Res. Lett.*, 21(3):189–192.

Blunier, T. and Brook, E. J. (2001). Timing of millennial-scale climate change in antarctica and greenland during the last glacial period. *Science*, 291(5501):109–112. ISI Document Delivery No.: 389VJ Times Cited: 368 Cited Reference Count: 33.

Blunier, T. and Schwander, J. (2000). *Gas enclosure in ice: age difference and fractionation*, pages 307–326. Hokkaido University Press, Sapporo.

Bräunlich, M., Aballanin, O., Marik, T., Jockel, P., Brenninkmeijer, C. A. M., Chappellaz, J., Barnola, J. M., Mulvaney, R., and Sturges, W. T. (2001). Changes in the global atmospheric methane budget over the last decades inferred from c-13 and d isotopic analysis of antarctic firn air. *J. Geophys. Res.-Atm*, 106(D17):20465–20481.

Buizert, C., Martinerie, P., Petrenko, V. V., Severinghaus, J. P., Trudinger, C. M., Witrant, E., Rosen, J. L., Orsi, A. J., Rubino, M., Etheridge, D. M., Steele, L. P., Hogan, C., Laube, J. C., Sturges, W. T., Levchenko, V. A., Smith, A. M., Levin, I., Conway, T. J., Dlugokencky, E. J., Lang, P. M., Kawamura, K., Jenk, T. M., White, J. W. C., Sowers, T., Schwander, J., and Blunier, T. (2011). Gas transport in firn: multiple-tracer characterisation and model intercomparison for neem, northern greenland. *Atmos. Chem. Phys. Discuss.*, 11:15975–16021.

Butler, J. H., Battle, M., Bender, M. L., Montzka, S. A., Clarke, A. D., Saltzman, E. S., Sucher, C. M., Severinghaus, J. P., and Elkins, J. W. (1999). A record of atmospheric halocarbons during the twentieth century from polar firn air. *Nature*, 399(6738):749–755.

Caillon, N., Severinghaus, J. P., Barnola, J. M., Chappellaz, J., Jouzel, J., and Parrenin, F. (2001). Estimation of temperature change and of gas age - ice age difference, 108 kyr b.p., at vostok, antarctica. *J. Geophys. Res.*, 106(D23):31893–31901.

Caillon, N., Severinghaus, J. P., Jouzel, J., Barnola, J.-M., Kang, J., and Lipenkov, V. Y. (2003). Timing of atmospheric co_2 and antarctic temperature changes across termination iii. *Science*, 299(5613):1728–1731.

Capron, E., Landais, A., Lemieux-Dudon, B., Schilt, A., Masson-Delmotte, V., Buiron, D., Chappellaz, J., Dahl-Jensen, D., Johnsen, S., Leuenberger, M., Loulergue, L., and Oerter, H. (2010). Synchronising edml and northgrip ice cores using [delta]18o of atmospheric oxygen ([delta]18oatm) and ch4 measurements over mis5 (80-123 kyr). *Quaternary Sci. Rev.*, 29(1-2):222–234. doi: DOI: 10.1016/j.quascirev.2009.07.014.

Clark, I. D., Henderson, L., Chappellaz, J., Fisher, D., Koerner, R., Worthy, D. E. J., Kotzer, T., Norman, A.-L., and Barnola, J.-M. (2007). Co2 isotopes as tracers of firn air diffusion and age in an arctic ice cap with summer melting, devon island, canada. *J. Geophys. Res.*, 112.

Colbeck, S. C. (1989). Air movement in snow due to windpumping. *J. Glaciol.*, 35(120):209–213.

Courville, Z., Hörhold, M., Hopkins, M., and Albert, M. (2011). Lattice-boltzmann modeling of the air permeability of polar firn. *J. Geophys. Res.*, 115(F4):F04032.

Craig, H., Horibe, Y., and Sowers, T. (1988). Gravitational separation of gases and isotopes in polar ice caps. *Science*, 242(4886):1675–1678.

Dreyfus, G. B., Jouzel, J., Bender, M. L., Landais, A., Masson-Delmotte, V., and Leuenberger, M. (2010). Firn processes and δ^{15}n: potential for a gas-phase climate proxy. *Quaternary Sci. Rev.*, 29(1-2):28–42.

Dullien, F. A. L. (1975). Single phase flow through porous media and pore structure. *The Chemical Engineering Journal*, 10(1):1–34.

Etheridge, D. M., Steele, L. P., Langenfelds, R. L., Francey, R. J., Barnola, J. M., and Morgan, V. I. (1996). Natural and anthropogenic changes in atmospheric co_2 over the last 1000 years from air in antarctic ice and firn. *J. Geophys. Res.*, 101(D2):4115–4128.

Fabre, A., Barnola, J. M., Arnaud, L., and Chappellaz, J. (2000). Determination of gas diffusivity in polar firn: Comparison between experimental measurements and inverse modeling. *Geophys. Res. Lett.*, 27(4):557–560.

Fischer, H., Wahlen, M., Smith, J., Mastroianni, D., and Deck, B. (1999). Ice core records of atmospheric co_2 around the last three glacial terminations. *Science*, 283(5408):1712–1714.

Francey, R., Allison, C., Etheridge, D., Trudinger, C., Enting, I., Leuenberger, M., Langenfelds, R., Michel, E., and Steele, L. (1999). A 1000-year high precision record of delta C-13 in atmospheric CO_2. *Tellus B*, 51(2):170–193.

Freijer, J. I. and Leffelaar, P. A. (1996). Adapted fick's law applied to soil respiration. *Water Resour. Res.*, 32(4):791–800.

Freitag, J., Dorbrindt, U., and Kipfstuhl, J. (2002). A new method for predicting transport properties of polar firn with respect to gases on the pore-space scale. *Ann. Glaciol.*, 35:538–544. doi:10.3189/172756402781816582.

Freitag, J., Wilhelms, F., and Kipfstuhl, J. (2004). Microstructure-dependent densification of polar firn derived from x-ray microtomography. *J. Glaciol.*, 50:243–250. doi:10.3189/172756504781830123.

Fujita, S., Okuyama, J., Hori, A., and Hondoh, T. (2009). Metamorphism of stratified firn at dome fuji, antarctica: A mechanism for local insolation modulation of gas transport conditions during bubble close off. *J. Geophys. Res.*, 114.

Goujon, C., Barnola, J. M., and Ritz, C. (2003). Modeling the densification of polar firn including heat diffusion: Application to close-off characteristics and gas isotopic fractionation for antarctica and greenland sites. *J. Geophys. Res.-Atm*, 108(D24):18.

Herron, M. M. and Langway, C. C. (1980). Firn densification - an emperical model. *J. Glaciol.*, 25(93):373–385.

Huber, C., Beyerle, U., Leuenberger, M., Schwander, J., Kipfer, R., Spahni, R., Severinghaus, J. P., and Weiler, K. (2006). Evidence for molecular size dependent gas fractionation in firn air derived from noble gases, oxygen, and nitrogen measurements. *Earth Planet Sc. Lett.*, 243(1-2):61–73.

Ishijima, K., Sugawara, S., Kawamura, K., Hashida, G., Morimoto, S., Murayama, S., Aoki, S., and Nakazawa, T. (2007). Temporal variations of the atmospheric nitrous oxide concentration and its delta n-15 and delta o-18 for the latter half of the 20th century reconstructed from firn air analyses. *J. Geophys. Res.-Atm*, 112(D3):12.

Johnsen, S. J. (1977). Stable isotope homogenization of polar firn and ice.

Kaspers, K. A., van de Wal, R. S. W., van den Broeke, M. R., Schwander, J., van Lipzig, N. P. M., and Brenninkmeijer, C. A. M. (2004). Model calculations of the age of firn air across the antarctic continent. *Atmos. Chem. Phys.*, 4(5):1365–1380.

Kawamura, K., Parrenin, F., Lisiecki, L., Uemura, R., Vimeux, F., Severinghaus, J. P., Hutterli, M. A., Nakazawa, T., Aoki, S., Jouzel, J., Raymo, M. E., Matsumoto, K., Nakata, H., Motoyama, H., Fujita, S., Goto-Azuma, K., Fujii, Y., and Watanabe, O. (2007). Northern hemisphere forcing of climatic cycles in antarctica over the past 360,000 years. *Nature*, 448(7156):912–U4.

Kawamura, K., Severinghaus, J. P., Ishidoya, S., Sugawara, S., Hashida, G., Motoyama, H., Fujii, Y., Aoki, S., and Nakazawa, T. (2006). Convective mixing of air in firn at four polar sites. *Earth Planet Sc. Lett.*, 244(3-4):672–682.

Kipfstuhl, S., Faria, S. H., Azuma, N., Freitag, J., Hamann, I., Kaufmann, P., Miller, H., Weiler, K., and Wilhelms, F. (2009). Evidence of dynamic recrystallization in polar firn. *J. Geophys. Res.*, 114(B5):B05204.

Landais, A., Barnola, J. M., Kawamura, K., Caillon, N., Delmotte, M., Van Ommen, T., Dreyfus, G., Jouzel, J., Masson-Delmotte, V., Minster, B., Freitag, J., Leuenberger, M., Schwander, J., Huber, C., Etheridge, D., and Morgan, V. (2006). Firn-air delta n-15 in modern polar sites and glacial-interglacial ice: a model-data mismatch during glacial periods in antarctica? *Quaternary Sci. Rev.*, 25(1-2):49–62.

Landais, A., Caillon, N., Goujon, C., Grachev, A. M., Barnola, J. M., Chappellaz, J., Jouzel, J., Masson-Delmotte, V., and Leuenberger, M. (2004). Quantification of rapid temperature change during do event 12 and phasing with methane inferred from air isotopic measurements. *Earth Planet Sc. Lett.*, 225(1-2):221–232.

Lemieux-Dudon, B., Blayo, E., Petit, J.-R., Waelbroeck, C., Svensson, A., Ritz, C., Barnola, J.-M., Narcisi, B. M., and Parrenin, F. (2010). Consistent dating for antarctic and greenland ice cores. *Quaternary Sci. Rev.*, 29(1-2):8–20.

Leuenberger, M. C., Lang, C., and Schwander, J. (1999). Delta(15)n measurements as a calibration tool for the paleothermometer and gas-ice age differences: A case study for the 8200 bp event on grip ice. *J. Geophys. Res.-Atm*, 104(D18):22163–22170. ISI Document Delivery No.: 239UZ Times Cited: 40 Cited Reference Count: 37.

Levchenko, V. A., Francey, R. J., Etheridge, D. M., Tuniz, C., Head, J., Morgan, V. I., Lawson, E., and Jacobsen, G. (1996). The ^{14}c "bomb spike" determines the age spread and age of co$_2$ in law dome firn and ice. *Geophys. Res. Lett.*, 23(23):3345–3348.

Loulergue, L., Parrenin, F., Blunier, T., Barnola, J. M., Spahni, R., Schilt, A., Raisbeck, G., and Chappellaz, J. (2007). New constraints on the gas age-ice age difference along the epica ice cores, 0-50 kyr. *Climate of the Past*, 3(3):527–540. ISI Document Delivery No.: 215CJ Times Cited: 3 Cited Reference Count: 68 Loulergue, L. Parrenin, F. Blunier, T. Barnola, J.-M. Spahni, R. Schilt, A. Raisbeck, G. Chappellaz, J.

Loulergue, L., Schilt, A., Spahni, R., Masson-Delmotte, V., Blunier, T., Lemieux, B., Barnola, J. M., Raynaud, D., Stocker, T. F., and Chappellaz, J. (2008). Orbital and millennial-scale features of atmospheric ch4 over the past 800,000 years. *Nature*, 453(7193):383–386. ISI Document Delivery No.: 301AI Times Cited: 3 Cited Reference Count: 27 Loulergue, Laetitia Schilt, Adrian Spahni, Renato Masson-Delmotte, Valerie Blunier, Thomas Lemieux, Benedicte Barnola, Jean-Marc Raynaud, Dominique Stocker, Thomas F. Chappellaz, Jerome.

Lüthi, D., Le Floch, M., Bereiter, B., Blunier, T., Barnola, J.-M., Siegenthaler, U., Raynaud, D., Jouzel, J., Fischer, H., Kawamura, K., and Stocker, T. F. (2008). High-resolution carbon dioxide concentration record 650,000-800,000[thinsp]years before present. *Nature*, 453(7193):379–382.

Martinerie, P., Lipenkov, V. Y., Raynaud, D., Chappellaz, J., Barkov, N. I., and Lorius, C. (1994). Air content paleo record in the vostok ice core (antarctica): A mixed record of climatic and glaciological parameters. *J. Geophys. Res.*, 99:10565–10576.

Martinerie, P., Raynaud, D., Etheridge, D. M., Barnola, J. M., and Mazaudier, D. (1992). Physical and climatic parameters which influence the air content in polar ice. *Earth Planet Sc. Lett.*, 112(1-4):1–13.

Massmann, J. and Farrier, D. F. (1992). Effects of atmospheric pressures on gas transport in the vadose zone. *Water Resour. Res.*, 28(3):777–791.

Mischler, J. A., Sowers, T. A., Alley, R. B., Battle, M., McConnell, J. R., Mitchell, L., Popp, T., Sofen, E., and Spencer, M. K. (2009). Carbon and hydrogen isotopic composition of methane over the last 1000 years. *Global Biogeochem. Cy.*, 23.

Montzka, S. A., Aydin, M., Battle, M., Butler, J. H., Saltzman, E. S., Hall, B. D., Clarke, A. D., Mondeel, D., and Elkins, J. W. (2004). A 350-year atmospheric history for carbonyl sulfide inferred from antarctic firn air and air trapped in ice. *J. Geophys. Res.-Atm*, 109(D22):11.

Morgan, V., Delmotte, M., van Ommen, T., Jouzel, J., Chappellaz, J., Woon, S., Masson-Delmotte, V., and Raynaud, D. (2002). Relative timing of deglacial climate events in antarctica and greenland. *Science*, 297(5588):1862–1864.

Petit, J. R., Jouzel, J., Raynaud, D., Barkov, N. I., Barnola, J. M., Basile, I., Bender, M., Chappellaz, J., Davis, M., Delaygue, G., Delmotte, M., Kotlyakov, V. M., Legrand, M., Lipenkov, V. Y., Lorius, C., Pepin, L., Ritz, C., Saltzman, E., and Stievenard, M. (1999). Climate and atmospheric history of the past 420,000 years from the vostok ice core, antarctica. *Nature*, 399(6735):429–436. ISI Document Delivery No.: 202TH Times Cited: 1329 Cited Reference Count: 52.

Raynaud, D., Lipenkov, V., Lemieux-Dudon, B., Duval, P., Loutre, M. F., and Lhomme, N. (2007). The local insolation signature of air content in antarctic ice. a new step toward an absolute dating of ice records. *Earth Planet Sc. Lett.*, 261(3-4):337–349.

Rommelaere, V., Arnaud, L., and Barnola, J. M. (1997). Reconstructing recent atmospheric trace gas concentrations from polar firn and bubbly ice data by inverse methods. *J. Geophys. Res.-Atm*, 102(D25):30069–30083.

Schwander, J. (1989). The transformation of snow to ice and the occlusion of gases. In Oescher, H. and Langway, C., editors, *The Environmental record in glaciers and ice sheets*, pages 53–67. John Wiley, New York.

Schwander, J., Barnola, J. M., Andrie, C., Leuenberger, M., Ludin, A., Raynaud, D., and Stauffer, B. (1993). The age of the air in the firn and the ice at summit, greenland. *J. Geophys. Res.-Atm*, 98(D2):2831–2838.

Schwander, J., Sowers, T., Barnola, J. M., Blunier, T., Fuchs, A., and Malaize, B. (1997). Age scale of the air in the summit ice: Implication for glacial-interglacial temperature change. *J. Geophys. Res.-Atm*, 102(D16):19483–19493.

Schwander, J. and Stauffer, B. (1984). Age difference between polar ice and the air trapped in its bubbles. *Nature*, 311(5981):45–47.

Schwander, J., Stauffer, B., and Sigg, A. (1988). Air mixing in firn and the age of the air at pore close-off. In *Ann. Glaciol.*, volume 10, pages 141–145.

Severinghaus, J. P., Albert, M. R., Courville, Z. R., Fahnestock, M. A., Kawamura, K., Montzka, S. A., Muhle, J., Scambos, T. A., Shields, E., Shuman, C. A., Suwa, M., Tans, P., and Weiss, R. F. (2010). Deep air convection in the firn at a zero-accumulation site, central antarctica. *Earth Planet Sc. Lett.*, 293(3-4):359–367.

Severinghaus, J. P. and Battle, M. O. (2006). Fractionation of gases in polar lee during bubble close-off: New constraints from firn air ne, kr and xe observations. *Earth Planet Sc. Lett.*, 244(1-2):474–500.

Severinghaus, J. P. and Brook, E. J. (1999). Abrupt climate change at the end of the last glacial period inferred from trapped air in polar ice. *Science*, 286(5441):930–934.

Severinghaus, J. P., Grachev, A., and Battle, M. (2001). Thermal fractionation of air in polar firn by seasonal temperature gradients. *Geochem. Geophy. Geosy.*, 2.

Severinghaus, J. P., Sowers, T., Brook, E. J., Alley, R. B., and Bender, M. L. (1998). Timing of abrupt climate change at the end of the younger dryas interval from thermally fractionated gases in polar ice. *Nature*, 391(6663):141–146.

Siegenthaler, U., Friedli, H., Loetschewr, H., Moor, E., Neftel, A., Oeschger, H., and Stauffer, B. (1988). Stable-isotope ratios and concentration of co2 in air from polar ice cores. *Ann. Glaciol.*, 10:151–156.

Sowers, T., Bender, M., Raynaud, D., and Korotkevich, Y. S. (1992). Delta-n-15 of n_2 in air trapped in polar ice - a tracer of gas-transport in the firn and a possible constraint on ice age-gas age-differences. *J. Geophys. Res.-Atm*, 97(D14):15683–15697.

Spahni, R., Schwander, J., Flückiger, J., Stauffer, B., Chappellaz, J., and Raynaud, D. (2003). The attenuation of fast atmospheric ch_4 variations recorded in polar ice cores. *Geophys. Res. Lett.*, 30(11):1571.

Stone, J. O. (2000). Air pressure and cosmogenic isotope production. *J. Geophys. Res.-Solid Earth*, 105(B10):23753–23759. ISI Document Delivery No.: 364MG Times Cited: 374 Cited Reference Count: 29.

Sturges, W. T., McIntyre, H. P., Penkett, S. A., Chappellaz, J., Barnola, J. M., Mulvaney, R., Atlas, E., and Stroud, V. (2001a). Methyl bromide, other brominated methanes, and methyl iodide in polar firn air. *J. Geophys. Res.*, 106(D2):1595–1606.

Sturges, W. T., Penkett, S. A., Barnola, J., Marc, Chappellaz, J., Atlas, E., and Stroud, V. (2001b). A long-term record of carbonyl sulfide (cos) in two hemispheres from firn air measurements. *Geophys. Res. Lett.*, 28(21):4095–4098.

Sturrock, G. A., Etheridge, D. M., Trudinger, C. M., Fraser, P. J., and Smith, A. M. (2002). Atmospheric histories of halocarbons from analysis of antarctic firn air: Major montreal protocol species. *J. Geophys. Res.-Atm*, 107(D24):14.

Sugawara, S., Kawamura, K., Aoki, S., Nakazawa, T., and Hashida, G. (2003). Reconstruction of past variations of delta c-13 in atmospheric co_2 from its vertical distribution observed in the firn at dome fuji, antarctica. *Tellus B*, 55(2):159–169.

Thorstenson, D. C. and Pollock, D. W. (1989). Gas transport in unsaturated zones: Multicomponent systems and the adequacy of fick's laws. *Water Resour. Res.*, 25(3):477–507.

Trudinger, C. M. (2001). *The carbon cycle over the last 1000 years inferred from inversion of ice core data*. PhD thesis, Monash University, Australia.

Trudinger, C. M., Enting, I. G., Etheridge, D. M., Francey, R. J., Levchenko, V. A., Steele, L. P., Raynaud, D., and Arnaud, L. (1997). Modeling air movement and bubble trapping in firn. *J. Geophys. Res.-Atm*, 102(D6):6747–6763.

Trudinger, C. M., Etheridge, D. M., Rayner, P. J., Enting, I. G., Sturrock, G. A., and Langenfelds, R. L. (2002). Reconstructing atmospheric histories from measurements of air composition in firn. *J. Geophys. Res.-Atm*, 107(D24):13.

Waddington, E. D. and Cunningham, J. (1996). The effects of snow ventilation on chemical concentrations.

Weiler, K., Schwander, J., Leuenberger, M., Blunier, T., Mulvaney, R., Anderson, P. S., Salmon, R., and Sturges, W. T. (2009). *Seasonal Variations of Isotope Ratios and CO_2 Concentrations in Firn Air*, volume 68, pages 247–272. Institute of Low Temperature Science, Hokkaido University, Sapporo.

Witrant, E., Martinerie, P., Hogan, C., Laube, J. C., Kawamura, K., Capron, E., Montzka, S. A., Dlugokencky, E. J., Etheridge, D., Blunier, T., and Sturges, W. T. (2011). A new multi-gas constrained model of trace gas non-homogeneous transport in firn: evaluation and behavior at eleven polar sites. *Atmos. Chem. Phys. Discuss.*, 11(8):23029–23080.

3

Gas transport in firn: multiple-tracer characterisation and model intercomparison for NEEM, Northern Greenland

C. Buizert, P. Martinerie, V. V. Petrenko, J. P. Severinghaus, C. M. Trudinger, E. Witrant, J. L. Rosen, A. J. Orsi, M. Rubino, D. M. Etheridge, L. P. Steele, C. Hogan, J. C. Laube, W. T. Sturges, V. A. Levchenko, A. M. Smith, I. Levin, T. J. Conway, E. J. Dlugokencky, P. M. Lang, K. Kawamura, T. M. Jenk, J. W. C. White, T. Sowers, J. Schwander and T. Blunier[1]

3.1 Introduction

The compacted snow (firn) found in the accumulation zone of the major ice sheets acts as a unique archive of old air, preserving a continuous record of atmospheric composition from the present up to a century back in time (Battle et al., 1996). Sampling of this archive has allowed for reconstruction of the recent atmospheric history of many trace gas species (e.g. Butler et al., 1999; Sturrock et al., 2002; Aydin et al., 2004; Montzka et al., 2004; Assonov et al., 2007; Martinerie et al., 2009) and their isotopologues (e.g. Francey et al., 1999; Ferretti et al., 2005; Bernard et al., 2006). Because of its temporal range it naturally bridges the age gap between direct atmospheric observations and the ice core record (Etheridge et al., 1998). Firn air analysis has some significant advantages over the ice core technique. First, firn air can be sampled directly using a pumping line (Schwander et al., 1993), making an ice extraction step unnecessary. Second, large sample sizes can be obtained making this method very suited for studying e.g. recent changes in the isotopic composition

---

[1] This chapter has been published as C.Buizert et al.: Gas transport in firn: multiple-tracer characterisation and model intercomparison for NEEM, Northern Greenland., Atmos. Chem. Phys. Discuss. 11:15975-6021 (2011).

of trace gases (Sugawara et al., 2003; Röckmann et al., 2003; Ishijima et al., 2007). Third, because bubble occlusion introduces additional smoothing, firn air records can achieve higher temporal resolution than ice cores (Trudinger et al., 2004).

Another important motivation for studying firn air is the interpretation of ice core records. All air found in glacial ice has first traversed the firn, and has thus been affected by its transport properties and the bubble close-off process. Some of the most commonly described artifacts of firn air transport are: gravitational fractionation (Craig et al., 1988; Schwander, 1989), thermal fractionation in the presence of temperature gradients (Severinghaus et al., 2001), diffusive smoothing of rapid atmospheric variations (Spahni et al., 2003), molecular size fractionation during bubble close-off (Huber et al., 2006; Severinghaus and Battle, 2006), diffusive isotopic fractionation (Trudinger et al., 1997) and Δage, the finite age difference between gas bubbles and their surrounding ice (Schwander et al., 1997). In certain cases the peculiarities of firn air transport actually give rise to new proxies, e.g. for temperature (Severinghaus and Brook, 1999; Landais et al., 2004; Dreyfus et al., 2010) and local summer insolation (Kawamura et al., 2007).

Diffusion is the dominant mechanism by which variations in atmospheric composition are transferred into the firn. The effective diffusivity decreases with depth as the pore space decreases; unfortunately diffusivities measured on small firn samples do not adequately describe the behaviour of the whole firn (Fabre et al., 2000). Consequently the diffusivity profile with depth needs to be reconstructed for each firn air site independently through an inverse method (Rommelaere et al., 1997; Trudinger et al., 2002; Sugawara et al., 2003). The procedure consists of forcing a firn air transport model with the atmospheric history of a selected reference gas, often CO_2, and subsequently optimising the fit to measured mixing ratios in the firn by adjusting ("tuning") the effective diffusivity profile.

With few exceptions, the firn air modeling studies found in literature tune their effective diffusivity profile to a single tracer. For the NEEM firn air site in Northern Greenland we have chosen to tune the effective diffusivity to an ensemble of ten tracers, namely CO_2, CH_4, SF_6, CFC-11, CFC-12, CFC-113, HFC-134a, CH_3CCl_3, $^{14}CO_2$ and $\delta^{15}N_2$. The studies by Trudinger et al. (1997, 2002, 2004) also use a wide variety of tracers, including halocarbons, greenhouse gases and radiocarbon ($\Delta^{14}CO_2$), to characterise firn air transport. The main difference with these works is that we show how multiple tracers can be combined in a methodical tuning process. By systematically analysing all the uncertainties, both in the data and in the atmospheric histories of the references gases, we assign a unique weight to each data point in the tuning procedure. Using these uncertainty estimates we define an objective root mean square deviation (RMSD) criterion that is minimised in the tuning. We introduce tracers that have not previously been used in firn air studies, and provide atmospheric reconstructions for these species with realistic uncertainty estimates.

Our approach has several advantages. A central difficulty in reconstructing the diffusivity profile is that the problem is under-determined, with (infinitely) many solutions optimising the fit (Rommelaere et al., 1997). By adding more tracers, each with a unique atmospheric history, the diffusivity profile is constrained more strongly.

The final reconstructed profile is a trade-off between the demands of the different tracers. Second, many trace gases of interest, such as halocarbons, have a free air diffusivity that differs from CO_2 by up to a factor of 2. It is not a priori clear whether a profile tuned to CO_2 alone provides a good solution for these gases. The tracers in this study have a wide range of free air diffusivities, where the fastest tracer (CH_4) has a free air diffusivity that is three times that of the slowest one (CFC-113). Third, when using ten tracers the available dataset is much larger, with several data points at each sampling depth. This makes the final result more robust, i.e. less susceptible to effects of outliers and analytical biases. Finally, our method is less sensitive to errors in the reconstructed atmospheric history of individual reference gases. Our analysis shows that uncertainties in the atmospheric reconstruction are the largest source of potential error.

Apart from presenting a new methodology for characterising firn air sites, this work will also serve as a reference for other studies using NEEM firn air. The modeling in a number of forthcoming publications in this issue will be based on the diffusivity reconstructions presented here.

We further present a model intercomparison between six state of the art one-dimensional firn air transport models. All the models are tuned to the same dataset, using the same physical firn parameters, such as porosity, free-air diffusion coefficients, etc. To diagnose model performance we introduce four synthetic scenarios that are designed to probe specific aspects of the model physics.

For many sections in this work more information is available in the Supplement. Because of the vast amount of material we have chosen to structure it the same as this work for easy referencing. Sections marked with an asterisk (*) in this work have a corresponding section in the Supplement where additional information can be found. The Supplement also includes all the firn air data and atmospheric reconstructions used in this study.

3.2 Methods

3.2.1 NEEM 2008 firn air campaign*

The firn air used in this study was sampled during 14–30 July 2008 from two boreholes near the NEEM deep ice core drilling site, Northern Greenland (77.45° N 51.06° W). The sampling site was 1.5 km outside of the main camp and chosen to avoid contamination by going upwind of the prevailing wind direction. The two boreholes, S2 and S3, were separated by 64 m. Firn air was sampled by drilling through the firn layers to the desired depth, and lowering the firn air sampling system into the borehole. The sampling system consists of a purge and sample line, running through an inflatable bladder to seal off the firn air from the overlying atmosphere during sampling. S2 was sampled using the firn air system of the University of Bern (Schwander et al., 1993); S3 with the US firn air system (Battle et al., 1996). For this reason the boreholes are referred to as the “EU” and “US” holes, respectively. The CO_2 mixing ratio was monitored on the purge line with LICOR (US site) and

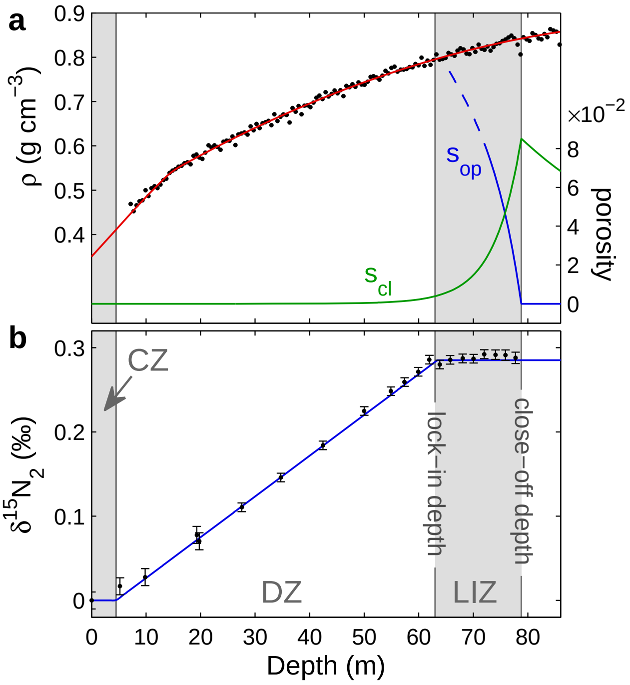

Figure 3.1: **(a)** *Firn density ρ (left axis), and the open and closed porosity s_{op} and s_{cl}, respectively (right axis). Black dots show firn density measurements in 0.55 m segments, the red line is the fit used in this study.* **(b)** *Gravitational enrichment as shown by $\delta^{15}\mathrm{N}_2$, corrected for thermal effects (Severinghaus et al., 2001). The blue line shows the barometric slope $\Delta M g(z-4.5)/RT$, where we use $\Delta M = 1\times10^{-3}$ kg mol^{-1}. Convective zone (CZ), diffusive zone (DZ) and lock-in zone (LIZ) are indicated by changes in shading.*

MAIHAK (EU site) CO_2 analysers to assess whether the firn air being pumped had been purged of modern air prior to sampling. A site map and a complete list of sampling depths can be found in the Supplement.

3.2.2 Physical characterisation of NEEM firn air site*

We use the assumption commonly made in firn air modeling that the firn density profile is in steady state, and that the site has been climatically stable over the study period. For the firn density profile $\rho(z)$ we use an empirical fit to the NEEM main ice core density measurements averaged over 0.55 m segments (S. J. Johnsen, personal communication, 2009). For each of the three stages of the densification process (Arnaud et al., 2000) we use a combination of quadratic and exponential functions to fit the data, where care is taken that the derivative is continuous over the transitions between the stages. The fit is generated on a $\Delta z = 0.2$ m grid, which is the spatial resolution used in this study. The density data and fit are shown in Fig. 3.1a. Following the temperature relationship given by Schwander et al. (1997), a solid ice density $\rho_{\mathrm{ice}} = 0.9206\,\mathrm{g\,cm^{-3}}$ is used.

We use an accumulation rate of $A = 0.216\,\mathrm{m\,yr^{-1}}$ ice equivalent, as derived from the 2007 NEEM S1 shallow core (D. Dahl-Jensen, personal communication, 2010). Since the model runs cover the period 1800–2008 CE, we used the average rate over the same period as a best estimate. This long-term average is slightly lower than our best estimate for the current day accumulation of $0.227\,\mathrm{m\,yr^{-1}}$.

The total porosity $s = 1 - \rho/\rho_{\mathrm{ice}}$ is divided into open and closed porosity (s_{op}, s_{cl}) using the parameterisation of Goujon et al. (2003):

$$s_{\mathrm{cl}} = 0.37s \left(\frac{s}{s_{\mathrm{co}}}\right)^{-7.6} \tag{3.1}$$

where s_{co} is the mean close-off porosity. The deepest point at which firn air could be sampled successfully was $z = 77.75\,\mathrm{m}$. The depth of total pore closure ($s_{\mathrm{op}} = 0$) was determined experimentally in the field by drilling the EU hole to a depth of $z = 83\,\mathrm{m}$, and subsequently raising the bladder in 0.5 m steps. The deepest point at which air could be pulled was $z = 79\,\mathrm{m}$, though the flow was insufficient for sampling. To be consistent with this observation we use $s_{\mathrm{co}} = 9.708 \times 10^{-2}$ in Eq. (3.1), which leads to total pore closure ($s_{\mathrm{op}} = 0$) at depth $z = 78.8\,\mathrm{m}$, as shown in Fig. 3.1a.

We use an annual mean site temperature of $-28.9\,^{\circ}\mathrm{C}$ as obtained from borehole thermometry on the EU hole, and assume an isothermal firn for this modeling exercise. Atmospheric pressure is 745 hPa.

Traditionally the firn column is divided into three zones, based on the gravitational enrichment with depth (Sowers et al., 1992). For NEEM the $\delta^{15}N_2$ together with the zonal division is shown in Fig. 3.1b. Using the barometric line fitting method (Kawamura et al., 2006), we obtain a convective zone (CZ) thickness of 4.5 m. The zone below is called the diffusive zone (DZ), as diffusion dominates the transport at these depths. The lock-in depth is defined as the depth at which gravitational enrichment stops, which happens at $z = 63\,\mathrm{m}$. Below we find the lock-in zone (LIZ), where advection with the ice matrix dominates the transport. This is also the region where the majority of the bubble occlusion occurs, as can be seen from the s_{cl} curve.

3.2.3 Gas measurements*

A total of 345 samples were taken from the boreholes, with atmospheric samples taken at three occasions during the sampling period. Different flask types were used (SilcoCan, stainless steel flasks and glass flasks); for the tracers used in this study no effect of flask type could be found in data comparison. We use firn air data from six different laboratories; an overview is given in Table 3.1.

Where applicable, data from IUP were corrected for known calibration offsets to place all data on the NOAA scales used in the atmospheric reconstructions. After the calibration correction no systematic offsets were observed between the different laboratories. As discussed below, there are significant offsets between the two boreholes, and data from the holes are not combined but treated separately. The $\Delta^{14}CO_2$ data and atmospheric reconstruction were both converted to a (mass conserving) ppm scale to allow $^{14}CO_2$ to be modeled like a regular tracer. Wherever multiple data

Table 3.1: Overview of firn air data used in this study. Acronyms represent: the School of Environmental Sciences at the University of East Anglia (UEA; Laube et al., 2010), NOAA Earth System Research Laboratory, Boulder CO (NOAA; Conway et al., 1994; Dlugokencky et al., 1994), the Institut für Umweltphysik at the University of Heidelberg (IUP; Levin et al., 2010, 2011), the Commonwealth Scientific and Industrial Research Organisation, Marine and Atmospheric Research (CSIRO; Francey et al., 2003), the Australian Nuclear Science and Technology Organisation (ANSTO; Smith et al., 1999), and Scripps Institution of Oceanography at the University of California, San Diego in collaboration with the National Institute of Polar Research, Japan (SIO/NIPR; Severinghaus et al., 2003).

Tracer	EU borehole	US borehole
CO_2	NOAA, CSIRO, IUP	NOAA, IUP
CH_4	NOAA, CSIRO	NOAA, IUP
SF_6	NOAA, IUP, UEA	NOAA, IUP
CFC-11	UEA	-
CFC-12	UEA	-
CFC-113	UEA	-
HFC-134a	UEA	-
CH_3CCl_3	UEA	-
$\Delta^{14}CO_2$	ANSTO	-
$\delta^{15}N_2$	SIO/NIPR	SIO/NIPR
$\delta^{86}Kr$ *	SIO/NIPR	SIO/NIPR

* Used for gravitational correction only

points were available for a certain depth, they were averaged in the following order: first replicate measurements from one laboratory were averaged, then the resulting values from the different labs were averaged. In this way one composite dataset was created that contains 204 data points for the 10 tracers on the EU hole, and 77 data points for the 4 tracers on the US hole. The $\delta^{15}N_2$ profile is the same for both holes, and a combination of EU and US depths are used in the final dataset. This gives a final dataset of 260 data points.

3.2.4 Reconstruction of atmospheric histories of selected tracers*

A best-estimate atmospheric history was reconstructed for each of the reference tracers used in the tuning. Additionally we reconstructed a $\delta^{13}CO_2$ history which was used to convert the $\Delta^{14}CO_2$ reconstruction to a ppm scale (Stuiver and Polach, 1977). Four different types of data were used in the reconstructions:

- Direct atmospheric measurements from sampling networks or archived air. Northern hemisphere high latitude stations (i.e. Alert, Summit and Barrow) are used whenever available. When using data from other stations a correction should be made to account for the latitudinal gradient. This is done whenever the gradient could be reliably determined. We used station data from the NOAA-ESRL network for CO_2, CH_4, SF_6 and HFC-134a (Conway et al., 1994; Dlugokencky et al., 1994; Geller et al., 1997; Montzka et al., 1996); from ALE/GAGE/AGAGE for CFC-11, CFC-12, CFC-113 and CH_3CCl_3 (Prinn et al., 2000, 2005; Cunnold et al., 1997; Fraser et al., 1996); from CSIRO for $\delta^{13}CO_2$ (Francey et al., 2003). All ALE/GAGE/AGAGE data were converted to NOAA calibrations scales; all $\delta^{13}CO_2$ data are kept on the CSIRO calibration scale. Furthermore we used the SIO Mauna Loa record for CO_2 between 1958–1985 CE (Keeling et al., 2009), and the Cape Grim air archive for $\delta^{13}CO_2$ between 1978–1991 (Francey et al., 1999). The $^{14}CO_2$ history between 1963–1993 is based on Fruholmen, Norway, for its proximity to Greenland (Nydal and Lövseth, 1996); data from other stations were used to complete time coverage (Manning and Melhuish, 1994; Levin and Kromer, 2004; Levin et al., 2008).

- High resolution firn air/ice core measurements from the high accumulation Law Dome sites, Antarctica. The reconstructions of CO_2 before 1958, and CH_4 before 1983 are based on Etheridge et al. (1996, 1998) and MacFarling Meure et al. (2006); $\delta^{13}CO_2$ before 1976 is based on Francey et al. (1999).
- Dendrochronologically-dated tree-ring measurements of radiocarbon. The reconstruction of atmospheric $^{14}CO_2$ before 1955 is based on Reimer et al. (2004).
- Emission-based estimates using a 2-D atmospheric transport model that includes latitudinal source and sink distribution (Martinerie et al. (2009) and references therein). This has been used to complete time coverage for SF_6 and halocarbons before the onset of direct atmospheric measurements.

All the atmospheric reconstructions start in the year 1800 and have monthly resolution. We use 2008.54 (mid July) as the decimal sampling date in the models. Where applicable the reconstructions were converted to the most recent NOAA scale to be consistent with the data.

3.2.5 Gravitational correction*

The gravitational fractionation of gases in the firn column with depth, $\delta_{\mathrm{grav}}(z)$, is well established both theoretically and experimentally (Craig et al., 1988; Schwander, 1989; Sowers et al., 1992). All data used in this study, with the exception of $^{15}N_2$, have been corrected for the effect of gravity prior to the modeling. Consequently the models are run with either the molecular weight of all gases set equal to that of air ($M = M_{\mathrm{air}}$) or gravity set to zero ($g = 0$). Since the correction is based on actual measurements of $\delta^{86}Kr$ ($^{86}Kr/^{82}Kr$), this procedure ensures that the effect of gravity is included correctly. When, on the other hand, the effect of gravity is handled by the model, errors can be introduced when the modeled $\delta_{\mathrm{grav}}(z)$ deviates from the true observed values. The empirical correction can potentially also be used to correct for mass-dependent sampling artifacts (Severinghaus and Battle, 2006).

3.2.6 Differences between the EU and US boreholes

Though the boreholes are separated by a mere 64 m, within the lock-in zone we find differences in the mixing ratio profiles for CO_2, CH_4 (Fig. 3.2) and SF_6 (not shown) that exceed the estimated uncertainty of the combined sampling-measurement procedure (indicated with errorbar, see Sect. 3.2.7 for details). Note that we cannot

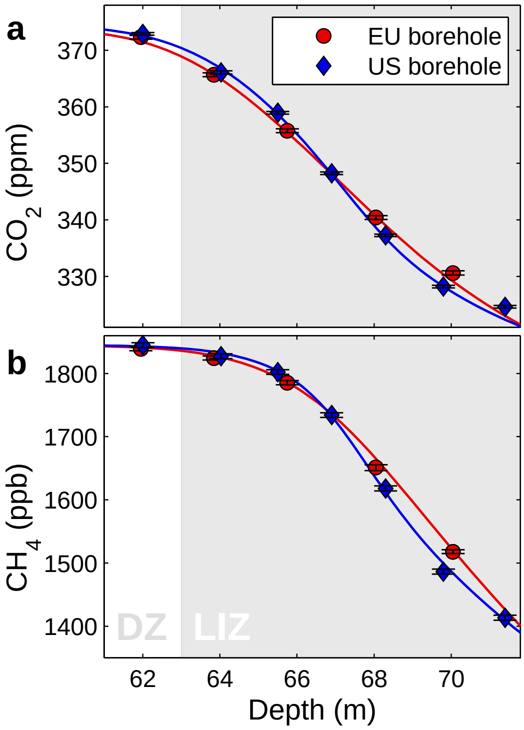

Figure 3.2: Comparison of **(a)** *CO_2 and* **(b)** *CH_4 data in the lock-in zone of the two boreholes. Data from three laboratories are averaged; the 1σ uncertainty bar is a combination of analytical and sampling uncertainties as specified in Sect. 3.2.7. Curves are modeled profiles using the CIC model, see Sect. 3.3.3.*

make the same comparison for the other gas species since only data from the EU hole are available. We attribute these differences to lateral inhomogeneity in the firn stratigraphy, possibly originating from surface wind features that have been preserved in the densification process. Because of these differences we have chosen to model both holes separately.

For SF_6 we furthermore observe a ~ 0.25 ppt offset in the 5–50 m depth range, contrary to the CO_2 and CH_4 profiles that agree well between the holes at these depths. This excludes differences in age distribution of the air as the origin. Alternative explanations we considered, such as incomplete flask flushing, sample contamination, procedural blanks and bladder outgassing, could all be excluded. Since we found no objective reason to reject data from either hole, we account for the discrepancy by assigning an additional errorbar to the SF_6 data from both holes in this depth range (see below).

Table 3.2: Relative contributions to the total uncertainty, averaged over the firn column (EU borehole).

Tracer	Analytical	Reconstruction	Contamination	Sampling	Other
CO_2	0.02	0.47	0.00	0.17	0.15[a], 0.19[b]
CH_4	0.08	0.85	0.01	0.05	-
SF_6	0.07	0.54	0.04	0.08	0.27[c]
CFC-11	0.11	0.81	0.04	0.04	-
CFC-12	0.35	0.48	0.06	0.11	-
CFC-113	0.55	0.38	0.04	0.03	-
HFC-134a	0.29	0.63	0.04	0.04	-
CH_3CCl_3	0.10	0.73	0.00	0.17	-
$\Delta^{14}CO_2$	0.14	0.80	0.00	0.00	0.06[a]
$\delta^{15}N_2$	0.91	-	0.05	0.04	-

[a] In situ artifacts

[b] Undersampling of seasonal cycle

[c] EU-US borehole SF_6 offset

3.2.7 Full uncertainty estimation*

Having accurate uncertainty estimates is essential for our multiple-tracer methodology. A unique uncertainty estimate has been assigned to each of the 260 individual data points used in this study based on the following seven potential sources of uncertainty: (1) analytical precision as specified by the laboratories. (2) Uncertainty in atmospheric reconstructions. (3) Contamination with modern air in the deepest firn samples; the estimates are based on HFC-134a, SF_6 and CFCs, which should be absent in the deepest samples. (4) Sampling effects estimated from inter-laboratory and inter-borehole offsets. (5) Possibility of in-situ CO_2 artifacts (e.g. Tschumi and Stauffer, 2000) and CO_2 enrichment due to close-off fractionation (Huber et al., 2006; Severinghaus and Battle, 2006). (6) Undersampling of seasonal cycle in the monthly atmospheric reconstruction (CO_2 only). (7) Large unexplained EU-US borehole difference in the diffusive zone (SF_6 only).

The errors are assumed to be independent of each other. The uncertainties in the atmospheric reconstructions are converted from a time scale to a depth scale by running them through the CIC firn air model (Sect. 3.3.2). Details are given in the Supplement. The relative contribution of the seven sources, averaged over the firn column, is given in Table 3.2. For most tracers the atmospheric reconstruction is the largest contributor to the total uncertainty, followed by the analytical precision.

3.3 Modeling firn air transport at NEEM

3.3.1 Tuning of the diffusivity profile*

How the diffusive transport changes with depth needs to be reconstructed through an inverse method for each firn air site independently. The procedure consists of forcing the transport models with the atmospheric history of one or several selected reference tracer(s), and subsequently optimising the fit to the measured mixing ratios in the firn by adjusting the effective diffusivity values at each depth (Rommelaere et al., 1997; Trudinger et al., 2002; Sugawara et al., 2003).

Here we will use diffusion as a generic term for mass transfer processes that are driven by a concentration gradient, and well described by Fick's law. The diffusivity profile we reconstruct is composed of two parts:

Molecular diffusion is a microscopic process originating in the thermal motion of the molecules constituting the firn air. The effective molecular diffusion coefficient of gases in the open porosity decreases with depth as the diffusive path becomes increasingly tortuous due to the densification process (Schwander et al., 1988). The diffusion coefficient of gas X at depth z is given by

$$D_X(z) = s_{\mathrm{op}} \frac{D_X^0}{\tau(z)} = s_{\mathrm{op}} \gamma_X \frac{D_{\mathrm{CO_2}}^0}{\tau(z)} \tag{3.2}$$

where D_X^0 is the diffusion coefficient in free air, $\tau(z)$ is the tortuosity at depth z, and $\gamma_X = D_X / D_{\mathrm{CO_2}}$ is the ratio of diffusion coefficients (Trudinger et al., 1997). It is clear from Eq. (3.2) that the molecular diffusivity profiles for the different gas species scale linearly with each other. The γ_X used in this study are based on measurements by Matsunaga et al. (1993, 1998, 2002a,b), or a theoretical formula (Chen and Othmer, 1962) for gas species where no experimental data are available (Supplement).

Eddy diffusion refers to mass transfer caused by air flow patterns in the open porosity which the models cannot resolve directly, and are instead parameterised through the inclusion of a diffusion coefficient $D_{\mathrm{eddy}}(z)$. Unlike molecular diffusion, D_{eddy} is equal for all gases as the process is macroscopic in origin. The first contribution to D_{eddy} is convective mixing in the top few meters due to seasonal temperature gradients and wind pumping (Colbeck, 1989; Severinghaus et al., 2001; Kawamura et al., 2006). Some of the models also include a D_{eddy} term in the deep firn to represent dispersive mass transfer. The classical example of dispersive mixing is Taylor dispersion, where (viscous) shear flow in a circular tube enhances the effective diffusivity of a solute (Aris, 1956). Viscous flow can be induced in the deep firn by low frequency pressure fluctuations at the surface (Schwander, 1989), as well as air expulsion due to pore compaction (Rommelaere et al., 1997). In soils, viscous flow induced by atmospheric pressure fluctuations has been shown to be an important transport mechanism (Massmann and Farrier, 1992). Pore compaction causes a non-uniform velocity distribution between air expelled upwards, and air remaining behind in the pores. This spread in velocities results in additional (dispersive) mixing.

The extensive uncertainty analysis we introduced in Sect. 3.2.7 assesses how reliable each data point is, and consequently how much weight should be assigned to it in the tuning procedure. This allows us to combine multiple tracers in the tuning, and the final reconstructed diffusivity profile is a trade-off between the constraints placed by the different tracers. All models in this study tuned their effective

Table 3.3: Overview of firn air transport models. See text for explanation.

Model	Coordinates	Advection	Convection	Time stepping	Tuning
CIC	static	flux	exponential	Crank-Nic.	automated
CSIRO	moving	coordinates	exponential	Crank-Nic.	automated
INSTAAR	static	flux	exponential	explicit	manual
LGGE-GIPSA	static	flux	tuned	implicit	automated
OSU	static	boxes	exponential	Crank-Nic.	manual
SIO	static	boxes	exponential	explicit	automated

diffusivity profiles to minimise the root mean square deviation

$$\mathrm{RMSD} = \left(\frac{1}{N} \sum_{i=1}^{N} \frac{(m_i - d_i)^2}{\sigma_i^2} \right)^{\frac{1}{2}} \tag{3.3}$$

where the d_i are the data for a given borehole (all tracers), m_i are the linearly interpolated modeled values at the same depths, and σ_i give the total uncertainties. The index i runs over all data points, where $N = 204$ for the EU hole, and $N = 77$ for the US hole.

3.3.2 Model description*

Six 1-D firn air transport models are tuned to the NEEM 2008 firn air data in the way outlined above. The models (in alphabetical order) were developed at the Centre for Ice and Climate (CIC), Commonwealth Scientific and Industrial Research Organisation (CSIRO, Trudinger et al., 1997), Institute of Arctic and Alpine Research (INSTAAR), Laboratoire de Glaciologie et Géophysique de l'Environnement and Grenoble Image Parole Signal Automatique (LGGE-GIPSA, Witrant et al., 2011), Oregon State University (OSU) and the Scripps Institution of Oceanography (SIO, Severinghaus and Battle, 2006).

Table 3.3 summarises a selection of relevant model characteristics. The second column indicates the kind of coordinate system used by each model. The CSIRO model is unique in using a coordinate system that moves downwards with descending ice layers (Lagrangian coordinates), giving a downward ice velocity $w_{\mathrm{ice}} = 0$ relative to the reference frame. The other models use a static (Eulerian) coordinate system where the surface stays at $z = 0$ and the ice layers move down at a finite velocity $w_{\mathrm{ice}} = A\rho/\rho_{\mathrm{ice}}$. The choice of coordinate system has consequences for the way advection of air with the ice matrix is handled (third column). In the CSIRO model the moving coordinate system automatically leads to advective transport without the need to include it explicitly. The models expressed in Eulerian coordinates use either an advective flux as described by Rommelaere et al. (1997), or use boxes of air that are shifted downwards at regular time intervals (Schwander et al., 1993). Convection (fourth column) is handled in two different ways. The LGGE-GIPSA model uses a D_{eddy} term that is tuned by the RMSD minimisation algorithm, in combination with zero gravitational fractionation for $z < 4\,\mathrm{m}$. The other models use the parameterisation of Kawamura et al. (2006) where a D_{eddy} term is included that falls off exponentially with depth. The fifth column of Table 3.3 indicates whether the time stepping used in solving the diffusion equation was either explicit (Euler forward), implicit (Euler backward) or mixed implicit-explicit (Crank-Nicolson method). Finally, some of the models were tuned through manual adjustments of the diffusivity profile, while others used an automated control method (e.g. Rommelaere et al., 1997; Trudinger et al., 2002).

3.3.3 Fit of modeled profiles to the data*

The modeled profiles for all 10 tracers from the EU borehole are shown in Fig. 3.3, profiles from the US borehole can be found in the Supplement.

For CO_2 (Fig. 3.3a) we find a pronounced mismatch for $z > 70\,\mathrm{m}$ which is reproduced consistently by all models and in both boreholes. The atmospheric reconstruction is based on the Law Dome record (Etheridge et al., 1996), and consequently the largest source of uncertainty is the interhemispheric CO_2 gradient. To explain the observed mismatch with an error in the atmospheric history would require a 6 ppm interhemispheric gradient in the 1950s, which can be ruled out (Keeling et al., 2010). Also contamination with modern air can be ruled out for these flasks, based on measurements of halocarbons. We cannot, however, exclude in-situ production of CO_2 from e.g. organic material or (bi)carbonates found in Greenland ice (e.g. Tschumi and Stauffer, 2000). There might also be a small close-off fractionation of CO_2, of order 1 ‰ or less, based on its effective molecular diameter (Huber et al., 2006; Severinghaus and Battle, 2006).

Both CH_3CCl_3 and $^{14}CO_2$ (Fig. 3.3d–e) have a peak within the LIZ. The peak height and position, which are sensitive to the shape and magnitude of the diffusivity profile, provide an important constraint in the tuning procedure. It is exactly at these peaks that the divergence between the models is most easily visible. It must be noted, however, that equally large model differences are found for other tracers as well (e.g. CO_2 and HFC-134a). Furthermore, models that fit the peak height exactly do not necessarily provide the best overall fit to the data.

To quantitatively assess how well the modeled profiles fit the data, we make a histogram of $(m_i - d_i)/\sigma_i$ where the index i goes over all 204 data points of the EU borehole. The σ_i are the unique uncertainties we assigned to each data point. This is shown in Fig. 3.4 together with a Gaussian distribution of width $\sigma = 1$ and a surface area equal to that of the histogram. The figure furthermore shows the RMSD from the data as given by Eq. (3.3). For all models we find a distribution that is more narrow than the Gaussian distribution, meaning that within the assigned uncertainties all data from the borehole can be modeled consistently. The good agreement gives confidence in the correctness of our reconstructed atmospheric histories, which will be of use in future firn air studies. For the US hole the RMSD ranges between 0.60–1.06.

Two models stand out as having a larger RMSD of 0.92 (CSIRO and OSU). For the CSIRO model this is caused by the absence of a back flow due to pore

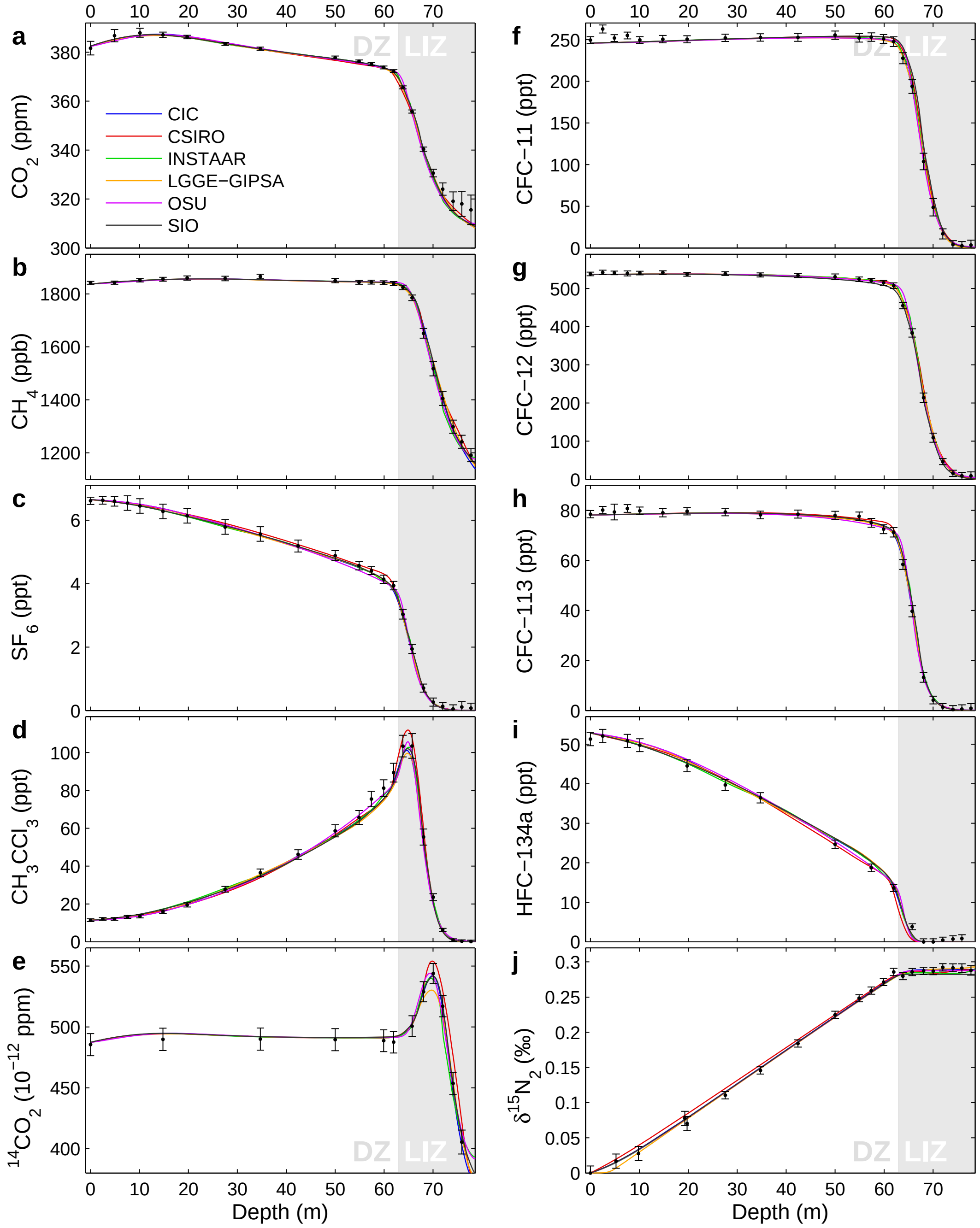

Figure 3.3: **(a–j)** *Modeled profiles for all 10 tracers from the EU borehole. With the exception of* **(j)** *data are gravity corrected and the models are run with gravity turned off. Errorbars correspond to full 1σ uncertainty as defined in Sect. 3.2.7.*

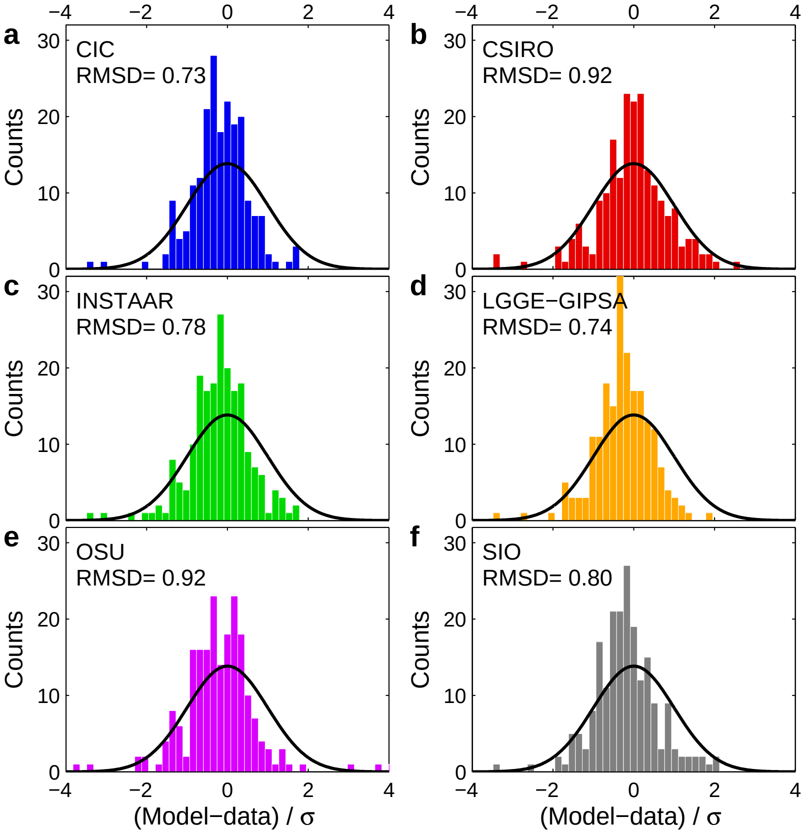

Figure 3.4: **(a–f)** *Histogram of* $(m_i - d_i)/\sigma_i$ *for the firn air transport models in this study using the EU borehole data. The black curve gives a Gaussian distribution of width* $\sigma = 1$*, normalised to have equal surface to the histogram. The RMSD is calculated using Eq. (3.3).*

compression in the transport description (Sect. 3.4.4.4). For the OSU model we attribute the larger RMSD to the tuning procedure for the molecular diffusivity, which has fewer degrees of freedom than the procedures used by the other models (Supplement).

Differences in RMSD give information on the performance of models, or model configurations, relative to each other; the RMSD as defined by Eq. (3.3) should not be interpreted in an absolute sense.

3.4 Model intercomparison and discussion

3.4.1 Diffusivity profiles*

All the models are tuned separately to optimise the fit to the data. Figure 3.5a shows the reconstructed molecular diffusivity profiles for CO_2. The spread between the solutions is caused by two factors. First, it reflects differences in model physics,

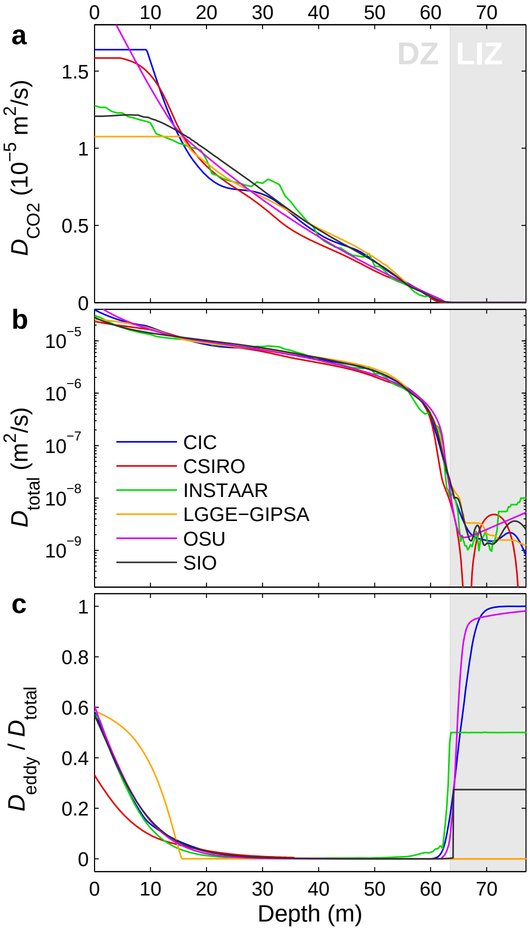

Figure 3.5: **(a)** *CO_2 molecular diffusivity profile with depth $D_{CO_2}(z)$ for the EU borehole.* **(b)** *Semi-log plot of the total CO_2 diffusivity profile $D_{\mathrm{total}}(z) = D_{CO_2}(z) + D_{\mathrm{eddy}}$.* **(c)** *Plot of $D_{\mathrm{eddy}}(z)/D_{\mathrm{total}}(z)$. Eddy diffusion near the surface corresponds to convective mixing; in the LIZ some of the models include dispersive mixing. The CSIRO model has zero eddy diffusivity in the LIZ; the line is not visible as the LGGE-GIPSA model is plotted on top of it.*

which are compensated for by adjustments to the diffusivity profile. Second, it relates to the degree in which the inverse problem of diffusivity reconstruction is underdetermined. By using 10 different tracers the problem is more strongly constrained than in the case of using only CO_2, but the solution is not unique.

A second important observation is that all models require a non-vanishing diffusivity on the order of $2 \times 10^{-9}\mathrm{m}^2\mathrm{s}^{-1}$ within the LIZ (see Fig. 3.5b). This contradicts the notion that diffusivity vanishes completely in the LIZ due to the presence of impermeable layers, which is frequently expressed in firn air studies (e.g. Battle et al., 1996; Trudinger et al., 2002; Assonov et al., 2005). Our findings confirm a recent study at Megadunes, Antarctica, that also reports a finite (eddy) diffusivity in the

LIZ (Severinghaus et al., 2010). We believe this result to be robust, since it is reproduced by all six firn air models. In particular, the well reproduced height of the $^{14}CO_2$ bomb spike, which falls entirely within the LIZ, provides strong evidence for finite LIZ diffusion at NEEM; letting diffusivity go to zero leads to a $^{14}CO_2$ peak that is too narrow and overshoots the measured values by $\sim 7\sigma$.

How the LIZ diffusivity is parameterised, however, varies strongly among the models as shown in Fig. 3.5c. The models use either molecular diffusion, dispersive mixing (eddy diffusion) or a mixture of both. To fit the $\delta^{15}N_2$ data, most models require some dispersive mixing in the LIZ, since molecular diffusion alone would lead to continued gravitational fractionation. The LGGE-GIPSA model circumvents this problem by using a combination of Fick's and Darcy's transport to describe almost-stagnant transport in the lower zones (Witrant et al., 2011), which allows for using purely molecular diffusion in the LIZ. The SIO model uses the ratio of eddy to molecular diffusion in the LIZ as a tuning parameter in the RMSD minimisation, and finds that the fit is optimised for 27 % eddy diffusion (Supplement). Models that reproduce the observations equally well can have completely different parameterisations, so our analysis does not tell us which scheme is more likely to be correct. These model differences do have important consequences for the modeling of isotopic ratios, as is discussed below.

3.4.2 Gas age distributions*

Firn air does not have a single age, but rather a distribution of ages (Schwander et al., 1993). The modeled gas age distribution, also referred to as Green's function, transfer function, response function or age spectrum, provides a complete description of the model transport properties (Rommelaere et al., 1997). Figure 3.6 compares CO_2 age distribution densities for the models at the lock-in depth ($z = 63\,\mathrm{m}$) and at the bottom of the LIZ ($z = 78\,\mathrm{m}$, close to the deepest EU hole sample at $z = 77.75\,\mathrm{m}$). The most relevant characteristics of the age distributions are summarised in Table 3.4. As a measure of the relative spread in model results, we list the 2σ standard deviation divided by the mean (μ).

The LIZ lies between the two depths depicted here. From the closed porosity parameterisation (Eq. 3.1), we find that $\sim 95\,\%$ of the air is trapped in this zone. The gas age distribution found in NEEM ice below the full close-off depth ($s_{\mathrm{op}} = 0$) will be intermediate to these two end members, with a tail of older air trapped already in the DZ. Interestingly, at the lock-in depth ($z = 63\,\mathrm{m}$), estimates of both the age and the distribution width show a spread of around 25 % between models that reproduce the data equally well. Clearly these properties are not as well determined as one would expect based on the similarity between the modeled curves alone. On traversing the LIZ to $z = 78\,\mathrm{m}$ the relative spread in modeled ages is reduced; the absolute spread grows slightly to about 5 yr, though. The spread in distribution widths remains large.

For the US borehole the spread in the calculated mean ages at $z = 63\,\mathrm{m}$ is even up to 40 %. This larger spread is due to the fact that we have only 4 tracers on the

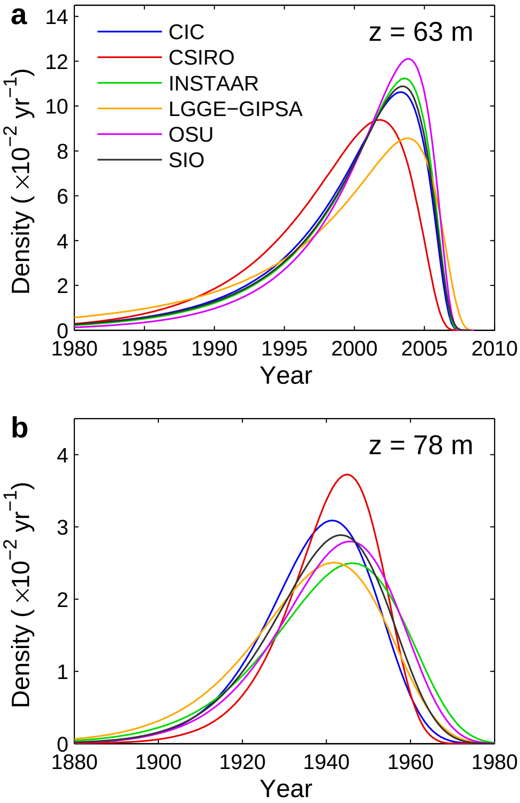

Figure 3.6: EU borehole modeled CO_2 age distribution densities for **(a)** *depth* $z = 63\,\mathrm{m}$ *(lock-in depth) and* **(b)** *depth* $z = 78$ *m (bottom of LIZ). On the horizontal axis are calendar years C.E.; decimal sampling year is 2008.54 (i.e. mid July). Age distributions are calculated by applying a surface forcing which is unity for* $0.2 \leq t < 0.4$ *yr, and zero elsewhere.*

US borehole, and therefore the mean ages are less strongly constrained by the data.

We can use the gas age distributions to calculate the NEEM modern day Δage, i.e. the difference between gas age and ice age below the firn-ice transition. From annual layer counting and matching of reference horizons to the NGRIP GICC05 timescale (Rasmussen et al., 2006), the ice at depth $z = 63$ (78) m is estimated to be 190.6 (252.5) ± 1 yr old (S. O. Rasmussen, personal communication, 2011). To calculate the true Δage we would require the gas age in the closed porosity. With the model results of Table 3.4 we can only calculate $\Delta\mathrm{age_{op}}$, i.e. the difference between ice age and gas age in the open pores. By averaging results from the six firn air models we find a $\Delta\mathrm{age_{op}}$ of 181 ± 2 and 183 ± 2 yr at $z = 63$ and 78 m, respectively. In the LIZ, ice and air are aging at roughly the same rate with depth. An estimated 4-5 % of the air is already trapped above 63 m, which biases our air age estimate young. This air fraction can introduce an error of at most 8 yr. Based on these considerations, our best estimate of the true Δage is 182^{+3}_{-9} yr (181^{+3}_{-9} yr) for the EU

Table 3.4: Mean age, Median age, Full Width at Half Maximum and Spectral Width (Δ, Eq. (1) in Trudinger et al., 2002) at the lock-in depth ($z = 63$ m) and at the bottom of the LIZ ($z = 78$ m). All values given in years. The 2σ standard deviation divided by the mean μ gives a measure of the spread in the model results.

Model	Mean	Median	FWHM	Δ
$z = 63$ m				
CIC	9.2	7.4	7.9	4.5
CSIRO	10.3	8.8	9.3	4.2
INSTAAR	8.7	7.0	7.4	4.2
LGGE-GIPSA	11.1	8.1	9.1	6.8
OSU	7.9	6.5	7.0	3.7
SIO	9.0	7.2	7.6	4.5
$2\sigma/\mu$	0.25	0.22	0.23	0.47
$z = 78$ m				
CIC	70.9	69.4	30.1	9.8
CSIRO	67.6	66.0	24.8	8.3
INSTAAR	68.3	66.1	37.1	12.4
LGGE-GIPSA	72.8	70.4	36.8	12.5
OSU	67.5	65.7	33.3	10.8
SIO	69.5	67.7	32.2	10.5
$2\sigma/\mu$	0.06	0.06	0.28	0.30

(US) borehole.

3.4.3 Borehole comparison

Here we compare the reconstructed diffusivity profiles and gas age distributions for the EU and US boreholes. Figure 3.7a shows the total diffusivity with depth for CO_2 on a semi-log scale, where we have averaged over the solutions from the different firn air models. We observe that the largest divergence between the boreholes occurs in the LIZ. Also the gas age distributions show divergence mainly in the LIZ. Figure 3.7b shows the age distributions at two depths, where again the curves represent an average over model output from the different firn air models. At the lock-in depth ($z = 63$ m) the age distributions of both boreholes are still very similar. After traversing the LIZ ($z = 76$ m, chosen to be near the final sampling depth on the US hole), we find that the firn air in the US hole has undergone more diffusive mixing, leading to a broader distribution width.

Polar firn is a layered medium that exhibits density variations with depth caused by seasonal variations in local climatic conditions and deposited snow density (e.g. Hörhold et al., 2011). Snow drift and redeposition at the surface lead to lateral inhomogeneities in the firn stratigraphy. The borehole comparison suggests that firn air transport in the LIZ is very sensitive to these lateral variations, whereas transport in the DZ is not. This is not unexpected since the formation of the LIZ has been linked to the degree of layering (Landais et al., 2006). If the amplitude of density variations is sufficiently large, the high-density layers will reach the close-off density before the low-density layers do, thus creating sealing layers that impede vertical diffusion

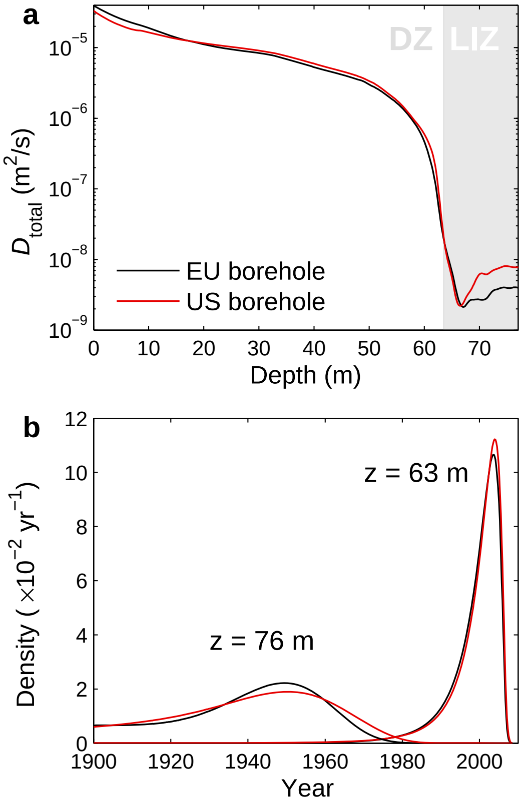

Figure 3.7: Comparison between the EU and US boreholes. **(a)** *Semi-log plot of the total CO_2 diffusivity profile $D_{\text{total}}(z) = D_{CO_2}(z) + D_{\text{eddy}}$ averaged over all six firn models.* **(b)** *Age distributions at depths $z = 63$ m (lock-in depth) and $z = 76$ m (bottom of LIZ) averaged over five firn models. The CSIRO model is excluded in the age distribution comparison as the US age distribution at $z = 76$ m is unreliable (Supplement).*

and prevent further gravitational fractionation of the gas mixture (Martinerie et al., 1992; Schwander et al., 1993; Sturrock et al., 2002). Earlier we presented evidence for finite vertical mixing in the LIZ despite the presence of such impeding layers. The amount of vertical mixing is expected to depend on the horizontal extent of the sealing layers, as well as the position of (micro)cracks and passageways. This could lead to a strong lateral variation in LIZ diffusion as observed. Note that such lateral processes cannot be represented adequately in one-dimensional transport models.

3.4.4 Synthetic diagnostic scenarios*

To diagnose model properties further, we developed four synthetic scenarios that probe specific aspects of the model physics. We present the individual scenarios below, and discuss the model differences they reveal.

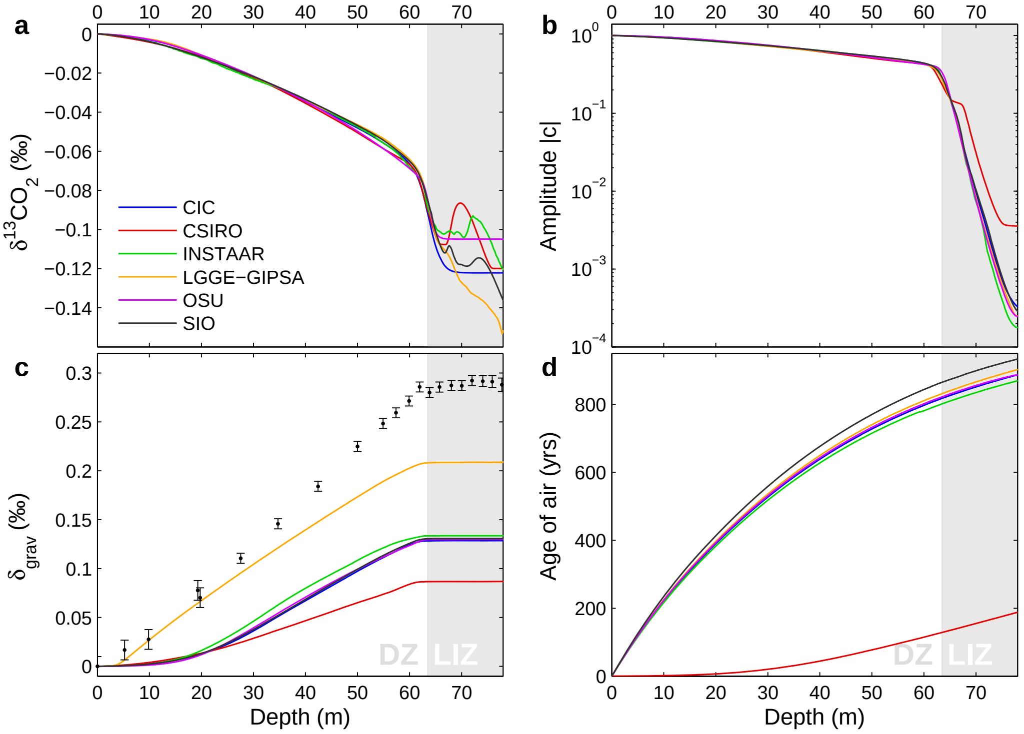

Figure 3.8: Model comparison using the four diagnostic scenarios and diffusivity tuned to the EU borehole data. **(a)** *Scenario I: diffusive fractionation for a hypothetical monotonic CO_2 increase.* **(b)** *Scenario II: attenuation of a 15 yr period sinusoidal CO_2 forcing with depth.* **(c)** *Scenario III: gravitational enrichment for gas X with $D^0_X = 0.025 D^0_{CO_2}$. Data show gravitational enrichment of $^{15}N_2$ corrected for the effect of thermal diffusion. See Supplement for details.* **(d)** *Scenario IV: mean age of gas Y when using advective transport only ($D^0_Y = 0$, i.e. diffusion is absent). With the exception of S-III all scenarios were run with the effect of gravity turned off.*

3.4.4.1 Scenario I: diffusive fractionation

For gas species whose atmospheric mixing ratios change over time, the disequilibrium in the firn leads to an isotopic fractionation with depth, even in the absence of changes in atmospheric isotopic composition (Trudinger et al., 1997). As a scenario we use a monotonic CO_2 increase of $\sim 1\,\mathrm{ppm\,yr^{-1}}$ without seasonal cycle, chosen to resemble the current anthropogenic increase (Keeling et al., 2010). The surface isotopic ratio is kept fixed at $\delta^{13}CO_2 = 0$. Because the $^{13}CO_2$ isotopologue has a lower diffusivity, it is transported less efficiently into the firn, leading to a depletion in $^{13}CO_2$ with depth. Ice core and firn air records need to be corrected for the effect of diffusive fractionation (DF). For example, the (site specific) corrections for the recent anthropogenic increase are ∼0.1 ‰ for $\delta^{13}CO_2$ at DE08, Law Dome (Francey et al., 1999), and 1.2 ‰ for $\delta^{13}CH_4$ at WAIS-Divide (Mischler et al., 2009).

Figure 3.8a shows the modeled isotopic signal with depth for the different models. Results in the DZ are consistent, however they diverge strongly once the LIZ is reached. For δ^{13}C of CO_2, the observed range between the different model solutions in the deepest firn is 0.05 ‰, which is around 40 % of the total DF signal. For isotopologues of CH_4 the DF is larger, because of the larger relative mass difference between the isotopologues. Based on the observed DF model disagreement we estimate an uncertainty of 0.5 ‰ for both δ^{13}C and δD of CH_4. For δD of CH_4 this uncertainty is smaller than the typical measurement uncertainty, as well as the atmospheric signal observed in the firn (Bräunlich et al., 2001; Mischler et al., 2009). However, for both $\delta^{13}CO_2$ and $\delta^{13}CH_4$ the model disagreement exceeds the typical instrumental precision. At this moment we have no objective way of determining which of the models predicts the DF correctly. This additional uncertainty should therefore be recognised when interpreting ice core and firn gas isotopic records of periods with rapid atmospheric variations. Sites with a thick LIZ, combined with a low accumulation rate, allow for reconstructing atmospheric mixing ratios further back in time. However, a thick LIZ also means a larger uncertainty in DF (and thereby isotopic reconstruction) due to the poorly constrained LIZ transport.

Molecular diffusion leads to DF between isotopologues because their diffusion coefficients are different. Advection, convection and dispersive mass transfer do not discriminate between isotopologues, and consequently do not fractionate the gas mixture. The observed model disagreement originates in the way in which LIZ transport is parameterised (Fig. 3.5c). The CIC and OSU models both smoothly go from purely molecular diffusion in the DZ to purely eddy diffusion in the LIZ. Once the molecular diffusion reaches zero, the DF ceases to increase with depth giving a horizontal line. The LGGE-GIPSA model on the other hand uses molecular diffusion all the way down to the close-off depth, giving a continued fractionation with depth. One way the DF uncertainty could be incorporated in future studies is by testing different parameterisations for LIZ diffusion, or by using transfer functions generated by different models.

The Law Dome-based records of $\delta^{13}CO_2$ (Francey et al., 1999) and $\delta^{13}CH_4$ (Ferretti et al., 2005) were both corrected for the effects of DF. The correction should not be affected much by our findings here for several reasons. Most importantly, the accumulation rate (and therefore the advective flux) at the Law Dome DE08 and DE08-2 sites is very large. This will strongly reduce DF in the LIZ as described above. Furthermore the LIZ is relatively thin (Trudinger, 2001). The study by Ferretti et al. (2005) combines ice core samples from the aforementioned high accumulation Law Dome sites with firn air measurements from the DSSW20K site, which has a rather low accumulation rate ($\sim 0.16\,\mathrm{m\,yr^{-1}}$ ice equivalent). After DF correction the results agree well. In other published firn air and ice core isotopic records that cover the recent anthropogenic increase (e.g. Bräunlich et al., 2001; Sugawara et al., 2003; Röckmann et al., 2003; Sowers et al., 2005; Bernard et al., 2006; Ishijima et al., 2007; Mischler et al., 2009) the uncertainty in the reconstruction due to the DF correction might have been underestimated.

3.4.4.2 Scenario II: attenuation of a sine wave with depth

Rapid atmospheric variations are attenuated in the firn, and recorded in the ice with a reduced amplitude (Spahni et al., 2003). To compare the firn smoothing effect between the models, we force them with a sinusoidal atmospheric variation in CO_2 that has a 15 yr period. Due to diffusion, the amplitude of the signal decreases with depth in the firn. For mathematical convenience we impose two separate atmospheric scenarios:

$$[C_1](t, z = 0) = 1 + \sin(2\pi t/15)$$
$$[C_2](t, z = 0) = 1 + \cos(2\pi t/15)$$

where t is the time in years. Note that both signals are attenuated to the same degree, and that the $\pi/2$ phase angle between them is preserved. To get the signal amplitude with depth, we combine them in the following way:

$$|[C](t, z)| = \sqrt{([C_1](t, z) - 1)^2 + ([C_2](t, z) - 1)^2} \tag{3.4}$$

The outcome is shown in Fig. 3.8b. We observe that signal attenuation in the LIZ is stronger than in the DZ. This is because transport in the DZ is efficient; the mean CO_2 age at the lock-in depth is around 9 yr, which is less than the period of the atmospheric oscillation. The mixing ratios in most of the DZ will be “in phase” with the atmospheric signal, giving little attenuation. By comparison, air in the LIZ is nearly stagnant. It takes around 70 yr to be transported over 15 m, corresponding to almost 5 periods of the sinusoid. As air of different ages (i.e. different phases of the atmospheric cycle) gets mixed, the signal amplitude is reduced.

Within the DZ the models agree well. In the LIZ there are two intervals ($65 < z < 68$ m and $74 < z < 78$ m) where the CSIRO model has significantly less attenuation with depth. These intervals correspond to the depths where the reconstructed CSIRO diffusivity goes to zero (Fig. 3.5b). On the US borehole this effect is even more pronounced (Supplement).

Earlier we touched upon the question of whether or not there is continued diffusion in the LIZ; our diffusivity reconstructions indicate that there is at NEEM. Scenario II shows that this remnant LIZ diffusivity causes very strong attenuation of the atmospheric signal. Therefore, the question of LIZ diffusivity has important consequences for the temporal resolution at which we can hope to reconstruct atmospheric variations back in time using ice cores.

3.4.4.3 Scenario III: balance of transport fluxes

The total gas flux is the sum of the advective, diffusive and convective fluxes. Within the DZ, molecular diffusion overwhelms the other transport mechanisms; in this scenario we bring the different fluxes into balance by considering a hypothetical gas X with a very small diffusion coefficient $D^0_X = 0.025 D^0_{CO_2}$, and a mass $M_X =$

$M_{\text{air}} + 1 \times 10^{-3}\,\text{kg}\,\text{mol}^{-1}$. The relative strength of the different mechanisms is shown by the gravitational enrichment with depth.

Figure 3.8c shows the model output together with the true gravitational enrichment as measured for $^{15}\text{N}_2$. In thermodynamic equilibrium the enrichment is given by the barometric equation: $\delta_{\text{grav}}(z) = [\exp(\Delta Mgz/RT) - 1] \approx \Delta Mgz/RT$ (Sowers et al., 1992). The advective and convective fluxes drive the air column out of equilibrium reducing $\delta_{\text{grav}}(z)$ below the barometric case. For gas X the diffusive flux is not large enough to oppose the other two, leading to a final δ_{grav} which is about half that of $^{15}\text{N}_2$. In this way the enrichment with depth represents the balance between diffusion on one hand, and advection and convection on the other.

The differences in implementation of the convective mixing are clearly visible. The LGGE-GIPSA model uses no gravitational enrichment in the top 4 m, followed by a tuned eddy diffusion. The convective mixing in the other models, which all use the parameterisation by Kawamura et al. (2006), penetrates much deeper into the firn. In the DZ there are also clear differences; here the gravitational slope mostly represents the balance between diffusion and advection. The CSIRO has a stronger advection term due to the absence of pore compression back flow (see below); this is reflected in a more reduced slope. A higher advective flux can partially be compensated in the diffusivity tuning by a lower diffusivity, and vice versa. This explains why the diffusivity profile reconstructed through the CSIRO model is slightly lower than those of the other models (see Fig. 3.5a).

3.4.4.4 Scenario IV: advection with the ice matrix

Bubble trapping removes air from the open pores, which is subsequently advected downwards with the ice matrix. A downward flux of air in the open pores compensates for this removal. In the last scenario we study hypothetical gas Y, which is not subject to diffusion or convection, and is transported into the firn by this advective flux alone. Both eddy and molecular diffusion are set to zero. Its atmospheric history is a linear decrease by $1\,\text{ppm}\,\text{yr}^{-1}$, until it reaches zero at the final model date. This leads to a mixing ratio of gas Y in the firn that equals the age of the air at each depth. The results are shown in Fig. 3.8d. In the absence of diffusion most models find an age of around 900 yr at the bottom of the firn column. The CSIRO model stands out with a much lower gas age. Differences in total air flux, and thereby the total air content in mature ice, affect the advective transport. Also, artificial numerical diffusion in the models reduces the calculated gas ages.

There are significant differences in the way advective transport is treated by the models. The key difference is whether or not the model includes an upward air flow relative to descending ice layers to account for compression of open pores (Rommelaere et al., 1997; Sugawara et al., 2003). This term is neglected in the CSIRO model (Trudinger et al., 1997), which leads to a gas age that equals the ice age. Note that the observed difference is not related to the choice of reference frame (static vs. moving). In the LIZ air transport is dominated by advection, so this is where we expect to see the effect of the back flow most clearly. Indeed we see that in the LIZ the CSIRO model diverges most strongly from the other models, e.g. in the total reconstructed diffusivity (Fig. 3.5b) and the diffusive smoothing of scenario II (Fig. 3.8b).

Neglecting the back flow term corresponds to a physical model of the firn where all the air is transported downwards with the ice layers. This would be possible if e.g. the denser firn layers succeed in completely sealing off the air below (Martinerie et al., 1992; Schwander et al., 1993). In the case such impermeable layers are present in the LIZ, pressure will build up in the pore space below. At some of the Law Dome sites (e.g. DSSW20K) outgassing was observed from freshly drilled boreholes, which could be caused by the venting of such pressurised pores to the atmosphere. However, at these sites the effects of wind pumping could not be excluded as the origin of the observed air flow. At NEEM, no outgassing from pressurised pores was observed. More evidence for the absence of sealing layers comes from the observation of diffusive mixing in the LIZ, as discussed above. Furthermore, the total air content implied by the assumption of fully pressurised pores in the LIZ is incompatible with observed air content in mature ice (Martinerie et al., 1992).

For these reasons we believe that at the NEEM site the back flow due to pore compression can not be neglected when describing the firn air transport. This makes the assumptions in the CSIRO model less valid, explaining why it obtains a higher RMSD than most other models (Fig. 3.4). Preliminary tests show that by including the advective back flux in the CSIRO model the RMSD reduces to 0.74 (Trudinger et al., 2011).

3.5 Summary and conclusions

We presented a new multi-tracer method for characterising the firn air transport properties of a site. We applied the method to NEEM, Northern Greenland, by tuning six firn air models to an ensemble of ten tracers. The firn air models used in this study were able to fit the data within a 1-σ normal distribution, meaning that the site can be modeled consistently within the estimated uncertainties. Each of the reference tracers constrains the firn profile differently through its unique atmospheric history and free air diffusivity, making our multiple-tracer characterisation method an improvement over the commonly used single-tracer tuning.

Six different firn air transport models were tuned to the NEEM site in this fashion, allowing a direct model comparison. We find that all the models require a non-vanishing diffusivity in the lock-in zone to reproduce the measured profiles of the reference gases. This is contrary to the commonly held notion that diffusive mixing is absent in the lock-in zone. A comparison between replicate boreholes located 64 m apart suggests that this lock-in zone diffusion is sensitive to lateral inhomogeneities in firn stratigraphy. Furthermore, we find that despite the fact that the models reproduce the measured profiles equally well, the gas age distributions they calculate can differ substantially. Often-used quantities, such as the mean age and distribution width, differed among the models by up to 25 %. The modern day Δage was calculated to be 182^{+3}_{-9} yr.

Finally we introduced four diagnostic scenarios that are designed to probe specific aspects of the model physics, from which we can draw two main conclusions. First, we studied the consequences of the different ways in which the models implement advection, in particular whether they include a back flow term to account for pore compression. Including the back flow term significantly improves the fit to the data, suggesting this term can not be neglected, as is done in the CSIRO model. Second, we find that the effect of isotopic diffusive fractionation is poorly constrained by the models. Near the close-off depth, the calculated diffusive fractionation differs by 40 % between the models. These differences are related to the way in which lock-in zone diffusion is parameterised. Molecular diffusion leads to continued fractionation, whereas dispersive transport (eddy diffusion) does not. Further work is needed to elucidate the true nature of lock-in zone diffusion. Meanwhile, when interpreting firn air and ice core isotopic records, an additional uncertainty needs to be included to account for the model discrepancy found here.

3.6 Acknowledgements

We would like to thank Stephen Montzka, Bradley Hall and Geoff Dutton from NOAA-ESRL for providing halocarbon and SF_6 atmospheric data and for their help on gas calibration scales; Ray Weiss and Ray Wang for their kind help on AGAGE atmospheric data and calibration scales; Paul Krummel for providing NOAA/AGAGE(SIO) concentration ratios for halocarbon species based on flask and in-situ measurements; Bradley Hall for providing IHALACE results prior to their publication. Comments and suggestions by two anonymous referees improved the manuscript considerably. This work benefited greatly from numerous data available in public databases, in particular: AGAGE (`http://cdiac.ornl.gov/ndps/alegage.html`), NOAA ESRL (`http://www.esrl.noaa.gov/gmd`) and EDGAR (`http://www.rivm.nl/edgar`). We thank the people involved in the acquiring, analysis, and accessibility of these data. NEEM is directed and organised by the Center for Ice and Climate at the Niels Bohr Institute and US NSF, Office of Polar Programs. It is supported by funding agencies and institutions in Belgium (FNRS-CFB and FWO), Canada (GSC), China (CAS), Denmark (FIST), France (IPEV, CNRS/INSU, CEA and ANR), Germany (AWI), Iceland (RannIs), Japan (NIPR), Korea (KOPRI), The Netherlands (NWO/ALW), Sweden (VR), Switzerland (SNF), United Kingdom (NERC) and the USA (US NSF, Office of Polar Programs). C. Buizert would like to thank Bruce Vaughn (INSTAAR, University of Colorado) for his hospitality and support; V. V. Petrenko has been supported by the NOAA Postdoctoral Fellowship in Climate and Global Change and NSF grants 0632222 and 0806387 (White); A. J. Orsi and J. P. Severinghaus were supported by NSF 0806377; UEA acknowledges NERC for awards NE/F021194/1, NE/F015585/1 and a PhD Studentship (Hogan); the CSIRO contributions to this work were partly supported by the Australian Climate Change Science Program, funded jointly by the Department of Climate Change and Energy Efficiency, the Bureau of Meteorology and CSIRO; the French contribution to this study was further supported by CNRS through INSIS/PEPS-automatique and INSU/LEFE programs.

3.7 References

Aris, R. (1956). On the dispersion of a solute in a fluid flowing through a tube. *Proc. R. Soc. Lond. A*, 235:67–77.

Arnaud, L., Barnola, J. M., and Duval, P. (2000). Physical modeling of the densification of snow/firn and ice in the upper part of polar ice sheets. In Hondoh, T., editor, *Physics of Ice Core Records*, pages 285–305. Hokkaido University Press.

Assonov, S. S., Brenninkmeijer, C. A. M., and Jockel, P. (2005). The o-18 isotope exchange rate between firn air co_2 and the firn matrix at three antarctic sites. *J. Geophys. Res.-Atm*, 110(D18):15.

Assonov, S. S., Brenninkmeijer, C. A. M., Jockel, P. J., Mulvaney, R., Bernard, S., and Chappellaz, J. (2007). Evidence for a co increase in the sh during the 20th century based on firn air samples from berkner island, antarctica. *Atmos. Chem. Phys.*, 7:295–308.

Aydin, M., Saltzman, E. S., De Bruyn, W. J., Montzka, S. A., Butler, J. H., and Battle, M. (2004). Atmospheric variability of methyl chloride during the last 300 years from an antarctic ice core and firn air. *Geophys. Res. Lett.*, 31(2):4.

Battle, M., Bender, M., Sowers, T., Tans, P. P., Butler, J. H., Elkins, J. W., Ellis, J. T., Conway, T., Zhang, N., Lang, P., and Clarket, A. D. (1996). Atmospheric gas concentrations over the past century measured in air from firn at the south pole. *Nature*, 383(6597):231–235.

Bernard, S., Röckmann, T. R., Kaiser, J., Barnola, J. M., Fischer, H., Blunier, T., and Chappellaz, J. (2006). Constraints on n_2o budget changes since pre-industrial time from new firn air and ice core isotope measurements. *Atmos. Chem. Phys.*, 6:493–503.

Bräunlich, M., Aballanin, O., Marik, T., Jockel, P., Brenninkmeijer, C. A. M., Chappellaz, J., Barnola, J. M., Mulvaney, R., and Sturges, W. T. (2001). Changes in the global atmospheric methane budget over the last decades inferred from c-13 and d isotopic analysis of antarctic firn air. *J. Geophys. Res.-Atm*, 106(D17):20465–20481.

Butler, J. H., Battle, M., Bender, M. L., Montzka, S. A., Clarke, A. D., Saltzman, E. S., Sucher, C. M., Severinghaus, J. P., and Elkins, J. W. (1999). A record of atmospheric halocarbons during the twentieth century from polar firn air. *Nature*, 399(6738):749–755.

Chen, N. H. and Othmer, D. F. (1962). New generalized equation for gas diffusion coefficient. *J. Chem. Eng. Data*, 7(1):37–41.

Colbeck, S. C. (1989). Air movement in snow due to windpumping. *J. Glaciol.*, 35(120):209–213.

Conway, T. J., Tans, P. P., Waterman, S., L., and Thoning, K. W. (1994). Evidence for interannual variability of the carbon-cycle from the National-Oceanic-and-Atmospheric-Administration Climate-Monitoring-and-Diagnostics-Laboratory Global-air-sampling-network. *J. Geophys. Res.-Atm*, 99(D11):22831–22855.

Craig, H., Horibe, Y., and Sowers, T. (1988). Gravitational separation of gases and isotopes in polar ice caps. *Science*, 242(4886):1675–1678.

Cunnold, D., Weiss, R., Prinn, R., Hartley, D., Simmonds, P., Fraser, P., Miller, B., Alyea, F., and Porter, L. (1997). GAGE/AGAGE measurements indicating reductions in global emissions of CCl_3F and CCl_2F_2 in 1992-1994. *J. Geophys. Res.-Atm.*, 102(D1):1259–1269.

Dlugokencky, E. J., Steele, L. P., Lang, P. M., and Masarie, K. A. (1994). The growth-rate and distribution of atmospheric methane. *J. Geophys. Res.-Atm*, 99(D8):17021–17043.

Dreyfus, G. B., Jouzel, J., Bender, M. L., Landais, A., Masson-Delmotte, V., and Leuenberger, M. (2010). Firn processes and δ^{15}n: potential for a gas-phase climate proxy. *Quaternary Sci. Rev.*, 29(1-2):28–42.

Etheridge, D., Steele, L., Francey, R., and Langenfelds, R. (1998). Atmospheric methane between 1000 AD and present: Evidence of anthropogenic emissions and climatic variability. *J. Geophys. Res.-Atm.*, 103(D13):15979–15993.

Etheridge, D. M., Steele, L. P., Langenfelds, R. L., Francey, R. J., Barnola, J. M., and Morgan, V. I. (1996). Natural and anthropogenic changes in atmospheric co_2 over the last 1000 years from air in antarctic ice and firn. *J. Geophys. Res.*, 101(D2):4115–4128.

Fabre, A., Barnola, J. M., Arnaud, L., and Chappellaz, J. (2000). Determination of gas diffusivity in polar firn: Comparison between experimental measurements and inverse modeling. *Geophys. Res. Lett.*, 27(4):557–560.

Ferretti, D. F., Miller, J. B., White, J. W. C., Etheridge, D. M., Lassey, K. R., Lowe, D. C., Meure, C. M. M., Dreier, M. F., Trudinger, C. M., van Ommen, T. D., and Langenfelds, R. L. (2005). Unexpected changes to the global methane budget over the past 2000 years. *Science*, 309(5741):1714–1717.

Francey, R., Allison, C., Etheridge, D., Trudinger, C., Enting, I., Leuenberger, M., Langenfelds, R., Michel, E., and Steele, L. (1999). A 1000-year high precision record of delta C-13 in atmospheric CO_2. *Tellus B*, 51(2):170–193.

Francey, R. J., Steele, L. P., Spencer, D. A., Langenfelds, R. L., Law, R. M., Krummel, P. B., Fraser, P. J., Etheridge, D. M., Derek, N., Coram, S. A., Coopen, L. N., Allison, C. E., Porter, L., and Baly, S. (2003). The csiro (australia) measurement of greenhouse gases in the global atmosphere. In Tindale, N. W., Derek, N., and Fraser, P. J., editors, *Baseline Atmospheric Program Australia 1999 – 2000*, pages 42–53. Bureau of Meteorology, Melbourne, Victoria, Australia.

Fraser, P., Cunnold, D., Alyea, F., Weiss, R., Prinn, R., Simmonds, P., Miller, B., and Langenfelds, R. (1996). Lifetime and emission estimates of 1,1,2-trichlorotrifluorethane (CFC-113) from daily global background observations June 1982 June 1994. *J. Geophys. Res.-Atm.*, 101(D7):12585–12599.

Geller, L., Elkins, J., Lobert, J., Clarke, A., Hurst, D., Butler, J., and Myers, R. (1997). Tropospheric SF_6: Observed latitudinal distribution and trends, derived emissions and interhemispheric exchange time. *Geophys. Res. Lett.*, 24(6):675–678.

Goujon, C., Barnola, J. M., and Ritz, C. (2003). Modeling the densification of polar firn including heat diffusion: Application to close-off characteristics and gas isotopic fractionation for antarctica and greenland sites. *J. Geophys. Res.-Atm*, 108(D24):18.

Hörhold, M. W., Kipfstuhl, S., Wilhelms, F., Freitag, J., and Frenzel, A. (2011). The densification of layered polar firn. *J. Geophys. Res.-Earth.*, 116.

Huber, C., Beyerle, U., Leuenberger, M., Schwander, J., Kipfer, R., Spahni, R., Severinghaus, J. P., and Weiler, K. (2006). Evidence for molecular size dependent gas fractionation in firn air derived from noble gases, oxygen, and nitrogen measurements. *Earth Planet Sc. Lett.*, 243(1-2):61–73.

Ishijima, K., Sugawara, S., Kawamura, K., Hashida, G., Morimoto, S., Murayama, S., Aoki, S., and Nakazawa, T. (2007). Temporal variations of the atmospheric nitrous oxide concentration and its delta n-15 and delta o-18 for the latter half of the 20th century reconstructed from firn air analyses. *J. Geophys. Res.-Atm*, 112(D3):12.

Kawamura, K., Parrenin, F., Lisiecki, L., Uemura, R., Vimeux, F., Severinghaus, J. P., Hutterli, M. A., Nakazawa, T., Aoki, S., Jouzel, J., Raymo, M. E., Matsumoto, K., Nakata, H., Motoyama, H., Fujita, S., Goto-Azuma, K., Fujii, Y., and Watanabe, O. (2007). Northern hemisphere forcing of climatic cycles in antarctica over the past 360,000 years. *Nature*, 448(7156):912–U4.

Kawamura, K., Severinghaus, J. P., Ishidoya, S., Sugawara, S., Hashida, G., Motoyama, H., Fujii, Y., Aoki, S., and Nakazawa, T. (2006). Convective mixing of air in firn at four polar sites. *Earth Planet Sc. Lett.*, 244(3-4):672–682.

Keeling, C. D., Piper, S. C., Whorf, T. P., and Keeling, R. F. (2010). Evolution of natural and anthropogenic fluxes of atmospheric co_2 from 1957 to 2003. *Tellus B*, 63:1–22.

Keeling, R. F., Piper, S. C., Bollenbacher, A. F., and Walker, J. S. (2009). Atmospheric co_2 records from sites in the sio air sampling network. In *Trends: A Compendium of Data on Global Change.* Carbon Dioxide Information Analysis Center, Oak Ridge National Laboratory, U.S. Department of Energy, Oak Ridge, Tenn., U.S.A.

Landais, A., Barnola, J. M., Kawamura, K., Caillon, N., Delmotte, M., Van Ommen, T., Dreyfus, G., Jouzel, J., Masson-Delmotte, V., Minster, B., Freitag, J., Leuenberger, M., Schwander, J., Huber, C., Etheridge, D., and Morgan, V. (2006). Firn-air delta n-15 in modern polar sites and glacial-interglacial ice: a model-data mismatch during glacial periods in antarctica? *Quaternary Sci. Rev.*, 25(1-2):49–62.

Landais, A., Caillon, N., Goujon, C., Grachev, A. M., Barnola, J. M., Chappellaz, J., Jouzel, J., Masson-Delmotte, V., and Leuenberger, M. (2004). Quantification of rapid temperature change during do event 12 and phasing with methane inferred from air isotopic measurements. *Earth Planet Sc. Lett.*, 225(1-2):221–232.

Laube, J. C., Martinerie, P., Witrant, E., Blunier, T., Schwander, J., Brenninkmeijer, C. A. M., Schuck, T. J., Bolder, M., Röckmann, T., van der Veen, C., Bönisch, H., Engel, A., Mills, G. P., Newland, M. J., Oram, D. E., Reeves, C. E., and Sturges, W. T. (2010). Accelerating growth of hfc-227ea (1,1,1,2,3,3,3-heptafluoropropane) in the atmosphere. *Atmos. Chem. Phys.*, 10(13):5903–5910.

Levin, I., Hammer, S., Eichelmann, E., and Vogel, F. (2011). Verification of greenhouse gas emission reductions: The prospect of atmospheric monitoring in polluted areas. *Philos. T. R. Soc. A.*

Levin, I., Hammer, S., Kromer, B., and Meinhardt, F. (2008). Radiocarbon observations in atmospheric CO_2: Determining fossil fuel CO_2 over Europe using Jungfraujoch observations as background. *Sci. Total Environ.*, 391(2-3):211–216.

Levin, I. and Kromer, B. (2004). The tropospheric (CO_2)-C-14 level in mid-latitudes of the Northern Hemisphere (1959-2003). *Radiocarbon*, 46(3):1261–1272.

Levin, I., Naegler, T., Heinz, R., Osusko, D., Cuevas, E., Engel, A., Ilmberger, J., Langenfelds, R. L., Neininger, B., Rohden, C. v., Steele, L. P., Weller, R., Worthy, D. E., and Zimov, S. A. (2010). The global sf_6 source inferred from long-term high precision atmospheric measurements and its comparison with emission inventories. *Atmos. Chem. Phys.*, 10(6):2655–2662.

MacFarling Meure, C., Etheridge, D., Trudinger, C., Steele, P., Langenfelds, R., van Ommen, T., Smith, A., and Elkins, J. (2006). Law dome co_2, ch_4 and n_2o ice core records extended to 2000 years bp. *Geophys. Res. Lett.*, 33(14).

Manning, M. and Melhuish, W. H. (1994). Atmospheric delta 14c record from wellington. In *Trends: A Compendium of Data on Global Change*. Carbon Dioxide Information Analysis Center, Oak Ridge National Laboratory, U.S. Department of Energy, Oak Ridge, Tenn., U.S.A.

Martinerie, P., Nourtier-Mazauric, E., Barnola, J. M., Sturges, W. T., Worton, D. R., Atlas, E., Gohar, L. K., Shine, K. P., and Brasseur, G. P. (2009). Long-lived halocarbon trends and budgets from atmospheric chemistry modelling constrained with measurements in polar firn. *Atmos. Chem. Phys.*, 9(12):3911–3934.

Martinerie, P., Raynaud, D., Etheridge, D. M., Barnola, J. M., and Mazaudier, D. (1992). Physical and climatic parameters which influence the air content in polar ice. *Earth Planet Sc. Lett.*, 112(1-4):1–13.

Massmann, J. and Farrier, D. F. (1992). Effects of atmospheric pressures on gas transport in the vadose zone. *Water Resour. Res.*, 28(3):777–791.

Matsunaga, N., Hori, M., and Nagashima, A. (1993). Mutual diffusion coefficients of halogenated-hydrocarbon refrigerant-air systems. *High Temp.-High Press.*, 25:185–192.

Matsunaga, N., Hori, M., and Nagashima, A. (1998). Diffusion coefficients of global warming gases into air and its component gases. *High Temp.-High Press.*, 30(1):77–83.

Matsunaga, N., Hori, M., and Nagashima, A. (2002a). Measurements of the mutual diffusion coefficients of gases by the taylor method (7th report, measurements on the sf_6-air, sf_6-n_2, sf_6-o_2, cfc12-n_2, cfc12-o_2, hcfc22-n_2 and hcfc22-o_2 systems). *Trans. Jpn. Soc. Mech. Eng. B.*, 68:550–555.

Matsunaga, N., Hori, M., and Nagashima, A. (2002b). Measurements of the mutual diffusion coefficients of gases by the taylor method (8th report, measurements on the hfc32-air, hcfc124-air, hcfc125-air, hcfc143a-air, and hfc43-10mee-air systems). *Trans. Jpn. Soc. Mech. Eng. B.*, 68:550–555.

Mischler, J. A., Sowers, T. A., Alley, R. B., Battle, M., McConnell, J. R., Mitchell, L., Popp, T., Sofen, E., and Spencer, M. K. (2009). Carbon and hydrogen isotopic composition of methane over the last 1000 years. *Global Biogeochem. Cy.*, 23.

Montzka, S., Myers, R., Butler, J., Elkins, J., Lock, L., Clarke, A., and Goldstein, A. (1996). Observations of HFC-134a in the remote troposphere. *Geophys. Res. Lett.*, 23(2):169–172.

Montzka, S. A., Aydin, M., Battle, M., Butler, J. H., Saltzman, E. S., Hall, B. D., Clarke, A. D., Mondeel, D., and Elkins, J. W. (2004). A 350-year atmospheric history for carbonyl sulfide inferred from antarctic firn air and air trapped in ice. *J. Geophys. Res.-Atm*, 109(D22):11.

Nydal, R. and Lövseth, K. (1996). Carbon-14 measurements in atmospheric co_2 from northern and southern hemisphere sites, 1962-1993. Carbon Dioxide Information Analysis Center, Oak Ridge National Laboratory, Oak Ridge, Tennessee.

Prinn, R., Huang, J., Weiss, R., Cunnold, D., Fraser, P., Simmonds, P., McCulloch, A., Harth, C., Reimann, S., Salameh, P., O'Doherty, S., Wang, R., Porter, L., Miller, B., and Krummel, P.

(2005). Evidence for variability of atmospheric hydroxyl radicals over the past quarter century. *Geophys. Res. Lett.*, 32(7).

Prinn, R., Weiss, R., Fraser, P., Simmonds, P., Cunnold, D., Alyea, F., O'Doherty, S., Salameh, P., Miller, B., Huang, J., Wang, R., Hartley, D., Harth, C., Steele, L., Sturrock, G., Midgley, P., and McCulloch, A. (2000). A history of chemically and radiatively important gases in air deduced from ALE/GAGE/AGAGE. *J. Geophys. Res.-Atm*, 105(D14):17751–17792.

Rasmussen, S., Andersen, K., Svensson, A., Steffensen, J., Vinther, B., Clausen, H., Siggaard-Andersen, M., Johnsen, S., Larsen, L., Dahl-Jensen, D., Bigler, M., Rothlisberger, R., Fischer, H., Goto-Azuma, K., Hansson, M., and Ruth, U. (2006). A new Greenland ice core chronology for the last glacial termination. *J. Geophys. Res.-Atm.*, 111(D6).

Reimer, P., Baillie, M., Bard, E., Bayliss, A., Beck, J., Bertrand, C., Blackwell, P., Buck, C., Burr, G., Cutler, K., Damon, P., Edwards, R., Fairbanks, R., Friedrich, M., Guilderson, T., Hogg, A., Hughen, K., Kromer, B., McCormac, G., Manning, S., Ramsey, C., Reimer, R., Remmele, S., Southon, J., Stuiver, M., Talamo, S., Taylor, F., van der Plicht, J., and Weyhenmeyer, C. (2004). IntCal04 terrestrial radiocarbon age calibration, 0-26 cal kyr BP. *Radiocarbon*, 46(3):1029–1058.

Röckmann, T., Kaiser, J., and Brenninkmeijer, C. A. M. (2003). The isotopic fingerprint of the pre-industrial and the anthropogenic n_2o source. *Atmos. Chem. Phys.*, 3:315–323.

Rommelaere, V., Arnaud, L., and Barnola, J. M. (1997). Reconstructing recent atmospheric trace gas concentrations from polar firn and bubbly ice data by inverse methods. *J. Geophys. Res.-Atm*, 102(D25):30069–30083.

Schwander, J. (1989). The transformation of snow to ice and the occlusion of gases. In Oescher, H. and Langway, C., editors, *The Environmental record in glaciers and ice sheets*, pages 53–67. John Wiley, New York.

Schwander, J., Barnola, J. M., Andrie, C., Leuenberger, M., Ludin, A., Raynaud, D., and Stauffer, B. (1993). The age of the air in the firn and the ice at summit, greenland. *J. Geophys. Res.-Atm*, 98(D2):2831–2838.

Schwander, J., Sowers, T., Barnola, J. M., Blunier, T., Fuchs, A., and Malaize, B. (1997). Age scale of the air in the summit ice: Implication for glacial-interglacial temperature change. *J. Geophys. Res.-Atm*, 102(D16):19483–19493.

Schwander, J., Stauffer, B., and Sigg, A. (1988). Air mixing in firn and the age of the air at pore close-off. In *Ann. Glaciol.*, volume 10, pages 141–145.

Severinghaus, J. P., Albert, M. R., Courville, Z. R., Fahnestock, M. A., Kawamura, K., Montzka, S. A., Muhle, J., Scambos, T. A., Shields, E., Shuman, C. A., Suwa, M., Tans, P., and Weiss, R. F. (2010). Deep air convection in the firn at a zero-accumulation site, central antarctica. *Earth Planet Sc. Lett.*, 293(3-4):359–367.

Severinghaus, J. P. and Battle, M. O. (2006). Fractionation of gases in polar lee during bubble close-off: New constraints from firn air ne, kr and xe observations. *Earth Planet Sc. Lett.*, 244(1-2):474–500.

Severinghaus, J. P. and Brook, E. J. (1999). Abrupt climate change at the end of the last glacial period inferred from trapped air in polar ice. *Science*, 286(5441):930–934.

Severinghaus, J. P., Grachev, A., and Battle, M. (2001). Thermal fractionation of air in polar firn by seasonal temperature gradients. *Geochem. Geophy. Geosy.*, 2.

Severinghaus, J. P., Grachev, A., Luz, B., and Caillon, N. (2003). A method for precise measurement of argon 40/36 and krypton/argon ratios in trapped air in polar ice with applications to past firn thickness and abrupt climate change in greenland and at siple dome, antarctica. *Geochim. Cosmochim. Ac.*, 67(3):325–343.

Smith, A. M., Levchenko, V. A., Etheridge, D. M., Lowe, D. C., Hua, Q., Trudinger, C. M., Zoppi, U., and Elcheikh, A. (1999). In search of in-situ radiocarbon in law dome ice and firn. In *8th International Conference on Accelerator Mass Spectrometry*, pages 610–622, Vienna, Austria. Elsevier Science Bv.

Sowers, T., Bender, M., Raynaud, D., and Korotkevich, Y. S. (1992). Delta-n-15 of n_2 in air trapped in polar ice - a tracer of gas-transport in the firn and a possible constraint on ice age-gas age-differences. *J. Geophys. Res.-Atm*, 97(D14):15683–15697.

Sowers, T., Bernard, S., Aballain, O., Chappellaz, J., Barnola, J., and Marik, T. (2005). Records of the delta C-13 of atmospheric CH4 over the last 2 centuries as recorded in Antarctic snow and ice. *Global Biogeochem. Cy.*, 19(2).

Spahni, R., Schwander, J., Flückiger, J., Stauffer, B., Chappellaz, J., and Raynaud, D. (2003). The attenuation of fast atmospheric ch_4 variations recorded in polar ice cores. *Geophys. Res. Lett.*, 30(11):1571.

Stuiver, M. and Polach, H. A. (1977). Reporting of c-14 data - discussion. *Radiocarbon*, 19(3):355–363.

Sturrock, G. A., Etheridge, D. M., Trudinger, C. M., Fraser, P. J., and Smith, A. M. (2002). Atmospheric histories of halocarbons from analysis of antarctic firn air: Major montreal protocol species. *J. Geophys. Res.-Atm*, 107(D24):14.

Sugawara, S., Kawamura, K., Aoki, S., Nakazawa, T., and Hashida, G. (2003). Reconstruction of past variations of delta c-13 in atmospheric co_2 from its vertical distribution observed in the firn at dome fuji, antarctica. *Tellus B*, 55(2):159–169.

Trudinger, C. M. (2001). *The carbon cycle over the last 1000 years inferred from inversion of ice core data*. PhD thesis, Monash University, Australia.

Trudinger, C. M., Enting, I. G., Etheridge, D. M., Francey, R. J., Levchenko, V. A., Steele, L. P., Raynaud, D., and Arnaud, L. (1997). Modeling air movement and bubble trapping in firn. *J. Geophys. Res.-Atm*, 102(D6):6747–6763.

Trudinger, C. M., Etheridge, D. M., Rayner, P. J., Enting, I. G., Sturrock, G. A., and Langenfelds, R. L. (2002). Reconstructing atmospheric histories from measurements of air composition in firn. *J. Geophys. Res.-Atm*, 107(D24):13.

Trudinger, C. M., Etheridge, D. M., Sturrock, G. A., Fraser, P. J., Krummel, P. B., and McCulloch, A. (2004). Atmospheric histories of halocarbons from analysis of antarctic firn air: Methyl bromide, methyl chloride, chloroform, and dichloromethane. *J. Geophys. Res.-Atm*, 109(D22):15.

Tschumi, J. and Stauffer, B. (2000). Reconstructing past atmospheric co_2 concentration based on ice-core analyses: open questions due to in situ production of co_2 in the ice. *J. Glaciol.*, 46(152):45–53.

Witrant, E., Martinerie, P., Hogan, C., Laube, J. C., Kawamura, K., Capron, E., Montzka, S. A., Dlugokencky, E. J., Etheridge, D., Blunier, T., and Sturges, W. T. (2011). A new multi-gas constrained model of trace gas non-homogeneous transport in firn: evaluation and behavior at eleven polar sites. *Atmos. Chem. Phys. Discuss.*, 11(8):23029–23080.

4

Diffusive fractionation in the firn

4.1 Introduction

The different isotopologues of a trace gas have different masses, and therefore a different free air diffusion coefficient. This difference in diffusivity can lead to an isotopic signal in the firn, even in the absence of changes in the atmospheric isotopic composition of the trace gas (Trudinger et al., 1997). This so-called diffusive fractionation (DF) is shown schematically in Fig. 4.1 for a theoretical monotonic atmospheric CO_2 increase. The heavier $^{13}CO_2$ isotopologue diffuses more slowly into the firn, leading to a depletion with depth relative to the lighter $^{12}CO_2$ isotopologue. The resulting isotopic fractionation ε_{DF} is shown in the right panel. Note that DF only occurs when the atmospheric mixing ratio of a trace gas is changing with time; if constant we will get $\varepsilon_{DF} = 0$ throughout the firn column.

Both firn and ice core gas records have to be corrected for the effect of DF. For example, the (site specific) corrections for the recent anthropogenic increase are $\sim$0.1 ‰ for $\delta^{13}CO_2$ at DE08, Law Dome (Francey et al., 1999), and 1.2 ‰ for $\delta^{13}CH_4$ at WAIS-Divide (Mischler et al., 2009). When the transport properties of a firn site are well characterized using reference tracers, the DF is automatically included when modeling firn air transport. However, in section 3.4.4 we showed that the magnitude of the DF differs substantially between different firn air models.

Ice core records of e.g. $\delta^{13}C$–CO_2 or $\delta^{13}C$–CH_4 should in principle be corrected for the effect of diffusive fractionation. A complete description of the problem would require two things. First, using a dynamical firn densification model the firn density profile and close-off depth need to be reconstructed back in time (Goujon et al., 2003; Barnola et al., 1991). This requires accurate estimates of past accumulation rates and temperature. Second, the movement of trace gases in the porosity needs to be modeled using a firn air transport model. As the diffusivity–depth relationship is unknown, a parameterization of the firn tortuosity has to be applied (Schwander, 1989). The parameterisation is based on measurements on finite-size firn samples,

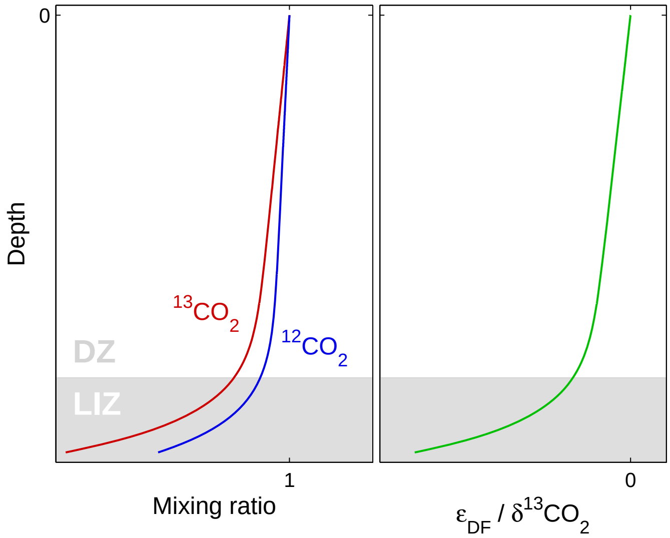

Figure 4.1: The principle of diffusive fractionation in the firn, gravity turned to zero for clarity. The left panel shows schematic mixing ratio profiles for ^{12}CO$_2$ *and* ^{13}CO$_2$ *isotopologues for a hypothetical monotonous atmospheric increase in mixing ratio. The right panel shows the diffusive fractionation given as* $[^{13}\mathrm{CO}_2]/[^{12}\mathrm{CO}_2] - 1$.

which do not accurately represent the transport properties of the entire firn pack (Fabre et al., 2000). Consequently, the fit to experimental data obtained with diffusivity parameterizations is generally not very good (section 2.5.1).

In this chapter we will derive an analytical expression for the DF, which shows what parameters control the magnitude of this effect. Using modern, well-characterized firn air sites, we find an empirical expression for the gas age at the lock-in depth. On combining these two results we have a convenient framework to estimate $\varepsilon_{\mathrm{DF}}$ for the ice core record. This approach has several advantages:

1. It requires little computational effort.
2. It requires only commonly available ice core data, namely trace gas mixing ratios and the diffusive column height (DCH) estimated from δ^{15}N–N$_2$.
3. It is not subject to the uncertainties inherent to estimating the accumulation rate, temperature, close-off depth and depth-diffusivity relationship back in time.
4. It does not require knowledge of the true atmospheric variations; rather it uses the mixing ratios as recorded in the ice core after diffusion in the firn column.
5. With the exception of modern, well-characterized firn air sites, our method arguably gives more accurate results.

To test the accuracy and dynamic response of our method we compare it to a full firn air transport model forced with atmospheric signals at different time scales. Finally we show the magnitude of ϵ_{DF} for measured ice core trace gas records.

4.2 Analytical description of diffusive fractionation

Let $C_i(z,t)$ and $C(z,t)$ denote the mixing ratio of the rare and abundant isotopologue, respectively. We let $R_{\mathrm{std}} = (C_i/C)_{\mathrm{std}} = 1$, so that $\delta = C_i/C - 1$. We introduce $\Delta C = C_i - C$. Using this notation we get $\varepsilon_{\mathrm{DF}} = C_i/C - 1 = \Delta C/C$.

We assume a simple atmospheric forcing of the form:

$$C(0,t) = C_i(0,t) = C_0 + kt \tag{4.1}$$

where k is the atmospheric growth rate, and $k \ll C$. This atmospheric history is unique in having the property:

$$\begin{aligned} C(z,t) &= C(0, t - \Gamma(z)) \\ C_i(z,t) &= C(0, t - \Gamma_i(z)) \end{aligned} \tag{4.2}$$

where Γ is the age of the air with depth. What Eq. (4.2) says is that the mixing ratio at each depth is identical to that at the surface, with a delay given by the gas age $\Gamma(z)$. Note that the gas ages are isotopologue specific. This formulation allows us to write the diffusive fractionation as:

$$\varepsilon_{\mathrm{DF}} = \frac{\Delta C}{C} = \frac{k(\Gamma_i - \Gamma)}{C_0 + k(t - \Gamma)} \approx \frac{k\Delta\Gamma}{C} \tag{4.3}$$

with $\Delta\Gamma$ the age difference between the isotopologues.

As diffusive fractionation mostly occurs in the DZ, we will neglect the effect of advection. The fractionation that occurs as the gases diffuse down becomes:

$$\begin{aligned} \frac{\partial}{\partial z}\varepsilon_{\mathrm{DF}} &= \frac{\partial}{\partial z}\frac{C_i - C}{C} \\ &= \frac{C\frac{\partial}{\partial z}C_i - C_i\frac{\partial}{\partial z}C}{C^2} \\ &= \frac{C_i\frac{J}{D} - C\frac{J_i}{D_i}}{C^2} \end{aligned} \tag{4.4}$$

where in the last step we have used the fact that the diffusive flux $J = -D\frac{dC}{dz}$. We can rewrite Eq. (4.4) as:

$$\frac{\partial}{\partial z}\varepsilon_{\mathrm{DF}} = \frac{1}{C}\left(\frac{C_i/C}{D} - \frac{J_i/J}{D_i}\right)J \tag{4.5}$$

because $\frac{C_i}{C} \approx \frac{J_i}{J} \approx 1$ we can simplify to:

$$\frac{\partial}{\partial z}\varepsilon_{\mathrm{DF}} = \frac{1}{C}\left(\frac{1}{D} - \frac{1}{D_i}\right) J = \frac{1}{C}\left(\frac{D}{D_i} - 1\right)\frac{\partial C}{\partial z} \tag{4.6}$$

using the fact that $\frac{\partial C}{\partial z} = -k\frac{\partial \Gamma}{\partial z}$, we find:

$$\frac{\partial}{\partial z}\varepsilon_{\mathrm{DF}} = -\frac{k}{C}\left(\frac{D}{D_i} - 1\right)\frac{\partial \Gamma}{\partial z}$$

and

$$\boxed{\varepsilon_{\mathrm{DF}}(z) \approx -\frac{k}{C}\left(\frac{D}{D_i} - 1\right)\Gamma(z)} \tag{4.7}$$

From Eq. 4.7 we can draw a number of interesting conclusions:

- It is not the increase k itself that matters, but rather the relative increase k/C. For an exponential atmospheric increase (constant k/C), the DF in the firn is constant with time.
- The DF scales linearly with $(D/D_i - 1)$. This quantity is shown in Table 4.1 for several trace gases relevant to ice core studies. The effect is largest for light gases such as methane and H_2. Because the molecules are relatively light ($M_{\mathrm{CH}_4} = 16.04$ kg mol^{-1} and $M_{\mathrm{H}_2} = 2.02$ kg mol^{-1}), the isotopic substitution of ^{13}C (D, i.e. ^{2}H) for ^{12}C (H) makes a large difference for the mass ratio, and thereby the diffusivity ratio.
- The DF scales linearly with the age of the gas. The gas age at the firn-ice transition, where the air is trapped, depends strongly on the length of the firn column. The DF is larger in the deep firns of the Antarctic plateau than in the shallow firns of the (warmer) Antarctic coastal and Greenlandic sites.
- As both isotopologues diffusive through the same firn column, the exact shape of the depth-diffusivity profile (i.e. the tortuosity) does not matter. The ratio of molecular diffusivities is constant throughout the firn column.

The result of Eq. 4.7 is valid only in the diffusive zone (DZ) where advection is negligible. In the lock-in zone (LIZ) advection dominates the transport. Advection does not discriminate between isotopologues, giving no continued fractionation with depth. For this reason the fractionation $\varepsilon_{\mathrm{DF}}$ along the firn whole column is well approximated by

$$\varepsilon_{\mathrm{DF}} = \begin{cases} -\frac{k}{C}\left(\frac{D}{D_i} - 1\right)\Gamma(z) & \text{for } z \le z_{\mathrm{lid}} \\ -\frac{k}{C}\left(\frac{D}{D_i} - 1\right)\Gamma(z_{\mathrm{lid}}) & \text{for } z > z_{\mathrm{lid}} \end{cases} \tag{4.8}$$

with z_{lid} the lock-in depth which separates the DZ and LIZ.

Table 4.1: Diffusivity ratios of isotopologues following Buizert et al. (2011) and Trudinger et al. (1997). If the atom mass is not specified, is represents the average weight (i.e. the sum of the isotopic masses multiplied by their relative abundance).

Isotopologue ratio	$^a\left(\frac{D}{D_i}-1\right)$	$^b\left(\frac{D}{D_i}-1\right)$
HH/HD	20.50×10^{-2}	-
$^{12}\mathrm{CH_4}/^{13}\mathrm{CH_4}$	1.95×10^{-2}	1.79×10^{-2}
$\mathrm{CH_4/CH_3D}$	1.96×10^{-2}	-
$^{12}\mathrm{CO}/^{13}\mathrm{CO}$	0.89×10^{-2}	-
$\mathrm{C^{16}O/C^{18}O}$	1.74×10^{-2}	-
$^{12}\mathrm{CO_2}/^{13}\mathrm{CO_2}$	0.44×10^{-2}	0.42×10^{-2}
$\mathrm{CO_2}/^{14}\mathrm{CO_2}$	0.87×10^{-2}	0.83×10^{-2}
$\mathrm{C^{16}O^{16}O/C^{18}O^{16}O}$	0.88×10^{-2}	-
$^{14}\mathrm{N}^{14}\mathrm{NO}/^{15}\mathrm{N}^{14}\mathrm{NO}$	0.44×10^{-2}	-
$\mathrm{NN^{16}O/NN^{18}O}$	0.88×10^{-2}	-

[a] Buizert et al. (2011)
[b] Trudinger et al. (1997)

In deriving Eq. 4.8 we made some assumptions and simplifications. To verify its correctness we now compare the analytical result to the modeled DF at NEEM for six firn air transport models (synthetic scenario I in section 3.4.4). The scenario consists of a hypothetical monotonic $\mathrm{CO_2}$ increase following:

$$[^{12}\mathrm{CO_2}] = [^{13}\mathrm{CO_2}] = 225\exp\left[2.5\times10^{-3}(t-1800)\right] \quad \mathrm{ppm} \tag{4.9}$$

with t the time in years C.E. Equation (4.9) corresponds to a constant $k/C = 2.5\times10^{-3}$. The final decimal model date is 2008.54, corresponding to the sampling date at NEEM. For the mean age $\Gamma(z)$ we use the first moment of the NEEM $\mathrm{CO_2}$ age distribution $G(z,t)$ calculated with the CIC firn air model:

$$\Gamma(z) = \int_0^\infty G(z,t)\times t\; dt \tag{4.10}$$

The modeled solutions are compared to the analytical result in Fig. 4.2. We find that within the DZ the models and the analytical result agree very well. Within the LIZ the model solutions diverge strongly, as discussed in detail in section 3.4.4. The analytical solution falls within the spread observed among the models. From this we can conclude that Eq. 4.8 gives an accurate prediction of the diffusive isotopic fractionation in the firn.

4.3 Parameterizing gas age at the lock-in depth

Equation (4.8) in principle allows us to calculate $\varepsilon_{\mathrm{DF}}$ in the ice core record in order to correct isotopic measurements. The values of C and k can be derived from

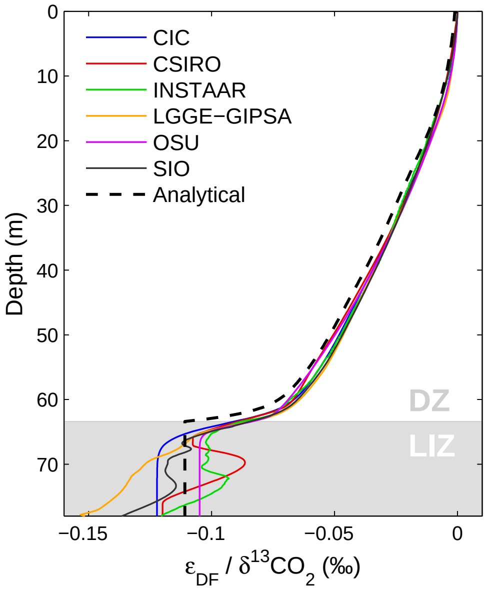

Figure 4.2: Isotopic diffusive fractionation in the NEEM firn for a hypothetical atmospheric CO_2 scenario. See section 3.3.2 for model acronyms and details.

Table 4.2: Overview of firn air sites used in the gas age parameterization. See Table 2.1 for more details.

Site	p (hPa)	T (°C)	A (cm ice yr^{-1})	DCH (m)	Year sampled
NEEM	745	-28.9	22	59.8	2008
NGRIP	691	-31.1	19	66.5	2001
Berkner Island	895	-26	13	50.0	2003
Dome C	658	-54	3.2	93.0	1999
South Pole	681	-51	8	115.0	1995

measured trace gas mixing ratios, the mean age Γ is the only unknown. Here we derive a parameterization of $\Gamma(z_{\text{lid}})$, i.e. the mean gas age at the lock-in depth. Since the vast majority of the air is occluded within the LIZ ($\sim$ 95% at NEEM), the value of ε_{DF} at the lock-in depth gives a good estimate of ε_{DF} recorded in the ice.

We tuned the CIC firn air model (Chapter 5) to five modern firn air sites representing both hemispheres and a wide range of climatic conditions. The sites are summarized in Table 4.2. For each site we reconstructed the diffusivity-depth profile using reference tracers of known atmospheric history (see Sections 2.5.1, 3.3.1 and 5.6). For this purpose the lock-in depth is chosen as the depth where the tortuosity of the pore geometry reduces the effective diffusivity by three orders of magnitude below the free air diffusivity; this is generally equal to the depth where gravitational

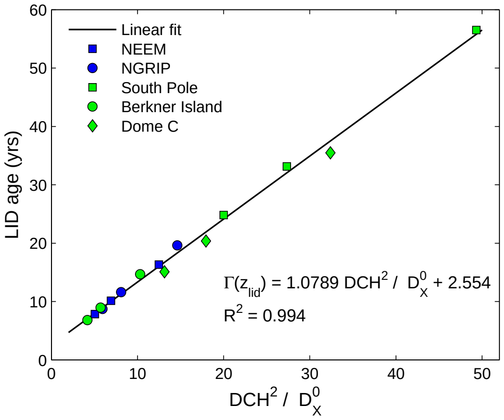

Figure 4.3: Gas age at the Lock-in depth z_{lid} *for 5 different firn air sites* $(50 \leq \mathrm{DCH} \leq 115\ \mathrm{m})$, *and three different gases* ($\mathrm{SF_6}$, $\mathrm{CO_2}$ *and* $\mathrm{CH_4}$ *with* $\gamma_X = 0.554$, $\gamma_X = 1$ *and* $\gamma_X = 1.367$, *respectively*). *The Lock-in depth is defined as the depth where the effective diffusivity is reduced by three orders of magnitude below the free air diffusivity,* $D_X(z_{\mathrm{lid}}) = D_X^0 \times 1 \cdot 10^{-3}$. *The diffusive column height* (DCH) *is derived from the* $\delta^{15}\mathrm{N}$–$\mathrm{N_2}$ *in the LIZ,* $\mathrm{DCH} = \ln\left(\delta^{15}\mathrm{N}/10^3 + 1\right) \times RT/\Delta Mg$.

enrichment ceases, but easier to calculate consistently or in the absence of $\delta^{15}\mathrm{N}$–$\mathrm{N_2}$ data. The mean age of the air $\Gamma(z_{\mathrm{lid}})$ is calculated using Eq. 4.10.

The modeled gas age for three gases ($\mathrm{SF_6}$, $\mathrm{CO_2}$ and $\mathrm{CH_4}$) is shown in Fig. 4.3 as a function of the diffusive column height (DCH). We find that the gas age follows a linear relationship given by

$$\boxed{\Gamma(z_{\mathrm{lid}}) = 1.0789 \times \frac{\mathrm{DCH}^2}{D_X^0} + 2.554} \tag{4.11}$$

Note that the calculated age will be given in years when diffusivity D_X^0 is expressed in $\mathrm{m^2\,yr^{-1}}$, and in seconds when D_X^0 has units of $\mathrm{m^2\,s^{-1}}$. The intersect with the age-axis at 2.554 yrs is perhaps unexpected, as the age should go to zero in the limits $D_X^0 \to \infty$ and $\mathrm{DCH} \to 0$. A deviation from Eq. (4.11) is indeed observed for highly-diffusive gases ($\gamma_X > 5$), making the trend curve down towards the origin. The range of diffusion coefficients used in the fit ($0.554 \leq \gamma_X \leq 1.367$) is suitable for all atmospheric trace gases, with the exception of the very fast diffusing species He and $\mathrm{H_2}$. Sites with a DCH close to zero have not been found in the accumulation zones of the major ice sheets. The range of the DCH at the sites ($50 \leq \mathrm{DCH} \leq 115$) represents the spread found in nature. Equation (4.11) should be used with caution outside of the DCH and γ_X ranges indicated here.

There are good reasons for using the DCH rather than the lock-in depth itself in the age parameterization. First, the DCH can directly be obtained from measurements of $\delta^{15}\mathrm{N}$–$\mathrm{N_2}$ or $\delta^{40}\mathrm{Ar}$. The lock-in depth, on the other hand, needs to be

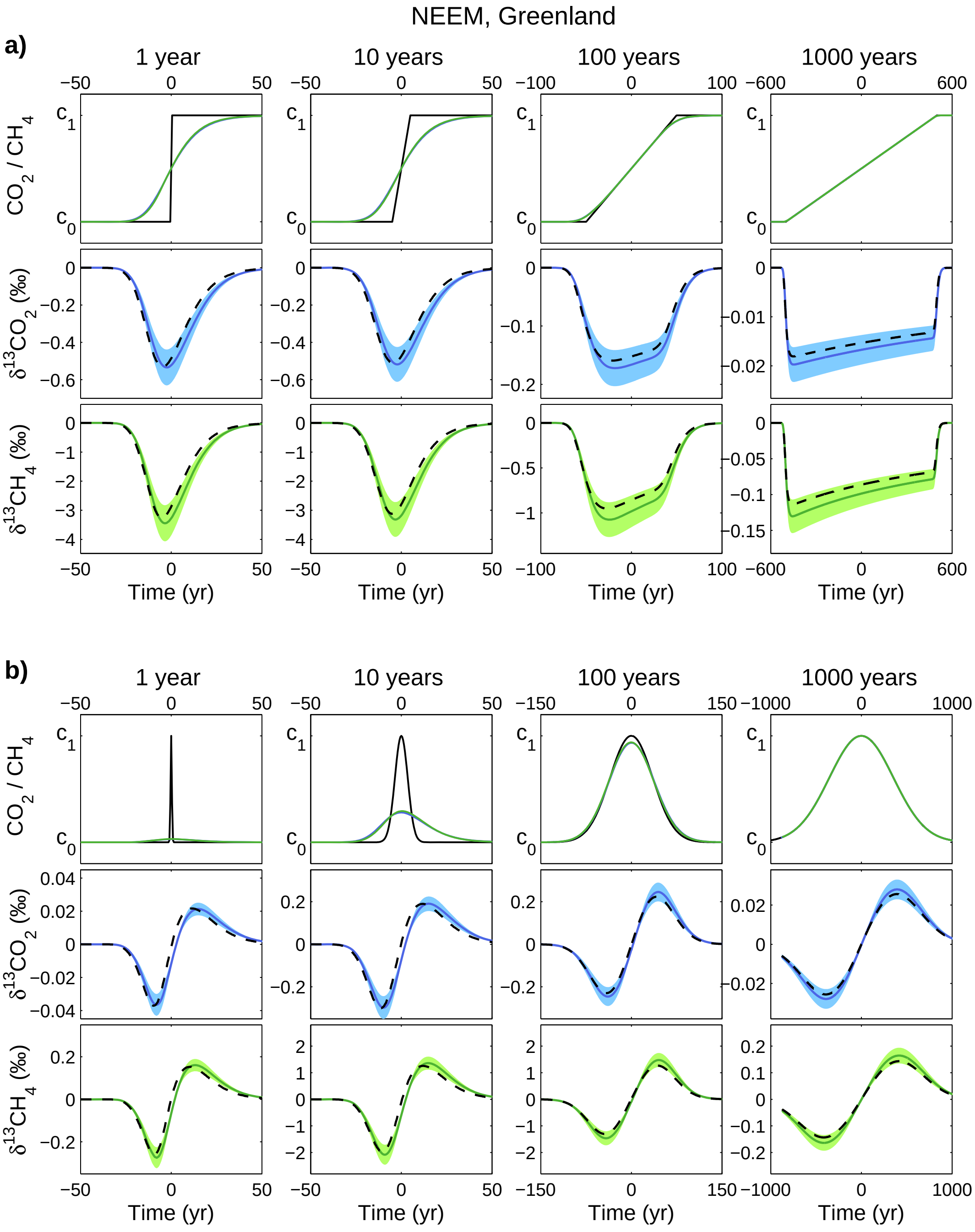

Figure 4.4: Accuracy and dynamic response of the method compared to the CIC firn air model for the NEEM site in Greenland. The upper panels show the atmospheric forcing in black, and the corresponding signal recorded in the ice core in blue (green) for CO_2 (CH_4). The middle (lower) panels give the DF for $\delta^{13}CO_2$ ($\delta^{13}CH_4$), where the CIC output is given as a solid curve. The shading represents the spread in LIZ model solutions observed in the NEEM model intercomparison of Fig. 4.2. The dashed black line shows the result from Eqs (4.7) and (4.11). **(a)** *Response to a linear ramp from $c_0 = 190$ (400) to $c_1 = 270$ (700) for CO_2 (CH_4) Duration indicated above.* **(b)** *Response to a Gaussian perturbation of indicated 2σ width.*

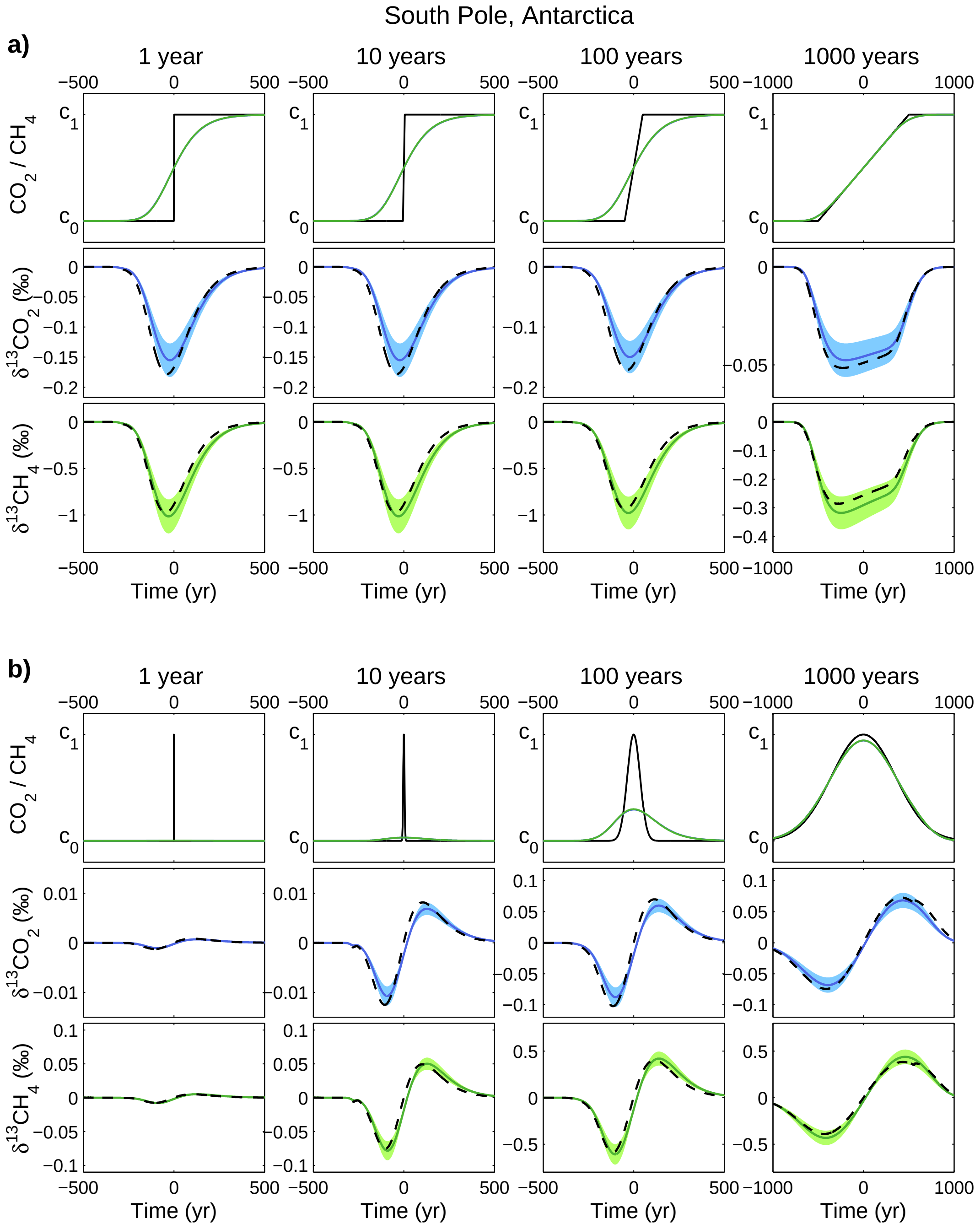

Figure 4.5: Accuracy and dynamic response of the method compared to the CIC firn air model for the South Pole site in Antarctica. The upper panels show the atmospheric forcing in black, and the corresponding signal recorded in the ice core in blue (green) for CO_2 (CH_4). The middle (lower) panels give the DF for $\delta^{13}CO_2$ ($\delta^{13}CH_4$), where the CIC output is given as a solid curve. The shading represents the spread in LIZ model solutions observed in the NEEM model intercomparison of Fig. 4.2. The dashed black line shows the result from Eqs (4.7) and (4.11). **(a)** *Response to a linear ramp from $c_0 = 190$ (0.4) ppm to $c_1 = 270$ (0.7) ppm for CO_2 (CH_4) Duration indicated above.* **(b)** *Response to a Gaussian perturbation of indicated 2σ width.*

reconstructed using firn densification models, which are laborious, have inherent uncertainties, and show a pronounced mismatch with experimental data for the glacial period in Antarctic ice cores (Landais et al., 2006). Second, due to vigorous ventilation, air at the bottom of the CZ is effectively of modern composition, i.e. has a gas age of zero. The gas ages within the DZ, and therefore the gas age at z_{lid} depends mostly on the DCH.

The age parameterization of Eq. (4.11) can also be used when modeling Δage back in time with densification models. The ice age is calculated with the firn densification model, yet to obtain Δage the gas age should be subtracted. As the details of the diffusivity-depth profile are unknown, Eq. (4.11) can be used to calculate the age based on the DCH alone.

4.4 Diffusive fractionation in the ice core record

4.4.1 Comparison to the CIC firn air model

To test the accuracy and dynamic response of our method we compare it the output of the full CIC firn air model for a number of scenarios. First, we use a ramp, where the atmospheric mixing ratio increases linearly from $c_0 = 190$ (0.40) ppm to $c_1 = 270$ (0.70) ppm for CO_2 (CH_4). These values were chosen to represent the glacial-interglacial natural variability range of both gases. To test the dynamic response of our method the duration of the ramp is varied over three orders of magnitude from 1, 10, 100 to 1000 years. Second, we use a Gaussian bell curve, where the atmospheric mixing ratio changes from c_0 to c_1. The 2σ width is varied from 1, 10, 100 to 1000 years.

The results for NEEM and South Pole are shown in Figures 4.4 and 4.5, respectively. The upper row of panels each time shows the atmospheric forcing in black, with the CO_2 (CH_4) signal as recorded in the ice core in blue (green). Note that the blue line line is often not visible as the green line is plotted on top of it. The middle (lower) row of panels shows the resulting DF for $\delta^{13}CO_2$ ($\delta^{13}CH_4$). The CIC model result is plotted as a solid line, with a shaded area around it representing the DF model spread observed in the NEEM model intercomparison study (section 3.4.4). We let the model calculate the mixing ratios in the closed bubbles (section 5.7). Our empirical method, consisting of Eqs. (4.7) and (4.11), is plotted as a dashed black line. In Eq. (4.7) we use $k = dC/dt$ and C from the signals that would be recorded in the ice core, rather than the original atmospheric forcing. This is more realistic, as this would be the data available from real ice cores.

We find that our method agrees very well with the full model results over a wide range of time scales as well as for completely different firn air sites. For rapid signals (1,10 years) there appears to be a timing difference of a few years between our method and the full model results. Note that these rapid cases are mostly academic, as such rapid variations are not observed in the ice core record. For processes on longer, more realistic time scales (100, 1000 years) the timing offset is negligible. As noted above, in our empirical method we use the smoothed concentrations as recorded in the ice rather than the original atmospheric variations. As it turns out, this gives better results. The reason is that the DF signal and the trace gas mixing ratios are smoothed to the same degree by both firn diffusion and bubble trapping. This is a major advantage of our new method; in a full model effort to calculate $\varepsilon_{\mathrm{DF}}$, one would first need to reconstruct the original atmospheric variations (Spahni et al., 2003; Köhler et al., 2011).

Apart from the minor timing issue for rapid variations, our method gives results that fall within the shaded areas that represent the model uncertainty. Generally our method gives a slightly lower isotopic fractionation than the CIC model does. This is to be expected from the firn column comparison shown in Fig. 4.2.

4.4.2 DF in the ice core gas record

We will now apply our method to ice core measurements, and calculate $\varepsilon_{\mathrm{DF}}$ for past atmospheric variations. The results are shown in Figs. 4.6 and 4.7, for Greenland (GISP2 and NGRIP) and Antarctica (EPICA Dome C), respectively. For Greenland we consider fractionation of CH_4 isotopologues only. Due to the presence of CO_2 artifacts, there is no reliable northern hemisphere CO_2 record from Greenland (e.g. Tschumi and Stauffer, 2000).

The fractionation $\varepsilon_{\mathrm{DF}}$ is calculated in three steps. First, we calculate the DCH from the gravitational signal shown in Fig. 4.6c (4.7d). Second, we insert the DCH in Eq. (4.11) and obtain the mean gas age at the lock-in depth, shown in Fig. 4.6d (4.7e). Last, this mean age Γ is used in Eq. (4.7) together with the derivative of the measured mixing ratios to calculate $\varepsilon_{\mathrm{DF}}$. The result is shown in Fig. 4.6e (4.7f-g), note that the scale has been inverted. The $\varepsilon_{\mathrm{DF}}$ calculated for CH_4 applies to both δD and δ^{13}C , since they have essentially the same isotopologue diffusivity ratio (Table 4.1). In section 4.5 we will discuss the uncertainties of the method, as well as the implications of our results.

4.4.3 Correcting δ^{13}C–CH_4 data for DF

Finally we look at published records of δ^{13}C–CH_4 over the last glacial termination (Fischer et al., 2008) and the 8.2 kyr event (Sowers, 2010), and correct them for the effect of DF. For the last termination the results are shown in Fig. 4.8c, with the original (uncorrected) data in blue and the DF corrected data in orange (with errorbar). Note that the isotopic scale has been inverted. During each rapid variation in atmospheric CH_4 concentration (indicated by the grey bars) we find a substantial DF signal. For these three transitions the correction ranged from 0.30–0.53 ‰, more than double the analytical precision of 0.15 ‰ in the study. The errorbars on the

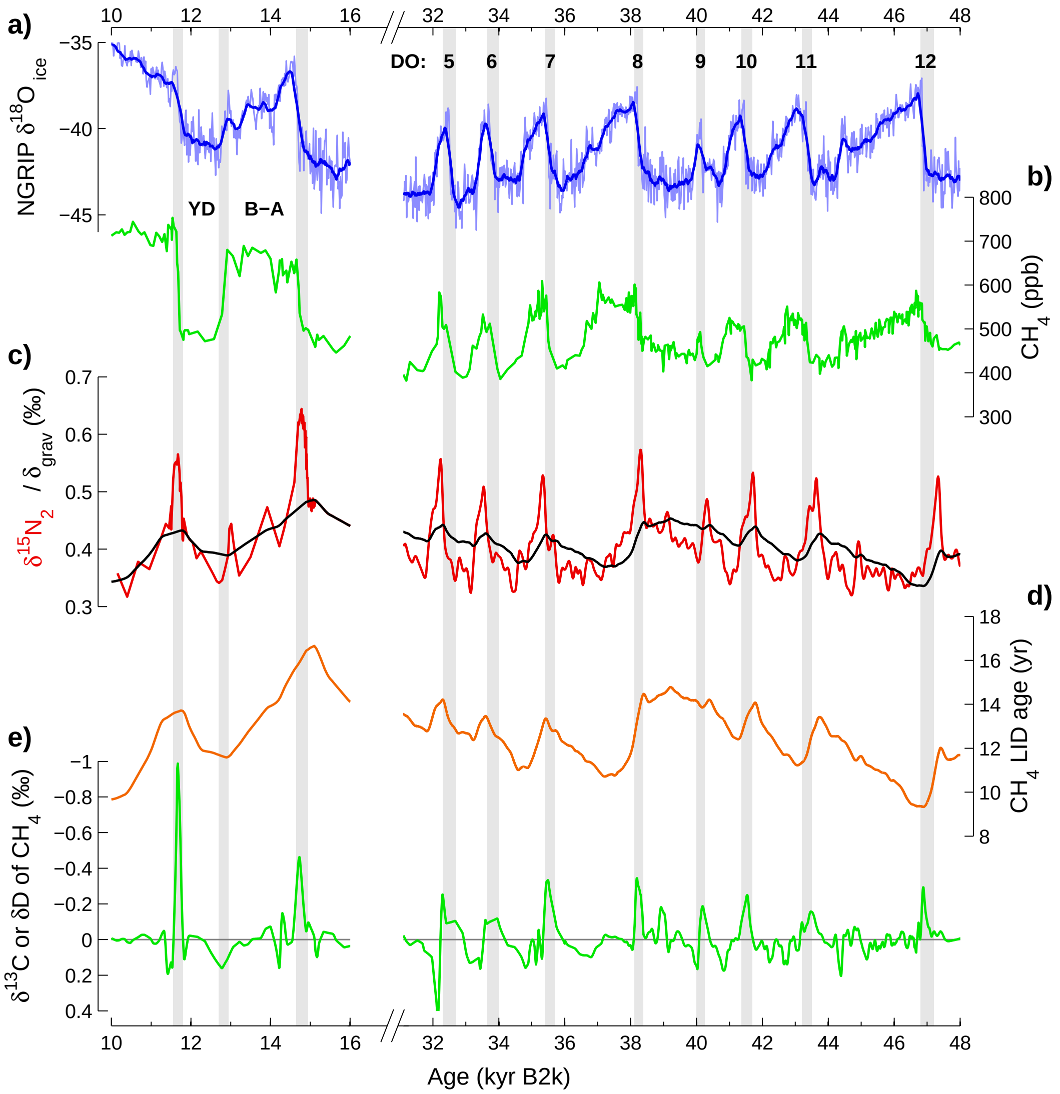

Figure 4.6: Diffusive isotopic fractionation for CH_4 in Greenland. Ages are before the year 2000 C.E. (B2k). **a)** *Precipitation $\delta^{18}O$ as a proxy for site temperature from the NGRIP ice core on the GICC05 time scale (NGRIP community members, 2004).* **b)** *Composite record of northern hemisphere CH_4 mixing ratio based on GRIP, GISP2 and NGRIP ice core samples (Blunier et al., 2007).* **c)** *In red the measured $\delta^{15}N$ from NGRIP (30–48 kyr B2k; Huber et al., 2006) and GISP2 (10–16 kyr B2k, Severinghaus and Brook, 1999). In black the estimated gravitational signal δ_{grav} for NGRIP (30–48 kyr B2k, modeled; Huber et al., 2006) and GISP2 (10–16 kyr B2k, done by hand).* **d)** *Calculated age $\Gamma(z_{\mathrm{lid}})$ using Eq. (4.11).* **e)** *Calculated DF signal $\varepsilon_{\mathrm{DF}}$ from Eq. (4.7). Note that the signal is (nearly) identical for δD and $\delta^{13}C$ of CH_4.*

corrected data include the uncertainty in our method, which we estimate below. As we do not know the original atmospheric δ^{13}C–CH_4, we can not provide conclusive proof for the correctness of our method. Having said this, we do believe that the corrected dataset is more consistent with the CH_4 mixing ratios. The Younger-Dryas to

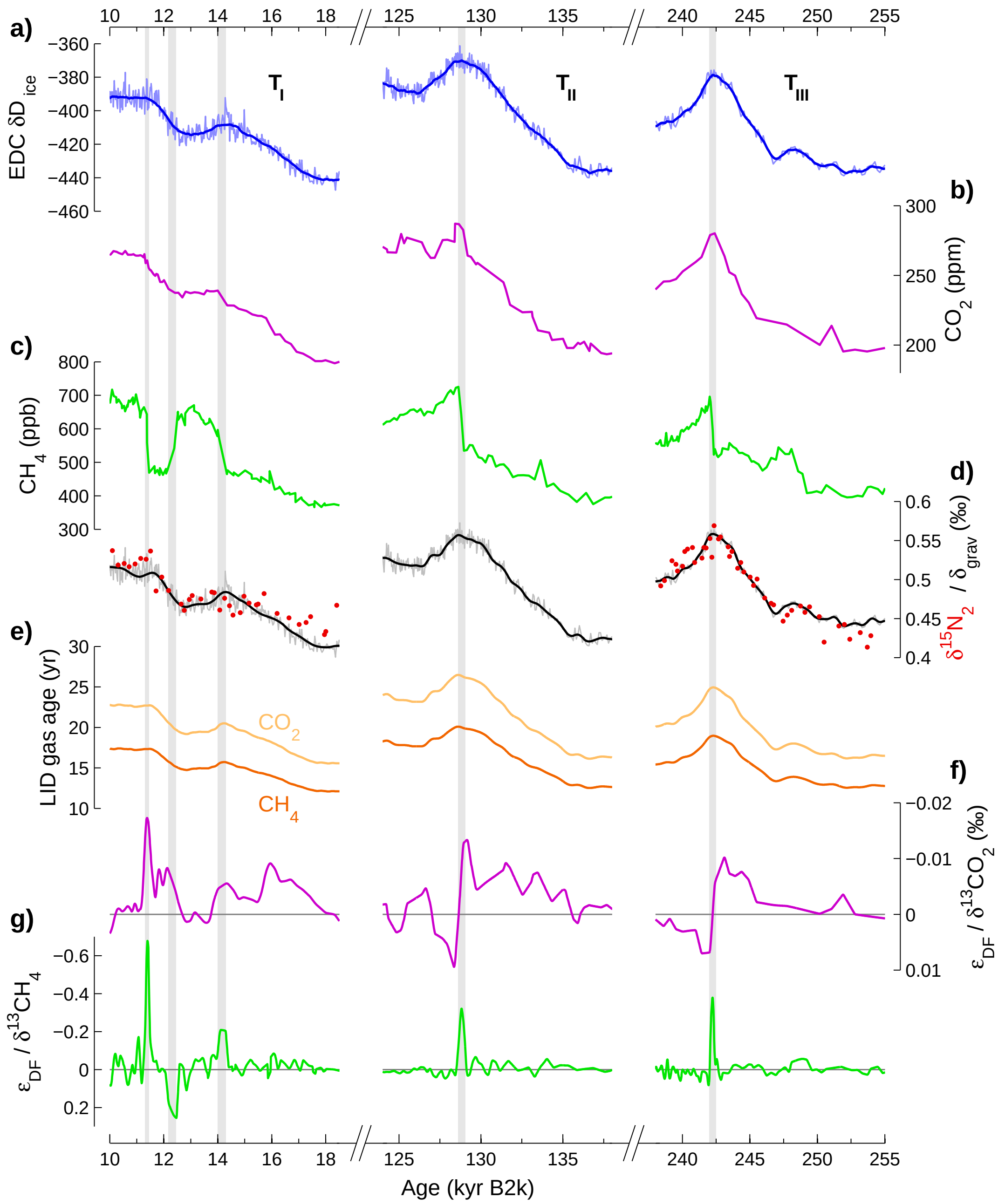

Figure 4.7: Diffusive isotopic fractionation for CH_4 and CO_2 in the EPICA Dome C ice core, Antarctica. Ages are before the year 2000 C.E. (B2k). **a)** *Precipitation δD as a proxy for site temperature on the EDC-3 timescale.* **b)** *CO_2 mixing ratio from EDC and Vostok ice core samples (Lüthi et al., 2008).* **c)** *CH_4 mixing ratio from EDC ice core samples (Loulergue et al., 2008).* **d)** *In red the measured $\delta^{15}N$; in black the δ_{grav} calculated using the $\delta^{15}N$-δD relationship from Dreyfus et al. (2010); for T_{III} an ad-hoc 0.02 ‰ was added to improve the fit.* **e)** *Calculated age $\Gamma(z_{\mathrm{lid}})$ using Eq. (4.11).* **f)** *Calculated CO_2 DF signal $\varepsilon_{\mathrm{DF}}$ from Eq. (4.7).* **g)** *Calculated CH_4 DF signal. Note that the signal is (nearly) identical for δD and $\delta^{13}C$ of CH_4.*

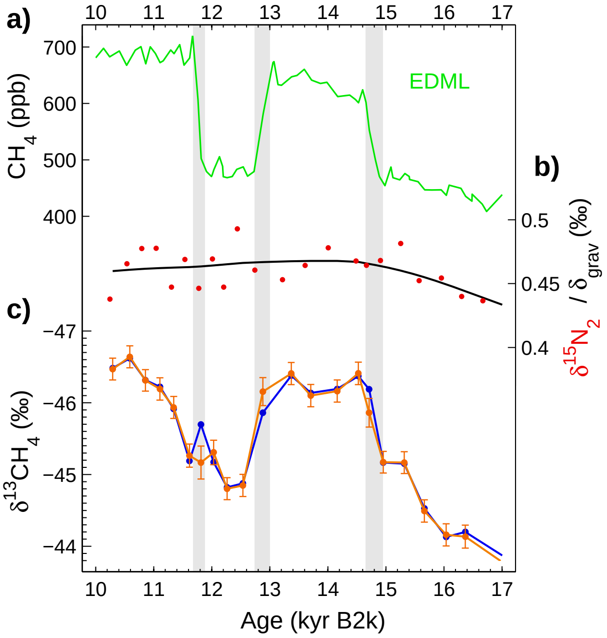

Figure 4.8: DF correction of δ^{13}C–CH$_4$ data over the last glacial termination. **a)** *EDML CH$_4$ data from EPICA community members (2006).* **b)** *δ_{grav} (black) from Fischer et al. (2008) and δ^{15}N–N$_2$ data (red) from A. Landais (personal communication, 2011).* **c)** *δ^{13}C–CH$_4$ data from Fischer et al. (2008) before (blue), and after DF correction (orange, with error bars).*

Preboreal (YD-PB) transition at 11.7 kyr BP shows a remarkable isotopic excursion in the uncorrected dataset. After the correction this prominent feature has disappeared, giving an intuitively more realistic monotonic rise in δ^{13}C–CH$_4$. Also the transition into the Bølling interstadial (14.8 kyr BP) arguably looks more realistic after DF correction, with the isotopes following the atmospheric CH$_4$ signal more closely.

The 8.2 kyr event is an abrupt climate event within the climatically stable Holocene, which brought dry and cold conditions to large regions of the Northern hemisphere (Alley and Ágústsdóttir, 2005). It has been attributed to a freshening of the North Atlantic by an outburst flood, slowing down the meridional circulation that transports heat northwards from lower latitudes. The 8.2kyr event shows a very prominent and abrupt CH$_4$ response, with a drop in CH$_4$ mixing ratios of around 90 ppb after correction for diffusive smoothing in the firn (Spahni et al., 2003). This rapid variation leads to a large ε_{DF}, as shown in Fig. 4.9c, again with the original (uncorrected) data in blue and the DF corrected data in orange (with errorbar). The DF correction is on the same order of magnitude as the analytical precision, which is around 0.3 ‰ for this study. We reject one datapoint as an outlier (shown in grey). Including this datapoint would imply that in less than 30 years the isotopic composition jumped by nearly a permil and back again; such a rapid variation is incompatible with the diffusive smoothing of the firn, and cannot be of atmospheric

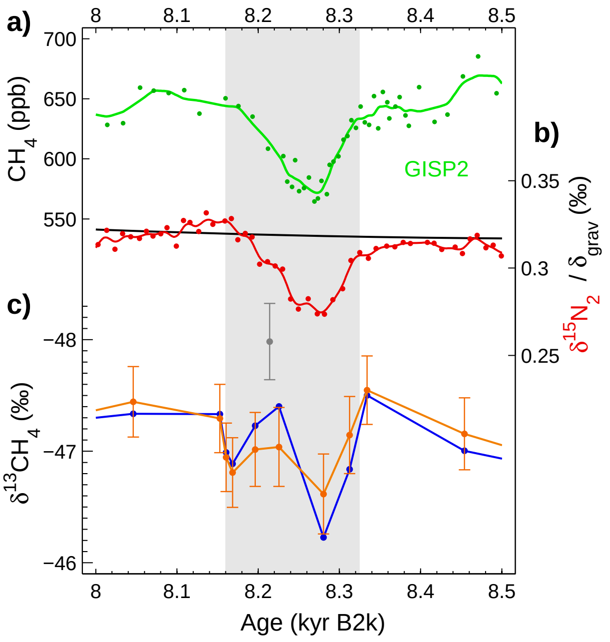

Figure 4.9: DF correction of δ^{13}C–CH$_4$ data over the 8.2 kyr event. **a)** *High resolution GISP2 CH$_4$ and* **b)** *δ^{15}N–N$_2$ data from Kobashi et al. (2007). The plotted δ_{grav} signal (in black) is a quadratic fit to the reconstructed δ_{grav} based on $\delta^{15}N_{\text{excess}} = \delta^{15}N - \delta^{40}Ar/4$.* **c)** *$\delta^{13}$C–CH$_4$ data from Sowers (2010) before (blue), and after DF correction (orange, with error bars).*

origin.

After correction we observe an enrichment in δ^{13}C–CH$_4$ for the duration of the event, which hints at reduced wetland emissions in a colder/dryer Northern hemisphere climate. The δ^{13}C–CH$_4$ signal appears to have the right order of magnitude: ~0.6 ‰ for a 75 ppb drop in CH$_4$, compared to a 1.5 ‰ signal for the 180 ppb drop from the Allerød to the YD. Both these NH cold spells are thought to be triggered by the same mechanism, and we could expect to see a similar response in the CH$_4$ isotopic composition. Again, we cannot verify the correctness of our DF correction method, as we do not posses knowledge of the true atmospheric history. However, an enrichment of more modest amplitude that persists throughout the event seems more plausible than the two separated, high amplitude excursions found in the uncorrected time series.

4.5 Discussion

4.5.1 Relevance of the DF correction

In principle, all ice core records of trace gas isotopic composition should be corrected for the effect of DF. Whether this correction is relevant depends on the magnitude of ε_{DF} compared to 1) the analytical precision of the ice core measurements of trace gas isotopes, 2) the magnitude and uncertainty of the applied gravitational correction,

Table 4.3: Typical magnitude of $\varepsilon_{\mathrm{DF}}$ compared to other factors; results from Greenland and EDC are combined. The columns give typical $\varepsilon_{\mathrm{DF}}$ values for trace gas increases in the recent anthropogenic era, over the glacial terminations T_I–T_{III}, and over Dansgaard-Oeschger (DO) cycles. For comparison, we give the typical analytical precision of the ice core analysis, the gravitational correction, and the isotopic range of the atmospheric signal (maximum value minus minimum value).

	$\varepsilon_{\mathrm{DF}}$ Anthr. (‰)	$\varepsilon_{\mathrm{DF}}$ $\mathrm{T_{I-III}}$ (‰)	$\varepsilon_{\mathrm{DF}}$ DO (‰)	Analytical (‰)	δ_{grav} [†] (‰)	Atm. signal (‰)
δ^{13}C–CH_4	1.2^a	0.4–1.0	0.2–0.4	0.18^b–0.3^c	$\sim 0.45 \pm 0.01$	$\sim 5^c$
δD–CH_4	1.2^a	0.4–1.0	0.2–0.4	2.1^b–4.2^d	$\sim 0.45 \pm 0.01$	$\sim 20^e$–40^d
δ^{13}C–CO_2	0.12^f	0.01–0.017	< 0.005	0.025^g–0.1^h	$\sim 0.45 \pm 0.01$	$\sim 1.3^h$
δ^{15}N–N_2O	0.12^i	0.01–0.03	0.005–0.018	$0.5^{b,j}$	$\sim 0.45 \pm 0.01$	$\sim 4^j$
δ^{18}O–N_2O	0.24^i	0.02–0.06	0.01–0.035	0.69^b–2^j	$\sim 0.9 \pm 0.02$	$\sim 8^j$

[†] Typical value. The stated uncertainty is the upper end of the $\delta^{15}N_2$ analytical uncertainty. In case of poor depth coverage of $\delta^{15}N_2$ data the uncertainty will be higher.

[a] Modern day WAIS–Divide, Mischler et al. (2009)

[b] Sapart et al. (2011)

[c] Fischer et al. (2008)

[d] Sowers (2006)

[e] Bock et al. (2010)

[f] Modern day Law Dome, Trudinger et al. (1997)

[g] Francey et al. (1999)

[h] Lourantou et al. (2010)

[i] Modern day NGRIP Ishijima et al. (2007)

[j] Sowers et al. (2003)

and 3) the amplitude of atmospheric variations. This is summarized in Table 4.3, where we list typical values of $\varepsilon_{\mathrm{DF}}$ for the anthropogenic increase, for the last three glacial terminations, and over Dansgaard-Oeschger (DO) cycles. The values for N_2O isotopologues are calculated in the same way as for CO_2 and CH_4, using the EPICA Dome C N_2O mixing ratios by Schilt et al. (2010).

For all gases the largest fractionation is obtained for the current anthropogenic increase, showing the profound impact mankind has on the chemical composition of our atmosphere. For δ^{13}C of both CO_2 and CH_4 the diffusion correction can certainly not be neglected, as it exceeds the typical analytical precision. For the other isotopologue ratios it must be kept in mind that the analytical precision is listed for ice core gas extractions; for firn air samples the precision is much better. For all the listed isotopologues, diffusion correction should be applied for the anthropogenic increase. Note that these recent atmospheric variations are reconstructed from firn air or shallow ice core samples; in these cases there is no need for the method developed here, as regular firn air models can be applied (with their effective diffusivity tuned to reference tracers).

On comparing the different gases, it is clear that for methane the diffusive effect is strongest. The reason is twofold. First, because of the small molecular mass, isotopic substitution has a large impact on the molecular mass and thereby the molecular diffusivity. This enhances DF, as is evident from Eq. (4.7). Second, because of its short atmospheric lifetime of around 8 years (Lelieveld et al., 1998), the CH_4 mixing ratio can change very rapidly. The methane record shows the most abrupt changes of all atmospheric trace gases. The magnitude of ε_{DF} is identical for both δD and δ^{13}C of CH_4, yet the relevance is different to both signals. For δ^{13}C the calculated ε_{DF} for both glacial terminations and the DO cycles exceed the typical analytical precision. The correction is comparable to, or larger than, the gravitational correction that is routinely applied to the data. Therefore DF correction of δ^{13}C–CH_4 is recommended for samples that lie within climatic transitions. For δD–CH_4 the situation is different. Although ε_{DF} has the same magnitude, it is smaller than both the analytical measurement precision and the large amplitude of atmospheric variations observed in the ice core record (Bock et al., 2010; Sowers, 2006). For these reasons one could justify omitting the DF correction for δD–CH_4.

Nitrous oxide provides a simple case. With the exception of the anthropogenic signal, the DF correction is more than an order of magnitude smaller than the analytical precision. In most cases ε_{DF} is smaller than the uncertainty in the gravitational correction. The effect of DF can safely be ignored for N_2O records. The case of CO_2 is similar. However, because the analytical precision is so much better for $\delta^{13}CO_2$, one could consider applying the DF correction during the deglaciations, which are accompanied by a strong CO_2 increase.

In summary, δ^{13}C–CH_4 is the only trace gas isotopic signal for which the DF correction should always be applied during transitions, as there the ε_{DF} exceeds the typical experimental precision. For δD–CH_4 and δ^{13}C–CO_2 the magnitude of ϵ_{DF} gets to about half the analytical precision only during glacial terminations; one could consider DF correction during these special intervals. In all other cases the effects of DF can safely be neglected.

We believe that the method presented here also has merits in cases where ε_{DF} is very small. Calculating the magnitude of the DF correction is reduced from a modeling project to a back-of-the-envelope calculation. This will enable experimentalists to quickly asses whether they need to worry about DF correcting their data or not.

4.5.2 Accuracy of our method

Here we will estimate the uncertainty in our method. We distinguish three major sources of uncertainty:

1) The DCH estimate based on δ^{15}N–N_2 data. The analytical precision of the δ^{15}N measurements is on the order of 0.005–0.01 ‰ (Dreyfus et al., 2010); since the depth coverage is not always equally good for each ice core, we estimate the uncertainty at 0.02 ‰. More problematic is the possibility of thermal fractionation in the firn column caused by temperature gradients (Severinghaus et al., 2001). In Greenland, rapid variations in surface temperature give rise to transient excursions in δ^{15}N–N$_2$ that do not reflect changes in the DCH (Severinghaus and Brook, 1999). This is shown in Fig. 4.6c, where we plot measured δ^{15}N–N$_2$ data in red, and a reconstructed gravitational signal δ_{grav} representing the DCH in black (Huber et al., 2006). In Antarctica temperature variations are too gradual to impose large gradients in the firn. However, during glacial conditions the reduced downward advection of cold ice (due to low accumulation), in combination with the thermal heat flux from the bed and an increased thermal insulation provided by the deep glacial firn column, can lead to a temperature gradient of up to a few K between the surface and the close-off depth (Goujon et al., 2003). We estimate the error due to the thermal fractionation δ_{therm} from the difference between the apparent and true DCH in the Huber et al. (2006) study, i.e. the red and black curves in 4.6c. We disregard the rapid isotope excursions that are easily identified as thermal signals, and take the root mean square (RMS) of the remaining δ_{therm} dataset. This way we obtain an uncertainty estimate of 0.032 ‰ due to thermal fractionation, leading to a total uncertainty on δ_{grav} of 0.038 ‰. Note that this uncertainty can be reduced by either more advanced experimental methods that require additional δ^{40}Ar and δKr/Ar measurements (Severinghaus et al., 2003), or modeling of heat diffusion in the firn and ice (e.g. Goujon et al., 2003).

2) The uncertainty in firn air model calculations of ε_{DF}. Figure 4.2 shows the disagreement among six firn air models on the magnitude of DF in the LIZ; a disagreement originating from our limited understanding of LIZ transport. This uncertainty also influences the accuracy of our method. The observed model divergence in ε_{DF} increases with depth in the LIZ. Therefore the disagreement is much larger in the open pores than in the closed pores, as the trapping process averages over the entire LIZ. We estimated the 1σ standard deviation in the closed pores in the following way. First we take the standard deviation of the six modeled profiles at each depth. We multiply these standard deviations by the trapping rate of Eq. (5.8), and integrate this over the firn column. This way we obtain $\sigma = 0.013$ ‰ compared to a total trapped $\epsilon_{\text{DF}} = -0.115$ ‰; i.e. a relative uncertainty of 0.11 (i.e. 11%).

3) The age parameterization of Eq. (4.11). Our lock-in depth age parameterization provides a surprisingly good fit to the modeled ages, with a coefficient of determination $R^2 = 0.994$. On average the difference between the modeled ages and those predicted by Eq. (4.11) is 0.77 year; a relative error of 0.04. However, Antarctic glacial conditions lie outside the climatic range of modern day firn sites on which the parameterization is based. In particular, the hypothesis of a deepened convective zone during Antarctic glacial conditions could significantly influence the firn transport properties (Landais et al., 2006). It must be noted that the CZ thickness has very limited impact on $\Gamma(z_{\text{lid}})$, as we discussed earlier in section 4.3. Since Eq. (4.11) provides a good fit over a wide range of climatic conditions, we believe that even under Antarctic glacial conditions the error in the age estimation will be small compared to the uncertainties listed under points 1 and 2 above.

Using standard error propagation methods, and assuming all errors to be uncorrelated, we get a relative error of around 0.2 (i.e. 20%) in ϵ_{DF}, at a typical value δ^{15}N–N$_2$ = 0.4 ‰. If more accurate DCH estimates are available (from either heat diffusion modeling or additional δ^{40}Ar or δKr/Ar data) the uncertainty in the methed reduces to around 15%.

For the recent anthropogenic increase the DF correction can be performed with greatest accuracy, as one can use a firn air transport model with the effective diffusivity-depth relationship tuned to reference tracers of known atmospheric history. In this case the only major uncertainty is the LIZ model disagreement as shown in Fig. 4.2.

In the ice core record the alternative to our DF correction method is a full modeling study, in which the coupled heat diffusion and firn densification is modeled for the past firn column, after which the DF can be calculated in this reconstructed firn column using a firn air transport model. This approach would only be more accurate for point 1) above, since the modeled temperature gradient in the firn allows for estimating the true DCH by correcting δ^{15}N data for thermal fractionation.

Apart from the more accurate DCH estimate, a full modeling approach is subject to many other uncertainties that do not matter to our approach. We list them below, without attempting to estimate their magnitude:

- The firn densification model requires past accumulation and temperature estimates as an input, both of which have their uncertainty.

- There is an inherent uncertainty to the densification modeling; e.g. different models can produce close-off depth values that differ by several meters. Under Antarctic glacial conditions, densification models systematically predict a deepening of the firn column, whereas δ^{15}N–N$_2$ data show a shortening of the DCH (Landais et al., 2006). The hypothesis of a deepened glacial CZ is often invoked to explain this mismatch, which would require a CZ thickness of up to 40 m at Dome Fuji (Severinghaus et al., 2010).

- The close-off and lock-in depths need to be estimated from the density profile. The former is estimated using the parameterization by Martinerie et al. (1994), which is often (slightly) in disagreement with field data from firn sampling campaigns; the latter is often estimated by the ad-hoc assumption that the lock-in density simply lies 14 $\mathrm{kg\,m^{-3}}$ below the close-off density (Schwander et al., 1997; Blunier and Schwander, 2000).

- The effective diffusivity-depth relationship is generally unknown. The best available parameterization by (Schwander, 1989) often gives unsatisfactory results to field data (Fig. 2.5a).

- The true atmospheric mixing ratios are unknown; the ice core record is a convolution of the atmospheric signal with the firn and bubble trapping transfer functions. The rapid variations that cause the strongest DF are attenuated in the firn (Spahni et al., 2003; Köhler et al., 2011). By contrast, our empirical method works best when using the mixing ratios as recorded in the ice core (Figs. 4.4 and 4.5).

Considering the above we contend that, compared to a full model approach, our DF correction method is certainly more accurate whenever good DCH estimates are available, and probably more accurate whenever the DCH is based directly on δ^{15}N–N$_2$ data uncorrected for thermal fractionation.

4.6 Summary and Conclusions

Fist, we derived an analytical expression for diffusive isotopic fractionation in the firn column. Second, based on data from five modern firn air sites we derived a parameterization of the mean gas age at the lock-in depth. By combining both results we obtain a convenient empirical framework for correcting ice core data for the effect of diffusive fractionation. The age parameterization can also be used to improve estimates of Δage back in time.

We test the accuracy and dynamic response of our method by comparing it to a firn air transport model for two modern, well-characterized firn air sites. We find an excellent agreement on timescales relevant for ice core data ($\geq$ 100 years). We apply our method to CH$_4$, CO$_2$ and N$_2$O mixing ratios found in ice cores. We find that δ^{13}C–CH$_4$ is the only trace gas isotopic signal for which the diffusive correction should always be applied during transitions, as there the $\varepsilon_{\mathrm{DF}}$ exceeds the typical experimental precision. For δD–CH$_4$ and δ^{13}C–CO$_2$ the magnitude of the diffusive fractionation gets to about half the analytical precision only during glacial terminations; one could consider data correction during these special intervals. In all other cases the effects of DF can safely be neglected.

We apply the DF correction to published δ^{13}C–CH$_4$ records over the last glacial termination and the 8.2 kyr event. In both cases the DF correction exceeds the analytical precision of the data during abrupt transitions. We argue that the corrected time series are more consistent than the uncorrected ones.

We show that our method has an uncertainty of around 15% in the case thermal fractionation-corrected δ^{15}N–N$_2$ data is used, and around 20% when uncorrected δ^{15}N–N$_2$ data is used. We argue that our empirical method is more accurate than the alternative of a full modeling study.

Our method requires little computational effort and only commonly available ice core data. If offers experimentalists a convenient framework for assessing whether their data should be corrected for the effects of diffusive fractionation.

4.7 References

Alley, R. B. and Ágústsdóttir, A. M. (2005). The 8k event: cause and consequences of a major holocene abrupt climate change. *Quaternary Science Reviews*, 24(10-11):1123 – 1149.

Barnola, J. M., Pimienta, P., Raynaud, D., and Korotkevich, Y. S. (1991). CO_2-climate relationship as deduced from the Vostok ice core - A reexamination based on new measurements and on a reevaluation of the air dating. *Tellus B*, 43(2):83–90.

Blunier, T. and Schwander, J. (2000). *Gas enclosure in ice: age difference and fractionation*, pages 307–326. Hokkaido University Press, Sapporo.

Blunier, T., Spahni, R., Barnola, J. M., Chappellaz, J., Loulergue, L., and Schwander, J. (2007). Synchronization of ice core records via atmospheric gases. *Clim. Past*, 3(2):325–330.

Bock, M., Schmitt, J., Behrens, M., Moller, L., Schneider, R., Sapart, C., and Fischer, H. (2010). A gas chromatography/pyrolysis/isotope ratio mass spectrometry system for high-precision delta D measurements of atmospheric methane extracted from ice cores. *Rapid Communications in Mass Spectrometry*, 24(5):621–633.

Buizert, C., Martinerie, P., Petrenko, V. V., Severinghaus, J. P., Trudinger, C. M., Witrant, E., Rosen, J. L., Orsi, A. J., Rubino, M., Etheridge, D. M., Steele, L. P., Hogan, C., Laube, J. C., Sturges, W. T., Levchenko, V. A., Smith, A. M., Levin, I., Conway, T. J., Dlugokencky, E. J., Lang, P. M., Kawamura, K., Jenk, T. M., White, J. W. C., Sowers, T., Schwander, J., and Blunier, T. (2011). Gas transport in firn: multiple-tracer characterisation and model intercomparison for neem, northern greenland. *Atmos. Chem. Phys. Discuss.*, 11:15975–16021.

Dreyfus, G. B., Jouzel, J., Bender, M. L., Landais, A., Masson-Delmotte, V., and Leuenberger, M. (2010). Firn processes and δ^{15}N: potential for a gas-phase climate proxy. *Quaternary Sci. Rev.*, 29(1-2):28–42.

EPICA community members (2006). One-to-one coupling of glacial climate variability in greenland and antarctica. *Nature*, 444(7116):195–198.

Fabre, A., Barnola, J. M., Arnaud, L., and Chappellaz, J. (2000). Determination of gas diffusivity in polar firn: Comparison between experimental measurements and inverse modeling. *Geophys. Res. Lett.*, 27(4):557–560.

Fischer, H., Behrens, M., Bock, M., Richter, U., Schmitt, J., Loulergue, L., Chappellaz, J., Spahni, R., Blunier, T., Leuenberger, M., and Stocker, T. F. (2008). Changing boreal methane sources and constant biomass burning during the last termination. *Nature*, 452(7189):864–867.

Francey, R., Allison, C., Etheridge, D., Trudinger, C., Enting, I., Leuenberger, M., Langenfelds, R., Michel, E., and Steele, L. (1999). A 1000-year high precision record of delta C-13 in atmospheric CO_2. *Tellus B*, 51(2):170–193.

Goujon, C., Barnola, J. M., and Ritz, C. (2003). Modeling the densification of polar firn including heat diffusion: Application to close-off characteristics and gas isotopic fractionation for Antarctica and Greenland sites. *J. Geophys. Res.-Atm*, 108(D24):18.

Huber, C., Leuenberger, M., Spahni, R., Fluckiger, J., Schwander, J., Stocker, T., Johnsen, S., Landals, A., and Jouzel, J. (2006). Isotope calibrated Greenland temperature record over Marine Isotope Stage 3 and its relation to CH(4). *Earth Planet. Sci. Lett.*, 243(3-4):504–519.

Ishijima, K., Sugawara, S., Kawamura, K., Hashida, G., Morimoto, S., Murayama, S., Aoki, S., and Nakazawa, T. (2007). Temporal variations of the atmospheric nitrous oxide concentration and its δ^{15}N and δ^{18}O for the latter half of the 20th century reconstructed from firn air analyses. *J. Geophys. Res.-Atm*, 112(D3):12.

Kobashi, T., Severinghaus, J. P., Brook, E. J., Barnola, J.-M., and Grachev, A. M. (2007). Precise timing and characterization of abrupt climate change 8200 years ago from air trapped in polar ice. *Quat. Sci. Rev.*, 26(9-10):1212–1222.

Köhler, P., Knorr, G., Buiron, D., Lourantou, A., and Chappellaz, J. (2011). Abrupt rise in atmospheric CO_2 at the onset of the Bølling/Allerød: in-situ ice core data versus true atmospheric signals. *Clim. Past.*, 7(2):473–486.

Landais, A., Barnola, J. M., Kawamura, K., Caillon, N., Delmotte, M., Van Ommen, T., Dreyfus, G., Jouzel, J., Masson-Delmotte, V., Minster, B., Freitag, J., Leuenberger, M., Schwander, J., Huber, C., Etheridge, D., and Morgan, V. (2006). Firn-air delta N-15 in modern polar sites and glacial-interglacial ice: a model-data mismatch during glacial periods in Antarctica? *Quaternary Sci. Rev.*, 25(1-2):49–62.

Lelieveld, J., Crutzen, P. J., and Dentener, F. J. (1998). Changing concentration, lifetime and climate forcing of atmospheric methane. *Tellus B*, 50(2):128–150.

Loulergue, L., Schilt, A., Spahni, R., Masson-Delmotte, V., Blunier, T., Lemieux, B., Barnola, J. M., Raynaud, D., Stocker, T. F., and Chappellaz, J. (2008). Orbital and millennial-scale features of atmospheric CH_4 over the past 800,000 years. *Nature*, 453(7193):383–386.

Lourantou, A., Chappellaz, J., Barnola, J. M., Masson-Delmotte, V., and Raynaud, D. (2010). Changes in atmospheric CO_2 and its carbon isotopic ratio during the penultimate deglaciation. *Quaternary Sci. Rev.*, 29(17-18):1983–1992. doi: DOI: 10.1016/j.quascirev.2010.05.002.

Lüthi, D., Le Floch, M., Bereiter, B., Blunier, T., Barnola, J.-M., Siegenthaler, U., Raynaud, D., Jouzel, J., Fischer, H., Kawamura, K., and Stocker, T. F. (2008). High-resolution carbon dioxide concentration record 650,000-800,000 years before present. *Nature*, 453(7193):379–382.

Martinerie, P., Lipenkov, V. Y., Raynaud, D., Chappellaz, J., Barkov, N. I., and Lorius, C. (1994). Air content paleo record in the vostok ice core (antarctica): A mixed record of climatic and glaciological parameters. *J. Geophys. Res.*, 99:10565–10576.

Mischler, J. A., Sowers, T. A., Alley, R. B., Battle, M., McConnell, J. R., Mitchell, L., Popp, T., Sofen, E., and Spencer, M. K. (2009). Carbon and hydrogen isotopic composition of methane over the last 1000 years. *Global Biogeochem. Cy.*, 23.

NGRIP community members (2004). High-resolution record of Northern Hemisphere climate extending into the last interglacial period. *Nature*, 431(7005):147–151.

Sapart, C. J., van der Veen, C., Vigano, I., Brass, M., van de Wal, R. S. W., Bock, M., Fischer, H., Sowers, T., Buizert, C., Sperlich, P., Blunier, T., Behrens, M., Schmitt, J., Seth, B., and Röckmann, T. (2011). Simultaneous stable isotope analysis of methane and nitrous oxide on ice core samples. *Atmospheric Measurement Techniques Discussions*, 4(4):4473–4503.

Schilt, A., Baumgartner, M., Blunier, T., Schwander, J., Spahni, R., Fischer, H., and Stocker, T. F. (2010). Glacialial–interglacial and millennial-scale variations in the atmospheric nitrous oxide concentration during the last 800,000 years. *Quaternary Science Reviews*, 29(1-2):182 – 192.

Schwander, J. (1989). The transformation of snow to ice and the occlusion of gases. In Oescher, H. and Langway, C., editors, *The Environmental record in glaciers and ice sheets*, pages 53–67. John Wiley, New York.

Schwander, J., Sowers, T., Barnola, J. M., Blunier, T., Fuchs, A., and Malaize, B. (1997). Age scale of the air in the summit ice: Implication for glacial-interglacial temperature change. *J. Geophys. Res.-Atm*, 102(D16):19483–19493.

Severinghaus, J. P., Albert, M. R., Courville, Z. R., Fahnestock, M. A., Kawamura, K., Montzka, S. A., Muhle, J., Scambos, T. A., Shields, E., Shuman, C. A., Suwa, M., Tans, P., and Weiss, R. F. (2010). Deep air convection in the firn at a zero-accumulation site, central Antarctica. *Earth Planet Sc. Lett.*, 293(3-4):359–367.

Severinghaus, J. P. and Brook, E. J. (1999). Abrupt climate change at the end of the last glacial period inferred from trapped air in polar ice. *Science*, 286(5441):930–934.

Severinghaus, J. P., Grachev, A., and Battle, M. (2001). Thermal fractionation of air in polar firn by seasonal temperature gradients. *Geochem. Geophy. Geosy.*, 2.

Severinghaus, J. P., Grachev, A., Luz, B., and Caillon, N. (2003). A method for precise measurement of argon 40/36 and krypton/argon ratios in trapped air in polar ice with applications to past firn thickness and abrupt climate change in Greenland and at Siple Dome, Antarctica. *Geochim. Cosmochim. Ac.*, 67(3):325–343.

Sowers, T. (2006). Late quaternary atmospheric ch4 isotope record suggests marine clathrates are stable. *Science*, 311(5762):838–840.

Sowers, T. (2010). Atmospheric methane isotope records covering the holocene period. *Quaternary Sci. Rev.*, 29(1-2):213–221. doi: DOI: 10.1016/j.quascirev.2009.05.023.

Sowers, T., Alley, R. B., and Jubenville, J. (2003). Ice Core Records of Atmospheric N_2O Covering the Last 106,000 Years. *Science*, 301(5635):945–948.

Spahni, R., Schwander, J., Flückiger, J., Stauffer, B., Chappellaz, J., and Raynaud, D. (2003). The attenuation of fast atmospheric ch_4 variations recorded in polar ice cores. *Geophys. Res. Lett.*, 30(11):1571.

Trudinger, C. M., Enting, I. G., Etheridge, D. M., Francey, R. J., Levchenko, V. A., Steele, L. P., Raynaud, D., and Arnaud, L. (1997). Modeling air movement and bubble trapping in firn. *J. Geophys. Res.-Atm*, 102(D6):6747–6763.

Tschumi, J. and Stauffer, B. (2000). Reconstructing past atmospheric CO_2 concentration based on ice-core analyses: open questions due to in situ production of CO_2 in the ice. *J. Glaciol.*, 46(152):45–53.

5

The CIC firn air model

5.1 Introduction

In this chapter we describe the CIC firn air transport model in detail. In chapter 3 we evaluated the performance of the model for the NEEM site in Northern Greenland, and compared it to other published firn air models. In the comparison we found the performance to be comparable to, or in some cases better than, other published firn air models.

One of the major differences with other published models (Trudinger et al., 1997; Rommelaere et al., 1997; Sugawara et al., 2003; Severinghaus et al., 2001), is that we derive analytical expressions for the air velocity, bubble pressure and trapping rate. The expressions are used to include mass conservation in a rigorous way, and to predict the air content of ice below the firn-ice transition. We furthermore introduce a new method to reconstruct the effective diffusivity of the firn using reference tracers of known atmospheric history, and a new way to track the mixing ratio of trace gases in the closed porosity.

The CIC firn air model is a finite difference 1-D diffusion model coded in MATLAB. It uses implicit Crank-Nicholson time stepping to solve what is essentially an advection-diffusion-reaction equation, with radioactive decay and bubble trapping taking the place of the chemical reaction by removing trace gas molecules from the open pore space. The model uses a stationary reference frame with $z = 0$ at the surface. The firn column is assumed to be isothermal and in steady state with regard to ice flow and densification rates.

The model includes four types of transport in the open porosity. The first type is molecular diffusion, which is included through the effective molecular diffusion coefficient D_{X}, where the X denotes the trace gas under consideration. The second type is gravitational settling, which tends to enrich the firn in heavier molecules with depth (Sowers et al., 1992). The third type is advection, which we include through an average downward velocity of the air in the open pores w_{air}. The fourth type of transport is an eddy diffusion. It describes mass transfer caused by macroscopic flow patterns in the open porosity which the model cannot resolve directly, and are instead parameterised through the inclusion of an eddy diffusion coefficient D_{eddy}. Two effects were included as an eddy diffusivity. First, we use the parameterisation by Kawamura et al. (2006) to describe wind pumping and convection in the top firn layers (Colbeck, 1989). Second, we include dispersive mixing in the LIZ. Using a molecular diffusivity in the LIZ instead would lead to continued gravitational enrichment with depth, which contradicts observations.

The effects of thermal diffusion (Severinghaus et al., 2001) and close-off fractionation (Severinghaus and Battle, 2006; Huber et al., 2006) are not included in the model.

5.2 Bulk motion of air in open and closed porosity

To describe the transport of trace gases in the firn, we start by considering the bulk motion of air. Air is transported in both the closed and open porosities. The air flux in the closed pores consists of downward transport of (closed) bubbles by the ice matrix at velocity $w_{\mathrm{ice}} = \rho_{\mathrm{ice}}/\rho$, where A is the accumulation rate in $\mathrm{m\,yr^{-1}}$ ice equivalent and ρ (ρ_{ice}) is the density of firn (ice). The air flux in the open pores is determined by the downward velocity w_{air} of air in the open pores.

The fluxes in open and closed pores are then given by

$$\phi_{\mathrm{op}} = s^*_{\mathrm{op}} w_{\mathrm{air}} \tag{5.1}$$

$$\phi_{\mathrm{cl}} = s_{\mathrm{cl}} \frac{p_{\mathrm{cl}}}{p_0} w_{\mathrm{ice}} = s_{\mathrm{cl}} \frac{p_{\mathrm{cl}}}{p_0} A \frac{\rho_{\mathrm{ice}}}{\rho} \tag{5.2}$$

where the fraction p_{cl}/p_0 is the enhanced pressure in the closed porosity relative to the surface pressure due to compression of bubbles during firn densification, and s^*_{op} is the effective open porosity

$$s^*_{\mathrm{op}} = s_{\mathrm{op}} \exp\left(\frac{M_{\mathrm{air}} g z}{RT}\right) \tag{5.3}$$

i.e. the rescaled porosity to account for the barometric increase in pressure with depth.

A schematic of the bulk air motion is given in Fig. 5.1 for a depth interval between z and $z + \Delta z$. The quadrangles depict the closed and open porosities, which are respectively increasing and decreasing with depth. Arrows 1,2 give bulk air transport in the closed pores, arrows 3,4 in the open pores, and arrow 5 denotes the trapping process. Conservation of mass, with the assumption of steady state, demands that the air fluxes $\phi_1 + \phi_3 = \phi_2 + \phi_4$, where the subscript numbers refer to the arrows in Fig. 5.1. This can be generalized to hold for all z:

$$\phi_{\mathrm{op}}(z) + \phi_{\mathrm{cl}}(z) = \phi_{\mathrm{cl}}(z_{\mathrm{COD}}) + \phi_{\mathrm{op}}(z_{\mathrm{COD}}) = \phi_{\mathrm{cl}}(z_{\mathrm{COD}}) \tag{5.4}$$

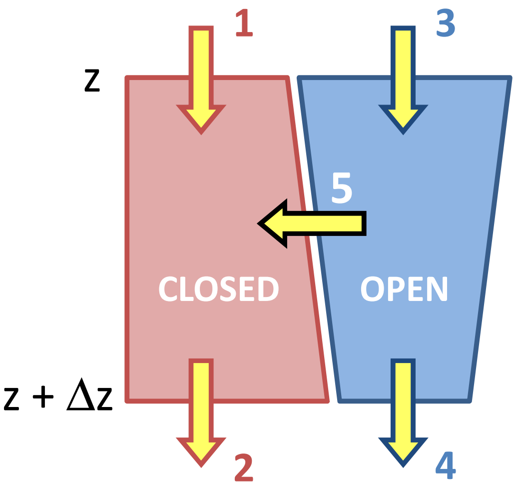

Figure 5.1: Schematic of air bulk motion in the firn. Shown is a section of the firn column between z and $z + \Delta z$. The total porosity decreases, and the closed porosity s_{cl} increases in the interval. Arrows give air fluxes.

where z_{COD} is the full close-off depth where all the air is occluded in bubbles ($s_{\mathrm{op}}(z_{\mathrm{COD}}) = 0$). What Eq. (5.4) says, is that at each depth the total flux of air must be equal. At the full bubble close-depth z_{COD} only closed porosity remains, and hence the the total air flux is given by $\phi_{\mathrm{cl}}(z_{\mathrm{COD}})$.

Combining Eqs. (5.1), (5.2) and (5.4) we can solve for the air velocity in the open pore space:

$$\boxed{w_{\mathrm{air}} = \frac{A\rho_{\mathrm{ice}}}{s^*_{\mathrm{op}}p_0}\left(\frac{s_{\mathrm{cl}}(z_{\mathrm{COD}})p_{\mathrm{cl}}(z_{\mathrm{COD}})}{\rho_{\mathrm{COD}}} - \frac{s_{\mathrm{cl}}(z)p_{\mathrm{cl}}(z)}{\rho(z)}\right)} \tag{5.5}$$

We see that w_{air} depends on the accumulation rate and the firn structure. In the previous chapter we introduced different parameterizations of the closed porosity; the only unknown variable in Eq.5.5 is the compression taking place in the closed bubbles p_{cl}/p_0. We will derive an expression for bubble compression in section 5.3 below.

The velocity calculated with Eq. (5.5) is shown in Fig. 5.2b, together with the velocity of the ice layers. The ice layers are moving downward at a higher velocity than the air in the open pores. In a Lagrangian reference frame moving down with the ice layers, it will appear as if the air is moving upward. This relative upward motion of the air is caused by pore compaction due to continued firn densification, which squeezes the air upwards out of the pores. It is important to emphasize that

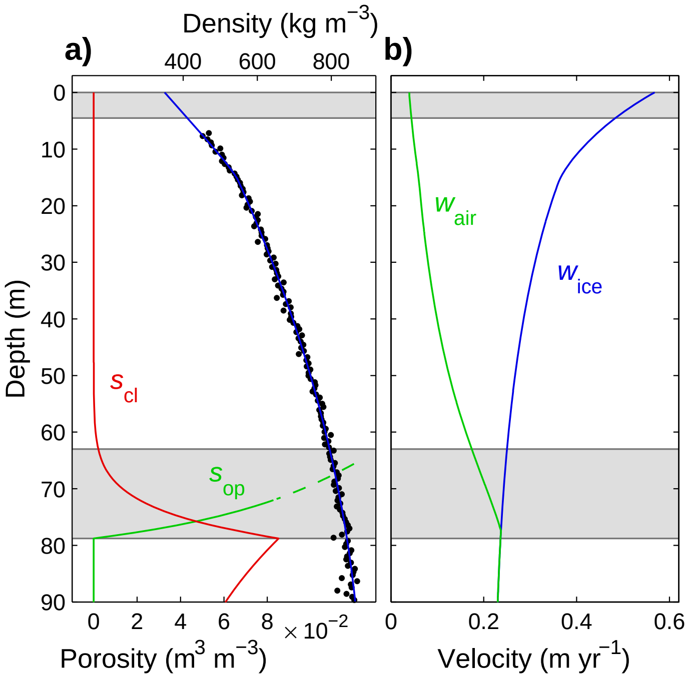

Figure 5.2: **a)**. *Closed and open porosity in NEEM firn using the parameterization of Schwander (1989).* **b)** *Ice velocity and open pore air velocity calculated with Eq. 5.5 using the closed pore pressure estimate of Eq. 5.12.*

the upward motion is only relative to the ice layers; in a stationary reference frame the air is moving downwards.

Finally we will derive the bubble trapping rate, corresponding to arrow 5 in Fig. 5.1. Using conservation of mass, we find that $\phi_5 = \phi_2 - \phi_1 = -(\phi_4 - \phi_3)$. The trapped flux is equal to $\phi_5 = \phi_t = s^*_{\text{op}}\theta\Delta z$, where θ is the trapping rate per unit open porosity in s^{-1}. From the mass conservation consideration we get the following expression for the trapping rate:

$$\theta = \frac{1}{s^*_{\text{op}}} \frac{\phi_{\text{cl}}(z+\Delta z) - \phi_{\text{cl}}(z)}{\Delta z} = -\frac{1}{s^*_{\text{op}}} \frac{\phi_{\text{op}}(z+\Delta z) - \phi_{\text{op}}(z)}{\Delta z} \tag{5.6}$$

Taking the limit $\Delta z \to 0$ gives

$$\theta = \frac{1}{s^*_{\text{op}}} \frac{d\phi_{\text{cl}}}{dz} = -\frac{1}{s^*_{\text{op}}} \frac{d\phi_{\text{op}}}{dz} \tag{5.7}$$

On inserting Eq. 5.1 we get a convenient expression for the trapping rate, which we shall need later on when describing transport of tracers in the open porosity:

$$\boxed{\theta = -\frac{1}{s^*_{\mathrm{op}}}\frac{d}{dz}\left(s^*_{\mathrm{op}} w_{\mathrm{air}}\right)} \tag{5.8}$$

5.3 Air pressure in the closed porosity

After a bubble is closed off from the open porosity, the air pressure inside the bubble will start to increase due to firn densification. Measurements of total air content in mature ice show that more air is occluded than one would get from multiplication of the porosity at the full close-off depth (z_{COD}) by the air pressure of the site. The close-off fractionation observed for $\delta\mathrm{Ne/N_2}$ and $\delta\mathrm{O_2/N_2}$, caused by the preferential exclusion of small molecules from closing bubbles, gives further evidence for an increased air pressure in closed bubbles within the LIZ (Severinghaus and Battle, 2006; Huber et al., 2006). Finally, below z_{COD} increasing bubble pressure is demanded by mass conservation.

The expression for air pressure we derive here is based on two fundamental assumptions

1. The firn column is in steady state with respect to accumulation, temperature and densification rates.
2. The closed pores are compacted at the same rate as the total porosity.

The first assumption is used in all firn air modeling, and is reasonably satisfied for the stable climate of the late Holocene. The second assumption is realistic if one considers the following. Firn densification is driven by the hydrostatic pressure of overlying precipitation. The vast majority of bubbles are formed within the LIZ, at 40-120 m depth. At this depth the overburden pressure that drives densification is on the order of 250-750 kPa. The maximum overpressure in the closed bubbles that we find below, is on the order of 20 kPa; i.e. one order of magnitude smaller than the overburden pressure. We can therefore reasonably assume that the closed pores will be compacted at a similar rate to open pores.

We let an imaginary ice parcel sink from depth z' to depth z, during which the pressure inside a bubble increases from p' to p. The porosity in the parcel is reduced from $s(z')$ to $s(z)$. However, the porosity is defined as the pore space per unit volume ($\mathrm{m^3 m^{-3}}$). In the sinking, the parcel gets compacted in the vertical direction by the firn densification from original length L' to length L (Fig. 5.3. The new length will be given by:

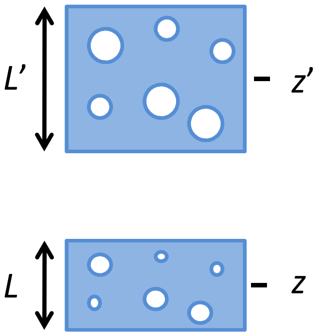

Figure 5.3: An imaginary ice parcel containing air bubbles sinks from depth z' to depth z.

$$L = L' + L' \int \frac{dw_{\text{ice}}}{dz''}\, dt = L' \left(1 + \int d \ln w_{\text{ice}}\right)$$

$$\frac{L}{L'} = 1 + \ln \frac{w_{\text{ice}}(z)}{w_{\text{ice}}(z')} \tag{5.9}$$

with $\dot{\varepsilon}_{zz} = dw_{\text{air}}/dz$ the strain rate in the firn. A bubble that is first trapped at depth z' will travel down with the ice, and when it reaches depth z its pressure will have increased by a factor p/p' that is given by:

$$p/p' = \xi(z', z) = \frac{L's(z')}{Ls(z)} = \frac{s(z')/s(z)}{1 + \ln\left[w_{\text{ice}}(z)/w_{\text{ice}}(z')\right]} \tag{5.10}$$

The closed porosity at any given depth z will be a mixture of bubbles trapped along the depth interval $0 \leq z' \leq z$. We can find the average bubble pressure through integration. For $z \leq z_{\text{COD}}$ the mean bubble pressure is given by

$$\frac{p_{\text{cl}}(z)}{p_0} = \int_0^z \frac{ds_{\text{cl}}}{dz'} \exp\left(\frac{M_{\text{air}} g z'}{RT}\right) \xi(z', z) dz' \tag{5.11}$$

and for $z > z_{\text{COD}}$ we get

$$\frac{p_{\text{cl}}(z)}{p_0} = \frac{p_{\text{cl}}(z_{\text{COD}})}{p_0} \xi(z_{\text{COD}}, z) \tag{5.12}$$

The average bubble overpressure $p_{\text{cl}}/(z)p_0$ is shown in Fig. 5.4b. The average pressure does not increase very much with depth, because new bubbles, which are at atmospheric pressure, are continuously added. The addition of new bubbles stops at z_{COD} (79 m), after which the pressure increases rapidly. In the top $\sim$ 50 m, there are essentially no bubbles, however the porosity parameterizations do give a finite value for s_{cl}. Therefore the calculated bubble pressure at these depths should not

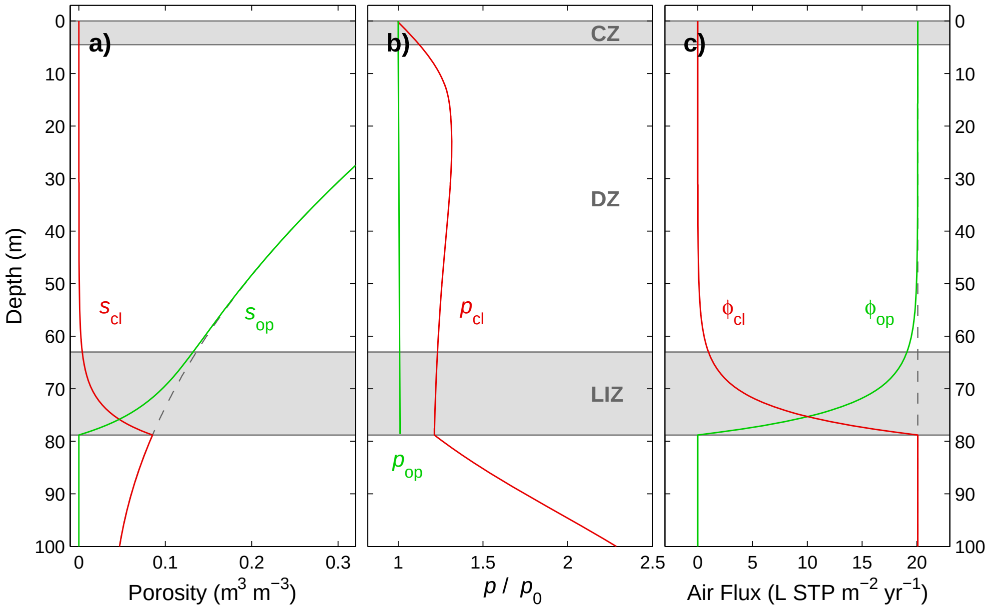

Figure 5.4: **a)**. *Closed and open porosity in NEEM firn using the parameterization of Goujon et al. (2003). The dashed line gives the total porosity s.* **b)** *Pressure in the closed and open porosity relative to atmosphere (p_0). Pressure in the closed bubbles is calculated with Eqs. (5.11) and (5.12); the open porosity follows the barometric pressure increase with depth.* **c)** *Air flux in closed and open pores in liters STP per year per m^2. The dashed line gives the total flux.*

be trusted. Around 50 m depth the bubble trapping really begins, and the values at these depths are more realistic.

Inserting the bubble pressure of Eqs. (5.11) and (5.12 and the air velocity of Eq. (5.5) in Eqs. (5.1) and (5.2), we can calculate the air fluxes ϕ_{op} and ϕ_{cl}. This is shown in Fig. 5.4c, using units of L m^{-2} yr^{-1} at standard temperature and pressure (STP). The total flux is also depicted as the dashed line. Below z_{COD} the flux remains constant, as required by mass conservation. This indicates that our description of bubble compression gives the right values below the firn-ice transition.

The air flux derived above gives the total air content of ice below the firn-ice transition. The total air content x_{air} can be calculated by:

$$x_{\text{air}} = s_{\text{cl}}(z_{\text{COD}}) \frac{p_{\text{cl}}(z_{\text{COD}})}{p_0} \frac{p_0}{101325} \frac{273.15}{T} \Big/ \rho_{\text{COD}} \tag{5.13}$$

where x_{air} is the total air content in m^3 STP air per kg of ice. For NEEM we model an air content of 101.0 mL kg^{-1}. This is not far from the true NEEM air content of 102 mL kg^{-1}, estimated from mass spectrometer inlet pressures (J. P. Severinghaus, personal communication, 2010). For South Pole, we model an air content of 94.8 mL kg^{-1}, which is close to the measured value of 92.5 ± 7 mL kg^{-1} (Martinerie et al., 1992). By contrast, assuming the closed porosity to have the same pressure as the open porosity, would give a far too low air content of 84.1 (81.2) mL kg^{-1} at NEEM (South Pole).

Direct measurements of air pressure in the closed firn porosity are very difficult, if not impossible, to achieve. This rules out a direct verification of the equations we derived here. In our derivation we made only two assumptions, both of which are realistic. Furthermore, our result (1) gives a physically realistic constant air flux below the LIZ, and (2) accurately predicts the total air content in mature ice for the two sites we tested.

5.4 Mass transfer of trace gases

The mathematical description of gas transport is based on Trudinger et al. (1997). The Lagrangian (moving) reference frame is replaced with a Eulerian (static) one, and we explicitly include the air movement and trapping processes we described above. We formulate the model in terms of mixing ratios (μmol mol^{-1}, or ppm) rather than concentrations (mol m^{-3}). This enables a direct comparison to firn air measurements, which always yield a mixing ratio.

Using Fick's law and the gravitational enrichment by (Schwander et al., 1993), the flux of a trace gas X in the firn is given by:

$$J_\mathrm{X} = -D_\mathrm{X}\left(\frac{\partial C}{\partial z} - \frac{\Delta M g C}{RT}\right) - D_\mathrm{eddy}\frac{\partial C}{\partial z} + w_\mathrm{air} C \tag{5.14}$$

where C is the mixing ratio of the trace gas, D_X the effective molecular diffusivity, D_eddy the eddy diffusivity representing both convection and deep firn dispersive mixing, and $\Delta M = M_\mathrm{X} - M_\mathrm{air}$ the molar mass deviation from dry air in kg mol^{-1}.

Imposing mass conservation gives

$$\frac{\partial C}{\partial t} = \frac{1}{s^*_\mathrm{op}}\frac{\partial}{\partial z}(s^*_\mathrm{op} J_\mathrm{X}) - \lambda_\mathrm{X} C - \theta C \tag{5.15}$$

where λ_X is the radioactive decay constant in s^{-1} and θ is the bubble trapping rate in s^{-1} that we derived earlier.

To implement Eq. (5.15) in a numerical scheme it is split up in the different derivatives in C.

$$\frac{\partial C}{\partial t} = \alpha\frac{\partial^2 C}{\partial z^2} + \beta\frac{\partial C}{\partial z} + \gamma C \tag{5.16}$$

with

$$\alpha = D_{\mathrm{X}} + D_{\mathrm{eddy}} \tag{5.17}$$

$$\beta = -D_{\mathrm{X}} \frac{\Delta M g}{RT} + \frac{1}{s^*_{\mathrm{op}}} \frac{d}{dz} \left[s^*_{\mathrm{op}} (D_{\mathrm{X}} + D_{\mathrm{eddy}}) \right] - w_{\mathrm{air}} \tag{5.18}$$

$$\gamma = -\frac{1}{s^*_{\mathrm{op}}} \left(\frac{\Delta M g}{RT} \frac{d}{dz} (s^*_{\mathrm{op}} D_{\mathrm{X}}) + \frac{d}{dz} (s^*_{\mathrm{op}} w_{\mathrm{air}}) \right) - \lambda_{\mathrm{X}} - \theta \tag{5.19}$$

On inserting Eq. (5.8) into Eq. (5.19) we obtain:

$$\gamma = -\frac{\Delta M g}{RT} \frac{1}{s^*_{\mathrm{op}}} \frac{d}{dz} (s^*_{\mathrm{op}} D_{\mathrm{X}}) - \lambda_{\mathrm{X}} \tag{5.20}$$

We see that the trapping rate is canceled out in the transport equations. This is to be expected, since the trapping process does not alter the mixing ratios in the open porosity – here we neglect molecular size dependent bubble close-off fractionation (Huber et al., 2006; Severinghaus and Battle, 2006).

5.5 Numerical implementation

The diffusion-advection-decay equation is solved with the implicit Crank-Nicolson method. The advantage of this method is its unconditional stability, giving reliable solutions even at large time steps Δt. Let C_i^n denote the mixing ratio at time step n and position i. We discretize the partial differential equation Eq. (5.16) in the following way:

$$\begin{aligned} \frac{C_i^{n+1} - C_i^n}{\Delta t} &= \frac{\alpha_i}{2(\Delta z)^2} \left(\left[C_{i+1}^{n+1} - 2C_i^{n+1} + C_{i-1}^{n+1} \right] + \left[C_{i+1}^n - 2C_i^n + C_{i-1}^n \right] \right) \\ &+ \frac{\beta_i}{4\Delta z} \left(\left[C_{i+1}^{n+1} - C_{i-1}^{n+1} \right] + \left[C_{i+1}^n - C_{i-1}^n \right] \right) \\ &+ \frac{\gamma_i}{2} \left(C_i^{n+1} + C_i^n \right) \end{aligned} \tag{5.21}$$

Note that α, β and γ have a subscript as they are depth dependent. We do not include seasonality due to e.g. thermal fractionation or convective strength; therefore they are not time dependent. To simplify the algebra we let

$$\alpha_i^* = \frac{\alpha_i \Delta t}{2(\Delta z)^2}, \quad \beta_i^* = \frac{\beta_i \Delta t}{4\Delta z}, \quad \gamma_i^* = \frac{\gamma_i \Delta t}{2} \tag{5.22}$$

On re-arranging Eq. (5.21) we obtain

$$\begin{aligned} &-(\alpha_i^* - \beta_i^*) C_{i-1}^{n+1} + (1 + 2\alpha_i^* - \gamma_i^*) C_i^{n+1} - (\alpha_i^* + \beta_i^*) C_{i+1}^{n+1} = \\ &(\alpha_i^* - \beta_i^*) C_{i-1}^n + (1 - 2\alpha_i^* + \gamma_i^*) C_i^n + (\alpha_i^* + \beta_i^*) C_{i+1}^n \end{aligned} \tag{5.23}$$

Now we let the vector $\mathbf{C}^n$ be

$$\mathbf{C}^n = \begin{bmatrix} C_0^n \\ C_1^n \\ \vdots \\ C_M^n \end{bmatrix} \quad \text{and} \quad \mathbf{C}^0 = C_{\text{atm}}(0) \cdot \begin{bmatrix} 1 \\ 1 \\ \vdots \\ 1 \end{bmatrix} \tag{5.24}$$

i.e. we initialize the firn column with a uniform mixing ratio that equals the initial ($t = 0$) value in our atmospheric surface forcing $C_{\text{atm}}(t)$. We can re-write Eq. (5.23) in matrix notation:

$$A\mathbf{C}^{n+1} = B\mathbf{C}^n \tag{5.25}$$

with A the $(M+1) \times (M+1)$ matrix

$$A = \begin{bmatrix} (1 + 2\alpha_0^* - \gamma_0^*) & -(\alpha_0^* + \beta_0^*) & 0 & & \cdots \\ -(\alpha_1^* - \beta_1^*) & (1 + 2\alpha_1^* - \gamma_1^*) & -(\alpha_1^* + \beta_1^*) & 0 & \\ 0 & -(\alpha_2^* - \beta_2^*) & (1 + 2\alpha_2^* - \gamma_2^*) & -(\alpha_2^* + \beta_2^*) & \\ \vdots & & & & \ddots \end{bmatrix}$$

and with B the $(M+1) \times (M+1)$ matrix

$$B = \begin{bmatrix} (1 - 2\alpha_0^* + \gamma_0^*) & (\alpha_0^* + \beta_0^*) & 0 & & \cdots \\ (\alpha_1^* - \beta_1^*) & (1 - 2\alpha_1^* + \gamma_1^*) & (\alpha_1^* + \beta_1^*) & 0 & \\ 0 & (\alpha_2^* - \beta_2^*) & (1 - 2\alpha_2^* + \gamma_2^*) & (\alpha_2^* + \beta_2^*) & \\ \vdots & & & & \ddots \end{bmatrix}$$

The vector $\mathbf{C}^{n+1}$ can now be found from the vector $\mathbf{C}^n$ using matrix inversion:

$$\mathbf{C}^{n+1} = A^{-1}\left(B\mathbf{C}^n\right) \tag{5.26}$$

Starting from our initial vector $\mathbf{C}^0$ we can solve for the time evolution of the system.

We have not yet considered the boundary conditions. Equation (5.16) is a second order PDE, meaning we need two boundary conditions. We use the following:

1. At the surface boundary $z = 0$ we prescribe the atmospheric mixing ratio of the tracer:

$$C_0^n = C_{\text{atm}}(n\Delta t) \tag{5.27}$$

2. At the ice boundary $z = M\Delta z$ we prescribe the slope of the mixing ratio to be zero:

$$C_M^n - C_{M-1}^n = 0 \tag{5.28}$$

The second boundary condition is not necessarily true in the firn. For this reason we extend the lower boundary $z = M\Delta z$ to 10 m below z_{COD}, which is sufficiently far not to influence the results in the true firn column. The first boundary condition is implemented by setting $A_{0,0} = 1$, $A_{0,1} = 0$ and $(B\mathbf{C}^n)_0 = C_{\mathrm{atm}}([n+1]\Delta t)$. The second boundary condition is implemented by setting $A_{M,M-1} = -1$, $A_{M,M} = 1$ and $(B\mathbf{C}^n)_M = 0$.

5.6 Reconstructing the effective diffusivity profile

The effective diffusivity D_X is given by Eq. (3.2):

$$D_X(z) = s_{\mathrm{op}} \frac{D_X^0}{\tau(z)} = s_{\mathrm{op}} \gamma_X \frac{D_{\mathrm{CO_2}}^0}{\tau(z)}$$

where $\gamma_X = D_X^0 / D_{\mathrm{CO_2}}^0$ is the free air diffusivity relative to CO$_2$, and τ is the firn tortuosity. We tune the inverse tortuosity profile $\tau^{-1}(z)$. As an initial guess for $\tau_0^{-1}(z)$ we use the parameterisation by Schwander (1989). The optimal diffusivity at a given site can be written as

$$\tau^{-1}(z) = \tau_0^{-1}(z) \times [1 + f(z)] \tag{5.29}$$

where $f(z)$ is a smooth function which we will try to estimate in the tuning procedure. We can write $f(z)$ as the weighted sum of a set of smooth functions $f_n(z)$ that are defined on the interval $0 \leq z \leq L$, with L the length of the firn column:

$$f(z) = \sum_{n=0}^{N} c_n \cdot f_n(z) \tag{5.30}$$

A first approach is to construct $f(z)$ from its Fourier components. For even-valued N this becomes:

$$\begin{array}{lll} f_0(z) & = 1 & \\ f_n(z) & = \sin\left(\frac{n\pi z}{2L}\right) & \text{for } n = 1 \ldots \frac{N}{2} \\ f_n(z) & = \cos\left(\frac{[n-N/2]\pi z}{2L}\right) & \text{for } n = \frac{N}{2}+1 \ldots N \end{array} \tag{5.31}$$

The value of N determines the rugosity of the final diffusivity profile. The advantage of using Eqs. (5.31) is that each $f(z)$ has a unique set of coefficients $\{c_n\}$. It was found that faster convergence was obtained with the following set of hand-picked equations:

$$
\begin{aligned}
f_0(z) &= 1 \\
f_1(z) &= \frac{z}{L} \\
f_2(z) &= 1 - \frac{z}{L} \\
f_3(z) &= \sin\left(\frac{\pi z}{L}\right) \\
f_4(z) &= \cos\left(\frac{\pi z}{L}\right) \\
f_5(z) &= \sin\left(\frac{3\pi z}{2L}\right) \\
f_6(z) &= \cos\left(\frac{3\pi z}{2L}\right) \\
f_7(z) &= \sin\left(\frac{2\pi z}{L}\right) \\
f_8(z) &= \cos\left(\frac{2\pi z}{L}\right) \\
f_n(z) &= \exp\left(-\frac{(z - nL/N_G)^2}{6L/N_G}\right) \quad \text{for } 9 \leq n \leq N
\end{aligned}
\tag{5.32}
$$

with N_G the number of Gaussian curves used, given as $N_G = N - 8$. The series of Gaussian curves ($f_n(z)$ for $n \geq 9$) serve to increase the diffusivity very locally, whereas the first 9 terms affect the entire firn column. The width of the Gaussian curves used is set by N_G, and can thereby be controlled. The disadvantage of using Eqs. (5.32) is that there is no unique set of coefficients $\{c_n\}$ that describes the final $f(z)$.

The coefficients $\{c_n\}$ are found through a gradient method. As the initial value we use $c_n = 0$; for each coefficient we set an initial step size $\Delta c_n = 0.01$. We go through the f_n one by one using a random permutation of the numbers $0 \leq n \leq N$. A symmetrical perturbation $c_n \Rightarrow c_n \pm \Delta c_n$ is applied, and the RMSD of Eq. (3.3) is calculated for both cases. There are three possibilities:

1. Either $c_n + \Delta c_n$ or $c_n - \Delta c_n$ reduces the RMSD *Action: the new value of* c_n *is stored,* Δc_n *remains the same.*
2. Neither of the perturbations reduces the RMSD. *Action:* c_n *remains the same,* Δc_n *is reduced by 25%.*
3. Both of the perturbations reduce the RMSD. This means there are local minima in the solution. This has never occurred so far.

This procedure can be repeated until the fit is sufficient. For the tuning of NEEM a value of $N = 28$ was used. We set $\max[\tau^{-1}(z)] = 1$, i.e. the diffusivity in the firn

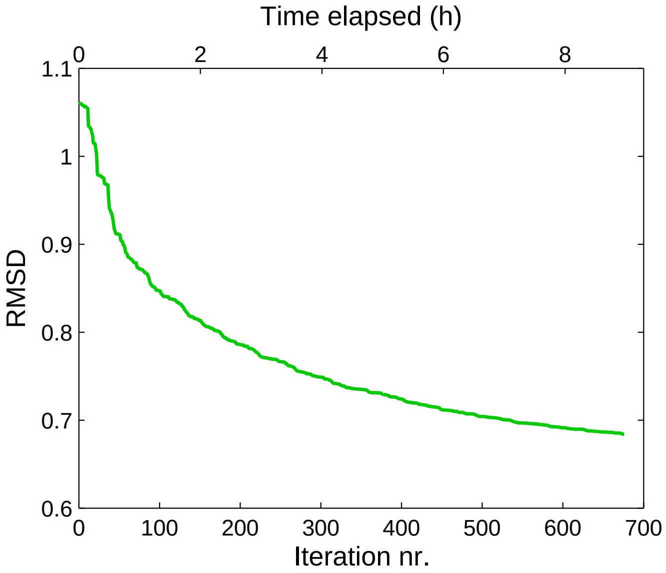

Figure 5.5: Progress during the effective diffusivity reconstruction on the NEEM US borehole. On the bottom axis the iteration nr is shown, where each symmetrical perturbation adds one count. On the top axis the required time is shown in hours (Lenovo T61 laptop computer with 2 GHz processor and 2 GB of RAM memory).

cannot exceed the free-air diffusivity.

The progress during a typical diffusivity reconstruction is shown in Fig. 5.5. In this example the RMSD is reduced from 1.07 to 0.68 for the NEEM US borehole during almost 9 hours. The process can easily be completed overnight on a regular laptop computer.

5.7 Mixing ratios in the closed porosity

When interpreting ice core records, we are interested in the trace gas mixing ratio in the closed bubbles. Here we implement a gradual gas occlusion that tracks air moving from the open to the closed pores. The model described above calculates trace gas mixing ratios in the open porosity, denoted as $C(z,t)$. The mixing ratio in the closed porosity is denoted $C_{\mathrm{cl}}(z,t)$.

The values of $C_{\mathrm{cl}}(z,t)$ depend only on the past mixing ratios in the open pores, and the bubble trapping. We calculate $C_{\mathrm{cl}}(z,t)$ off-line; there is no need to track bubble concentrations at the same time as $C(z,t)$ is calculated.

We now trace an ice layer down from the surface, which arrives at depth z on time t. We let $\mathcal{L}$ denote its path $(z'(t'),t')$. Then the mixing ratio in the closed pores

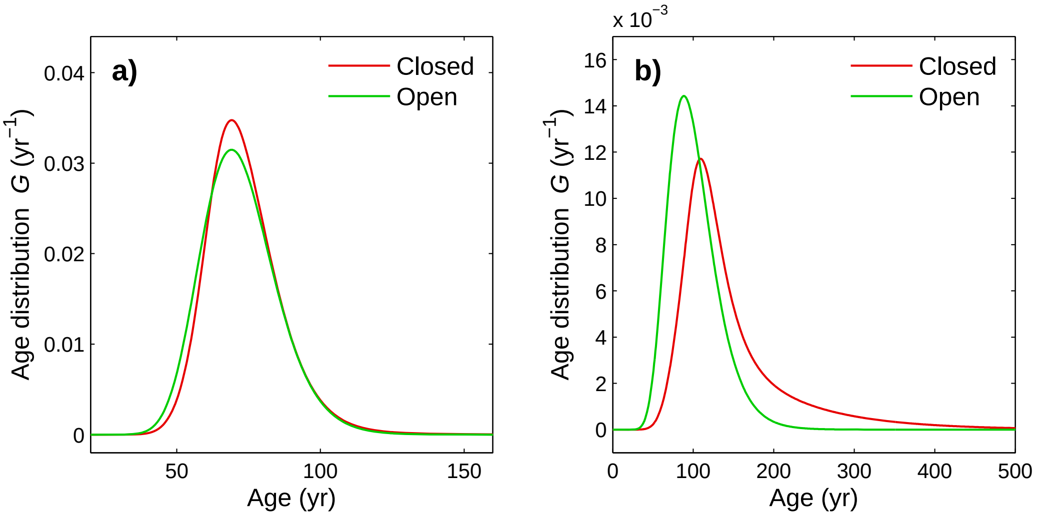

Figure 5.6: Calculated CH$_4$ age distributions at the bottom of the firn column in the open and closed porosities at **a)** *NEEM (z = 79 m) and* **b)** *South Pole (z = 123 m). Note the difference in scale on the horizontal and vertical axes.*

is given by

$$\begin{aligned} C_{\text{cl}}(z,t) &= \frac{1}{\phi_{\text{cl}}}\int_{\mathcal{L}} C(\mathcal{L})d\phi_{\text{cl}} \\ &= \frac{1}{\phi_{\text{cl}}}\int_{t-\eta}^{t} C(z'(t'),t')\frac{1}{w_{\text{ice}}}\frac{d\phi_{\text{cl}}}{dz'}dt' \end{aligned} \qquad (5.33)$$

where η is the time it takes the ice parcel to sink from 0 to z, given by

$$\eta = \frac{1}{A\rho_{\text{ice}}}\int_0^z \rho dz' \qquad (5.34)$$

The model first calculates the open pore mixing ratios $C(z,t)$, which are stored in a matrix C_{op} with a typical resolution of $\Delta z = 0.5$ m and $\Delta t = 0.01$ yr. We find the term $C(z'(t'),t')$ in Eq. 5.33 by linear interpolation along z' of the elements of the matrix C_{op}.

In Fig. 5.6 we show calculated CH$_4$ age distributions at the bottom of the firn column at the NEEM and South Pole sites. In Table. 5.1 we give the characteristics of the age distributions, using two commonly used metrics. The first one is the mean age $\Gamma(z)$, which is the first moment of the distribution:

$$\Gamma(z) = \int_0^{\infty} t \cdot G(z,t)\ dt \qquad (5.35)$$

Table 5.1: Mean age Γ and spectral width Δ for CH_4 at NEEM ($z = 79$ m) and South Pole ($z = 123$ m). All values are in years.

	Open pores	Closed pores
NEEM Γ	72.2	73.6
NEEM Δ	9.4	9.5
South Pole Γ	100.9	149.0
South Pole Δ	21.8	54.6

The second is the spectral width $\Delta(z)$, which is the second moment of the distribution (Trudinger et al., 2002):

$$\Delta^2(z) = \frac{1}{2}\int_0^\infty (t-\Gamma)^2 \cdot G(z,t)\ dt \tag{5.36}$$

The trapping process has two effects. First, the air in the closed pores is older than the air in the open pores, as can be seen from the mean age Γ. This is caused by a tail of older air that is already trapped in the DZ. Second, the trapping process causes some additional smoothing, which is shown by an increased distribution width Δ.

It is also clear that the effects of trapping are almost negligible at a high accumulation site such as NEEM. The low accumulation rate and long firn column at South Pole make the effects of the bubble trapping clearly visible. Another important difference between the two sites is the length of the LIZ, or non-diffusive zone. At NEEM the LIZ is very long, with only an estimated ∼5 % of the bubbles trapped above the lock-in depth. At South Pole the LIZ is very narrow, and an estimated ∼20 % is trapped above the lock-in depth (using the Goujon et al. (2003) parameterization in both cases). In particular bubble trapping in the DZ leads to additional broadening of the age distribution. Within the LIZ, bubble trapping does not lead to a significant broadening because the air is advected downwards at approximately the same velocity as the ice.

5.8 Summary and conclusions

In this chapter we introduced the CIC 1-D firn air transport model:

- Using the principle of mass conservation, we derived expressions for the air velocity in the open porosity and the bubble trapping rate.
- Based on two simple assumptions, we derived an expression for the pressurization of closed bubbles due to firn compaction. We tested the equations for NEEM and South Pole, and found they predicted the total air content accurately within 3%.

- We described the total flux of a tracer in the open porosity.
- We showed how the second order PDE describing the combined effects of diffusion, advection and radioactive decay was implemented numerically using the Crank-Nicolson method.
- We presented a new way to reconstruct the effective diffusivity profile with depth.
- We showed how mixing ratios in the closed porosity can be calculated, and showed how the trapping process broadens the age distribution. We found the additional broadening due to trapping to be negligible at NEEM, because of its high accumulation and long lock-in zone. At South pole there is significant broadening due to the lower accumulation rate and the short lock-in zone.

5.9 References

Colbeck, S. C. (1989). Air movement in snow due to windpumping. *J. Glaciol.*, 35(120):209–213.

Goujon, C., Barnola, J. M., and Ritz, C. (2003). Modeling the densification of polar firn including heat diffusion: Application to close-off characteristics and gas isotopic fractionation for antarctica and greenland sites. *J. Geophys. Res.-Atm*, 108(D24):18.

Huber, C., Beyerle, U., Leuenberger, M., Schwander, J., Kipfer, R., Spahni, R., Severinghaus, J. P., and Weiler, K. (2006). Evidence for molecular size dependent gas fractionation in firn air derived from noble gases, oxygen, and nitrogen measurements. *Earth Planet Sc. Lett.*, 243(1-2):61–73.

Kawamura, K., Severinghaus, J. P., Ishidoya, S., Sugawara, S., Hashida, G., Motoyama, H., Fujii, Y., Aoki, S., and Nakazawa, T. (2006). Convective mixing of air in firn at four polar sites. *Earth Planet Sc. Lett.*, 244(3-4):672–682.

Martinerie, P., Raynaud, D., Etheridge, D. M., Barnola, J. M., and Mazaudier, D. (1992). Physical and climatic parameters which influence the air content in polar ice. *Earth Planet Sc. Lett.*, 112(1-4):1–13.

Rommelaere, V., Arnaud, L., and Barnola, J. M. (1997). Reconstructing recent atmospheric trace gas concentrations from polar firn and bubbly ice data by inverse methods. *J. Geophys. Res.-Atm*, 102(D25):30069–30083.

Schwander, J. (1989). The transformation of snow to ice and the occlusion of gases. In Oescher, H. and Langway, C., editors, *The Environmental record in glaciers and ice sheets*, pages 53–67. John Wiley, New York.

Schwander, J., Barnola, J. M., Andrie, C., Leuenberger, M., Ludin, A., Raynaud, D., and Stauffer, B. (1993). The age of the air in the firn and the ice at summit, greenland. *J. Geophys. Res.-Atm*, 98(D2):2831–2838.

Severinghaus, J. P. and Battle, M. O. (2006). Fractionation of gases in polar lee during bubble close-off: New constraints from firn air ne, kr and xe observations. *Earth Planet Sc. Lett.*, 244(1-2):474–500.

Severinghaus, J. P., Grachev, A., and Battle, M. (2001). Thermal fractionation of air in polar firn by seasonal temperature gradients. *Geochem. Geophy. Geosy.*, 2.

Sowers, T., Bender, M., Raynaud, D., and Korotkevich, Y. S. (1992). Delta-n-15 of n_2 in air trapped in polar ice - a tracer of gas-transport in the firn and a possible constraint on ice age-gas age-differences. *J. Geophys. Res.-Atm*, 97(D14):15683–15697.

Sugawara, S., Kawamura, K., Aoki, S., Nakazawa, T., and Hashida, G. (2003). Reconstruction of past variations of delta c-13 in atmospheric co_2 from its vertical distribution observed in the firn at dome fuji, antarctica. *Tellus B*, 55(2):159–169.

Trudinger, C. M., Enting, I. G., Etheridge, D. M., Francey, R. J., Levchenko, V. A., Steele, L. P., Raynaud, D., and Arnaud, L. (1997). Modeling air movement and bubble trapping in firn. *J. Geophys. Res.-Atm*, 102(D6):6747–6763.

Trudinger, C. M., Etheridge, D. M., Rayner, P. J., Enting, I. G., Sturrock, G. A., and Langenfelds, R. L. (2002). Reconstructing atmospheric histories from measurements of air composition in firn. *J. Geophys. Res.-Atm*, 107(D24):13.

6

In situ cosmogenic radiocarbon production and 2-D ice flow line modeling for an Antarctic blue ice area

C. Buizert, V. V. Petrenko, J. L Kavanaugh, K. M. Cuffey, N. A. Lifton, E. J. Brook and J. P. Severinghaus[1]

6.1 Introduction

Old ice can not only be obtained from deep ice cores, but also at ice margins and Antarctic blue ice areas (BIAs) where it is being re-exposed by ablation (Reeh et al., 2002; Bintanja, 1999). For paleoclimate studies this provides an interesting alternative to ice coring, as sample retrieval is less challenging both from a technological and a logistical point of view. Ice can be sampled from near the surface, making the method especially well suited for experiments that require large ice samples (Petrenko et al., 2009). Dating of ice parcels is the principal problem when using ablation sites for climatic reconstruction (Sinisalo and Moore, 2010, and references therein). Several methods have been used, including radiometric dating of tephra layers (e.g. Dunbar et al., 2008), flow line modeling (Azuma et al., 1985; Grinsted et al., 2003; Moore et al., 2006), stratigraphical matching of gas and stable water isotope measurements to well-dated ice core records (e.g. Reeh et al., 2002; Petrenko et al., 2006; Aciego et al., 2007; Schaefer et al., 2009), and radiocarbon dating of micro-particles (Jenk et al., 2007). Early on it was realized that radiocarbon (^{14}C) dating of the CO_2 present in the air bubbles trapped in polar ice can potentially be used as an absolute dating method for ice cores and BIA samples (Fireman and Norris, 1982; Andree et al., 1984). However, interpretation of radiocarbon data is complicated by cosmogenic in situ production of ^{14}C from oxygen atoms found in ice (Lal et al., 1990). When this effect is corrected for, the air bubbles contained in the ice can be dated with an accuracy of a few thousands of years (Van de Wal

---

[1] This chapter has been submitted to the Journal of Geophysical Research – Earth Surface.

et al., 1994; Van Roijen et al., 1995; Van Der Kemp et al., 2002; De Jong et al., 2004; Van de Wal et al., 2007).

Apart from dating applications, there are other reasons for studying radiocarbon in ice. First, surface ^{14}C concentrations reflect ablation (or accumulation) rates at the site under study. At low ablation rate sites the ice parcels move slowly through the top ~5 m (where cosmogenic irradiation is strongest), leading to high surface activities as the in situ produced ^{14}C accumulates over time. And vice versa, where ablation rates are high, activities will be low. By this principle, measurements of ^{14}C have been used to estimate BIA ablation rates (e.g., Lal et al., 1990; Van Roijen et al., 1995; Van der Borg et al., 2001). It has also been suggested that ^{14}C in ice core samples can be used to infer past changes in accumulation rate (Lal et al., 1990, 2000).

Second, at well-dated ablation sites paleoclimate information can be obtained from radiocarbon measurements. Fossil carbon sources are depleted in ^{14}C, and in this way measuring ^{14}C activities of carbon-containing gas species can teach us about the fossil contribution to their past atmospheric variations. In particular, the ^{14}C variations in methane (CH_4) over the last glacial termination contain information on how much the destabilization of ^{14}C-depleted methane hydrates contributed to the observed CH_4 increases (Petrenko et al., 2008, 2009).

Here we study ^{14}C production at the Taylor Glacier BIA, Antarctica, where ice with ages between approximately 11.5 and 65 kyr is being exposed (Aciego et al., 2007; Kavanaugh et al., 2009b). Taylor Glacier is an outlet glacier of the East Antarctic Ice Sheet which originates at Taylor Dome, and terminates in the McMurdo Dry Valleys (Figure 6.1). Ablation is dominated by sublimation (Bliss et al., 2011); ablation rates are around 0.1-0.3 m yr^{-1} (Kavanaugh et al., 2009a), which is typical of Antarctic BIAs (Bintanja, 1999). The ice stratigraphy along the center flow line can be dated by matching trace gas mixing ratios and gas stable isotope measurements to ice core records, and matching of water stable isotopes to the Taylor Dome record (Steig et al., 2000). The large (~1000 kg) ice samples required for high precision ^{14}C measurements of trace gas species such as CH_4 and CO can be obtained from near the glacier surface (Petrenko et al., 2008).

Because measurable amounts of cosmogenic ^{14}C are produced down to a depth of ~ 200 m, the exposure history of ablating ice parcels is a function of their flow path in the glacier. The aim of this study is to combine 2-D flow line modeling with up-to-date cosmogenic exposure theory to obtain a best estimate for the ^{14}C activity of ablating Taylor Glacier ice. We present two new ways to parameterize vertical strain rates with depth, and we evaluate which method provides the better description for Taylor Glacier. The model allows us to assess the influence of glacier valley topography and solar modulation of cosmic ray intensity on the in situ ^{14}C production; both of which have been neglected in studies so far.

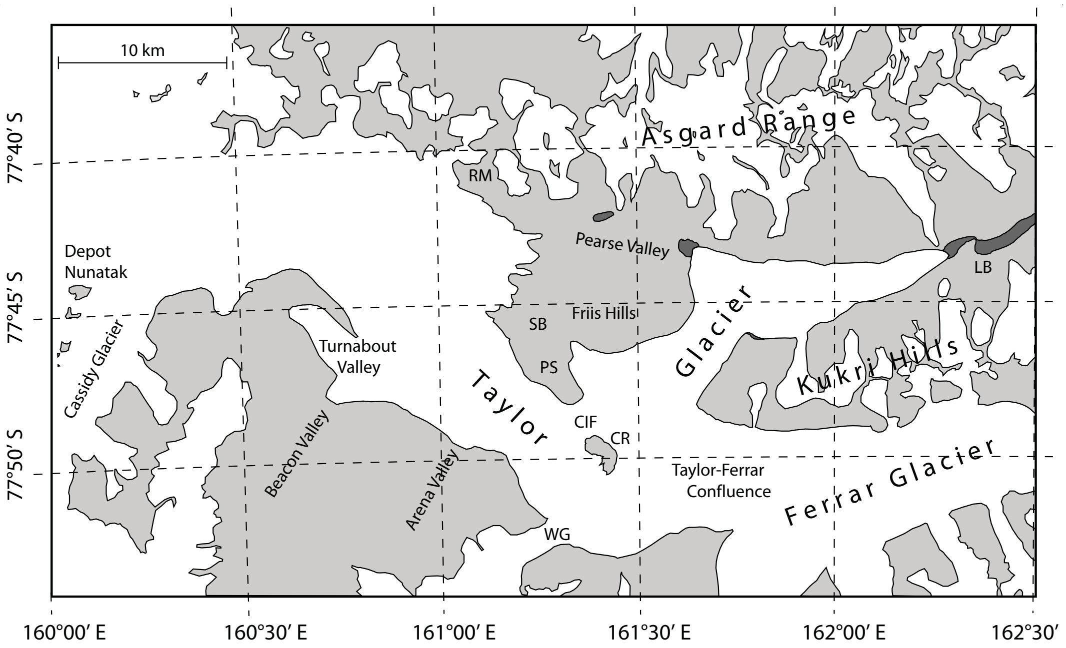

Figure 6.1: The Taylor Glacier with surroundings. Abbreviations are: Round Mountain (RM), Simmons Basin (SB), Pandora Spire (PS), the Cavendish Ice Falls (CIF), Cavendish Rocks (CR), Windy Gully (WG), and Lake Bonney (LB).

The modeling results presented here will furthermore be used for interpretation of future ^{14}C measurements. During a 2010/2011 Austral summer field campaign, samples for radiocarbon analyses were taken at Taylor Glacier with the purpose of constraining in situ production rates better. We will show that at the sampling location the influence of ice flow strain rates on ^{14}C activities is minimal, greatly simplifying data interpretation. More importantly, this work will serve as a framework for correcting ^{14}C of methane (^{14}CH$_4$) measurement over the last glacial termination for the effects of in situ production, with the purpose of reconstructing of the true paleo-atmospheric signal.

6.2 Cosmogenic production of ^{14}C in ice

Cosmic rays consist largely of charged subatomic particles originating from outside the Earth's magnetosphere. Upon entering the upper atmosphere, particles of sufficient energy cause nuclear disintegrations, from which a shower, or cascade, of secondary cosmic ray particles is produced. On interacting with the materials of Earth's surface, these secondary cosmic rays are capable of producing a wide variety of terrestrial cosmogenic nuclei (TCN); see Gosse and Phillips (2001) and references therein for an overview of TCN exposure theory. In ice, ^{14}C is produced cosmogenically, primarily through neutron spallation of oxygen atoms (Lal et al., 1990). After production, the ^{14}C atoms are predominantly oxidized to form either $^{14}CO_2$ or ^{14}CO. The reported fraction of ^{14}CO out of the total in situ ^{14}C ranges from 0.20-0.57 (Lal et al., 1990; Van Roijen et al., 1995; Lal et al., 2000; Van Der Kemp et al., 2002; De Jong et al., 2004). A recent study, however, suggests $^{14}CH_4$ is formed in small amounts as well (Petrenko et al., 2009).

Ice found in BIAs has experienced two intervals of exposure: one in the accumulation zone and one during ablation. Interpretation of the ablation signal is more straightforward because all the cosmogenic ^{14}C is retained. In the accumulation zone, the presence of a porous firn layer complicates interpretation. In their conceptual model of ^{14}C retention in the firn, Van de Wal et al. (2007) introduce a degassing rate at which ^{14}C is released from the ice matrix (where it is produced), into the open pore space. From there, the produced ^{14}C is lost to the overlying atmosphere through the action of diffusion and wind pumping. Some authors have argued that the degree to which ^{14}C is retained in the firn may depend on the accumulation rate (Lal et al., 2001; De Jong et al., 2004). Their arguments are based on the observation that the high accumulation Greenland GISP2 ice core (0.25 m yr^{-1} ice equivalent) showed high retention of in situ ^{14}C (Lal et al., 2000), while low accumulation sites such as Dome Concordia (0.03 m yr^{-1}), Vostok (0.02 m yr^{-1}) and Taylor Dome (0.06 m yr^{-1}) show low or no retention (Lal et al., 2001; De Jong et al., 2004). However, this hypothesis is contradicted by reported observations of high retention at a low accumulation site (Jull et al., 1994), as well as low retention at high accumulation sites (Smith et al., 2000, Petrenko et al., in preparation). It has also been proposed that the method used to extract gas from ice samples can influence the results (Smith et al., 2000; Van der Borg et al., 2001). Dry extraction methods, such as milling and grating (Van de Wal et al., 1994; Smith et al., 2000), will liberate gas molecules in air bubbles, but might not extract all the gas molecules dissolved in the ice. Since in situ cosmogenic ^{14}C is produced in the ice matrix rather than in the bubbles, dry extraction methods may underestimate cosmogenic ^{14}C content. Melt extraction with added phosphoric acid (Lal et al., 1990) will extract all gas molecules, however additional CO_2 will be produced from any (bi)carbonates present in the ice. With this technique CO_2 and CO may also be produced from organics in the ice. Given the results published to date, it is unclear how much of the ^{14}C that is produced in the accumulation zone is actually retained, if any. We focus our attention on ^{14}C production in the ablation zone. For ice older than $\sim$ 50 kyr, essentially all of the accumulation-zone cosmogenic ^{14}C will have decayed, and only the ablation-zone component is of importance.

We will consider four different mechanisms of in situ cosmogenic ^{14}C production in ice. Three of these involve nuclear reactions with oxygen; the fourth involves the capture of thermal neutrons by the nitrogen present in the air bubbles found in glacial ice.

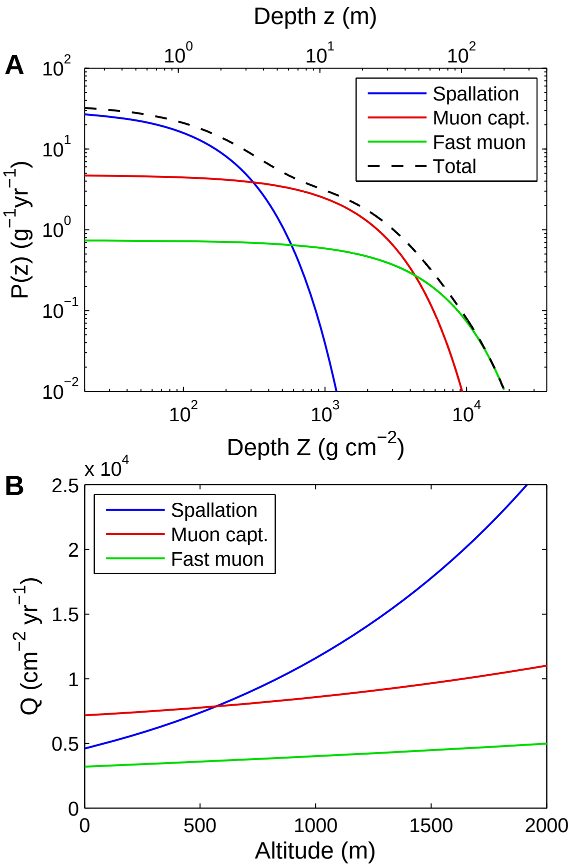

Figure 6.2: (A) In situ ^{14}C production rates with glacier depth using equation (6.1) and the values listed in Table 6.1. The glacier surface is taken at sea level. The black dashed line represents the sum of the individual mechanisms. (B) Altitude dependence of the production using the Lifton et al. (2005) model. The colors represent the three mechanisms, the vertical axis shows the integrated production $Q_i = \int_0^\infty P_i(z)dz$.

6.2.1 Spallogenic and muogenic production

We first consider neutron spallation reactions (Lal et al., 1990, 2000), negative muon capture (Van der Borg et al., 2001; Van Der Kemp et al., 2002; Heisinger et al., 2002a), and fast muon reactions (Heisinger et al., 2002b; Nesterenok and Naidenov, 2009). The neutron and muon fluxes incident on the glacier surface are attenuated in the ice, giving a production $P(z)$ that falls off with depth following

$$P_i(z) = P_i^0 e^{-Z/\Lambda_i} = P_i^0 e^{-\rho z/\Lambda_i} \tag{6.1}$$

where P_i^0 is the surface production rate, Z the overburden in g cm^{-2}, z the depth in cm, Λ_i the absorption mean free path in g cm^{-2}, and ρ the density of the medium (for ice we use $\rho = 0.92$ g cm^{-3}). Following Heisinger et al. (2002a), the subscript

Table 6.1: Constants used in ^{14}C production calculations, as well as the e-folding depths corresponding to the listed absorption mean free paths. Production rates are given at sea level and high latitude.

Mechanism i	Λ_i (gcm^{-2})	P_i^0 (g^{-1}yr^{-1})	Λ_i/ρ (m)
Neutrons	150[a]	30.7 ± 5[b]	1.6
Muon capture	1510[b]	4.75 ± 0.4[b]	16.4
Fast muons	4320[c]	0.74 ± 0.4[b]	47.1

[a] Lal et al. (1987); Van de Wal et al. (2007)
[b] Heisinger et al. (2002a)
[c] Heisinger et al. (2002b)

i can take the values h, μ^- and μ_f to denote neutron spallation (also referred to as the hadronic component), negative muon capture, and fast muons, respectively. The production constants used in this study are summarized in Table 6.1, where the last column gives the e-folding depth for each production mechanism. Figure 6.2A shows how the production rates fall off with depth.

Following convention, surface production rates are listed at sea level and at high latitude. At elevation there is less shielding by the overlying atmosphere, giving an increased cosmic ray flux and radionuclide production. At low latitudes, the Earth's magnetic field shields more of the incoming rays, leading to lower nuclide production. To incorporate both effects, scaling relations are used, which give nuclide production rates at any point at the Earth's surface relative to the reported high latitude sea level production rates (Lal, 1991; Dunai, 2000; Gosse and Phillips, 2001; Desilets and Zreda, 2003; Desilets et al., 2006; Lifton et al., 2005). We use the scaling model of Lifton et al. (2005), which provides the most detailed description of muogenic scaling factors based on muon monitor data covering a wide range of altitudes and latitudes. Furthermore, the Lifton scaling model includes the effect of solar modulation, which can alter the spallogenic production by $\sim 10\%$ at the high geomagnetic latitudes of our study site.

The altitude dependence is described by the atmospheric depth X (in g cm^{-2}), which equals the mass of the overlying atmosphere traversed by the incident cosmic rays at a given elevation. Note that X is directly proportional to the barometric pressure. Radionuclide studies often use the standard atmosphere as a basis for relating pressure to altitude (Lal, 1991). This works well in mid-latitudes, but due to spatial inhomogeneities in pressure this underestimates the cosmic ray flux over Antarctica by approximately 20%. For this reason the pressure-altitude relation over Anarctica from Stone (2000) is used. The latitudinal dependence of the cosmic ray flux is described by the effective vertical cutoff rigidity R_C, which is a measure of the threshold energy required for a (charged) cosmic ray particle to access a given point within the Earth's magnetosphere. R_C is inversely related to the geomagnetic latitude; it is highest near the equator where geomagnetic shielding is strong, and low at the poles where the threshold energy is low and essentially all cosmic rays of interest to cosmogenic nuclide production are admitted. The scaling model is latitude invariant at geomagnetic latitudes greater than approximately $\sim 60°$ S, equivalent to $R_C \leq 1.9$ (Lifton et al., 2005). Taylor glacier falls within this latitude range. Figure 6.2B shows how the integrated ice column production $Q_i = \int_0^\infty P_i(z)dz$ changes with altitude. The integrated production Q_i scales linearly with the surface production P_i^0, but is more informative since it shows the total amount of in situ ^{14}C that will be present in an ablating ice parcel. It is clear that the neutron flux is attentuated much more strongly by the atmosphere, giving a more pronounced altitude dependence.

6.2.2 Thermal neutron capture

Glacial ice contains a finite amount of trapped air, typically about 0.1 mL g^{-1} at standard temperature and pressure (STP). The final mechanism of ^{14}C production we consider is absorption of thermal neutrons by the nitrogen present in gas bubbles, following the ^{14}N(n,p)^{14}C nuclear reaction pathway. This is the dominant mechanism for radiocarbon production in the atmosphere. To the best of our knowledge, this mechanism has been ignored in studies of radiocarbon production in ice to date. However, because of the large capture cross-section of nitrogen ($\sigma_{\mathrm{th,N}} = 1.9 \times 10^{-24}$ cm^2), a thermal neutron contribution cannot be excluded a priori.

Low-energy neutrons, such as thermal neutrons, originate from fast (spallogenic) neutrons whose energy has been moderated through interaction with matter (Gosse and Phillips, 2001). On slowing down they first pass through the epithermal energy range (0.5eV $< E_n <$ 1 keV, with E_n the neutron energy). By this time, the particle trajectories have been fully randomized, and the epithermal neutron flux is diffusive in nature. While a fraction of the epithermal neutrons will be captured by surrounding nuclei, the remainder is moderated further and reaches the thermal energy range ($0 < E_n <$ 0.5 eV), where neutron energy is on the order of the thermal vibrations of their surroundings. At these energies they can no longer lose their energy by momentum transfer to incident nuclei, and the only sink mechanisms to the thermal neutron flux are capture and free neutron decay.

To calculate both the epithermal and thermal neutron fluxes near the ice-atmosphere interface, we use a model by Phillips et al. (2001). Table 6.2 lists the low-energy transport parameters used here, where for each element k we specified its mass A, average log decrement of energy loss per collision ξ, epithermal neutron scattering cross-section σ_{sc}, thermal neutron capture cross-section σ_{th} and the dilute resonance integral for absorption of epithermal neutrons I_{a}. We also specified the estimated concentrations in atoms per gram of the different elements for both ice and atmosphere (N_{ice} and N_{atm}, respectively). We first verified our low-energy neutron model by comparing our calculated fluxes to measured fluxes in a block of concrete at Los

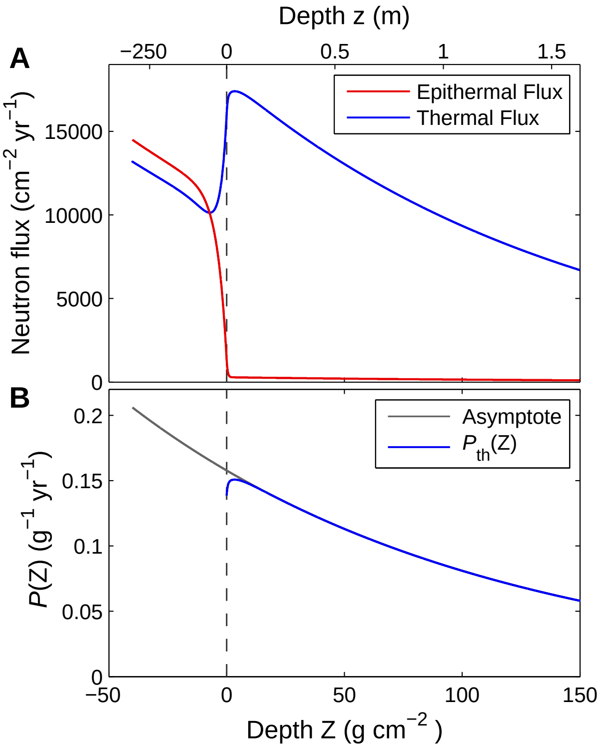

Figure 6.3: (A) Modeled thermal and epithermal neutron fluxes at the atmosphere-ice interface at high latitude ($R_C = 0$) and sea level. The ice surface is placed at $Z = 0$; for $Z < 0$ we have atmosphere, for $Z \geq 0$ ice. (B) Production rate of ^{14}C through the ^{14}N(n,p)^{14}C nuclear reaction given the calculated neutron fluxes, together with the asymptote given by equation (6.4).

Alamos National Laboratory, USA (Liu et al., 1994). The model reproduces the observations within 10%, giving us confidence that, at the very least, the model will calcluate the fluxes to the correct order of magnitude. Figure 6.3A shows the calculated epithermal and thermal fluxes ($\Phi_{\rm eth}$ and $\Phi_{\rm th}$, respectively) for an ice-atmosphere interface at sea level. We see that the epithermal flux in the ice is strongly reduced. This is due to the presence of hydrogen as the most abundant element, which is a very effective moderator of epithermal neutrons (Table 6.2). The probability that epithermal neutrons are absorbed in the ice is given by

$$p(E_{\rm eth}) = 1 - \exp\left(\frac{-\sum_k I_{{\rm a},k} N_{{\rm ice},k}}{\sum_k \sigma_{{\rm sc},k} N_{{\rm ice},k}}\right) < 1 \times 10^{-5} \tag{6.2}$$

This indicates that effectively all epithermal neutrons are further moderated into the thermal energy range, rather than absorbed. Accordingly, we see a large increase in the thermal neutron flux over the atmosphere-ice interface.

From the calculated flux we can derive the production of ^{14}C by thermal neutrons as

Table 6.2: Low-energy neutron transport parameters for the elements under consideration. Values are taken from Phillips et al. (2001) unless indicated differently.

k	A (g mol^{-1})	ξ (unitless)	$\sigma_{\rm sc}$ (10^{-24} cm^2)	$\sigma_{\rm th}$ (10^{-24} cm^2)	$I_{\rm a}$ (10^{-24} cm^2)	$N_{\rm ice}$ (10^{20} g^{-1})	$N_{\rm atm}$ (10^{20} g^{-1})
H	1	1	20.5	0.33	0	667	0
N	14	0.14	11.5^a	1.9^b	0.034^c	0.0456	325
O	16	0.12	3.76	0.0002	0.0004	334	87.1
Ar	39.9	0.049	0.68^a	0.675^a	0.41^c	0.0027	1.94

[a] Sears (1992)
[b] Wagemans et al. (2000)
[c] Mughabghab et al. (1992)

$$P_{\rm th}(Z) = \sigma_{\rm th,N} N_{\rm ice,N} \Phi_{\rm th}(Z) \tag{6.3}$$

This is shown in Figure 6.3B together with the curve

$$P_{\rm th}^{\rm AS}(Z) = \sigma_{\rm th,N} N_{\rm ice,N} \Phi^*_{\rm th,ice} e^{-Z/\Lambda_{\rm h}} \tag{6.4}$$

towards which $P_{\rm th}(Z)$ approaches asymptotically as $Z \to \infty$. The value of $\Phi^*_{\rm th,ice}$ is given by equation (21) in Phillips et al. (2001). From equation (6.4) it is clear that in first approximation the thermal neutron production has the same depth dependence as the production by neutron spallation (equation (6.1)); however, the surface production rate (and thereby the integrated column production), is more than 2 orders of magnitude smaller. We shall therefore neglect ^{14}C production by thermal neutrons in the remainder of this work. Since all thermal neutrons are ultimately captured by nuclei of the host material, one might wonder why the ^{14}C production rate is so small. On comparing the values in Table 6.2 it is clear that hydrogen absorbs the vast majority of thermal neutrons by virtue of its abundance and relatively large capture cross-section.

6.3 Taylor Glacier 2-D flow line modeling

6.3.1 Data input to the ice flow model

The 2-D ice flow line modeling presented here is based on a recent detailed study of the dynamics and mass balance of Taylor Glacier (Kavanaugh et al., 2009a; Kavanaugh and Cuffey, 2009; Kavanaugh et al., 2009b). From these studies we use the surface and basal digital elevation models; surface velocities obtained from both satellite radar interferometry (InSAR) and Global Positioning System (GPS) measurements of the displacement of a network of survey poles; ice-surface ablation rates; and modeled horizontal velocity profiles with depth.

Figure 6.4 shows the outline of the glacier, with the color scale depicting the magnitude of the surface velocity in m yr^{-1} obtained through remote sensing (Kavanaugh et al., 2009b). The red line indicates the flow line used in this study, along

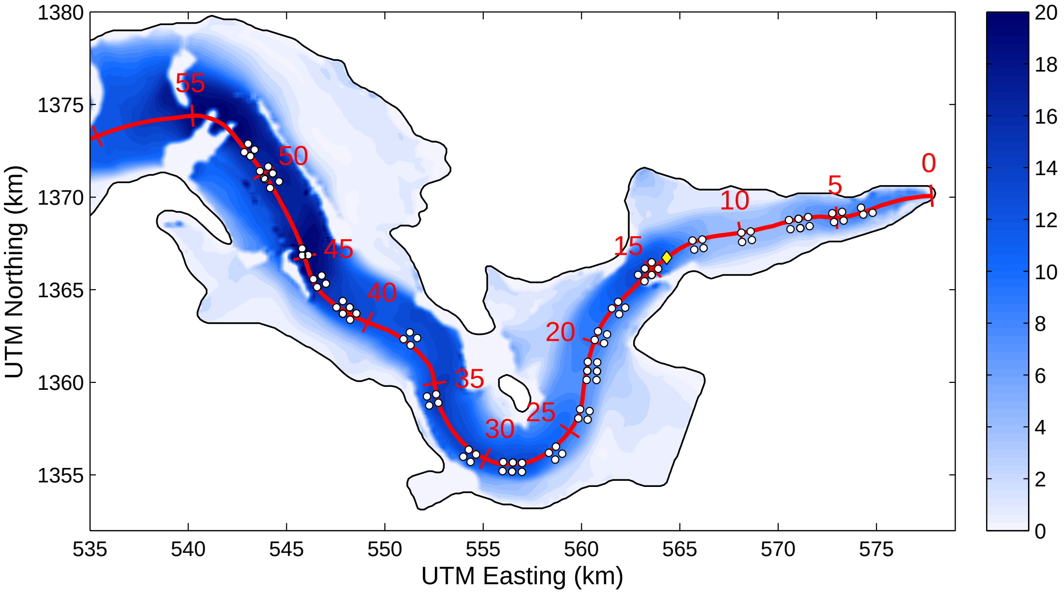

Figure 6.4: Color plot of glacier surface velocity in m yr^{-1} from InSAR (Kavanaugh et al., 2009b). Regions with missing data show up as light patches; here high surface deformation due to strain rates precludes phase unwrapping. White dots indicate survey poles used in this study, which are a subset of the stake network of Kavanaugh et al. (2009b), selected for their proximity to the center-line flow path. Ablation rate measurements as well as GPS velocity measurements are available for these poles. The red line with distance markers in km indicates the center flow line used in this study, the black line shows the glacier edge. The main ^{14}C sampling site of the 2010/2011 Austral summer field campaign (77.762° S, 161.720° E, or $x = 14.05$ km) is indicated with a yellow diamond.

which we shall calculate the exposure history of ablating ice parcels. The marks in red give the distance from the glacier terminus in km along the flow line. We let x be the flow-parallel coordinate with the origin at the terminus, y be perpendicular to the flow and z be the depth coordinate with $z = 0$ at the glacier surface. The flow line is constructed in two steps. The first part from $0 < x \leq 40.5$ km follows the sampling transect of a 2009-2010 field campaign, the aim of which was to accurately date the ablating ice (D. Baggenstos, in preparation). For $x > 40.5$ km we inverted the surface velocity field and traced back an imaginary ice parcel. The flow line crosses two narrow regions of missing data around $x = 53$ km; in these locations we adjusted the path by eye to obtain a smooth transition between the trajectories on both sides.

The ablation rate measurements are described by Kavanaugh et al. (2009a). We selected poles along the center flow line as shown in Figure 6.4. The poles were planted during the 2002/2003 Austral summer field season, and measured during the 2003/2004 season. The majority of poles relevant for this study were remeasured in the 2006/2007 season. We include additional data for a total of 17 poles that were remeasured during the 2009/2010 and 2010/2011 field seasons. Consequently we have 1- and 4-year ablation rate estimates for the majority of the poles, and a 7- or 8-year estimate for 17 of the poles. The 1- and 4-year ablation rate estimates differ significantly, with the former being 4.7 cm yr^{-1} more rapid averaged over the selected poles (Kavanaugh et al., 2009a). The 4-year estimates agree well with the and 7- and 8-year averages. For each pole we take the longest available measurement period as a best estimate. For 7 poles (all at $x > 50$ km) this period equals one year; their ablation estimate is adjusted by subtracting 4.7 cm yr^{-1}. The single year ablation offset from the long term average gives an estimate of the year to year variability; as an ablation rate uncertainty estimate we use 4.7 cm yr^{-1} divided by $\sqrt{N}$, where N is the period in years ($N = 1, 4, 7, 8$). Pole positions were projected perpendicularly onto the flow line; poles with their x coordinate less than 200 m apart were averaged. Between stakes we used linear interpolation of both ablation rates and uncertainty estimates. The peak near $x = 30$ km is caused by strong katabatic winds coming down Windy Gully (Figure 6.1; see Kavanaugh et al., 2009a).

6.3.2 Calculating vertical ice velocities relative to the surface

To trace the trajectories of ice parcels downwards back into the glacier, we need to calculate flow velocities in the x, z-plane. Let u, v, w be the velocity components along x, y, z; $\mathbf{u} = (u, v)$ the horizontal velocity vector, $\mathbf{u}_\mathrm{s} = (u_\mathrm{s}, v_\mathrm{s})$ the horizontal velocity vector at the glacier surface, and H the total ice thickness. The component w is the vertical velocity relative to the glacier surface. We write the horizontal velocity as (Azuma et al., 1985; Grinsted et al., 2003; Kavanaugh and Cuffey, 2009):

$$\begin{aligned} u(z) &= f(z)u_\mathrm{s} \\ v(z) &= f(z)v_\mathrm{s} = 0 \end{aligned} \tag{6.5}$$

where $f(z)$ is a scaling function which equals unity at the surface $f(0) = 1$. Kavanaugh and Cuffey (2009) conclude that Taylor Glacier is frozen to the bed; for this reason we include no basal sliding, and f goes to zero at bedrock $f(H) = 0$. We use the numerically solved scaling functions by Kavanaugh and Cuffey (2009) at six points along the flow line, and use linearly interpolated profiles in between. The profiles are accurate since they are based on the actual stresses and estimated temperature profiles in Taylor Glacier.

The vertical velocity at the surface equals the ablation rate $w_\mathrm{s} = a$. At finite depth $w(z)$ is given by

$$w(z) = a + \int_0^z \dot{\varepsilon}_{zz}(z')dz' \tag{6.6}$$

where $\dot{\varepsilon}_{zz}$ is the vertical strain rate $\dot{\varepsilon}_{zz} = \partial w/\partial z$. We will compare two methods to estimate $\dot{\varepsilon}_{zz}$.

Estimating $\dot{\varepsilon}_{zz}$ using mass conservation in the ice column

Kavanaugh et al. (2009a) have estimated that within the accuracy of their method, Taylor Glacier is in steady state. Under this assumption ($\partial H/\partial t = 0$), mass conservation in the ice column can be written as (Cuffey and Paterson, 2010)

$$a + H(\nabla \cdot \bar{\mathbf{u}}) + \bar{\mathbf{u}} \cdot (\nabla H) = 0 \tag{6.7}$$

where $\bar{\mathbf{u}}$ is the depth-averaged horizontal velocity. We introduce the commonly used assumption that the horizontal strain rates scale the same way with depth as the horizontal velocity (Grinsted et al., 2003; Kavanaugh and Cuffey, 2009)

$$\begin{aligned} \dot{\varepsilon}_{xx} &= \frac{\partial u}{\partial x} = f(z)\frac{\partial u_\mathrm{s}}{\partial x} \\ \dot{\varepsilon}_{yy} &= \frac{\partial v}{\partial y} = f(z)\frac{\partial v_\mathrm{s}}{\partial y} \end{aligned} \tag{6.8}$$

This is not always a good assumption near the bed, but works well for the near-surface flow that is relevant to cosmogenic production estimation. Using the fact that on the center flow line the transverse velocity $v_\mathrm{s} = 0$ we can rewrite equation (6.7) as

$$a + H\bar{f}\left(\frac{\partial u_\mathrm{s}}{\partial x} + \frac{\partial v_\mathrm{s}}{\partial y}\right) + \bar{f}u_\mathrm{s}\frac{\partial H}{\partial x} = 0 \tag{6.9}$$

where $\bar{f}$ is the column average $\bar{f} = \frac{1}{H}\int_0^H f(z)dz$. Equation (6.9) assumes that $\partial\bar{f}/\partial x$ can be neglected. Using the incompressibility of ice we can solve for the vertical strain rate

$$\dot{\varepsilon}_{zz}(z) = -\frac{f(z)}{H}\left(\frac{a}{\bar{f}} + u_\mathrm{s}\frac{\partial H}{\partial x}\right) \tag{6.10}$$

Note that this approach is similar to that developed by Grinsted et al. (2003); the main difference is the inclusion of the $u_\mathrm{s}\partial H/\partial x$ term on the right hand side of equation (6.10), which is neglected in the cited study. For Taylor Glacier we cannot neglect this term, as there are large longitudinal variations in glacier thickness. To calculate vertical velocities with this approach, we use measurements of: (1) ablation rates, (2) horizontal velocity field ($u_\mathrm{s}, v_\mathrm{s}$), and (3) ice thickness H along the flow line.

This method does not ensure that $w(H) = 0$. After calculating $w(z)$ using equation (6.6) and 6.9 we have forced the ice near the base ($0.8H < z < H$) to transition smoothly towards flow parallel to the bed, or $w(z) = \partial H/\partial x \cdot u(z)$. Note that because the ^{14}C production happens in the upper part of the column only, this will not significantly influence our results.

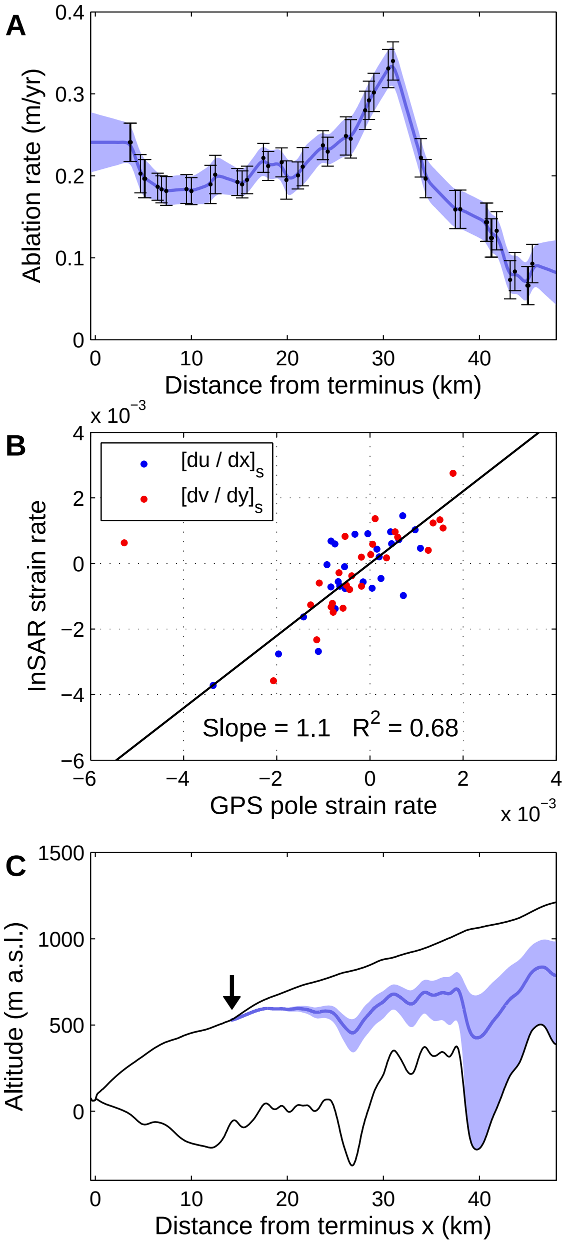

Figure 6.5: (A) Ablation rates from stake measurements (Kavanaugh et al., 2009a, black dots with error bars) together with the interpolated best estimate (blue line) and uncertainty estimate (light blue shading). The longitudinal ablation rate profile is further analyzed by Bliss et al. (2011). Details on the uncertainty estimate are given in the text. (B) Comparison of surface strain rates estimates obtained from the GPS stake network (Kavanaugh et al., 2009b, horizontal axis) and through remote sensing (vertical axis). Outlier on left rejected in the slope fitting. (C) Uncertainty in flow line reconstruction, details given in the text. The arrow shows the location of the ^{14}C sampling site of the 2010/2011 field campaign.

Estimating $\dot{\varepsilon}_{zz}$ from measured surface strain rates

As an alternative approach we calculate vertical strain from estimates of horizontal strain rates derived from InSAR and GPS surface flow velocities. Let $\dot{\varepsilon}^M_{xx,\mathrm{s}}$ and $\dot{\varepsilon}^M_{yy,\mathrm{s}}$ be the longitudinal and transverse surface strain rate estimates from measurements of $\mathbf{u}_\mathrm{s}$. Using assumption 6.8 and the incompressibility of ice we obtain

$$\dot{\varepsilon}_{zz}(z) = -\left(\dot{\varepsilon}^M_{xx,\mathrm{s}} + \dot{\varepsilon}^M_{yy,\mathrm{s}}\right) f(z) \tag{6.11}$$

The reliability of this approach depends on the accuracy of the surface strain rate estimates. Figure 6.5B shows a comparison between strain rate estimates based on the InSAR and GPS data. We see that the slope of the correlation deviates significantly from unity; there is one clear outlier in the transverse strain rate $\dot{\varepsilon}_{yy}$; there is much scatter in the data ($R^2 = 0.68$ when ignoring the outlier); and for ∼20% of the points the sign is reversed. In equation (6.11) the horizontal strain rates are added up. By doing so the potential for error is increased further, as their uncertainties also add up.

When calculating ice flow trajectories based on this second approach, we find that they fail to follow bedrock undulations as required. Furthermore, mass conservation is violated as ice parcels emerge from, and disappear into, the bed. For the reasons outlined above, we will use the first method (mass conservation in the ice column) to estimate ice parcel trajectories in the remainder of this study.

6.3.3 Tracing ice parcels

We calculate the (u, w) velocity field in the x, z-plane at a spatial resolution of $\Delta z = 5$ m and $\Delta x = 100$ m. Using a time step $\Delta t = 1$ yr we trace parcels back into the glacier, where we use linear 2-D interpolation of (u, w) to find the velocity at each newly calculated position. The result is plotted in Figure 6.6. The dashed line indicates the depth where cosmogenic production and radioactive decay balance out to give a ^{14}C concentration of 10 atoms g^{-1} to hypothetical ice parcels staying at that depth indefinitely. Since surface values are on the order of 1000 atoms ^{14}C g^{-1}, any errors in the trajectory calculation below this line can, at most, introduce a 1% error in calculated surface values.

Any choice of strain rate parameterization introduces an error. To account for this, we introduce two extreme flow cases which act as an error envelope to the true flow path. This is depicted in Figure 6.5C. The central dark blue flow path is our best estimate trajectory as described above. The extreme scenarios are calculated by using $\dot{\varepsilon}_{zz} \pm \sigma_{\dot{\varepsilon}_{zz}}$ in equation (6.6), where the strain rate uncertainty is arbitrarily set to $\sigma_{\dot{\varepsilon}_{zz}} = \max(0.2 \times |\dot{\varepsilon}_{zz}|\ , 4.0 \times 10^{-4}\ \mathrm{yr}^{-1})$. We expect the true flow path to lie within the shaded area enveloped by these two extreme flow cases. We will use this uncertainty envelope in the sensitivity study presented in section 6.4.3.

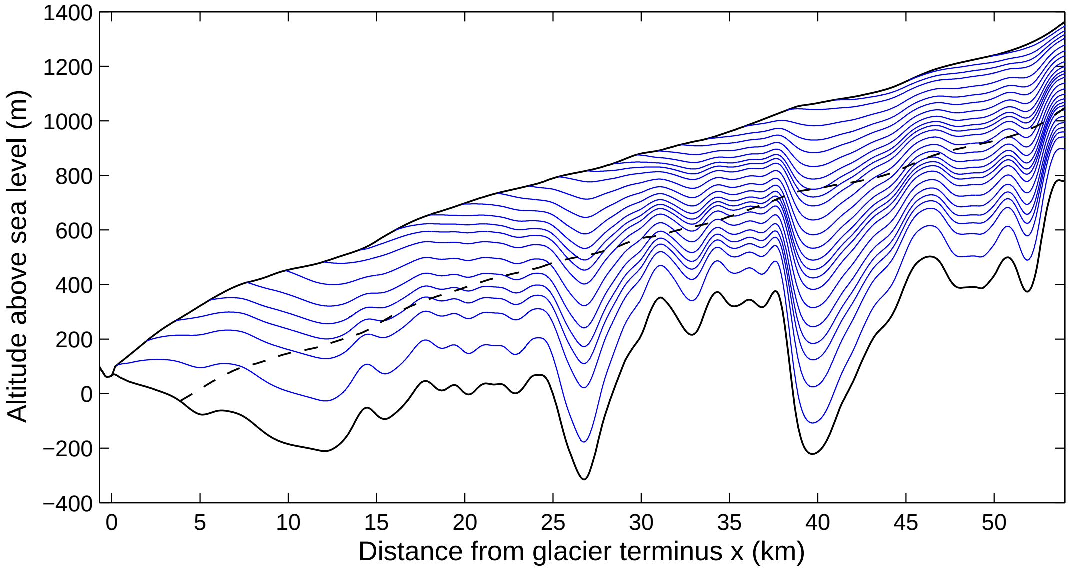

Figure 6.6: Modeled ice parcel trajectories along the center flow line. Model time step of 1 yr; parcels are traced 20 kyr back in time. The dashed line indicates the 10 atoms g^{-1} equilibrium depth.

6.4 Results and discussion

6.4.1 Taylor Glacier ^{14}C estimates

Knowing the path $(x(t), z(t))$ of an ice parcel back in time, we can calculate the time evolution of the cosmogenically produced ^{14}C concentration:

$$\begin{aligned}\frac{d[^{14}\mathrm{C}]_i}{dt} &= P_i^0(x(t))e^{\rho z(t)/\Lambda_i} - \lambda[^{14}\mathrm{C}]_i \\ [^{14}\mathrm{C}]_i(t) &= A_i + \int_0^t \frac{d[^{14}\mathrm{C}]_i}{dt'}dt' \end{aligned} \tag{6.12}$$

Here $[^{14}\mathrm{C}]_i$ denotes the concentration of ^{14}C in atoms g^{-1} produced by cosmogenic mechanism i, λ is the decay constant (1/8267 yr^{-1}), and A is the inheritance from previous cosmogenic exposure (e.g. in the accumulation zone). The 2010/2011 sampling site was selected to have an ice age >50 kyr (Aciego et al., 2007), meaning that all the ^{14}C inherited from the paleo-atmosphere and cosmogenic production in the accumulation zone has effectively decayed. Furthermore, we are interested in the ablation signal only. For these reasons we let the inheritance $A_i = 0$. The calculated concentrations are shown in Figure 6.7A. As we get further away from the terminus, the signal increases due to an enhanced cosmogenic surface production with greater altitude, as well as lower ablation rates. Around $x = 30$ km there is a local minimum in the ^{14}C concentration, which is due to the katabatic wind-induced ablation rate

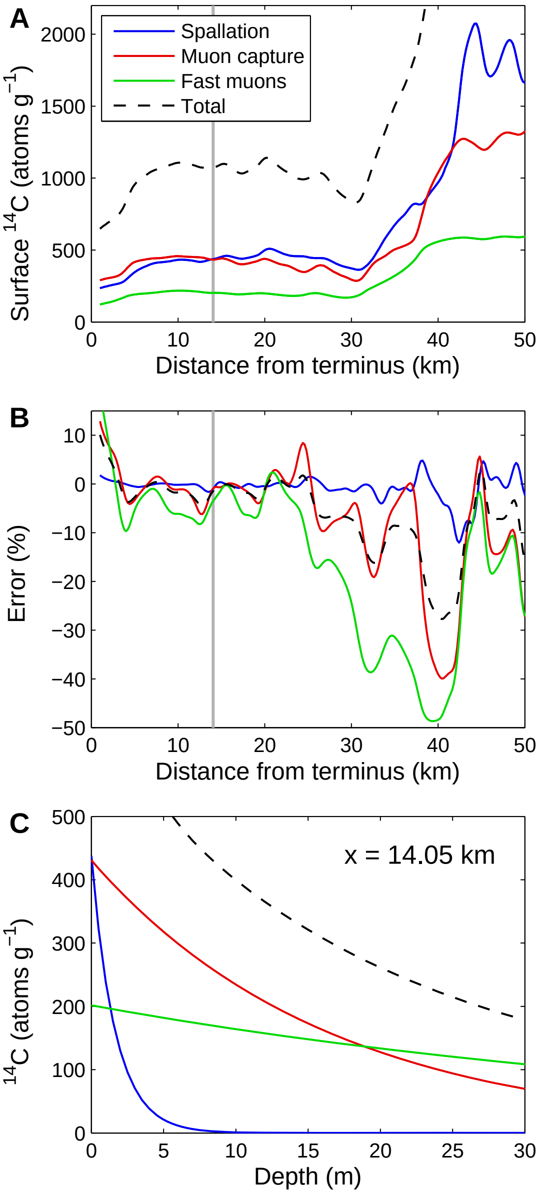

Figure 6.7: (A) Modeled surface cosmogenic ^{14}*C concentration (atoms* g^{-1}*) for the three production mechanisms. The black dashed line gives the total concentration, i.e. the sum of the three individual mechanisms. (B) Error when using the ablation-only approximation of equation (6.13), expressed as a percentage of the full 2-D model solution. Negative values means that the ablation-only approximation underestimates the true in situ production. (C) Depth profile of* ^{14}*C concentration for the three production mechanisms at the sampling site of the 2010/2011 field campaign,* $x = 14.05$ *km.*

maximum referred to earlier.

We can compare our calculated surface values to the estimate given by Lal et al. (1990):

$$[^{14}\mathrm{C}]_i(z) = \frac{P_i^0 e^{\rho z/\Lambda_i}}{\rho a/\Lambda_i + \lambda} \tag{6.13}$$

Note that equation (6.13) neglects the effects of strain rates and lateral flow. We shall refer to it as the ablation-only approximation. Figure 6.7B shows the error introduced when using equation (6.13), expressed as a percentage of the full 2-D trajectory modeling solution. The spallogenic component is only sensitive to ice flow in the top ∼20 m; consequently, there is not much difference between the trajectory modeling and the ablation-only approximation (as both use identical vertical ice velocity at the surface). The muogenic nuclide production deviates more strongly from the ablation-only case, as it also occurs at greater depths. Near the overdeepening at $x = 40$ km, the fast muon production differs by up to 50%. Because ice parcels come from upstream at greater altitude (and therefore higher production rates) the ablation-only approximation tends to underestimate nuclide production. Our 2010/2011 ^{14}C sampling site at $x = 14.05$ km (indicated by the vertical grey line) lies at a position where the deviation from the ablation-only case is near a minimum; when using equation (6.13) to interpret data, an error of ∼5% is introduced.

Several previous studies have used ^{14}C concentrations to estimate ablation rates in glaciers and BIAs (e.g., Lal et al., 1990; Van Roijen et al., 1995; Van der Borg et al., 2001). Our modeling results show that neglecting the flow history of the ice parcels can result in an error of up to 25% where topography is rugged (black dashed line in Figure 6.7B); the proximity of many Antarctic BIAs to mountain ranges and nunataks (Bintanja, 1999; Sinisalo and Moore, 2010) suggests that caution is warranted when estimating ablation rates from radiocarbon data.

Figure 6.7C shows the depth profiles of the different production mechanisms at the sampling site. During the 2010/2011 field campaign, a depth profile of large-volume (∼ 1000 kg each) ice samples was collected for ^{14}C analyses. Sample average depths ranged between 2.25 and 19.5 m, and should allow for both spallogenic and muogenic components of ^{14}C production to be characterized.

6.4.2 Solar modulation of the cosmic ray flux

We will now examine how solar modulation of the cosmic ray flux affects the ^{14}C content of ablating ice parcels. Variations in solar activity mostly influence low energy cosmic rays, while high energy rays are less affected (Lifton et al., 2005, and references therein). At low latitudes geomagnetic shielding prevents these low energy cosmic rays from reaching the atmosphere in the first place, making cosmogenic nuclide production there insensitive to solar activity. At high latitudes, however, the cosmic ray energy spectrum is softer, as essentially all energies are admitted.

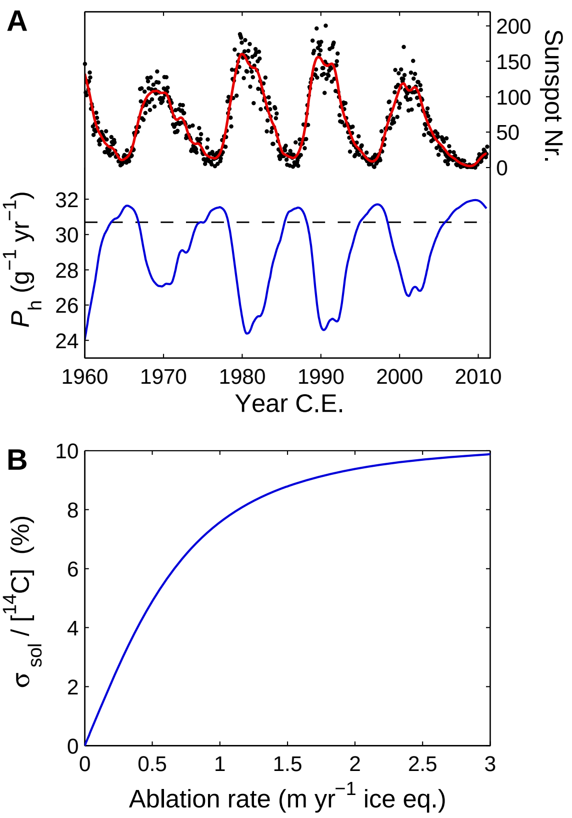

Figure 6.8: (A) Right axis: observational record of monthly averaged sunspot numbers (ftp://ftp.ngdc.noaa.gov/STP/SOLAR_DATA/SUN SPOT_NUMBERS/INTERNATIONAL/monthly/, black dots), together with a 1 year running average (red line). Left axis: Spallogenic surface production rate estimate using the Lifton et al. (2005) scaling model at high latitude ($R_C \leq 1.9$) and sea level. The dashed line shows the long term average production rate as given in Table 6.1, corresponding to a measure of solar modulation $S = 0.950$ in the Lifton et al. (2005) scaling model. Neutron monitor data showing how the actual changes in cosmic-ray flux with time are shown in Figure 1 of Lifton et al. (2005), for both high and low latitude sites. (B) Relative uncertainty in spallogenic production as a function of the ablation rate a given by equation (6.16), expressed as a percentage.

Therefore nuclide production at high latitude ice sheets is sensitive to variations in solar activity.

The scaling model by Lifton et al. (2005) incorporates the effect of solar modulation by relating cosmic ray intensity to sunspot numbers, of which there is an observational record dating back to the 17th century (Hoyt and Schatten, 1998). Following Lifton et al. (2005), the tree-ring ^{14}C-based sunspot number reconstruction by Solanki et al. (2004) is used prior to the existing observational record. Muons are produced by incoming primary cosmic ray particles of higher median energies than those that produce secondary neutrons, and consequently only spallogenic production rates are sensitive to solar modulation in the scaling model.

Figure 6.8A shows the changes in the spallogenic ^{14}C surface production rate for the last 4 solar cycles at sea level and high latitude ($R_C \leq 1.9$). Production is lowest during periods of high solar activity. The dashed line represents the long term average production rate as given in Table 6.1.

How much these variations influence the ^{14}C content of an ice parcel depends on the ablation rate. For simplicity we assume a sinusoidal solar modulation of the spallogenic surface production $P_h^0 = k + \mathbf{Re}\left\{\kappa \exp(2i\pi t/\tau + i\theta)\right\}$, where $\tau = 11$ yr is the period of the sunspot (or Schwabe) cycle, θ is the phase of the cycle, $k = 29$ and $\kappa = 3$ are estimated from Figure 6.8A, and $\mathbf{Re}\{..\}$ denotes the real part of the expression. Ignoring inheritance and radioactive decay, the spallogenic ^{14}C in an ice parcel that ablates at the glacier surface at $t = 0$ is given by

$$[^{14}\mathrm{C}]_h(z) = \mathbf{Re}\left\{\int_{-\infty}^{-z/a}\left[k + \kappa \exp\left(\frac{2i\pi t}{\tau} + i\theta\right)\right]\exp\left(\frac{\rho a t}{\Lambda_h}\right)dt\right\} \tag{6.14}$$

Note that this equation also holds for the accumulation zone, in which case the integral goes from 0 to z/a, and a is replaced by $-a$ in the integrand. The solution at the surface is given by

$$[^{14}\mathrm{C}]_h(0) = \frac{k}{\frac{\rho a}{\Lambda_h}} + \frac{\kappa \sin(\theta + \varphi)}{\sqrt{\left(\frac{2\pi}{\tau}\right)^2 + \left(\frac{\rho a}{\Lambda_h}\right)^2}} \tag{6.15}$$

with $\varphi = \arcsin\left(\frac{\rho a}{\Lambda_h}\Big/\sqrt{\left(\frac{2\pi}{\tau}\right)^2 + \left(\frac{\rho a}{\Lambda_h}\right)^2}\right)$. The first term in equation (6.15) gives the time-invariant long-term average ^{14}C concentration; the second term gives the time (i.e. θ) dependent part caused by solar modulation. When solar variation is neglected in the analysis of ^{14}C data, the phase θ of the sunspot cycle is not fixed, and an uncertainty σ_{sol} is introduced:

$$\frac{\sigma_{\mathrm{sol}}}{[^{14}\mathrm{C}]_h} \approx \frac{\kappa}{k}\frac{\frac{\rho a}{\Lambda_h}}{\sqrt{\left(\frac{2\pi}{\tau}\right)^2 + \left(\frac{\rho a}{\Lambda_h}\right)^2}} \tag{6.16}$$

How the uncertainty σ_{sol} changes as a function of a is plotted in Figure 6.8B, expressed as a percentage. For Taylor Glacier (a =0.1-0.3 m yr^{-1}) the influence of solar modulation is relatively small. The reason is that ice parcels are exposed to several sunspot cycles on their way to the surface, causing the variations to average out. Solar modulation should be considered at Greenlandic high ablation sites such as Pakitsoq, where annual rates of $\sim$ 2.5 m yr^{-1} can be found (Reeh et al., 2002; Petrenko et al., 2009). At such sites the ice parcels are transported through the exposed top $\sim$ 5m in a time much shorter than the duration of a sunspot cycle, causing a 10 % variation with time. At these sites the sampling date should be taken into account when analyzing measued radiocarbon activities.

Solar modulation mostly influences the spallogenic production. Cosmogenic ^{14}C production at depths $z > 5$ m is dominated by muogenic production, and therefore less sensitive to solar activity (and thereby sampling date). Consequently, for ablation sites solar modulation can be neglected at $z > 5$ m. For accumulation sites the solar variations in nuclide production are transported into the ice, and should always be considered when accumulation is high.

6.4.3 Sensitivity of results to the main sources of uncertainty

Although solar modulation does not play a major role at Taylor Glacier, the modeled ^{14}C concentrations are subject to a number of other uncertainties. We present a sensitivity study comparing the magnitude of potential errors, the results of which are shown in Figure 6.9A-C. The colors in the figure correspond to different sampling depths in the ice. We look at both the surface concentrations, as well as concentrations at depths which are more suited for gas measurements (i.e. ice not subjected to gas exchange through near-surface cracks, commonly observed at BIAs).

We analyze the three main sources of uncertainty: (1) the choice of strain rate parameterization, (2) the ablation rate estimate based on measurements from a limited number of years, and (3) uncertainty in the cosmogenic production rates as found in literature. For each plot the darker central lines give our modeled best estimate total cosmogenic ^{14}C concentrations, whereas the shaded areas gives the uncertainty estimate. Details are given in the figure caption. In our discussion of the sensitivity study, we shall focus on the part of the glacier that exposes the oldest ice, and is therefore most interesting for paleo-climate reconstructions (i.e. $x < 35$ km (Aciego et al., 2007)).

The uncertainty contribution of the strain rate parameterization (Figure 6.9A) shows little depth dependence between the surface and $z = 20$ m. This is because the strain rates mostly influence the flow at depth, whereas the near-surface trajectories are fixed by the ablation rate and are only minorly influenced by strain rate uncertainties. The fact that the best estimate solution does not lie in the middle of the uncertainty band, but rather at the lower end, results from the exponential depth dependence of the nuclide production.

As long as the ablation uncertainty σ_a is small relative to the ablation rate a, the resulting uncertainty in ^{14}C production is expected to be proportional to the amount of production itself as per equation (6.13). This is what is indeed observed for $x < 35$ km where a is large (Figure 6.9B). As σ_a approaches a (i.e. for $x > 35$ km), the uncertainty in ^{14}C increases rapidly with increasing x.

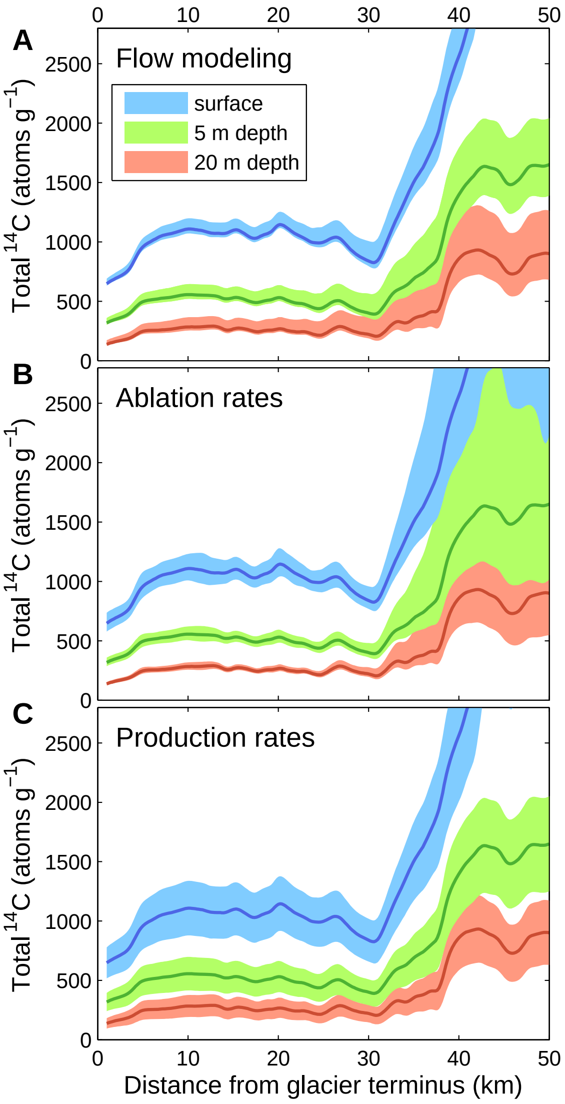

Figure 6.9: (A) Uncertainty in the strain rate parameterization. For each point along x, and at the indicated depths, we evaluated three potential back-trajectories; our best estimate trajectory and two extreme 'envelope' scenarios as shown in Figure 6.5C. The central dark line shows modeled ^{14}C concentrations using our best estimate strain parameterization, the shaded area is bordered by the two extreme envelope scenarios. (B) Uncertainty in the ablation rate estimate as shown in Figure 6.5A. The central dark line shows modeled ^{14}C concentrations using our best estimate ablation rates, the shaded area is bordered by model runs where an ablation rate of $a \pm 1\sigma_a$ is used. (C) Uncertainties due to the cosmogenic production rates found in literature, as summarized in Table 6.1. The central dark line shows modeled ^{14}C concentrations using he best estimate production rates, the shaded area is bordered by model runs where a production rate of $P_i^0 \pm 1\sigma_i$ is used.

For all depths considered, the surface production rates as found in literature are the largest source of uncertainty. In particular, the fast muon production rate has a large uncertainty of about 60 % (Table 6.1). As shown in Fig 6.7C, the spallation component is insignificant below 5 m depth. This implies that the deeper samples (5-20 m) collected at Taylor Glacier for ^{14}C analyses during the 2010/2011 season would allow us to improve substantially on the current estimates for muogenic ^{14}C production from ^{16}O. Such improved production estimates would be important for not just studies of ^{14}C in ice, but would also be transferable to other materials, such as e.g. quartz and carbonate rock used in exposure dating (Gosse and Phillips, 2001).

6.5 Summary and Conclusions

In this work we investigated in situ cosmogenic ^{14}C production at ablation sites. First, we implemented a thermal neutron flux model for the air-ice interface, and found that thermal neutron capture by nitrogen in air bubbles produces only negligible amounts of ^{14}C.

Second, by modeling the trajectories of ice parcels at the center line of Taylor Glacier we calculated a best-estimate ^{14}C concentration of ablating ice. We found that the commonly used ablation-only approximation by Lal et al. (1990) tends to underestimate production as the ice flows down from parts of the glacier that have higher production rates. For sections of the glacier where the basal topography is rugged, the ablation-only approximation deviates from the full model solution by up to 25%. This has important consequences when ^{14}C activity measurements are used to estimate ablation rates.

Third, we demonstrated that the influence of solar modulation is strongly dependent on ablation rate. At low ablation sites, such as Taylor Glacier, the effect is small due to temporal averaging over several sunspot cycles. At high ablation sites, such as Pakitsoq, Greenland, solar modulation introduces an uncertainty of 10 % in the spallogenic component. In these cases the sampling date needs to be considered when interpreting data.

We introduced two methods to parameterize vertical strain rates with depth. The first method is based on conservation of mass in the ice column; the second method is based on measured surface strain rates. The second method proved to be less reliable, because (1) estimated surface strain rates from InSAR and GPS measurements show a poor correlation, (2) flow lines do not follow bedrock, and (3) mass is not conserved.

We presented a sensitivity study where we compare potential errors introduced by uncertainties in the strain rate parameterization, the ablation rates, and the published cosmogenic production rates. We found that the cosmogenic production rates are the largest source of uncertainty. In the 2010/2011 Austral summer, Taylor

Glacier ice was sampled with the aim of constraining the cosmogenic production rates more strongly, as well as determining the ratio of $^{14}CH_4$ to ^{14}CO produced in situ in the ice. By sampling at depths > 5 m the muogenic components can be isolated, which have the largest uncertainty in their production rates. The modeling results presented here will aid us with the interpretation of ^{14}C measurements on these samples. Most importantly, this study will serve as a framework for correcting future $^{14}CH_4$ measurements for the effect of in situ production with the purpose of reconstructing the true atmospheric signal. This would allow to answer pressing questions about past changes in the global methane budget, such as whether marine clathrates can release large amounts of methane to the atmosphere.

6.6 Acknowledgments

We would like to thank Andy Bliss for his help on calculating ablation rates, Daniel Baggenstos for measuring ablation stakes in the field and providing locations of the 2009-2010 sampling transect, and Brent Goehring for fruitful discussions. C. Buizert would like to thank Thomas Blunier (Center for Ice and Climate, University of Copenhagen), Bruce Vaughn and Jim White (INSTAAR, University of Colorado) for their support and hospitality; V. V. Petrenko has been supported by the NOAA Postdoctoral Fellowship in Climate and Global Change, NSF grants 0632222 and 0806387 (White) and NSF grant 0839031 (Severinghaus); this work was partially supported by NSF grant OPP-0125579 to K. M. Cuffey and NSF grant 0838936 to E. J. Brook; N. A. Lifton is grateful for support by the CRONUS-Earth project (NSF EAR0345150) and the University of Arizona Accelerator Mass Spectrometry Laboratory.

6.7 References

Aciego, S. M., Cuffey, K. M., Kavanaugh, J. L., Morse, D. L., and Severinghaus, J. P. (2007). Pleistocene ice and paleo-strain rates at taylor glacier, antarctica. *Quaternary Res.*, 68:303–313.

Andree, M., Moor, E., Beer, J., Oeschger, H., Stauffer, B., Bonani, G., Hofmann, H., Morenzoni, E., Nessi, M., Suter, M., and Wolfli, W. (1984). C-14 dating of polar ice. *Nucl. Instrum. Meth. B* , 5(2):385–388.

Azuma, N., Nakawo, M., Higashi, A., and Nishio, F. (1985). Flow pattern near massif a in the yamato bare ice field estimated from the structures and the mechanical properties of a shallow ice core. *Memoirs of National Institute of Polar Research. Special issue*, 39:173–183.

Bintanja, R. (1999). On the glaciological, meteorological, and climatological significance of Antarctic blue ice areas. *Rev. Geophys.*, 37(3):337–359.

Bliss, A., Cuffey, K., and Kavanaugh, J. (2011). Sublimation and surface energy budget of taylor glacier, antarctica. *J. Glaciol.*, in press.

Cuffey, K. and Paterson, W. S. B. (2010). *The Physics of Glaciers, Fourth edition.* Elsevier.

De Jong, A., Alderliesten, C., Van der Borg, K., Van der Veen, C., and Van De Wal, R. (2004). Radiocarbon analysis of the EPICA Dome C ice core: no in situ C-14 from the firn observed. *Nucl. Instrum. Meth. B*, 223:516–520.

Desilets, D. and Zreda, M. (2003). Spatial and temporal distribution of secondary cosmic-ray nucleon intensities and applications to in situ cosmogenic dating. *Earth Planet. Sc. Lett.*, 206(1-2):21–42.

Desilets, D., Zreda, M., and Prabu, T. (2006). Extended scaling factors for in situ cosmogenic nuclides: New measurements at low latitude. *Earth Planet. Sc. Lett.*, 246(3-4):265–276.

Dunai, T. J. (2000). Scaling factors for production rates of in situ produced cosmogenic nuclides: a critical reevaluation. *Earth Planet. Sc. Lett.*, 176:157–169.

Dunbar, N. W., McIntosh, W. C., and Esser, R. P. (2008). Physical setting and tephrochronology of the summit caldera ice record at Mount Moulton, West Antarctica. *Geol. Soc. Am. Bull.*, 120(7-8):796–812.

Fireman, E. and Norris, T. (1982). Ages and composition of gas trapped in Allan-Hills and Byrd core ice. *Earth Planet. Sc. Lett.*, 60(3):339–350.

Gosse, J. C. and Phillips, F. M. (2001). Terrestrial in situ cosmogenic nuclides: theory and application. *Quaternary Sci. Rev.*, 20:1475–1560.

Grinsted, A., Moore, J., Spikes, V. B., and Sinisalo, A. (2003). Dating antarctic blue ice areas using a novel ice flow model. *Geophys. Res. Lett.*, 30(19):5.

Heisinger, B., Lal, D., Jull, A. J. T., Kubik, P., Ivy-Ochs, S., Knie, K., and Nolte, E. (2002a). Production of selected cosmogenic radionuclides by muons: 2. capture of negative muons. *Earth Planet. Sc. Lett.*, 200(3-4):357–369.

Heisinger, B., Lal, D., Jull, A. J. T., Kubik, P., Ivy-Ochs, S., Neumaier, S., Knie, K., Lazarev, V., and Nolte, E. (2002b). Production of selected cosmogenic radionuclides by muons 1. fast muons. *Earth Planet. Sc. Lett.*, 200(3-4):345–355.

Hoyt, D. V. and Schatten, K. H. (1998). Group sunspot numbers: A new solar activity reconstruction. *Sol. Phys.*, 181:491–491.

Jenk, T. M., Szidat, S., Schwikowski, M., Gaeggeler, H. W., Wacker, L., Synal, H.-A., and Saurer, M. (2007). Microgram level radiocarbon (C-14) determination on carbonaceous particles in ice. *Nucl. Instrum. Meth. B*, 259(1):518–525.

Jull, T. A. J., Lal, D., Donahue, D. J., Mayewski, P., Lorius, C., Raynaud, D., and Petit, J. R. (1994). Measurements of cosmic-ray-produced ^{14}c in firn and ice from antarctica. *Nucl. Instrum. Meth. B*, 92:326–330.

Kavanaugh, J. L. and Cuffey, K. M. (2009). Dynamics and mass balance of taylor glacier, antarctica: 2. force balance and longitudinal coupling. *J. Geophys. Res.-Earth*, 114:11.

Kavanaugh, J. L., Cuffey, K. M., Morse, D. L., Bliss, A. K., and Aciego, S. M. (2009a). Dynamics and mass balance of taylor glacier, antarctica: 3. state of mass balance. *J. Geophys. Res.-Earth*, 114:7.

Kavanaugh, J. L., Cuffey, K. M., Morse, D. L., Conway, H., and Rignot, E. (2009b). Dynamics and mass balance of taylor glacier, antarctica: 1. geometry and surface velocities. *J. Geophys. Res.-Earth*, 114:15.

Lal, D. (1991). Cosmic-ray labeling of erosion surfaces - in situ nuclide production-rates and erosion models. *Earth Planet. Sc. Lett.*, 104(2-4):424–439.

Lal, D., Jull, A., Donahue, D., Burr, G., Deck, B., Jouzel, J., and Steig, E. (2001). Record of cosmogenic in situ produced C-14 in Vostok and Taylor Dome ice samples: Implications for strong role of wind ventilation processes. *J. Geophys. Res.-Atm.*, 106(D23):31933–31941.

Lal, D., Jull, A. J. T., Burr, G. S., and Donahue, D. J. (2000). On the characteristics of cosmogenic in situ c-14 in some gisp2 holocene and late glacial ice samples. *Nucl. Instrum. Meth. B*, 172:623–631.

Lal, D., Jull, A. J. T., Donahue, D. J., Burtner, D., and Nishiizumi, K. (1990). Polar ice ablation rates measured using in situ cosmogenic c-14. *Nature*, 346(6282):350–352.

Lal, D., Nishiizumi, K., and Arnold, J. R. (1987). In situ cosmogenic h-3, c-14 and be-10 for determining the net accumulation and ablation rates of ice sheets. *J. Geophys. Res.-Solid*, 92(B6):4947–4952.

Lifton, N. A., Bieber, J. W., Clem, J. M., Duldig, M. L., Evenson, P., Humble, J. E., and Pyle, R. (2005). Addressing solar modulation and long-term uncertainties in scaling secondary cosmic rays for in situ cosmogenic nuclide applications. *Earth Planet. Sc. Lett.*, 239:140–161.

Liu, B., Phillips, F. M., Fabryka-Martin, J. T., Fowler, M. M., and Stone, W. D. (1994). Cosmogenic cl-36 accumulation in unstable landforms 1. effects of the thermal neutron distribution. *Water Resources Res.*, 30(11):3115–3125.

Moore, J. C., Nishio, F., Fujita, S., Narita, H., Pasteur, E., Grinsted, A., Sinisalo, A., and Maeno, N. (2006). Interpreting ancient ice in a shallow ice core from the south yamato (antarctica) blue ice area using flow modeling and compositional matching to deep ice cores. *J. Geophys. Res.-Atm.*, 111:17.

Mughabghab, S., Divadeenam, M., and Holden, N. E. (1992). *Neutron Resonance Parameters and Thermal Cross Sections*. Academic Press, New York.

Nesterenok, A. V. and Naidenov, V. O. (2009). Radiocarbon in the antarctic ice: The formation of the cosmic ray muon component at large depths. *Geomagn. Aeronomy*, 50:134–140.

Petrenko, V., Severinghaus, J., Brook, E., Reeh, N., and Schaefer, H. (2006). Gas records from the West Greenland ice margin covering the Last Glacial Termination: a horizontal ice core. *Quaternary Sci. Rev.*, 25(9-10):865–875.

Petrenko, V. V., Severinghaus, J. P., Brook, E. J., Muhle, J., Headly, M., Harth, C. M., Schaefer, H., Reeh, N., Weiss, R. F., Lowe, D., and Smith, A. M. (2008). A novel method for obtaining very large ancient air samples from ablating glacial ice for analyses of methane radiocarbon. *J. Glaciol.*, 54(185):233–244.

Petrenko, V. V., Smith, A. M., Brook, E. J., Lowe, D., Riedel, K., Brailsford, G., Hua, Q., Schaefer, H., Reeh, N., Weiss, R. F., Etheridge, D., and Severinghaus, J. P. (2009). (ch_4)-c-14 measurements in greenland ice: Investigating last glacial termination ch_4 sources. *Science*, 324:506–508.

Phillips, F. M., Stone, W. D., and Fabryka-Martin, J. T. (2001). An improved approach to calculating low-energy cosmic-ray neutron fluxes near the land/atmosphere interface. *Chem. Geol.*, 175(3-4):689–701.

Reeh, N., Oerter, H., and Thomsen, H. (2002). Comparison between Greenland ice-margin and ice-core oxygen-18 records. *Ann. Glaciol.*, 35:136–144.

Schaefer, H., Petrenko, V. V., Brook, E. J., Severinghaus, J. P., Reeh, N., Melton, J. R., and Mitchell, L. (2009). Ice stratigraphy at the Pakitsoq ice margin, West Greenland, derived from gas records. *J. Glaciol.*, 55(191):411–421.

Sears, V. F. (1992). Neutron scattering lengths and cross sections. *Neutron news*, 3(3):26–37.

Sinisalo, A. and Moore, J. C. (2010). Antarctic blue ice areas - towards extracting palaeoclimate information. *Antarct. Sci.*, 22(2):99–115.

Smith, A. M., Levchenko, V. A., Etheridge, D. M., Lowe, D. C., Hua, Q., Trudinger, C. M., Zoppi, U., and Elcheikh, A. (2000). In search of in-situ radiocarbon in law dome ice and firn. *Nucl. Instrum. Meth. B*, 172:610–622.

Solanki, S., Usoskin, I., Kromer, B., Schüssler, M., and Beer, J. (2004). Unusual activity of the Sun during recent decades compared to the previous 11,000 years. *Nature*, 431(7012):1084–1087.

Steig, E. J., Morse, D. L., Waddington, E. D., Stuiver, M., Grootes, P. M., Mayewski, P. A., Twickler, M. S., and Whitlow, S. I. (2000). Wisconsinan and holocene climate history from an ice core at taylor dome, western ross embayment, antarctica. *Geogr. Ann. A*, 82A:213–235.

Stone, J. O. (2000). Air pressure and cosmogenic isotope production. *Journal of Geophysical Research-Solid Earth*, 105(B10):23753–23759.

Van de Wal, R., Van Roijen, J., Raynaud, D., Van der Borg, K., De Jong, A., Oerlemans, J., Lipenkov, V., and Huybrechts, P. (1994). From C-14/C-12 measurements towards radiocarbon dating of ice. *Tellus B*, 46(2):94–102.

Van de Wal, R. S. W., Meijer, H. A. J., De Rooij, M., and Van der Veen, C. (2007). Radiocarbon analyses along the EDML ice core in Antarctica. *Tellus B*, 59(1):157–165.

Van der Borg, K., Van der Kemp, W., Alderliesten, C., De Jong, A., and Lamers, R. (2001). In-situ radiocarbon production by neutrons and muons in an antarctic blue ice field at Scharffenbergbotnen: A status report. *Radiocarbon*, 43(2B, Part 2):751–757.

Van Der Kemp, W., Alderliesten, C., Van Der Borg, K., De Jong, A., Lamers, R., Oerlemans, J., Thomassen, M., and Van De Wal, R. (2002). In situ produced C-14 by cosmic ray muons in ablating Antarctic ice. *Tellus B*, 54(2):186–192.

Van Roijen, J., Van der Borg, K., De Jong, A., and Oerlemans, J. (1995). A correction for in-situ C-14 in Antarctic ice with (CO)-C-14. *Radiocarbon*, 37(2):165–169.

Wagemans, J., Wagemans, C., Goeminne, G., and Geltenbort, P. (2000). Experimental determination of the $^{14}n(n,p)^{14}c$ reaction cross section for thermal neutrons. *Phys. Rev. C*, 61(6):064601.

List of publications

Koppens, F. H. L., Buizert, C., Tielrooij, K. J., Vink, I. T., Nowack, K. C., Meunier, T., Kouwenhoven, L. P., and Vandersypen, L. M. K. (2006). Driven coherent oscillations of a single electron spin in a quantum dot. *Nature*, 442(7104):766–771.

Koppens, F. H. L., Buizert, C., Vink, I. T., Nowack, K. C., Meunier, T., Kouwenhoven, L. P., and Vandersypen, L. M. K. (2007). Detection of single electron spin resonance in a double quantum dot. *J. Appl. Phys.*, 101(8).

Buizert, C., Oiwa, A., Shibata, K., Hirakawa, K., and Tarucha, S. (2007). Kondo universal scaling for a quantum dot coupled to superconducting leads. *Phys. Rev. Lett.*, 99(13).

Shibata, K., Buizert, C., Oiwa, A., Hirakawa, K., and Tarucha, S. (2007). Lateral electron tunneling through single self-assembled InAs quantum dots coupled to superconducting nanogap electrodes. *Appl. Phys. Lett.*, 91(11).

Buizert, C., Koppens, F. H. L., Pioro-Ladriere, M., Tranitz, H.-P., Vink, I. T., Tarucha, S., Wegscheider, W., and Vandersypen, L. M. K. (2008). In Situ Reduction of Charge Noise in GaAs/$\mathrm{Al}_x\mathrm{Ga}_{1-x}$As Schottky-Gated Devices. *Phys. Rev. Lett.*, 101(22).

Buizert, C., Martinerie, P., Petrenko, V. V., Severinghaus, J. P., Trudinger, C. M., Witrant, E., Rosen, J. L., Orsi, A. J., Rubino, M., Etheridge, D. M., Steele, L. P., Hogan, C., Laube, J. C., Sturges, W. T., Levchenko, V. A., Smith, A. M., Levin, I., Conway, T. J., Dlugokencky, E. J., Lang, P. M., Kawamura, K., Jenk, T. M., White, J. W. C., Sowers, T., Schwander, J., and Blunier, T. (2011). Gas transport in firn: multiple-tracer characterisation and model intercomparison for neem, northern greenland. *Atmos. Chem. Phys. Discuss.*, 11:15975–16021.

Sapart, C. J., van der Veen, C., Vigano, I., Brass, M., van de Wal, R. S. W., Bock, M., Fischer, H., Sowers, T., Buizert, C., Sperlich, P., Blunier, T., Behrens, M., Schmitt, J., Seth, B., and Röckmann, T. (2011). Simultaneous stable isotope analysis of methane and nitrous oxide on ice core samples. *Atmos. Meas. Tech. Discuss.*, 4(4):4473–4503.

Buizert, C. Studies of firn air. In Elias, S. A., editor, *submitted as invited chapter for: Encyclopedia of Quaternary Sciences, 2nd Edition*. Elsevier.

Buizert, C., Petrenko, V. V., Kavanaugh, J. L., Cuffey, K. M., Lifton, N. A. Brook,

E. J., and Severinghaus, J. P. In situ cosmogenic radiocarbon production and 2-d ice flow line modeling for an antarctic blue ice area. *submitted to J. Geophys. Res.-Earth.*

Hietanen, S., Jäntti, H., Buizert, C., Jürgens, K., Labrenz, M., Voss, M., , and Kuparinena, J. Hypoxia and nitrogen processing in the baltic sea water column. *submitted to Limnol. Oceanogr.*

Special thanks

Although this thesis should reflect what I did during my PhD, it does not come close to capturing the full experience of my time in Copenhagen. The thesis is arguably a little dull and hard to get through; the last three years have been rather the opposite: great fun, and gone by way too fast. While I take full responsibility for the state of the thesis, I have to credit others for all the good times.

The CIC (Center for Ice and Climate / Cake, Ice and Coffee) has been a wonderful community to be a part of. It has not only given me many great colleagues, but also good friends. First of all I want to thank my advisor (doctorvater) Thomas for his help and support throughout these last three years; I knew you were always there for me. Various gaslab members, myself included, failed to ever fully adapt to the Swiss time zone, though. Also thanks to Dorthe for having done so much to make the CIC the wonderful place that it is.

There are many other people at the CIC who deserve a special word of thanks. In particular Peter, who I have known as a roommate, mass-spec mechanic, cheese fondue accomplice, family guy and friend (not necessarily in that order). Although labwork was often frustrating, we mostly kept a good spirit and laughed a lot. I am leaving exactly at the moment you got the setup running (knock on wood); you deserve those data more than anyone else. I look forward to spending much more time with you and Colleen in the future. If I ever find out you'll have a second wedding in New Zealand, I hereby invite myself. High up on any list should be Sigfus and Palla, who have treated me like family during the last three years. Five minutes after meeting them for the very first time I was invited to their summer house, where the beers and grilled Icelandic lamb were as abundant as their hospitality. Or in the words of Sigfus: “You are so welcome, you cannot believe it”. Thank you so very much. Ivana, we all know that behind your lovely sarcasm hides a very sweet person, and most probably you will be both grumpy and charmed when reading this. Once you left to Berkeley I turned soft, like Paul McCartney without Lennon. I hope to meet His Imperial Highness one day. Christopher, it was a ton of fun hanging out with you in Greenland, Greece and of course Copenhagen. I hope you'll get your Master's degree soon (it would be about time). Myriam, ever since I heard you playing the harp in Utrecht I knew you were a special person. I am sure an angel like you can find it in her heart to forgive us our stupid jokes (I still think the CPR/herring joke is hilarious). Theo, it's been a pleasure getting to know you, Tanina and little Naja. She is a lucky girl with such awesome parents. Jesper, I have always loved your Nordic sense of humor. I should have been homeless much earlier on in my PhD; I got to know you (and Amager) much better in this last week sleeping on your couch. Thanks for offering your place to crash. Please tell Darling that I will miss him. Trev, I would listen to 70's rock LPs, ride the metro for hours, and ruin Mauro's dinner parties with you any day of the week. Come to think of it, for a few months that's pretty much what we did any day of the week. Mads, I know she already said this, but you were often the most hilarious person in the building. I still haven't found the secret bacon message in your paper. Anne, thanks for all the good times on the ice and in Boulder. All the best with Kasper and the baby. Steff, you are a bad ass. Ever since you spent one hour showing holiday pictures and explaining biker's slang at an official CIC meeting you are my hero. You also impressed me in the field by filing less than 100 μm off a drillhead, after which we went from empty to full barrels. Thanks also to Vasileos, who is just as stubborn as I am. I can't remember what we were arguing about the other day, but I was right! I loved our stay in Litohoro. I left you a graduation present; don't open it until you have defended you thesis. BF Italian, I cannot believe you have been crushing my balls for three years now. Before you showed me what Real Culture is like, I was a barbarian using garlic and onion in the same dish. Sorry for making you sleep in the closet. Corentin: your Karthaus year was definitely the most fun, and I blame you. The glass pyramid was not our brightest moment. Thanks for making me look punctual, by arriving even later at GasLab meetings than I did. I hope you find what you are looking for. Ernesto, wat heerlijk om toch nog met iemand Nederlands te kunnen praten. Vooral iemand die zo veel van taal (en backgammon!) houdt. Heel veel succes in Gent. Michelle, I don't think you realize how infinitely funny you can be. Hope to see you in the States next year. Thanks to Lone for her happy smiles in the morning; to Sebastian, my awesome officemate and the only other person in town who cares about firn; to Hans Christian for looking so mantastic in every possible situation; to Mai, with whom I shared the stress of thesis writing in the last weeks; to Paul for his Aussie slang lessons; David for 'aving the same ridiculous accent and for letting me run naked through his yard; Sune for his great jokes and skill in fighting the bureaucrats; and to all the other lovely people at the CIC that I did not mention here, even though they deserve it just as much.

During my stay in Copenhagen I have been blessed with the sweetest roommates one can wish for. First there was Arantxa, who technically never lived with us but made herself very much at home all the same. Then there were the many incarnations of the Gypsy family; some of the best roommates in the history of house sharing. Even though our housing was never cheap, sound-proof or well furnished, I wouldn't want to live anywhere else. The cast, in order of appearance: Jay D.B. Armas, the only person I know who can run a bar, edit a magazine, organize a lecture series, do a PhD, have three (presumably open-minded) girlfriends, write a book and sail across the Atlantic all at the same time. Never a dull moment. Lars, a mixologist, entrepreneur, and blissfully irresponsible spirit; always up for jiggery-pokery of any kind. You still owe me money! Christina, architect and furniture designer. You were always such a pleasure to have around, we never really recovered after you left. I hope you can get into the PhD. Lucas, musician by day, barman by night. It was my pleasure. All the best with your music, and I told you I wouldn't crash your moped! Carmen, our pig-nose-bacteria veterinarian and illicit film distributor. I am your biggest fan and enjoyed all the time we spent together (which was a lot towards the end!) Fillipe is the dumbest idiot in the world for letting you go. And last but not least, My: Train driver by day and musician by night, sweet on the outside, but fond of arm wrestling on the inside. I will miss you all.

During my PhD I had the pleasure of spending 5 months in Boulder, Colorado at the Institute of Arctic and Alpine Research. Thanks to Bruce and Jim for their support and help. Gentlemen, I had a great time at your lab. Vas, thanks for the cross-country skiing lessons, the many great parties you threw and of course for inviting me to join the fieldwork at Taylor Glacier. I am happy to know we'll have many more opportunities to work together in the near future. All the best in Rochester with Christie and the cats. Thanks also to Emily, the only person in Boulder who understands that bike rides are more fun without spandex and with a nice cold beer in the middle. Tyler, thanks for all the good times and the camping trip. Still the absolute highlight of my stay in Boulder is not scientific. Thank you Erica, for walking into our kitchen and into my life that summer evening. It makes me very happy to know that next year the Atlantic will shrink, and I can be with you every day.

The life of a scientist involves (too?) much travel, and it's not always easy to live far away from friends and family. I want to thank my parents and my three wonderful sisters, Dineke, Petra and Annemiek. Dineke, I am very excited to know I will be an uncle soon, and I wish you much strength in the coming months. I will be there in April to meet my little niece or nephew. I also want to thank all of my many good friends back in Holland. For all of you back home: I have not seen you as much as I would have liked to, but I will keep trying!

This all goes to show that, in a figurative sense, no thesis is written on an island. In a very literal sense, much of this thesis was written on an actual island (note to Danish readers: Sjælland is not really an island). I am very grateful to Maria Matos Nascimento for letting me stay for one month in her beautiful old house in Horta, Faial on the Azorean Archipelago. The Azorean abundance of isolation and insolation kept me both focused and, more importantly, tanned.

Appendices

A

Gas transport in firn – Supplement

**C. Buizert, P. Martinerie, V. V. Petrenko, J. P. Severinghaus,
C. M. Trudinger, E. Witrant, J. L. Rosen, A. J. Orsi, M. Rubino,
D. M. Etheridge, L. P. Steele, C. Hogan, J. C. Laube,
W. T. Sturges, V. A. Levchenko, A. M. Smith, I. Levin,
T. J. Conway, E. J. Dlugokencky, P. M. Lang, K. Kawamura,
T. M. Jenk, J. W. C. White, T. Sowers, J. Schwander and
T. Blunier**[1]

A.1 Introduction

This appendix is the supplement to Buizert et al. (2011), which has been included as Chapter 3 in this thesis. It aims to provide more background information on the methods, as well as present additional modeling results which were omitted in the main article to improve readability. Most results from the US borehole are presented here.

The structure of this document closely follows that of the main text. Sections marked with an asterisk (*) in the main article have a corresponding section here, where additional information can be found.

A.2 Methods

A.2.1 NEEM 2008 firn air campaign

The location of the North Greenland Eemian ice drilling project (NEEM) camp and the site of the 2008 firn air campaign are shown in Fig. A.1. For the sampling a 16 kW generator was placed at 80 m distance downwind. In order to minimise air contamination, vehicles were parked near the generator and within the last 80 m all equipment was transported by manhauling. Drilling was performed alternatively in both holes with the Danish electromechanical shallow drill. The hole

---

[1] This appendix has been published as the supplement to C.Buizert et al.: Gas transport in firn: multiple-tracer characterisation and model intercomparison for NEEM, Northern Greenland., Atmos. Chem. Phys. Discuss. 11:15975-6021 (2011).

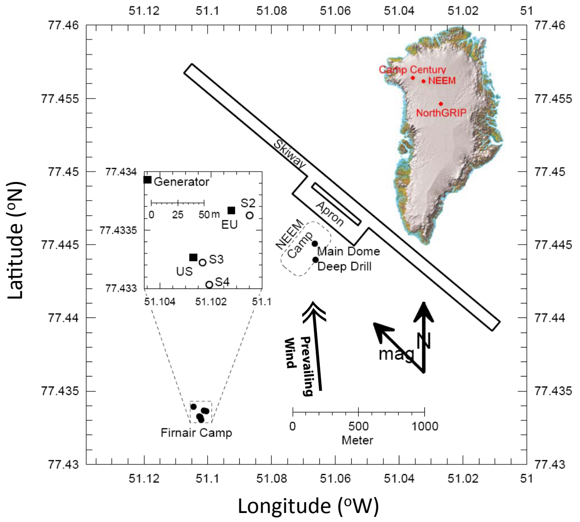

Figure A.1: Location of NEEM main structures and the site of the 2008 firn air campaign. The inset shows the position of the NEEM camp in Northern Greenland.

diameter is 103.6 mm. In order to have an undisturbed surface for the first sampling levels, the first 10 m were drilled with a hand auger producing the same diameter core and hole.

Table A.1 lists the sampling depths on both boreholes.

A.2.2 Physical characterisation of NEEM firn air site

For the density profile we use a fit to the NEEM main core density data averaged over 0.55m segments (Johnsen, personal communication, 2009). For the three stages of densification (Arnaud et al., 2000) we use a separate fit. Data fitting was done by eye, and care was taken that the second derivative is continuous over the transitions between the stages. Surface density was chosen as $\rho = 0.35$ g cm^{-3}. The density fit is given by

$$\begin{aligned} \rho &= a_1 + a_2 z + a_3 e^{a_4(16-z)} && \text{for } z < 16\text{m} \\ \rho &= a_5 + a_6 z + a_7 z^2 && \text{for } 16 \le z < 110\text{m} \\ \rho &= a_8 + a_9 \left(1 - e^{a_{10}(z-110)}\right) && \text{for } z \ge 110\text{m} \end{aligned} \tag{A.1}$$

The constants in Eq. (A.1) obtained in the fitting procedure can be found in Table A.2. The density data together with the fit are shown in Fig. 1 of the main document.

We use the closed porosity parameterisation of Goujon et al. (2003):

$$s_{\text{cl}} = 0.37 s \left(\frac{s}{s_{\text{co}}}\right)^{-7.6} \tag{A.2}$$

with s_{co} the close-off porosity consistent with the mean close-off density relation by Martinerie et al. (1994). Changing s_{co} results in changing the complete close-off depth ($s_{\text{op}} = 0$). Field data indicate the last successful air pumping depth in firn and a depth at which no air could be extracted. The depth at which open firn porosity becomes zero should be located in this interval. Using the mean close-off density of Martinerie et al. (1994) in Eq. (A.2) generally gives a complete close-off

Table A.1: *Firn air sampling depths in meters for the EU (S2) and US (S3) boreholes.*

Level	EU depth (m)	US depth (m)
0	0.00	0.00
1	2.50	2.85
2	4.90	5.23
3	7.55	9.83
4	10.10	19.30
5	14.80	34.70
6	19.75	49.70
7	27.54	57.47
8	34.72	59.90
9	42.42	62.00
10	50.00	64.03
11	54.90	65.50
12	57.40	66.90
13	59.90	68.30
14	61.95	69.80
15	63.85	71.40
16	65.75	72.85
17	68.05	73.80
18	70.05	75.60
19	72.00	-
20	74.08	-
21	75.90	-
22	77.75	-

depth ($s_{\mathrm{op}} = 0$) inconsistent with field data. The cause of this discrepancy is not clear; it could be due to e.g. firn heterogeneity, or biases and uncertainties in firn density measurements. In the case of NEEM, it leads to a complete close-off depth higher than the last measurement depth. A different mean close-off density value is used in order to obtain a complete close-off depth consistent with field data. At NEEM the last successful air pumping depth was $z = 77.75$ m; a decreased air flow (insufficient for sampling) was observed at $z = 79$ m depth. It was thus considered that air was isolated from the atmosphere at that depth, and used 78.8m as the zero open porosity level, equivalent to a mean close-off density $\rho_{\mathrm{co}} = 0.8312\ \mathrm{g\,cm^{-3}}$. Note that s_{op} is not necessarily zero below the deepest sampling depth (Aydin et al., 2010).
The accumulation rate estimate is based on the dated NEEM 2007 shallow S1 core (Dahl-Jensen, personal communication, 2010). The derived variations of the accumulation rate with time are shown in Fig. A.2. For all the tracers we run the models from 1800 to the sampling date 2008.54. As a best estimate of the accumulation rate we use the mean value over this period of $A = 0.216$ $\mathrm{m\,yr^{-1}}$ ice equivalent. The best estimate for the current day value is $A = 0.227\ \mathrm{m\,yr^{-1}}$, which is within the range of variability observed in the past.

A.2.3 Gas measurements

For SF_6, the IUP data (EU and US holes) have been rescaled by 0.9912 to place the data on the NOAA scale that we use in our atmospheric reconstructions (rescaling corresponds to a modern day offset of 0.06 ppt). The NOAA and UEA SF_6 data were provided on the NOAA scale. After correcting the IUP data no inter-laboratory offsets were observed on either borehole.

For the US hole NOAA CH_4 data have been used exclusively where available (13 depth levels). For a remaining 5 depths we have no NOAA measurements, and for these depths we have used IUP data after scaling them in the following way to place them on the NOAA scale:

Table A.2: Constants used in the density fitting Eq.(A.1).

Constant		
a_1	3.500000	$\times 10^{-1}$
a_2	1.359319	$\times 10^{-2}$
a_3	-1.569421	$\times 10^{-2}$
a_4	-4.300000	$\times 10^{-1}$
a_5	4.332293	$\times 10^{-1}$
a_6	7.976252	$\times 10^{-3}$
a_7	-3.536121	$\times 10^{-5}$
a_8	8.82746379	$\times 10^{-1}$
a_9	3.7853621	$\times 10^{-2}$
a_{10}	-5.198599	$\times 10^{-3}$

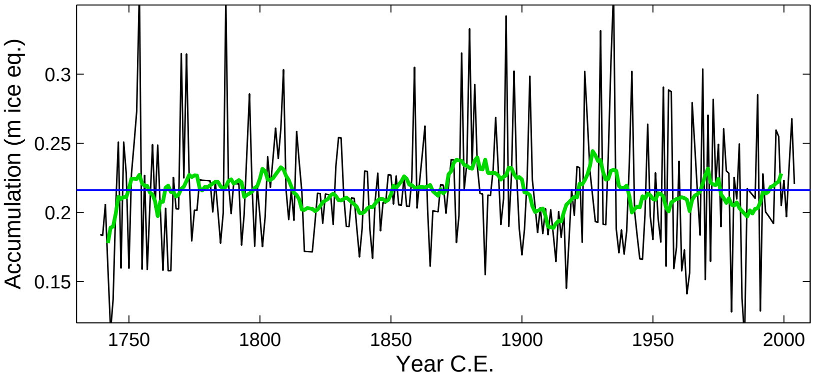

Figure A.2: Accumulation rate estimate from the NEEM 2007 S1 shallow core. The black line shows the yearly values, the green line gives a running 15 year average and the blue horizontal line shows the average value over the modeled period 1800-2008.

$$[\mathrm{CH_4}]_{\mathrm{NOAA}} = 0.9933[\mathrm{CH_4}]_{\mathrm{IUP}} + 10.12 \tag{A.3}$$

This equation was obtained by correlating NOAA and IUP data on the US hole for depths where we have data from both labs (13 depths, R^2 =0.9995). The NOAA and CSIRO data on the EU borehole agree well and show no systematic offset.

Table A.3 lists the radiocarbon measurements. CO_2 was extracted in May 2009 from 0.5 L glass sample flasks also used for CSIRO gas analysis, and in September 2009 the extracted CO_2 was graphitised at ANSTO. Measurements of $\Delta^{14}CO_2$ were performed on the ANTARES accelerator mass spectrometer (Fink et al., 2004). Since the sample collected at 70.05 m depth was lost during the initial graphitisation, it was extracted again in October 2009 from air samples collected in 3 L stainless steel containers also used for CSIRO gas analysis, and measured in January 2010. The samples collected at 68.05 and 72 m depth were extracted together with the lost 70 m sample, to check for any discrepancy between the first (May 2009) and the second (October 2009) extraction. The replicates agreed within the estimated uncertainty of the graphitisation at ANSTO. Since the samples were measured shortly after sampling, there is no need to correct for the decay that occurred within the flasks.

Table A.3: Overview of radiocarbon measurements on NEEM firn air, expressed in $\Delta^{14}C$ notation. The replicate dev. gives the deviation of the replicate measurement from the first one.

Depth (m)	Δ^{14}C (‰)	ANSTO error (‰)	Replicate dev. (‰)	[^{14}CO$_2$] ($\times10^{-12}$ ppm)	Flask type
0.00	44.9	6.3	-	485.5	Glass
14.80	40.1	6.8	-	490.3	Glass
34.72	55.9	6.2	-	491.3	Glass
50.00	64.9	6.8	-	491.4	Glass
59.90	74.5	6.9	-	491.0	Glass
61.95	76.3	6.8	-	489.9	Glass
65.75	156.0	7.5	5.9	503.1	Glass
68.05	276.1	7.6	3.4	531.4	Glass, Stainless
70.05	349.0	6.3	-	546.5	Stainless
72.00	309.3	8.2	0.5	519.6	Glass, Stainless
74.08	165.4	7.3	-	455.8	Glass
75.90	45.1	7.2	4.8	407.4	Glass

From these Δ^{14}C values we convert to a mass conserving mole fraction [^{14}CO$_2$] using

$$\begin{aligned}[^{14}\mathrm{CO_2}] &= \left(\frac{\Delta^{14}\mathrm{C}}{1000}+1\right)\left(\frac{\delta^{13}\mathrm{C}/1000+1}{-25/1000+1}\right)^2 \\ &\quad \times A_{\mathrm{abs}} \times [\mathrm{CO_2}] \end{aligned} \tag{A.4}$$

where we use the commonly used value of $A_{\mathrm{abs}} = 1.1764 \times 10^{-12}$ (Karlen et al., 1968). The values of δ^{13}C and [CO$_2$] are known from measurements of NEEM firn air from CSIRO Aspendale. Note that in the Δ^{14}C notation used here the activity of the isotopic reference material is decay-corrected, whereas the activity of the sample is not. Decay correction of the sample is not necessary, and simply not possible since the firn samples have an unknown mixture of ages. Sample decay is included through a decay term in the firn air models (Trudinger et al., 1997).

The δ^{15}N$_2$ data used as a tracer is corrected for the effect of thermal fractionation following the method described in Severinghaus et al. (2001). In this method the observed $\delta^{15}\mathrm{N}_{\mathrm{obs}}$ is split up as $\delta^{15}\mathrm{N}_{\mathrm{obs}} = \delta^{15}\mathrm{N}_{\mathrm{grav}} + \delta^{15}\mathrm{N}_{\mathrm{therm}}$, where the right hand side consists of a gravitational and a thermal term respectively. The gravitational fractionation scales linearly with the mass difference ΔM between the isotopologues. The thermal diffusion term $\delta^{15}\mathrm{N}_{\mathrm{therm}}$ is calculated using borehole temperature measurements and the SIO firn air model. This way one can solve for $\delta^{15}\mathrm{N}_{\mathrm{grav}}$.

A.2.4 Reconstruction of atmospheric histories of selected tracers

A.2.4.1 Combining different data series

The first major issue for combining different data series is calibration scale, which is not always fully documented in available metadata. In the case of AGAGE, all available data (ALE, GAGE and AGAGE) are on the same scale (SIO-2005). NOAA halocarbon data are currently under re-analysis. For this study only data converted to the most recent calibration scale were used (Geoff Dutton and Bradley Hall, personal communication).

Calibration (and/or procedural) differences between different atmospheric networks are less documented and understood. Synthetic results of intercomparisons between AGAGE and NOAA halocarbon data were kindly provided to the NEEM gas group (Paul Krummel, personal communication); they are shown in Table A.4. Two different comparison results are provided: comparisons of atmospheric data at a common measurement site (American Samoa) and comparisons of air tanks

Table A.4: *Concentration ratios (NOAA/AGAGE) for halocarbon species.*

Species	Multiple sites[a,b] flask/in-situ	Samoa[a] in-situ/in-situ	IHALACE[c]	This study (prelim.IHALACE)	Scales	Comment
CFC-11	1.0100	1.0095	1.0058	1.0081	NOAA-1993/SIO-05	time dependent
CFC-11	1.0057	1.0080	-	1.0081	NOAA-1993/SIO-05	2007-2009 only
CFC-12	0.9973	0.9965	0.9978	0.9978	NOAA-2008/SIO-05	
CFC-113	1.0199	1.0251	1.0266	1.0215	NOAA-2003/SIO-05	
CH_3CCl_3	1.0339	1.0379	1.0572 / - [d]	1.0627 / 1.0526[d]	NOAA-2003/SIO-05	ECD detector
CH_3CCl_3	1.0158	-	1.0081 / - [d]	1.0081 / 1.0030[d]	NOAA-2003/SIO-05	GCMS detector

[a] Krummel, personal communication

[b] Based on Mace Head, Trinidad Head, Samoa and Cape Grim

[c] Hall, B.D., Engle, A., Mühle, J., Elkins, J. et al., Results from the International Halocarbons in Air Comparison Experiment (IHALACE), in preparation

[d] Ratios for tanks at 22 ppt and 18 ppt respectively

circulated around measurement labs (IHALACE: International HALocarbons in Air Comparison Experiment; Bradley Hall, personal communication). The comparisons are consistent for CFC-12 and CFC-113. Concentration ratios at American Samoa are time-dependent for CFC-11. For CH_3CCl_3 Samoa and IHALACE results are inconsistent (note that IHALACE tanks had low concentration levels), and different results are obtained with Electron Capture Detector (ECD) and Gas chromatography–mass spectrometry (GCMS). As old trend data were obtained with ECD, GCMS measurements are not used for this species; a NOAA/AGAGE ratio of 1.035 is used.

A.2.4.2 Description of the reconstructions

CO_2: Summit and Alert NOAA-ESRL monthly record from 6/1985 - 12/2008. For months when both Summit and Alert records are available we use the average of the two. For months when only data from either one of the stations is available that station is used, with a correction for the average Alert-Summit offset for that given month. Mauna Loa (MLO) NOAA-ESRL (7/1976-5/1985) and SIO (3/1958-6/1976) records are used for indicated periods with a latitudinal correction applied based on the mean of the modern day MLO-Summit and MLO-Alert offset. Plots for offset vs. time revealed no trend, so a constant correction is used. A months 2-4/1964 gap in the SIO MLO record is filled by linear interpolation.

Prior to the MLO instrumental record, mean annual values are based on the the Law Dome mean-annual 20-yr smoothed record (1832-1958) and the Law Dome 75-yr smoothed mean annual record (1800-1831) (Etheridge et al., 1996), corrected for the Law Dome-NEEM offset. For missing years data points are interpolated linearly. Both the value and the trend of the Law Dome-NEEM offset were determined for the period 1959-1978 where the records overlap. In 1931 this results in NEEM concentration equaling the Law Dome concentration, so the inter-polar gradient goes to zero. For simplicity, beyond this point we simply set NEEM equal to Law Dome. A seasonal CO_2 cycle is added based on NEEM reconstructed monthly values for 1959-2008.

CH_4: Summit and Alert NOAA-ESRL monthly record from 6/1985-12/2008. For months when the Summit record is available, NEEM is set equal to Summit. For months where Summit record is unavailable, the NEEM reconstruction is based on Alert with a correction for the Summit-Alert offset for that month applied. Alert-Summit offsets show no significant trends with time.

Prior to the Alert record mean annual values are based on the Law Dome firn record (1978-1985) and the Law Dome ice core record (1800-1978) (Etheridge et al., 1998), scaled by 1.0124 to convert the data to the NOAA 2004 CH_4 calibration scale, and with a correction applied for the Law Dome-NEEM offset. The inter-polar gradient (IPG) is assumed to be constant at 45 ppb from 1800-1885 (Etheridge et al., 1998). For 1886-1985 it is assumed that the IPG is a function of both Law Dome $[CH_4]$ and $d[CH_4]/dt$. The IPG correction is tuned to the period 1986-1998 where direct atmospheric measurements are available and there is an appreciable growth rate $d[CH_4]/dt$. A seasonal CH_4 cycle is added based on the reconstructed NEEM monthly values for 1986-2008. It is assumed that the amplitude of the seasonal cycle is directly proportional to the mean annual concentration.

$^{14}CO_2$: The atmospheric $^{14}CO_2$ record from Fruholmen, Norway, is used for its proximity to Greenland, from 1/1963-6/1993 (Nydal and Lövseth, 1996). Atmospheric measurements from central Europe have been used from 6/1993-12/2008 (Vermunt and Jungfraujoch, Levin et al., 2008) and from 2/1959-12/1962 (Vermunt, Levin and Kromer, 2004). In the period 1990-2010 the reconstruction agrees within a few per mil with a recent atmospheric record from Alert station (Levin et al., 2010b), which was not yet available at the time we finalised the reconstruction.

Southern hemisphere atmospheric $^{14}CO_2$ measurements are used from 1954-1959 (Manning and Melhuish, 1994) with a correction of 30 ‰ on average to account for the interhemispheric gradient.

Prior to 1955 no direct atmospheric records exist and the reconstruction is equal to $\Delta^{14}CO_2$ reconstructed from dendrochronologically dated tree-ring samples (Reimer et al., 2004). The atmospheric $\Delta^{14}CO_2$ has been converted to a ppm scale using Eq. (A.4).

It should be noted that, unlike the firn air ^{14}C measurements, the atmospheric histories have been age-corrected for decay between the time that the sample was "collected" (in the case of trees, since the tree removed the CO_2 from the air), and the time that the sample was measured.

$\delta^{13}CO_2$: A $\delta^{13}CO_2$ reconstruction is required to convert $\Delta^{14}CO_2$ values from a permil scale to a mass-conserving ppm scale as described by Eq. (A.4). The Alert CSIRO monthly record from 1/1990-6/2008 is used without correction.

Prior to the Alert record we use the Cape Grim air archive record (1978-1989) and the Law Dome ice core record (1800-1978) (Francey et al., 1999), with a correction applied for the Law Dome-NEEM offset. The correction is assumed to scale linearly with the atmospheric growth rate of CO_2, and is calibrated to the period 1990-2008 where CSIRO Alert and Cape Grim monthly records are available.

CFC-11: Emission-based model results from Martinerie et al. (2009) before 7/1978. Mid Northern latitudes combined AGAGE monthly record 7/1978-3/2009. Overall scenario converted to NOAA scale with NOAA / AGAGE = 1.0081 (IHALACE).

CFC-12: Mid Northern latitudes combined AGAGE monthly record 1/1981- 3/2009 (early record ignored because of missing data and high inter-hemispheric gradient). 2D model results from Martinerie et al. (2009) before. Overall scenario converted to NOAA scale with NOAA / AGAGE = 0.9978 (IHALACE).

CFC-113: Mid Northern latitudes combined AGAGE monthly record 6/1986- 3/2009 (early record ignored because of missing data and high inter-hemispheric gradient). Emission-based model results from Martinerie et al. (2009) before. Overall scenario converted to NOAA scale with NOAA / AGAGE = 1.0215 (IHALACE).

SF_6: Barrow NOAA-ESRL combined (Geoff Dutton) monthly record 1/1999- 7/2009 (Barrow data for 1995-1998 ignored because of variable N/S gradient. Emission-based model results from Martinerie et al. (2009) before.

CH_3CCl_3: Mid Northern latitudes combined AGAGE monthly record 7/1978- 3/2009. Emission-based model results before 7/1978 (visual rescaling by 1.05). Overall scenario converted to NOAA scale with a NOAA / AGAGE = 1.035 (Samoa data with ECD detection).

HFC-134a: Barrow NOAA monthly record 2/1995- 3/2009, Emission-based model results before 02/1995 (visual rescaling by 1.10).

The mid-latitude AGAGE data could not be extrapolated to high latitudes for halocarbons. The first reason is the highly time dependent meridional concentration gradients; for species phased out under the Montreal Protocol, due to strongly reduced emissions, even the inter-polar gradient is close to zero in recent years. Another difficulty arises from the fact that the NOAA-ESRL mid

Northern latitude site (Niwot Ridge) is a high altitude site, thus the effects of altitude and latitude on concentrations cannot be separated.

δ^{15}N-N$_2$: There is no need for a δ^{15}N-N$_2$ reconstruction since the isotopic composition of Nitrogen is constant in the atmosphere on the timescales considered here. Formally, calculating the isotopic ratio would require both ^{15}N^{14}N and ^{14}N^{14}N isotopologues to be modeled separately. However, the ^{14}N^{14}N isotopologue constitutes nearly 80% of the air molecules, violating the assumption used by the firn models of modeling diffusion of trace gases into air. We have instead chosen to use an atmospheric forcing $[^{15}\mathrm{N}^{14}\mathrm{N}](t) = 1$ for all t, and we assume that the ^{14}N^{14}N istopologue has unity mixing ratio everywhere $[^{14}\mathrm{N}^{14}\mathrm{N}](z) = 1$. This is tantamount to assuming that ^{14}N^{14}N is the only non-trace gas in air (molecular diffusivity of ^{15}N^{14}N into air is used, however, rather than ^{15}N^{14}N into ^{14}N^{14}N). The δ^{15}N-N$_2$ signal is then given as $\delta^{15}\mathrm{N}\text{-}\mathrm{N}_2(z) = 10^3 \times ([^{15}\mathrm{N}^{14}\mathrm{N}](z) - 1)$.

A.2.4.3 Uncertainty estimates on atmospheric reconstructions

Table A.5 summarises the elements used for the uncertainty estimates. The dates refer to the period for which the comparison was made (thus the uncertainty should be applied from the beginning of the earliest data series to the end date of the comparison). The biases between labs can be large and time varying for halocarbons. To distinguish the mean bias from the variability of the differences between data series, these variabilities are noted dev. instead of σ, because the distributions are obviously not Gaussian in many cases.

Uncertainties are overall much higher for halocarbons than for other gases. For halocarbons, uncertainties on emissions are likely more pessimistic than uncertainties on concentrations. As an illustration, Martinerie et al. (2009) rescaled halocarbon emissions so that modeled atmospheric concentrations fit the early part of atmospheric datasets. Rescaling factors for CFC-11, CFC-12, CFC-113, CCl$_4$ and SF$_6$ range between 5 and 10% for the rising part of the trends.

Niwort Ridge halocarbon concentrations are mostly lower than Barrow concentrations, suggesting a dominant effect of altitude rather than latitude. Differences between Summit and Barrow are much lower. This suggests that the mid-latitude to Greenland concentration gradient is within the noise on the data for halocarbons.

Using the values in Table A.5 uncertainties are constructed in the following way:

CO$_2$ uncertainties: 1985-2008: half the ALT/SUM offset, 1976-1985: half the ALT/SUM offset and the standard deviation of the ALT/MLO-NOAA offset, 1958-1976: half the ALT/SUM offset and the standard deviation of the ALT/MLO-SIO offset, 1930-1958: twice the 1σ Law Dome measurement uncertainty, the IPG uncertainty estimate, 1800-1930: three times the 1σ Law Dome uncertainty and the IPG uncertainty estimate. In each period the listed terms are added quadratically to estimate the total uncertainty.

CH$_4$ uncertainties: The CH$_4$ uncertainty is dominated by the uncertainty in the IPG estimate, which is large for CH$_4$. For this reason three independent reconstructions were made, and the uncertainty was taken as the maximum difference between the reconstructions. The first method is described in Sect. A.2.4.2, a second method assumes the IPG is linearly related to the CH$_4$ mixing ratio, a third method uses the a linear regression analysis between atmospheric growth rate and IPG. The comparison leads to an uncertainty ranging from 5-42 ppb.

For halocarbons, expressing emission-related uncertainties in % results in an unrealistic zero uncertainty at the start date of emissions. Thus somewhat arbitrarily, a minimum absolute uncertainty (in ppt) was set to the present-day uncertainty. The large increase in uncertainty when switching from atmospheric records to emission based estimates is applied gradually (over about 2 years) for all halocarbon species.

Table A.5: Elements for uncertainty estimates. ALT: Alert, Canada, BRW: Pt. Barrow, Alaska USA,MLO: Mauna Loa, Hawaii USA, SUM: Summit Greenland, ADR: Adrigole, Ireland, MHD: Mace Head, Ireland, CMO: Cape Meares, USA, THD: Trinidad Head, USA, CGO: Cape Grim, Tasmania, SPO: South Pole, Antarctica, Measurement types: cn (continuous), fl (flasks). Other notations: instrument names/types.

Species	Source	scale	dates	error	comment
CO_2	Etheridge 1996	CSIRO	before 1942	1.1ppm	1 σ ice core data
	Etheridge 1996	CSIRO	1942-1958	0.1ppm	1 σ firn air data
	Inter-polar gradient	NOAA	before 1985	2ppm	Estimated IPG uncertainty
	NOAA website	NOAA	1997-2008	0.5ppm	mean bias (ALT/SUM)
	NOAA website	NOAA	1985-2008	0.8ppm	dev. of bias (ALT/MLO-NOAA)
	NOAA & GAW	-	1985-2008	0.8ppm	dev. of bias (ALT/MLO-SIO)
	NOAA website	NOAA	2000-2008	0.15/2ppm	1 σ on monthly values (South/North)
CH_4	Etheridge 1998	CSIRO	before 1944	5 ppb	1 σ ice core data
	Etheridge 1998	CSIRO	1944-1978	2.2 ppb	1 σ firn air data
	Inter-polar gradient	NOAA	before 1985	5-42ppb	Difference between 3 IPG estimates
	NOAA & GAW	NOAA	2000-2008	3/15ppb	1 σ on monthly values (South/North)
CFC-11	WMO (2007)	emissions	before 1978	18%	Table 1-7, p1.44 in WMO (2007)
	AGAGE website	AGAGE	1980-1983	-0.2%	mean bias (ADR/THD)
	AGAGE website	AGAGE	1987-1989	-0.3%	mean bias (CMO/THD)
	AGAGE website	AGAGE	1996-2009	-0.07%	mean bias (MHD/THD)
	AGAGE & NOAA	-	1991-2009	-0.3%	mean bias (AGAGE/NOAA)
	AGAGE & NOAA	-	1991-2009	-1./1%	center/dev of bias (AGAGE/NOAA)
	AGAGE website	AGAGE	1995-2009	0.2/0.3ppt	1 σ on monthly values (South/North)
	AGAGE website	AGAGE	1978-1995	1./1.5ppt	1 σ on monthly values (South/North)
CFC-12	WMO (2007)	emissions	before 1981	7.5%	Table 1-7, p1.44 in WMO (2007)
	AGAGE website	AGAGE	1981-1983	+2.0%	mean bias (ADR/THD)
	AGAGE website	AGAGE	1987-1989	+0.4%	mean bias (CMO/THD)
	AGAGE website	AGAGE	1996-2009	-0.1%	mean bias (MHD/THD)
	AGAGE & NOAA	-	1991-2009	+0.3%	mean bias (AGAGE/NOAA)
	AGAGE & NOAA	-	after 1996	+0.1/.1%	center/dev of bias (AGAGE/NOAA)
	AGAGE & NOAA	-	before 1996	+1.0/1.%	center/dev of bias (AGAGE/NOAA)
	AGAGE website	AGAGE	after 1996	.5/.6ppt	1 σ on monthly values (South/North)
	AGAGE website	AGAGE	before 1996	1.5/3.ppt	1 σ on monthly values (South/North)
CFC-113	WMO (2007)	emissions	before 1986	8.4%	Table 1-7, p1.44 in WMO (2007)
	AGAGE website	AGAGE	1987-1989	-0.9%	mean bias (CMO/THD)
	AGAGE website	AGAGE	1996-2006	-0.2%	mean bias (MHD/THD md)
	AGAGE website	AGAGE	2005-2009	+0.01%	mean bias (MHD/THD medusa)
	AGAGE & NOAA	-	1996-2003	+0.04%	mean bias (AGAGE/NOAA)
	AGAGE & NOAA	-	1996-2003	+0.2/1%	center/dev of bias (AGAGE/NOAA)
	AGAGE website	AGAGE	after 1996	0.2/0.2ppt	1 σ on monthly values (South/North)
	AGAGE website	AGAGE	before 1996	0.6/1.0ppt	1 σ on monthly values (South/North)
SF_6	WMO (2007)	emissions	before 1999	40.%	p1.51 in WMO (2007)
	NOAA website	NOAA	1998-2003	+0.2%	mean bias (cn/fl)
	AGAGE & NOAA	-	2001-2009	-0.9%	mean bias (AGAGE/NOAA)
	AGAGE & NOAA	-	2001-2009	-1./1.%	center/dev of bias (AGAGE/NOAA)
	NOAA website	NOAA	1997-2009	.06/.05ppt	1 σ on monthly values (South/North)
CH_3CCl_3	WMO (2007)	emissions	before 1978	4.2%	p1.45 in WMO (2007)
	AGAGE website	AGAGE	1981-1983	+3.5%	mean bias (ADR/THD)
	AGAGE website	AGAGE	1987-1989	+0.8%	mean bias (CMO/THD)
	AGAGE website	AGAGE	1996-2009	+0.09%	mean bias (MHD/THD)
	AGAGE website	AGAGE	2005-2009	+0.4%	mean bias (MHD/THD medusa)
	AGAGE & NOAA	-	1991-2009	+1.1%	mean bias (AGAGE/NOAA)
	AGAGE & NOAA	-	1991-2009	+1/4%	center/dev of bias (AGAGE/NOAA)
	AGAGE website	AGAGE	after 2000	0.3/0.4ppt	1 σ on monthly values (South/North)
	AGAGE website	AGAGE	before 2000	0.8/2.5ppt	1 σ on monthly values (South/North)
HFC-134a	WMO (2007)	emissions	before 1995	8.4%	Table 1-7, p1.44 in WMO (2007)
	NOAA website	NOAA	1995-2009	+0.1%	mean ALT/BRW
	AGAGE & NOAA	-	1998-2009	±0.5%	mean bias (AGAGE/NOAA)
	AGAGE & NOAA	-	after 2000	+1/2.%	center/dev of bias (AGAGE/NOAA)
	AGAGE & NOAA	-	before 2000	+0/6.%	center/dev of bias (AGAGE/NOAA)
	NOAA website	NOAA	1995-2009	0.2/0.3ppt	1 σ on monthly values (South/North)
$\Delta^{14}CO_2$	(Hua and Barbetti, 2004)	-	1955-1969	18 ‰	latitudinal $\Delta^{14}CO_2$ variations

CFC-11 uncertainties: 1995-2010: 1.5%, 1990-1994: 2.5%, 1978-1989: 3.5%, before 1978: 18%. The changes in uncertainty after 1978 roughly reflect an increasing bias between AGAGE and NOAA measurements when going back in time.

CFC-12 uncertainties: 1996-2010: 0.5%, 1981-1995: 2%, before 1981: 7.5%.

CFC-113 uncertainties: 1996-2010: 1%, 1986-1995: 2.5%, before 1986: 8.4%.

SF_6 uncertainties: 1999-2010: 1.5%, 1985-1998: 3.5% South. Hem. and 5% North. Hem., 1978-1984: 3.5% South. Hem. and 10% North. Hem., before 1978: 40%. The high uncertainty on emissions reflects mismatches between bottom-up and top-down estimates (WMO, 2007). Levin et al. (2010a) mention a 20% mismatch between their recent estimates.

CH_3CCl_3 uncertainties: 2000-2010: 4.%, before 2000: 6%. These uncertainties are high compared to the 4.2% uncertainty on emissions from WMO (2007). They reflect the variability of the AGAGE/NOAA ratio and the dispersion around monthly mean values.

HFC-134a uncertainties: 2000-2010: 3.%, 1995-1999: 6% before 1995: 8.4%.

$\Delta^{14}CO_2$ uncertainties: direct atmospheric records are long compared to other tracers, and the largest source of uncertainty is latitudinal gradients. Hua and Barbetti (2004) estimate that for the period 1955-1969 the maximum variability found between stations in the high latitude northern hemisphere is 18 ‰. This uncertainty exceeds the typical measurement precision of around 5 ‰ (Levin and Kromer, 2004). We therefore use the 18 ‰ estimate for our atmospheric reconstruction.

A.2.5 Gravitational correction

Before the modeling all data were corrected for the effect of gravity. The correction is made using the formula

$$[\mathrm{X}]_{\mathrm{gravcorr}}(z) = \frac{[\mathrm{X}]_{\mathrm{meas}}(z)}{\Delta M(\delta_{\mathrm{grav}}(z)/1000 + 1)} \tag{A.5}$$

where $[\mathrm{X}]_{\mathrm{gravcorr}}$ is the mixing ratio of gas species X after gravitational correction, $[\mathrm{X}]_{\mathrm{meas}}$ the mixing ratio as measured, $\Delta M = M_{\mathrm{X}} - M_{\mathrm{air}}$ is the difference in molar mass between gas X and air and $\delta_{\mathrm{grav}}(z)$ is the gravitational fractionation per unit mass difference at depth z. The values of $\delta_{\mathrm{grav}}(z)$ are listed in Tables A.6 and A.7 for the EU and US boreholes, respectively. They are based on measurements of the gravitational enrichment of δ^{86}Kr (^{86}Kr/^{82}kr) with depth, and corrected for the effect of thermal fractionation (Severinghaus et al., 2001). The rationale for using Kr rather than N_2, is that its free-air diffusivity is closer to that of most of the tracers we use, so it should represent the disequilibrium effects on gravitational fractionation more accurately.

A.2.7 Overall uncertainty estimation

When tuning to multiple gases it is important to have realistic uncertainty estimates for both the data and the atmospheric reconstruction. These will determine how much weight is given to the different gases during the tuning procedure. Therefore consistency between the different gases is more important than the absolute accuracy of the uncertainty estimates. These uncertainties are not a fixed number for each gas, but can be expressed as a function of depth. Here we identify seven sources of uncertainty.

Analytical precision We use the analytical precision as specified by the laboratories. In case we have data from several laboratories for a single gas species, the largest of the specified uncertainties is used. Where there are multiple data points available for the same depth we additionally calculated the standard deviation between the data points. The assigned analytical uncertainty for a specific depth is taken as the larger of (1) the 1 σ standard deviation for that depth and (2) the (depth independent) lab specified uncertainty.

Uncertainty in atmospheric reconstruction The uncertainties in the atmospheric reconstructions, as described in Sect. A.2.4.3, are produced on a time scale. By calculating the mean age of the gases, the estimates can be mapped from a timescale onto a depth scale. This is

Table A.6: Gravitational correction δ_{grav} for the EU hole.

Depth (m)	δ_{grav} (‰)
0.00	0.000
2.50	0.004
4.90	0.014
7.55	0.025
10.10	0.036
14.80	0.058
19.75	0.080
27.54	0.116
34.72	0.152
42.42	0.190
50.00	0.227
54.90	0.250
57.40	0.262
59.90	0.273
61.95	0.282
63.85	0.285
65.75	0.285
68.05	0.285
70.05	0.285
72.00	0.285
74.08	0.285
75.90	0.285
77.75	0.285

more practical from a modeling point of view. The conversion is done by treating the uncertainty estimate as a regular gas history, and running it through the CIC firn air model. This approach is valid since the diffusion model is linear with respect to the atmospheric input.

The complication that arises is the following: The depth estimates are used as *input* to the tuning procedure, but at the same time they rely on model *output* (the mean ages are calculated using the firn model). This could lead to a circular/iterative procedure where we refine the uncertainties indefinitely. To avoid this situation we use only the CIC model with near-finalised tuning, where the calculated mean ages are estimated to be off by only a few years. Since the uncertainty estimates do not have a temporal resolution better than a few years to begin with, this model offset will not influence the final result greatly. Furthermore, we have checked the validity of this approach afterwards, by re-calculating the mean ages after finalising the tuning of the model. Indeed the mean ages obtained by the nearly-finalised and finalised model tuning did not differ by more than four years in the deepest firn.

Sample contamination For the deepest samples it becomes increasingly difficult to pump air from the firn. The reduced sample flow can lead to contamination due to incomplete flushing of flasks, and air leaking past the sealing bladder. Several halocarbon species should be absent at the deepest sampling levels, and we use these to estimate sample contamination. All contaminations are assumed to be with modern air, and expressed as a fraction of sample volume.

Figure A.3 shows estimates of sample contamination from different gases, and the contamination estimate for NEEM as the black line (1.6% contamination for the deepest samples). Note that we do not make any corrections to the data, but rather assign an additional uncertainty to the deepest samples because we have indication of contamination. The fraction of contaminated air is taken to be

Table A.7: Gravitational correction δ_{grav} for the US hole.

Depth (m)	δ_{grav} (‰)
0.00	0.000
2.85	0.005
5.23	0.015
9.83	0.035
19.30	0.078
34.70	0.152
49.70	0.226
57.47	0.262
59.90	0.273
62.00	0.282
64.03	0.285
65.50	0.285
66.90	0.285
68.30	0.285
69.80	0.285
71.40	0.285
72.85	0.285
73.80	0.285
75.60	0.285

$$\frac{V_{\mathrm{contam}}}{V} = \begin{cases} 0 & \text{if } z < 70\mathrm{m} \\ 0.016 \times (z - 70)/8 & \text{if } z \geq 70\mathrm{m} \end{cases} \tag{A.6}$$

where V_{contam}/V is the fraction of the sample volume that comes from the modern atmosphere rather than from the open pores of the firn layer being sampled. The uncertainty introduced by the contamination is calculated by multiplying the fraction of modern air by the difference between modern atmospheric and measured firn air mixing ratios.

Sampling errors The sampling procedure introduces errors which are not easily estimated. For CO_2, CH_4 and SF_6 we have data from several labs, as well as from both boreholes. We use these to estimate the influence of the sampling procedure. IUP CH_4 and SF_6 data have been corrected as described in Sect. A.2.3.

We treat each gas species and borehole separately. First, we consider sampling depths for which we have data from at least two labs, and calculate the standard deviation of the data for that depth. The sampling uncertainty is estimated as the average of the obtained standard deviations. The assigned sampling uncertainty for a specific depth is taken as the larger of (1) the 1 σ standard deviation for that depth (when available) and (2) the average sampling uncertainty as described above.

The average sampling uncertainties thus obtained are:

CO_2:	0.32	ppm (EU),	0.19	ppm	(US)
CH_4:	1.8	ppb (EU),	2.7	ppb	(US)
SF_6:	0.035	ppt (EU),	0.029	ppt	(US)

The sampling error is found to be independent of depth (Fig. A.4).

For gases where we have data from only one lab (mostly halocarbon data from the EU hole) we cannot determine the sampling errors is such a direct way. An estimate is made based on the CO_2,

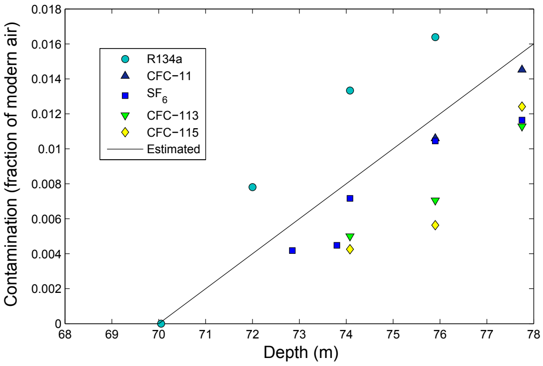

Figure A.3: Contamination as calculated from gas measurements, with in black the values used as the uncertainty estimate for contamination in all NEEM samples.

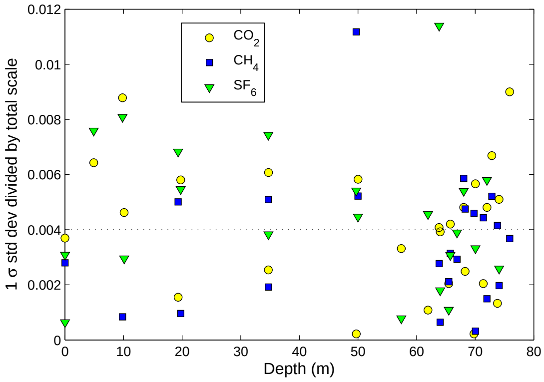

Figure A.4: Sampling uncertainties estimated from the standard deviation for each sampling depth. Standard deviations are divided by the total scale, meaning the highest measured concentration minus the lowest measured concentration.

CH_4 and SF_6 values given above. In Fig. A.4 calculated sampling uncertainties are plotted, divided by the total signal in the firn (i.e. the highest concentration - lowest concentration). This quantity is comparable for all analysed data. The mean value (indicated by the dotted line) is 0.004. For all gases where we have only data from a single lab we used this value (0.4 % of total scale) as an estimate of sampling uncertainties.

Possible in-situ CO_2 artifacts Due to the presence of organic material and (bi)carbonates in Greenland ice there is the possibility of in-situ CO_2 contamination artifacts (Tschumi and Stauffer, 2000; Guzman et al., 2007). We observe a CO_2 model-data mismatch in the deepest firn on the order of 5 ppm (Fig. A.5a and Fig. 3a of the main text). For this reason we include the following uncertainty for CO_2:

$$u_{CO_2}(z) = \begin{cases} 0 & \text{if } z < 68\text{m} \\ 0.5 \times (z - 68) & \text{if } z \geq 68\text{m} \end{cases} \tag{A.7}$$

This uncertainty estimate also covers the possibility of CO_2 enrichment due to close-off fractionation of the CO_2/air ratio, which occurs at the same depths (Severinghaus and Battle (2006) could not exclude a 1 ‰ effect).

In-situ cosmogenic production of $^{14}CO_2$ from nuclear spallation is known to occur (Lal et al., 1990). The production is too low by orders of magnitude to alter the CO_2 mixing ratio, however it could affect the $^{14}CO_2$ tracer. Though only the upper firn is exposed to cosmic radiation, the spallation products could be retained in the ice matrix and be released into the pore space at depth. Any in-situ $^{14}CO_2$ released into the pore space within the convective zone (top 5 m), will be lost to the atmosphere due to the vigorous ventilation. Release at lower depths would be detectable in the firn air $^{14}CO_2$ measurements. We can get an upper boundary on the ^{14}C release by looking at the deepest samples below the 'bomb-spike'. The deepest sample has a $\Delta^{14}CO_2$ of 44.9 ‰. The CO_2 mean age at this depth is from the late 1950s, for which our atmospheric reconstruction gives a atmospheric value of around 100 ‰. There is therefore no indication that the cosmogenically produced $^{14}CO_2$ has been released from the ice matrix at depth. The uncertainty related to in situ CO_2 production, however, has been translated into an uncertainty in $\Delta^{14}CO_2$ (~ 13 ‰ in the deepest firn).

Undersampling of the seasonal cycle in CO_2 The atmospheric reconstructions used in this study have a monthly resolution. In the deepest firn this is of little concern since the seasonal cycle is averaged out by the diffusion process. In the top layers undersampling of the seasonal cycle leads to a potential misfit between modeled profiles and data. We include this effect in the following way. First we linearly interpolate the CO_2 reconstruction to a $\frac{1}{2}$ month resolution. Then we run the CIC model (with nearly finalised tuning) twice, with final dates at $\pm\frac{1}{2}$ month around the firn air sampling date. The uncertainty estimate is set to half the difference between these two runs.

This test is done for all gases that vary seasonally; the effect is found to be only significant for CO_2.

In theory a strong seasonal variation, in combination with seasonality in firn transport properties (e.g. in convective mixing strength), can also bias mixing ratios in the deep firn. No evidence has been found for such a rectifier effect (Severinghaus et al., 2001), and we do not take it into account.

@*series*SF_6 offset between the EU and US holes As discussed in the main text we observe an unexplained ~ 0.25 ppt offset between the EU and US boreholes for @*series*$\mathbf{SF_6}$ in the depth range $z \sim 5-50$ m. We can exclude differences in gas age, incomplete flask flushing, sample contamination, procedural blanks and bladder outgassing as the origin. Since we found no objective reason to reject data from either hole, we account for the discrepancy by assigning an additional errorbar to the SF_6 data from both holes. The magnitude of the assigned uncertainty is given in Table A.8. We have no reason to suspect other tracers are affected by a similar offset.

A.3 Modeling firn air transport at NEEM

A.3.1 Tuning of the diffusivity profile

A.3.1.1 Trace gas diffusion coefficients in air

Different trace gases have different free air diffusion coefficients (D^0_{X}), which result in different diffusion speeds in firn air. When the firn diffusivity profile is established for a reference gas (e.g. CO_2), it can be applied to another gas by scaling with $\gamma_X = D_{\mathrm{X}}/D_{\mathrm{CO_2}}$ (Trudinger et al., 1997). Gilliland (1934) expressed diffusion coefficients for binary gas mixtures (D_{AB}) as a function of their molecular masses (M_A, M_B) and volumes (V_A, V_B), temperature (T) and pressure (p):

$$D_{AB} = \frac{\alpha T^{\beta}}{p} \frac{\sqrt{1/M_A + 1/M_B}}{(V_A^{1/3} + V_B^{1/3})^2} \tag{A.8}$$

with α=0.0043, and β=3/2. In the theoretical frame of Eq. (A.8), the γ_X diffusivity ratios are independent from temperature and pressure. Fuller et al. (1966) propose an equation similar to Eq. (A.8), with different values of α and β (α=0.001, β=1.75) and new estimates of atomic and molecular volumes. However, no estimates are provided for the fluorine and bromine atoms. Massman (1998)

Table A.8: Uncertainty estimate to account for borehole offset for @series$\mathbf{SF_6}$*. Depths on EU and US boreholes are mixed together.*

Depth (m)	u_{SF_6} (ppt)
2.50	0.050
2.85	0.050
4.90	0.100
5.23	0.150
7.55	0.200
9.83	0.200
10.10	0.200
14.80	0.200
19.30	0.200
19.75	0.200
27.54	0.200
34.70	0.200
34.72	0.200
42.42	0.150
49.70	0.100
50.00	0.100
54.90	0.050

suggest that the Chen and Othmer (1962) formula has greater predictive capabilities. Chen and Othmer (1962) proposed a semi-empirical formula developed in terms of critical temperature and molar volumes, which are available for a number of molecules (e.g. CRC, 2002):

$$\begin{aligned} D_{AB} &= \frac{\alpha (T/T_0)^{\beta}}{(p_0/p)} \frac{\sqrt{1/M_A + 1/M_B}}{(Tc_A Tc_B/10^4)^{0.1405}} \times \\ & \frac{1}{[(Vc_A/100)^{0.4} + (Vc_B/100)^{0.4}]^2} \end{aligned} \qquad \text{(A.9)}$$

with $\alpha = 2.616$, $\beta = 1.81$, For most gases, diffusion coefficients in N_2 and air (and often O_2) are similar (e.g. Marrero and Mason, 1972; Matsunaga et al., 1993, 1998, 2002b, 2003, 2005, 2006, 2007, 2009).

The only exception in the Matsunaga data set is H_2 (Matsunaga et al., 2002a). Blanc's law (Blanc, 1908) is often used (e.g. Marrero and Mason, 1972) to calculate diffusion coefficients of gas X in multi-component mixtures from diffusion coefficients in binary mixtures. In the case of air, it can be written as:

$$D^{-1}_{\text{X-air}} = \frac{[O_2]}{D_{\text{X-}O_2}} + \frac{[N_2]}{D_{\text{X-}N_2}} \qquad \text{(A.10)}$$

where $[O_2]$ and $[N_2]$ are molar fractions (e.g. 0.21 and 0.79). Matsunaga et al. (2002a) diffusion coefficients for H_2 in N_2, O_2 and air are 6.863×10^{-5}, 7.144×10^{-5} and 6.874×10^{-5} m^2/s respectively. Equation (A.10) leads to 6.919×10^{-5} m^2/s in the 20.6% O_2 - 79.4% N_2 mixture used by Matsunaga et al. (2002a). It differs by 0.65% from the experimental value.

A consistent set of diffusion coefficient measurements has been published for the major greenhouse gases (Matsunaga et al., 1998), halocarbons (Matsunaga et al., 1993, 2009), SF_6 (Matsunaga et al., 2002b) and other gases with experimental precisions of about ± 2%. A comparison with previous measurements, when available, is provided as well as temperature-dependent equations fitted to the data of the form:

$$D_{AB} = \chi T^{\eta} \qquad \text{(A.11)}$$

Table A.9: Molecular diffusion coefficients and ratios: comparison of measurements from Matsunaga et al. (1998, 2002b,a,c, 2005, 2006, 2007, 2009), a1: Barr and Watts (1972), a2: Watts (1971), a3: Cowie and Watts (1971), b: Lugg (1968), c: Massman (1998, 1999) and d: Marrero and Mason (1972) with calculated values: Chen and Othmer (1962), (Bzowski et al., 1990). D_X values are in m^2 s^{-1}.

		Matsunaga et al.		Other	Calc.
X	$D_{X\text{-air}} = \chi\ T^{\eta}$	γ_X at -50° C	γ_X at 0° C	γ_X at 0° C conv.	γ_X at 0° C
CO_2	$5.75\times10^{-10}T^{1.81}$	1	1	0.958^{a1}, 0.935^{c} 0.940^{d}	1
CH_4	$7.04\times10^{-10}T^{1.83}$	1.364	1.370 (+0.6%)	1.306^{a3} (-4.1%) $1.321/1.413^{c}$ (-3.0/+3.7%) $1.258/1.338^{d}$ (-7.6/-1.8%)	1.362 (1.405)
N_2O	$5.34\times10^{-10}T^{1.82}$	0.980	0.982 (-0.3%)	0.849^{a1} (-13.8%) $0.972/1.040^{c}$ (-1.3/+5.6%)	0.985 (1.005)
SF_6	$3.76\times10^{-10}T^{1.78}$	0.556	0.553 (-9.5%)	$0.550/0.584^{d}$ (-10.0/-4.4%)	0.611 (0.625)
H_2	$41.9\times10^{-10}T^{1.73}$	4.73	4.650 (-3.1%)	$4.521/4.807^{d}$ (-5.8/-0.2%)	4.799
CFC-11	$3.19\times10^{-10}T^{1.80}$	0.526	0.525 (+0.2%)		0.524
CFC-12	$4.77\times10^{-10}T^{1.75}$	0.600	0.592 (+1.2%)	0.569^{a1} (-2.7%)	0.585
CFC-113	$2.75\times10^{-10}T^{1.80}$	0.453	0.452 (+2.0%)		0.443
CFC-114	$3.97\times10^{-10}T^{1.75}$	0.499	0.493 (+2.7%)		0.480
CFC-115	$4.03\times10^{-10}T^{1.76}$	0.535	0.529 (-1.1%)		0.535
HCFC-22	$7.47\times10^{-10}T^{1.70}$	0.717	0.701 (+1.9%)		0.688
HCFC-123	$4.30\times10^{-10}T^{1.74}$	0.512	0.505 (+2.2%)		0.494
HFC-134a	$5.04\times10^{-10}T^{1.75}$	0.634	0.626 (+1.3%)		0.618
CH_3CCl_3	$2.64\times10^{-10}T^{1.82}$	0.485	0.486 (+0.8%)	0.459^{b} (-4.8%)	0.482
CCl_4	$2.17\times10^{-10}T^{1.85}$	0.469	0.472 (-2.1%)	0.469^{a2} (-2.7%), 0.457^{a3} (-5.2%)	0.482
CH_3Br	$5.57\times10^{-10}T^{1.76}$	0.739	0.732 (+6.9%)		0.685
CH_3I	$5.26\times10^{-10}T^{1.75}$	0.661	0.653 (-4.9%)		0.604
CF_4	$11.4\times10^{-10}T^{1.65}$	0.835	0.808 (+2.9%)		0.785 (0.791)
C_3H_8	$4.65\times10^{-10}T^{1.77}$	0.651	0.646 (-8.0%)	0.689^{a1} (-1.9%)	0.702
C_3H_6	$5.08\times10^{-10}T^{1.76}$	0.674	0.667 (-9.4%)		0.736
0.530^{b} (+0.2%)	0.529				
CO	-	-	-	$1.223/1.308^{c}$ (-2.2/+4.6%) $1.243/1.322^{d}$ (-0.6/+5.8%)	1.250 (1.303)
CH_3Cl	-	-	-	0.864^{a3} (+9.5%)	0.789
$CHCl_3$	-	-	-	0.546^{a2} (+4.0%), 0.519^{a3} (-1.1%) 0.513^{b} (-2.3%)	0.525
CH_2Cl_2	-	-	-	0.630^{a2} (-0.9%), 0.628^{a3} (-1.3%) 0.599^{b} (-5.8%)	0.636
CH_3CCl_3	-	-	-	0.459^{b} (-4.8%)	0.482
CCl_4	-	-	-	0.469^{a2} (-2.7%), 0.457^{a3} (-5.2%) 0.478^{b} (-0.8%)	0.482
Hg	-	-	-	0.822^{b} (-5.3%)	0.868
	-	-	-	$0.808/0.865^{c}$ (-6.9/-0.3%)	
H_2O	-	-	-	$1.474/1.577^{c}$ (+7.3/+14.8%) $1.414/1.504^{d}$ (+2.9/+9.5%)	1.374
N_2	-	-	-	$1.210/1.295^{c}$ (-5.1/+1.6%)	1.275
O_2	-	-	-	$1.232/1.318^{c}$ (-5.4/+1.2%)	1.302
C_5H_{12}	-	-	-	0.516^{a1} (+2.2%), 0.486^{b} (-3.8%)	0.505

where χ and η are species-dependent scalars. As coefficient η is species-dependent, the derived γ_X ratios are slightly temperature dependent (0.2% to 1.4% in the 0 to -50° C temperature range for CH_4, CFCs and SF_6). Measurements were performed at positive temperatures and are extrapolated to -50° C using Eq. (A.11) (Table A.9). These data are compared with the results of the semi-empirical calculation of Chen and Othmer (1962) (%) values at 0° C in Table A.9. This calculation provides better results than those from Gilliland (1934) or Fuller et al. (1966) for CFCs (Martinerie et al., 2009, Supplement). Among the 24 analysed γ_X, 18 show discrepancies between calculated and measured values $\leq \pm 3.1\%$. The 6 other species: SF_6, CH_3Br, CH_3I, C_3H_8, C_3H_6 and CH_3OCH_3 show distinctly higher discrepancies of 5 to 10% ; these large deviations can be negative or positive.

Two other sets of relatively recent and consistent multi-species measurements are found in the literature. Results are reported only for a limited number of species (measured in firn air or in the above data set). A Canadian group performed diffusion coefficient measurements for the 3 major greenhouse gases, some halocarbons and organic species (Watts, 1971; Cowie and Watts, 1971; Barr and Watts, 1972). Lugg (1968) performed another series of measurements on some organic and halocarbon species, as well as Mercury. Lugg (1968) did not measure $D^0_{\mathrm{CO_2}}$, thus the value from Matsunaga et al. (1998) at 25°C is used to calculate γ_X in this case. Only Watts (1971) provides temperature-dependent data, other references report measurements at 25°C. The γ_X in Table A.9 are relative to the Matsunaga et al. (1998) data. It should be noted that $D^0_{\mathrm{CO_2}}$ from Matsunaga et al. (1998) is higher than all other reported values. Deviations of the Canadian data (Watts, 1971; Cowie and Watts, 1971; Barr and Watts, 1972) from calculated values (Chen and Othmer, 1962) are variable within the range: -13.8 to +9.5%. The differences between γ_X derived from Lugg (1968) and calculated values are mostly negative and range between -5.8 and +0.2%.

Table A.9 also shows γ_X values from two diffusion coefficient data compilations (Marrero and Mason, 1972; Massman, 1998, 1999). These compilations do not include the data set by the Matsunaga group. As the data are generally different for the various reported chemical species, the “best” $D^0_{\mathrm{CO_2}}$ value to be used for the calculation of γ_X is unclear in the case of data compilations. Thus both values are calculated in Table A.9 under the form X/Y, where X uses $D^0_{\mathrm{CO_2}}$ from Matsunaga et al. (1998) and Y uses $D^0_{\mathrm{CO_2}}$ from the data compilation. Deviations from the calculated values (Chen and Othmer, 1962) are somewhat similar: -6.9 to +14.8% for Massman (1998, 1999), and -10.0 to +9.5% for Marrero and Mason (1972). It should be noted than for $\mathrm{SF_6}$, the data compilation from Marrero and Mason (1972) is more consistent with the Matsunaga et al. (1998) value than with the calculated value.

Finally, the Chen and Othmer (1962) calculated γ_X are compared with the results from Bzowski et al. (1990), shown between parentheses in the last column of Table A.9. Bzowski et al. (1990) used an elaborated calculation derived from the corresponding state theory to calculate diffusion coefficients in equimolar mixtures of $\mathrm{N_2}$ and several gases. The resulting γ_X are always larger that those from Chen and Othmer (1962) (+0.8 to +4.2%) and show increased differences with the data set by the Matsunaga group, except for $\mathrm{CF_4}$ (the two calculated values are very close in this case: 0.8%). The Bzowski et al. (1990) calculation further increases the large discrepancy with the data obtained for $\mathrm{SF_6}$ with the Chen and Othmer (1962) calculation.

A.3.1.2 Diffusion coefficients for trace gases and isotopic ratios at the NEEM site

The diffusion coefficient ratios γ_X for both trace gases and isotopic ratios that are used in this study are listed in Tables A.10 and A.11. The tables also include gases that are not directly used here, but might be of interest to firn air modeling studies in general.

We would like to add a few notes on how the diffusion coefficients were derived, and how they should be used. First, all diffusion coefficients reported here are the binary diffusivity of the gas into air. This satisfies the requirement, in order for Fick's Law of diffusion to be valid, that the gas species being modeled is diffusing into a background gas that is the major gas present. In our context, that major gas is air. The values are presented as ratios to the diffusivity of $\mathrm{CO_2}$-air. Thus the values presented are unitless. This convention is followed even in the case of isotopic species.

Second, experimental values reported by the Matsunaga group are used where possible, extrapolated to -28.9°C. Where this is not possible, calculated values are given using the method of Chen and Othmer (1962). The latter are identified in Table A.10 with an asterisk (*). Values for isotopic species are calculated using the “square root of the ratio of the reduced masses” law:

$$D_{\text{X-air}} = \sqrt{\frac{M_{\mathrm{X}}^{-1} + M_{\mathrm{air}}^{-1}}{M_{\mathrm{Y}}^{-1} + M_{\mathrm{air}}^{-1}}}\, D_{\text{Y-air}} \tag{A.12}$$

where X refers to the minor isotopic species, and Y to the major isotopic species. The mass M is calculated for air by assuming that water vapor in the firn is saturated at -28.9°C, and that the mole fraction of water vapor is given by $p\mathrm{H_2O}/p$, where p is the barometric pressure of 745 mbar at NEEM. The saturation vapor pressure over ice is:

$$p\mathrm{H_2O}(\mathrm{mbar}) = 6.1115 \exp\left[\frac{\Theta(23.036 - \Theta/333.7)}{279.82 + \Theta}\right] \tag{A.13}$$

Table A.10: Diffusion coefficients of several trace gases at the NEEM site as used in this study. $T = 244.25$ *K,* $p = 745$ *mbar. Values are based on Matsunaga et al. (1998, 2002b,a,c, 2005, 2006, 2007, 2009), unless marked with an asterisk. For those cases Eq. (A.9) is used (Chen and Othmer, 1962). For all these trace gases we use the natural isotopic abundance of the constituent atoms when calculating the molar mass.*

Gas (X)	γ_X
CO_2	1.000
CH_4	1.367
N_2O	0.981
SF_6	0.554
H_2	4.694
CFC-11	0.525
CFC-12	0.596
CFC-113	0.453
CFC-114	0.496
CFC-115	0.532
HCFC-22	0.710
HCFC-123	0.509
HFC-134a	0.630
HFC-32	0.866
HCFC-124	0.538
HFC-125	0.589
HFC-143a	0.647
HFC-43-10mee	0.383
CH_3Br	0.736
CH_3I	0.658
CF_4	0.823
C_3H_8	0.649
C_3H_6	0.671
CH_3OCH_3	0.827
$C_2H_5OC_2H_5$	0.525
CH_3CCl_3	0.485
CCl_4	0.470
CH_2Cl_2	0.709
@*series*$\mathbf{CHCl_3}$	0.595
@*series*$\mathbf{C_2H_5Cl}$	0.743
@*series*$\mathbf{CH_2ClCH_2Cl}$	0.600
@*series*$\mathbf{CH_2CCl_2}$	0.641
@*series*$\mathbf{CHClCCl_2}$	0.583
@*series*$\mathbf{CH_3Cl}$	0.789 *
CO	1.250 *
Hg	0.868 *
@*series*$\mathbf{H_2O}$	1.374 *
@*series*$\mathbf{N_2}$	1.275 *
@*series*$\mathbf{O_2}$	1.302 *
@*series*$\mathbf{C_5H_{12}}$	0.505 *
He	4.780 *
Ne	2.140 *
Ar	1.230 *
Kr	0.962 *
Xe	0.835 *

Table A.11: Diffusion coefficients for specific isotopologues. To model isotopic ratios both major and minor abundance isotopologues are to be modeled separately. Values calculated using natural abundance diffusion coefficients listed in Table A.10 in combination with Eq. (A.12) at $T = 244.25$ K and $p = 745$ mbar.

Isotopologue (X)	γ_X	for use in
HD	3.895386	δD
HH	4.693994	δD
$^{13}CH_4$	1.340806	$\delta^{13}C$
$^{12}CH_4$	1.366969	$\delta^{13}C$
CDH_3	1.340469 **	δD
CH_4	1.366676 **	δD
$^{14}CO_2$	0.991368 ***	$\Delta^{14}C$
CO_2	1.000000 †	$\Delta^{14}C$
$^{13}CO_2$	0.995613 ***	$\delta^{13}C$
$^{12}CO_2$	1.000048 ***	$\delta^{13}C$
$^{12}C^{18}O^{16}O$	0.991401	$\delta^{18}O$
$^{12}C^{17}O^{16}O$	0.995648	$\delta^{17}O$
$^{12}C^{16}O^{16}O$	1.000089	$\delta^{17}O$ and $\delta^{18}O$
$^{12}C^{18}O$	1.228754	$\delta^{18}O$
$^{12}C^{17}O$	1.239117	$\delta^{17}O$
$^{12}C^{16}O$	1.250172	$\delta^{17}O$ and $\delta^{18}O$
$^{15}N^{14}N^{16}O$	0.976915 ‡	$^{\alpha}\delta^{15}N$, $^{\beta}\delta^{15}N$
$^{18}ON_2$	0.972718	$\delta^{18}O$
$^{17}ON_2$	0.976884	$\delta^{17}O$
$^{16}ON_2$	0.981239	$^{\alpha}\delta^{15}N$, $^{\beta}\delta^{15}N$, $\delta^{17}O$,$\delta^{18}O$
$^{15}N^{14}N$	1.263893	$\delta^{15}N$
$^{14}N^{14}N$	1.275084	$\delta^{15}N$
$^{18}O^{16}O$	1.283719	$\delta^{18}O$
$^{17}O^{16}O$	1.292637	$\delta^{17}O$
$^{16}O^{16}O$	1.302087	$\delta^{17}O$ and $\delta^{18}O$
^{22}Ne	2.087122	$\delta^{22}Ne$ and δNe/Ar
^{20}Ne	2.145608	$\delta^{22}Ne$
^{40}Ar	1.229952	$\delta^{40}Ar$
^{38}Ar	1.243488	$\delta^{38}Ar$
^{36}Ar	1.258324	$\delta^{40}Ar$, $\delta^{38}Ar$, Kr,Xe,Ne
^{86}Kr	0.958741	$\delta^{86}Kr$
^{84}Kr	0.961616	$\delta^{84}Kr$ and δKr/Ar
^{82}Kr	0.964621	$\delta^{86}Kr$ and $\delta^{84}Kr$
^{136}Xe	0.832366	$\delta^{136}Xe$
^{132}Xe	0.834581	$\delta^{132}Xe$ and δXe/Ar
^{129}Xe	0.836327	$\delta^{136}Xe$ and $\delta^{132}Xe$

** Includes mass effect of ^{13}C-containing isotopologue in its natural abundance, in keeping with convention for reporting deuterium data

*** Includes mass effects of ^{17}O- and ^{18}O- containing isotopologues in their natural abundances, in keeping with conventions for reporting ^{14}C and ^{13}C data (e.g. Craig (1957), Stuiver and Polach (1977))

† Convention for reporting ^{14}C has it as the ratio to non-isotopic (i.e. natural abundance) C

‡ This value applies to both isotopomers having the ^{15}N at the central and terminal positions (Yoshida and Toyoda, 2000) .

where Θ is the temperature in °C. The mass of dry air is calculated from the 1976 US Standard Atmosphere (CRC, 2002), with a small adjustment for the increase in the mass of dry air due to a concentration update for the anthropogenic gases (CO_2 385 ppm, O_2 20.9367%, N_2 78.088%). This results in an air mass M_{air} of 28.9589 $\text{g}\,\text{mol}^{-1}$.

Third, an isotopic substitution in a gas molecule affects the diffusivity by changing the mass. The term "isotopologue" is used for a specific isotopic species. For example, $^{12}C^{18}O^{16}O$ is an isotopologue of carbon dioxide. Therefore, each isotopologue has its own value of diffusivity into air. To satisfy the above requirement for Fick's Law to be valid, each isotopologue must be modeled separately, as a trace gas diffusing into a major gas (i.e. air), each with its own diffusivity. Then, the customary delta value must be computed from the modeled depth profiles of the two isotopologues. For example, the $\delta^{18}O$ value for the $^{12}C^{18}O^{16}O$ isotopologue would be calculated from the outputs of two separate model runs, one for $^{12}C^{18}O^{16}O$-air and one for $^{12}C^{16}O^{16}O$-air:

$$\delta^{18}\text{O} = \left(\frac{[^{12}\text{C}^{18}\text{O}^{16}\text{O}]_{\text{model}}}{[^{12}\text{C}^{16}\text{O}^{16}\text{O}]_{\text{model}}} \Bigg/ \left.\frac{[^{12}\text{C}^{18}\text{O}^{16}\text{O}]}{[^{12}\text{C}^{16}\text{O}^{16}\text{O}]}\right|_{\text{std}} - 1 \right) \times 10^3 \tag{A.14}$$

where the square brackets denote a mole fraction of the isotopologue in air. The subscript 'model' refers to mole fractions as calculated by the model, and the subscript 'std' refers to the ratio of mole fractions of the reference standard used for reporting the delta value (here, this would be V-PDB).

Fourth, to relate the values of diffusivities for isotopic species (i.e. species with well defined isotopic substitutions) to the values for non-isotopic species (i.e. having no specified isotopic substitutions and a mass corresponding to the sum of all isotopes/isotopologues, weighed by their natural abundance) in an internally consistent way, we calculated the ratio of the diffusivity of gas Y (the major isotopologue) to the diffusivity of the non-isotopic species NI using the equation:

$$\frac{D_{\text{Y-air}}}{D_{\text{NI-air}}} = \sqrt{\frac{M_{\text{Y}}^{-1} + M_{\text{air}}^{-1}}{M_{\text{NI}}^{-1} + M_{\text{air}}^{-1}}} \tag{A.15}$$

The mass of the non-isotopic species M_{NI} for this purpose was the natural abundance mass (an abundance-weighted average of the masses of all the isotopes). This ratio was then multiplied by the value of D_{NI}/D_{CO_2} for the non-isotopic species (typically an experimental value), to produce the final values of D_{Y}/D_{CO_2} for the major, and D_{X}/D_{CO_2} for the minor isotopologue:

$$\gamma_Y = D_{\text{Y}}/D_{CO_2} = \frac{D_{\text{Y-air}}}{D_{\text{NI-air}}} \times D_{\text{NI}}/D_{CO_2} \tag{A.16}$$

$$\gamma_X = D_{\text{X}}/D_{CO_2} = \frac{D_{\text{X-air}}}{D_{\text{Y-air}}} \times D_{\text{Y}}/D_{CO_2} \tag{A.17}$$

The differences between D_{Y} and D_{NI} are not significant in most cases, but we nonetheless calculated them for the sake of conceptual clarity. For example, the value of D_{Y}/D_{CO_2} for the isotopologue $^{12}C^{16}O^{16}O$ is 1.000089, compared with the value of D_{NI}/D_{CO_2} of 1.000000 (by definition). The reason that the natural-abundance isotopic mixture diffuses slightly more slowly than the isotopologue $^{12}C^{16}O^{16}O$ is that the mixture contains trace amounts of heavier isotopologues such as $^{13}C^{16}O^{16}O$.

Fifth, the non-isotopic species are generally not used to calculate delta values ($\Delta^{14}C$ is an exception). Rather, the species in the denominator in the delta calculation is generally a specific isotope, usually the major isotope, such as ^{1}H, ^{12}C, ^{14}N, or ^{16}O. Also, Table A.10 only presents three or four significant figures for the diffusivities for non-isotopic species. This is not usually sufficient for delta calculations. So all δ calculations should use the diffusivities in Table A.11, which have 6 or 7 significant figures. Of course, the absolute values are not that well known, but the relative values of a pair are quite well known, as the relative values depend only on Eq. (A.12).

Sixth, the convention for reporting isotopic data usually includes all isotopologues containing a certain isotope, not just the most abundant one. For example, $\delta^{13}C$ is defined as:

$$\delta^{13}\mathrm{C} = \left(\left. \frac{^{13}\mathrm{C}}{^{12}\mathrm{C}} \right|_{\mathrm{sample}} \Bigg/ \left. \frac{^{13}\mathrm{C}}{^{12}\mathrm{C}} \right|_{\mathrm{V\text{-}PDB}} - 1 \right) \times 10^3 \tag{A.18}$$

For CO_2, the numerator here would include the sum of the abundances of not only $^{13}C^{16}O^{16}O$, but also $^{13}C^{17}O^{16}O$, $^{13}C^{18}O^{16}O$, $^{13}C^{18}O^{18}O$, etc. The denominator would include $^{12}C^{16}O^{16}O$, $^{12}C^{17}O^{16}O$, $^{12}C^{18}O^{16}O$, $^{12}C^{18}O^{18}O$, etc. Although it is impossible to measure all the minor ^{13}C-containing isotopologues with mass spectrometry, a correction is routinely applied that approximately accounts for all of these. Similarly, chemical transformations often bring all the various forms of isotopes into a single isotopologue, as part of a routine analysis. For example, H_2 gas is produced chemically during the analysis of deuterium/hydrogen ratios in methane. For this reason the mass used to calculate diffusion coefficients should be a weighted average of the various isotopologues that exist, which will ultimately contribute to the analysis.

We account for this effect in several cases, marked with asterisks. In other cases we neglect it as the abundances are too small to be significant (for example, ^{13}C is relatively abundant at 1 in 100 carbon atoms, so we account for it, but deuterium is extremely rare at 1 in 6500 hydrogen atoms, so we neglect its effect on the weighted average mass). In still other cases we neglect it because the precision of the measurements is far too low for this issue to matter (e.g., $^{15}N_2O$).

A.3.2 Model description

Below follows a brief description of the different firn air models in alphabetical order.

A.3.2.1 CIC model

The CIC firn air model is a finite difference 1-D diffusion model coded in MATLAB. It uses implicit Crank-Nicholson time stepping to solve what is essentially an advection-diffusion-reaction equation, with radioactive decay and bubble trapping taking the place of the chemical reaction by removing trace gas molecules from the open pore space. The model uses a stationary reference frame with $z = 0$ at the surface. The firn column is assumed to be isothermal and in steady state with regard to ice flow and densification rates.

The model includes four types of transport: molecular diffusion, gravitational settling, advection, and eddy diffusion. The last term includes convective transport following Kawamura et al. (2006), as well as dispersive mixing in the LIZ. Using a molecular diffusivity in the LIZ instead would lead to continued gravitational enrichment with depth, which contradicts observations.

The transport description closely follows Trudinger et al. (1997); the main differences being a static reference frame rather than a Lagrangian one, and the explicit inclusion of the trapping process in the equations of mass conservation. Advection is included through a flux in the open pores at a velocity w_{air}:

$$w_{\mathrm{air}} = \frac{A\rho_{\mathrm{ice}}}{s^*_{\mathrm{op}}p_0} \left(\frac{s_{\mathrm{cl}}(z_{\mathrm{COD}})p_{\mathrm{cl}}(z_{\mathrm{COD}})}{\rho_{\mathrm{COD}}} - \frac{s_{\mathrm{cl}}(z)p_{\mathrm{cl}}(z)}{\rho(z)} \right) \tag{A.19}$$

where z_{COD} is the full close-off depth where all the air is occluded in bubbles ($s_{\mathrm{op}}(z_{\mathrm{COD}}) = 0$), p_{cl}/p_0 is the pressure in closed bubbles relative to atmosphere and s^*_{op} is the effective open porosity

$$s^*_{\mathrm{op}} = s_{\mathrm{op}} \exp\left[\frac{M_{\mathrm{air}}gz}{RT}\right] \tag{A.20}$$

We tune the inverse tortuosity profile $\tau^{-1}(z)$; the effective molecular diffusivity is given as $D_{\mathrm{X}}(z) = D^0_{\mathrm{X}}\tau^{-1}(z)$. As an initial guess for $\tau_0^{-1}(z)$ we use the parameterisation by Schwander (1989). The optimal diffusivity for NEEM can be written as

$$\tau^{-1}(z) = \tau_0^{-1}(z) \times [1 + f(z)] \tag{A.21}$$

where $f(z)$ is a smooth function which we will try to estimate in the tuning procedure. We construct $f(z)$ from its Fourier components

$$f(z) = c_0 + \sum_{n=1}^{N} \left[c_n \sin\left(\frac{n\pi z}{2L}\right) + d_n \cos\left(\frac{n\pi z}{2L}\right) \right] \tag{A.22}$$

where L is the total length of the open porosity firn column (78 m), and N determines the smoothness of the final diffusivity profile. The optimal values of the coefficients c_n and d_n are found in an automated gradient method. For the tuning of NEEM a value of $N = 20$ was used. We set $\max[\tau^{-1}(z)] = 1$, i.e. the diffusivity in the firn cannot exceed the free-air diffusivity. It was found that including other functions $f_i(z)$, such as linear slopes $f_i(z) = z/L$, tends to speed up the convergence to the final solution. More details will be given elsewhere.

A.3.2.2 CSIRO model

The CSIRO firn model is based on the model described by Trudinger et al. (1997). Since then it has been rewritten into Fortran90, flux smoothing is no longer used, and an implicit time stepping, the same as that used by Rommelaere et al. (1997), has replaced the Euler predictor-corrector scheme. The time step used here was 0.1 years up to 2000 then 0.01 years to the end. An exponential eddy diffusion flux has been added following Severinghaus et al. (2001) to account for convective mixing near the surface, with 2 tuned parameters (surface magnitude and scale depth). A key difference between the CSIRO firn model and the other models is that it neglects the upward flux of air due to compression of pore space. A genetic algorithm (from Haupt and Haupt (1998)) is used to calibrate the diffusivity versus open porosity and the eddy diffusion parameters. We adjust the open porosity values corresponding to about 12 specified diffusivity values to give the diffusivity profile, with cubic splines used to interpolate between these points, and diffusivity capped at 500 $\mathrm{m^2\,yr^{-1}}$ (0.158×10^{-4} $\mathrm{m^2\,s^{-1}}$) near the surface. We only allow monotonic solutions (as defined by the points) but the cubic splines, which match the gradient of adjacent splines at each point, can often lead to non-monotonic diffusivity vs open porosity profiles. We therefore penalise oscillatory behaviour with an additional term added to the cost function that is the squared difference between a line integral following the cubic spline and a line integral for linear interpolation between the points. Any negative diffusivity values are set to zero. The best solution for the NEEM EU hole had the diffusivity going to zero, then increasing above zero below this. This was not intentional, but was caused by the cubic splines. The US case did not generate the same behaviour, instead the best fit was obtained with diffusivity that decreased to zero at about 63 m. The genetic algorithm does not require an initial guess, but does require a range for each parameter. The ranges were initially chosen as representative of values for other calibrated sites, and extended if solutions from the genetic algorithm with low values of the cost function collected near either end of the range. More detail on the calibration method will be given in Trudinger et al. (in preparation).

A.3.2.3 INSTAAR model

The INSTAAR one-dimensional firn gas transport model was originally based on a model described in Severinghaus and Battle (2006), but has evolved substantially. The model has fixed coordinates with only the gases moving through the firn matrix. The firn matrix is considered to be in steady state. The NEEM firn is parameterised with 1 m deep boxes between -0.5 and 59.5 m (top model box is half-free air, half-firn), and with 0.25 m deep boxes below 59.5 m.

Gases are moved through the firn by four mechanisms: (1) molecular diffusion (different for different gases), (2) gravitational settling, (3) eddy diffusion or turbulent mixing (same for all gases), (4) downward advection (same for all gases). For each box, the model keeps track of the gas content in the open porosity as well as in the ice-enclosed bubbles, but the gas mixing ratios are only tracked in the open porosity part. Rate of total downward air advection is determined from the air content of ice below close-off and the ice accumulation rate. From mass conservation, the total downward air advection should be the same at each level. The rate of advection in the open porosity at each level is therefore calculated as the total downward air advection rate minus the advection of air in the bubbles at that level (found from bubble air content and ice accumulation rate).

Unlike the model described in Severinghaus and Battle (2006), the INSTAAR model does not have any fundamental differences in the mechanisms of gas movement between the diffusive zone and the lock-in zone. In the INSTAAR model the reduced gas movement in the lock-in zone is achieved simply through adjusting the overall effective gas diffusivities to lower levels.

The model includes a seasonal temperature cycle and calculates firn temperature in each model box in the same way as the Severinghaus and Battle (2006) firn model.

The model uses explicit time stepping. To avoid computational instability the time step is always chosen to be smaller than $\Delta t < (\Delta z)^2/3D_{\text{total}}$, where Δt is the time step, Δz is the box size in m, and D_{total} is the total effective diffusivity in $\text{m}^2\,\text{s}^{-1}$. For all gases except H_2, this time step was set to 11,119 s (3.5×10^{-4} yr). For H_2, which has a much higher molecular diffusivity, the time step was set to 3,156 s (1×10^{-4} yr).

The equation used to calculate flux of gas X between two adjacent boxes due to molecular diffusion and gravity at each time step is as follows:

$$\begin{aligned} J_{X;\text{molec-grav}(i)} &= -\gamma_X D^0_{\text{CO}_2} \tau_i^{-1} s_{\text{op; mid}} \times \\ & \left(\frac{C_{i+1} - C_i}{\Delta z_{\text{mid}}} - \frac{\Delta M g}{R T_i} \frac{C_{i+1} + C_i}{2} \right) \end{aligned} \tag{A.23}$$

Here $J_{X;\text{molec-grav}(i)}$ is the gas flux between box i and $i+1$ (in units of e.g., $\text{ppm}\,\text{m}\,\text{s}^{-1}$). This can be thought of as the volume of the pure gas moving across a unit area of the boundary between boxes per unit time. $\gamma_X D^0_{\text{CO}_2}$ is the free-air diffusivity of gas X at the boundary between box i and $i+1$ in $\text{m}^2\,\text{s}^{-1}$, re-calculated at each time step to take into account firn temperature variations; τ_i^{-1} is the tuned dimensionless multiplier (or inverse tortuosity) to the free air diffusivity for box i. $s_{\text{op; mid}}$ is the open porosity (m^3/m^3) at the boundary between the two boxes. This is included because the flux should be proportional to the open porosity. C_i is the gas mixing ratio in box i (e.g., in ppm), Δz_{mid} is the distance (m) between the middles of box i and box $i+1$, ΔM is the molar mass difference ($\text{kg}\,\text{mol}^{-1}$) between the gas and bulk air, g is the acceleration due to gravity ($\text{m}\,\text{s}^{-2}$), R is the universal gas constant ($\text{J}\,\text{mol}^{-1}\,\text{K}^{-1}$) and T_i is the firn temperature (K) at the boundary between boxes i and $i+1$.

The basic form of the equation used to calculate the gas flux due to eddy diffusion or turbulent mixing is:

$$J_{\text{eddy}(i)} = -D_{\text{eddy}(i)} s_{\text{op; mid}} \frac{C_{i+1} - C_i}{\Delta z_{\text{mid}}} \tag{A.24}$$

where $J_{\text{eddy}(i)}$ is the gas flux due to eddy diffusion ($\text{ppm}\,\text{m}^3\,\text{m}^{-2}\,\text{s}^{-1}$) and $D_{\text{eddy}(i)}$ is the tuned eddy diffusivity (m^2s^{-1}) for box i.

Gas fluxes due to advection and flux of air into newly formed bubbles are also calculated at each time step. All of these fluxes are corrected to STP volumes (to account for varying temperature and pressure in the firn column) and are added to find the total flux of gas into the box (J_{in}) and the total flux of gas out of the box (J_{out}). The time derivative of the gas mixing ratio in box i is then calculated as:

$$\frac{\Delta C_i}{\Delta t} = \left(\frac{J_{\text{in}} - J_{\text{out}}}{s_{\text{op}(i)} \Delta z_i} \right) \tag{A.25}$$

where s_i is the open porosity in the box and Δz_i is the vertical length of box i.

The effective diffusivities in the INSTAAR model were manually tuned to optimise the fit to the suite of 10 gases. The initial guess for effective molecular diffusivities used the free-air diffusivity in the surface box, with effective diffusivities for CO_2 declining linearly to 2.0×10^{-9} $\text{m}^2\,\text{s}^{-1}$ at 64m and staying constant beyond 64 m. The initial guess for eddy diffusivity set the eddy diffusivity equal to molecular diffusivity for CO_2 in the surface box, and prescribed an exponential decrease with depth using an e-folding depth of 4 m. Below the depth where eddy diffusivity dropped to 1.0×10^{-8} $\text{m}^2\,\text{s}^{-1}$ it was held constant at this value.

A.3.2.4 LGGE-GIPSA model

In the LGGE-GIPSA model (Witrant et al., 2011), the transport processes described in (Rommelaere et al., 1997) have been revised in a poromechanics framework, where the ice lattice, the gases in open pores and the gases in closed pores are considered as an interconnected network constrained by mass conservation. The model dynamics is expressed in terms of densities and the diffusion process is described as a combination of Fick's and Darcy's transport, thus allowing to distinguish between a purely diffusive transport (molecular and eddy) in the convective layer and an almost-stagnant transport in the lower zones. The numerical implementation is done with an implicit time discretization with a one week step and combined central/Lax-Wendroff space discretization with a step of 0.2 m.

Firn diffusivity is calculated using a constrained non linear least square multi-gas optimization scheme, with the optimisation problem formulated by Witrant and Martinerie (2010). $\delta^{15}N_2$ was not used for diffusivity optimisation but kept for the physical model transport validation. By contrast with some of the other models in this intercomparison, only molecular diffusivity (no eddy-diffusivity) is considered in the deep firn. An eddy diffusion term (D_{eddy}) is taken into account in the upper firn to represent convective transport: when firn diffusivity calculated by our optimisation procedure exceeds the speed of molecular diffusion in free air D_X^0 corrected by a factor α to take into account the porosity effect (Severinghaus and Battle, 2006), the firn diffusivity is calculated as $\alpha D_X^0 + D_{\text{eddy}}$. D_{eddy} is then the quantity tuned by our least square multi-gas optimisation in order to best fit the firn data. No pre-defined depths are used to constrain the limits of the convective and lock-in zone except for the depth at which gravitational fractionation starts (set as 4 m for NEEM). The lower boundary for gravitational fractionation (lock-in depth) is calculated by the model.

The model has been evaluated on 12 additional Arctic (Devon Island, North GRIP, Summit) and Antarctic (DE08, Berkner Island, Siple Dome, Dronning Maud Land, South Pole 1995, South Pole 2001, Dome C, Vostok) previously simulated with the Rommelaere et al. (1997) model.

A.3.2.5 OSU model

The OSU firn air model is a finite-difference diffusion model based on the mixing ratio equations of Trudinger et al. (1997), Eqs. (A9) and (A13). However, the OSU model differs from this model in the following ways. First, an eddy-diffusion term is added to represent surface convection, based on the parameterisation of Kawamura et al. (2006), and also to account for the necessary mixing that is observed within the LIZ but cannot be due to molecular diffusion.

Second, the model uses an implicit Crank-Nicholson numerical scheme, which makes it stable over a large range of depth increments and time steps. Because of this, at the model time step of 0.005 years and depth resolution of 0.1 m, the flux smoothing technique of Trudinger et al. (1997) is not employed.

Lastly, vertical advection of the firn is accounted for by shuffling boxes down at every time step, rather than moving the reference frame (Schwander et al., 1993). An evenly spaced depth scale is used, which makes computation of the diffusion equation simpler but complicates shifting boxes as the firn densifies and the equally spaced boxes contain less and less air. To deal with this, the vertical displacement of the air at every depth and every time step is calculated. The vertical air velocity used to compute displacement differs from the ice velocity (Rommelaere et al., 1997) and is given by the equation of Buizert (Eq. (A.19)). This creates a new mixing-ratio profile with different depth values which is then interpolated back onto the fixed grid, and assigned the correct firn properties at each depth. The value of the top box is set to the atmospheric mixing ratio for the current time step during this process.

Bubble compression is accounted for only in the LIZ, because above this zone it is assumed that the pressure in the open porosity is equal to atmospheric pressure. Below the top of the LIZ, the model uses the following correction to account for the greater amount of air in the open porous volume:

Table A.12: Constants used in the OSU diffusivity tuning for the EU borehole

constant	value	unit
g_1	- 0.209	
g_2	1.515	
g_3	0.53	
g_4	3.17×10^{-10}	$\mathrm{m^2 s^{-1}}$
g_5	1.82	m
g_6	3.17×10^{-9}	$\mathrm{m^2 s^{-1}}$
g_7	0.11	m

$$s^*_{\mathrm{op}}(z) = s_{\mathrm{op}}(z)\frac{\rho(z)}{\rho_{\mathrm{LID}}} \tag{A.26}$$

where $s_{\mathrm{op}}(z)$ is the true open porosity at depth z (Eq. (A.2)), $\rho(z)$ is the density (Eq. (A.1)), and ρ_{LID} is the density at the lock-in depth, i.e. at the top of the LIZ. Bubble compression of the closed porosity is ignored since this is an open porosity model. The free air diffusivity of CO_2 ($D^0_{\mathrm{CO_2}} = 1 \times 10^{-5}$ $\mathrm{m^2\,s^{-1}}$) is first corrected for site temperature and pressure (Schwander et al., 1988), then adjusted for depth based on the porosity (note that this is based on the actual porosity, not the effective porosity defined above). The diffusivity parameterisation of Schwander et al. (1993) is used as a first estimate, but a second-order porosity dependence was added later to improve the fit. The form of the final diffusivity profile is:

$$D_X(z) = D^0_X\left[g_1 + g_2 s_{\mathrm{op}}(z) + g_3 s^2_{\mathrm{op}}(z)\right] \tag{A.27}$$

Values for constants g_1, g_2 and g_3 were manually adjusted to minimise the total root mean squared error of the model-data mismatch for all tracers, including δ^{15}N. Final values are listed in Table A.12. Where molecular diffusivity goes to zero in the LIZ, the model uses a synthetic exponential decrease to prevent numerical instabilities. This takes the form:

$$D_X(z) = g_4 + (D_X(z_{\mathrm{LID}}) - g_4)e^{-g_5(z-z_{\mathrm{LID}})}, \quad \text{for} \quad z > z_{\mathrm{LID}} \tag{A.28}$$

where g_4 is some relict molecular diffusivity and z_{LID} is the lock-in depth. Dispersive eddy diffusivity in the lock-in zone is parameterised by the following exponential:

$$D_{\mathrm{eddy}}(z) = g_6 e^{g_7(z-z_{\mathrm{LID}})}, \quad \text{for} \quad z > z_{\mathrm{LID}} \tag{A.29}$$

where again g_6 and g_7 were iteratively adjusted to provide the best fit to the data.

A.3.2.6 SIO model

The Scripps Institution of Oceanography (SIO) firn air model follows generally those of Schwander et al. (1993), Rommelaere et al. (1997), Severinghaus and Battle (2006), and Severinghaus et al. (2010) (hereafter S2010). Slight differences from the model of S2010 include the following. (i) Barometric pressure increases with depth, according to the isothermal barometric equation set with the initial mean-annual temperature, (ii) gravity is set to zero within the lock-in zone, (iii) molecular and eddy diffusion both continue throughout the LIZ, and (iv) the LIZ grid spacing is calculated with the air advection velocity until the close-off density (Martinerie et al., 1992) and thereafter with the firn velocity, whereas S2010 calculated it with the firn velocity in the entire LIZ.

The main differences between the SIO model and the other models in the present intercomparison are:

1) The model has a parallel heat transport model within it that predicts temperature as a function of depth and time. Using these temperatures, the model computes fractionation of gases and isotopes by thermal diffusion, gravitational settling, and temperature-sensitive kinetic disequilibrium

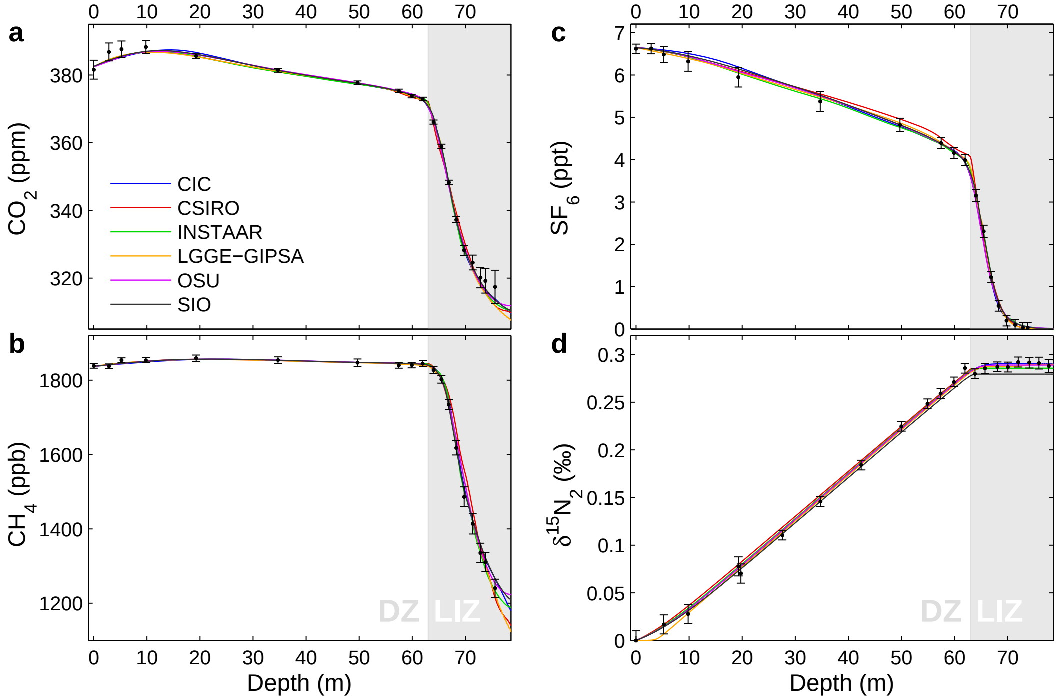

Figure A.5: **(a–d)** *Modeled profiles for all 4 tracers from the US borehole. With the exception of* **(d)** *data have been gravity corrected and the models are run with gravity turned off. Errorbars correspond to full 1σ uncertainty as defined in Sect. A.2.7.*

processes. Disequilibrium arises from convection in the near-surface layers, downward advection due to snow accumulation and bubble close-off, and transients in atmospheric gas mixing ratios and temperatures. For the NEEM intercomparison runs, the temperature model was disabled, but the full model was used to make thermal diffusion corrections to NEEM firn air δ^{15}N and δ^{86}Kr data used as inputs.

2) The SIO model treats downward air advection in the LIZ by shifting concentrations down by one grid point every 0.5 yr, rather than with explicit advection schemes. The grid points are spaced apart by distances such that the air advection velocity w_{air} would transport the air that distance in 0.5 yr. This scheme minimizes the numerical diffusion common to upwind advection schemes. As a result, the SIO model has the highest mixing ratio of tracer (oldest gas) in its lock-in zone in Diagnostic Test 4. This lack of numerical diffusion also implies that the diffusivities found by tuning to observed gas profiles should be slightly higher than those of the other models. This lock-in zone architecture was chosen so that second derivatives of atmospheric variations in trace gases would be preserved within the lock-in zone to the extent possible. For example, the dip in atmospheric CO$_2$ in the early 1940s can be preserved by the SIO model given a sufficiently high accumulation rate. The diffusion correction for ^{13}CO$_2$ and ^{13}CH$_4$ is also arguably more accurate with a minimum of numerical diffusion.

The inverse tortuosity profile $\tau^{-1}(z)$ is tuned using a generalised least square method. The initial guess $\tau_o^{-1}(z)$ is the parameterisation by Schwander (1989). Subsequent profiles are determined using:

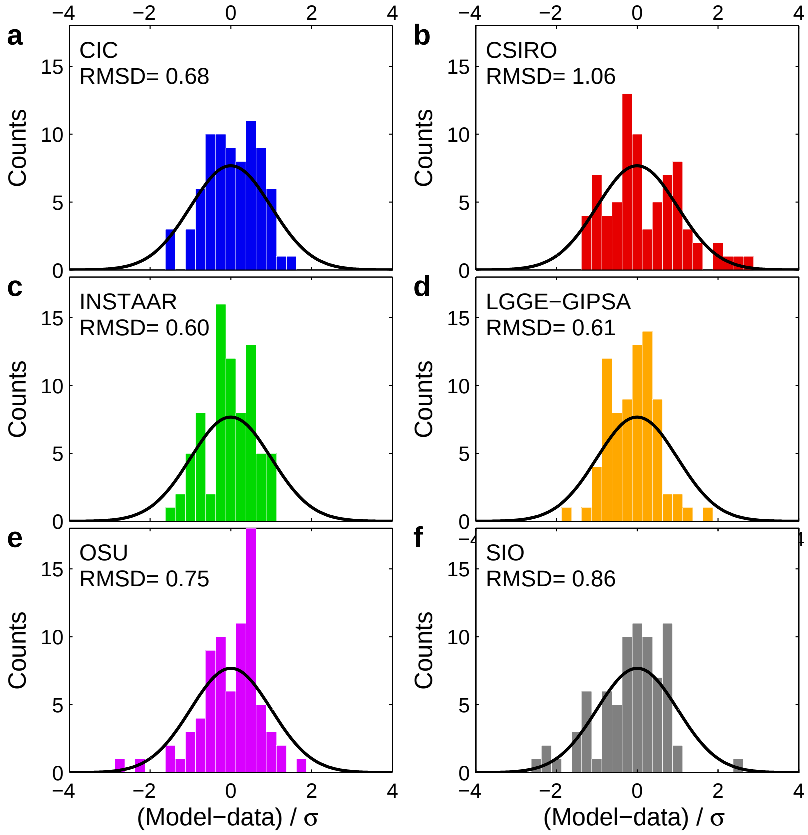

Figure A.6: **(a–f)** *Histogram of* $(m_i - d_i)/\sigma_i$ *for the firn air transport models in this study using the US borehole data. The black curve gives a Gaussian distribution of width* $\sigma = 1$*, normalised to have equal surface to the histogram. The RMSD is calculated with Eq. (3) of the main article.*

$$\tau^{-1}(z) = \tau_o^{-1}(z) + \sum_{i=1}^{N} h_i * f_i(z) \tag{A.30}$$

$$\begin{aligned}
f_i(z) &= 0 && z < i\Delta z \\
f_i(z) &= a(z - i\Delta z)/\Delta z && i\Delta z < z < (i+1)\Delta z \\
f_i(z) &= a((i+2)\Delta z - z)/\Delta z && (i+1)\Delta z < z < (i+2)\Delta z \\
f_i(z) &= 0 && z > (i+2)\Delta z
\end{aligned}$$

We use an amplitude $a = 10^{-6}\ \mathrm{m^2\,s^{-1}}$ between 0 and 60m, and $a = 10^{-8}\ \mathrm{m^2\,s^{-1}}$ between 60 and 80m. The half width Δz was set to $\Delta z = 0.5$ m. The coefficients h_i are optimised using a least square regression to minimise the RMS misfit given in Eq. (3) of the main text.

Near the surface, the eddy diffusivity due to wind pumping is parameterised by an exponential:

$$D_{\mathrm{eddy}}(z) = D^0_{\mathrm{eddy}} \exp\left(-\frac{z}{H}\right) \tag{A.31}$$

$D^0_{\mathrm{eddy}} = 1.6e^{-5}\ \mathrm{m^2\,s^{-1}}$ and $H = 5$ m are tuned to fit the δ^{15}N and δ^{86}Kr data, corrected for thermal fractionation.

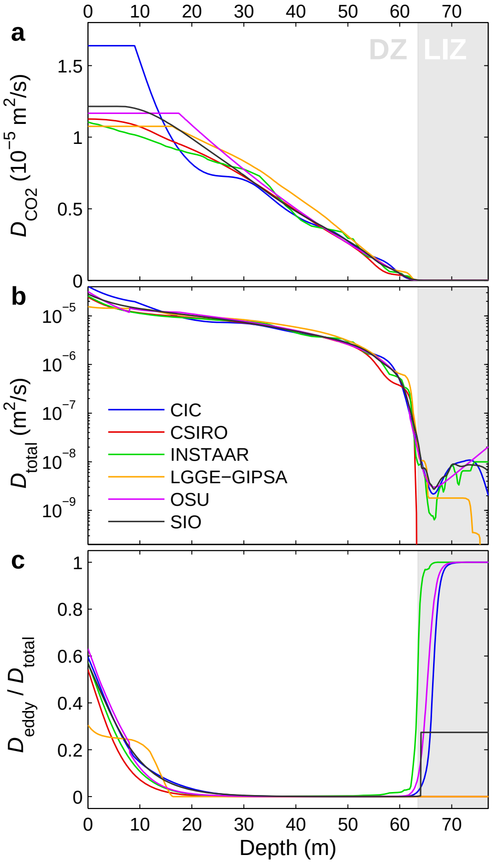

Figure A.7: **(a)** *CO_2 molecular diffusivity profile with depth $D_{CO_2}(z)$ for the US borehole.* **(b)** *Semi-log plot of the total CO_2 diffusivity profile $D_{total}(z) = D_{CO_2}(z) + D_{eddy}$.* **(c)** *Plot of $D_{eddy}(z)/D_{total}(z)$. The eddy diffusion near the surface corresponds to the convective mixing, in the LIZ some of the models have included dispersive mixing.*

In the lock in zone, the balance between molecular diffusion (affecting each gas differently) and dispersion (affecting all the gases proportionally) is determined by a single coefficient α varying between 0 and 1, rather than by having a free dispersion diffusivity profile, which is largely underconstrained. The molecular diffusivity is then:

$$D_X(z) = (1-\alpha)\frac{D_X^0}{\tau(z)} \tag{A.32}$$

And the dispersion, included as an eddy diffusivity, is:

$$D_{\text{eddy}}(z) = \alpha\frac{D_{\text{CO}_2}^0}{\tau(z)} \tag{A.33}$$

Here $D_{\text{CO}_2}^0$ is used as the reference, all gases experience the same $D_{\text{eddy}}(z)$. The optimum α was $\alpha_{\text{EU}} = 0.27$ for the EU hole, and $\alpha_{\text{US}} = 0.35$ for the US hole.

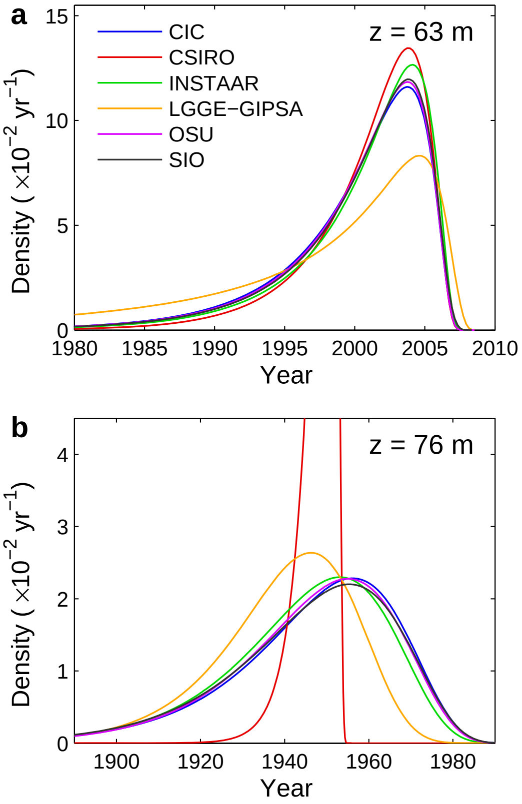

Figure A.8: US borehole modeled age distribution densities for **(a)** $z = 63$*m (lock-in depth) and* **(b)** $z = 76$*m (deepest sample). On the horizontal axis are calendar years C.E.; decimal sampling year is 2008.54 (i.e. mid July). Age distributions are generated by applying a surface forcing which is unity for* $0.2 \leq t < 0.4$ *yr, and zero elsewhere.*

A.3.3 Fit of modeled profiles to the data

The firn models were tuned separately to the US borehole, for which we have firn air data for four different tracers: CO_2, CH_4, SF_6 and $\delta^{15}N_2$. The fit to the data is shown in Fig. A.5. As for the EU borehole we find a mismatch at depths $z > 70$m for CO_2 (Fig. A.5A); the feature is reproduced consistently by all the firn air models.

To assess model performance we make a histogram of $(m_i - d_i)/\sigma_i$, where the index i goes over all the 77 data points of the US borehole. This is shown in Fig. A.6 together with a Gaussian distribution of width $\sigma = 1$ and a surface area equal to that of the histogram. The figure furthermore shows the root mean square deviation (RMSD) from the data as given by Eq. (3) of the main text. Most models perform better for the US borehole in terms of the RMSD, which is due to the fact that there are fewer tracers for the US borehole. The exception is the CSIRO model for which the RMSD is higher on the US hole. However, preliminary tests show that by including the advective back flux in the CSIRO model the RMSD improves to 0.79 (Trudinger et al., 2011).

Table A.13: Mean age, median age, Full Width at Half Maximum and Spectral Width (Δ, Eq. (1) in Trudinger et al., 2002) at the lock-in depth (z = 63 m) and bottom of the LIZ (z = 76 m) for the US borehole. All values given in years. We use the 2σ standard deviation divided by the mean ($2\sigma/\mu$) as a measure of the spread in model results.

Model	Mean	Median	FWHM	Δ
		$z = 63$ m		
CIC	8.3	6.7	7.2	4.0
CSIRO	7.3	6.1	6.4	3.1
INSTAAR	7.7	6.2	6.6	3.7
LGGE-GIPSA	12.2	8.2	8.5	8.3
OSU	8.2	6.6	7.1	4.0
SIO	8.1	6.5	7.0	3.9
$2\sigma/\mu$	0.41	0.23	0.21	0.84
		$z = 76$ m		
CIC	61.6	58.1	39.8	14.6
CSIRO	60.2	59.1	6.4	3.1
INSTAAR	63.5	60.5	39.8	14.0
LGGE-GIPSA	68.8	66.2	34.6	12.3
OSU	62.1	58.9	40.3	14.2
SIO	62.5	59.0	41.5	14.8
$2\sigma/\mu$	0.09	0.10	0.81	0.74

A.4 Model intercomparison and discussion

A.4.1 Diffusivity profiles

Figure A.7a shows the reconstructed molecular diffusivity profiles for CO_2 for the different models on the US borehole. Upon reaching the LIZ the effective molecular diffusion nearly vanishes. In Fig. A.7b the total diffusivity $D_{\text{total}}(z) = D_{\text{CO2}}(z) + D_{\text{eddy}}$ for CO_2 is plotted on a semilog scale. As for the EU borehole we observe that the models require a non-vanishing diffusivity within the LIZ to fit the data. Only the CSIRO model uses zero diffusivity in the LIZ for the US hole. This difference might explain why the CSIRO model has more difficulty fitting the US data, as expressed by the RMSD in Fig. A.6.

A.4.2 Gas age distributions

Figure A.8 compares age distribution densities for the models at the lock-in depth ($z = 63$ m) and near the deepest sample ($z = 76$ m) on the US hole. Table A.13 gives some characteristics of the distributions. On the EU hole we find a spread of up to 25% in the mean ages and distribution widths at 63 m depth. When looking at the US hole the spread in the calculated mean ages is even larger (40% of the mean age at 63 m). This large spread is mostly due to the LGGE-GIPSA model, which stands out as having a wider and flatter age distribution. However, since this model obtains a better fit to the experimental data than most models (Fig. A.6) this distribution is certainly realistic. We attribute the larger spread found in modeled US borehole mean ages to the fact that it has fewer tracers. This leaves the mean age more poorly constrained. The CSIRO age distribution at $z = 76$ m is very narrow compared to the other models, due to the absence of LIZ diffusion in the US hole. Since it differs so strongly from both the CSIRO model result on the EU hole, as well as from the other model results on the US hole, this age distribution was not included in the comparison in Fig. 7 of the main article.

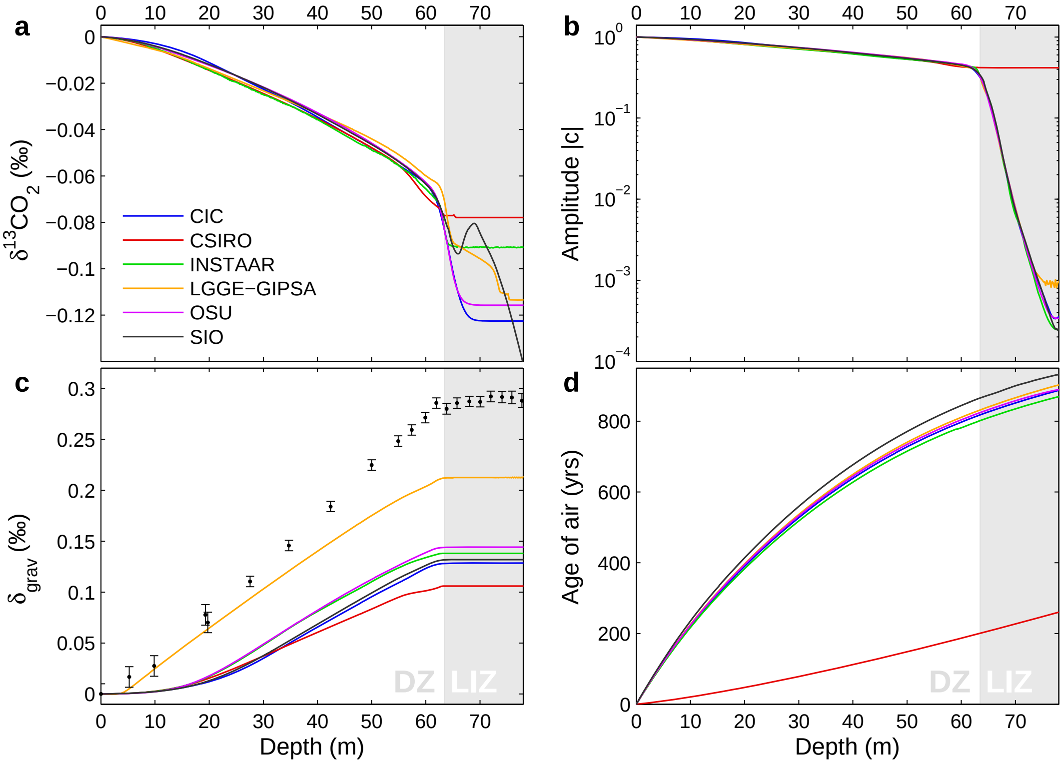

Figure A.9: Model comparison using the four diagnostic scenarios and diffusivity tuned to the US borehole data. **(a)** *Scenario I: Diffusive fractionation for a hypothetical monotonic CO2 increase.* **(b)** *Scenario II: Attenuation of a 15 yr period sinusoidal CO_2 forcing with depth.* **(c)** *Scenario III: Gravitational enrichment for gas X with $D^0_X = 0.025 D^0_{CO2}$. Data points show gravitational enrichment of $^{15}N_2$ corrected for the effect of thermal diffusion.* **(d)** *Scenario IV: Mean age of gas Y, using advective transport only ($D^0_Y = 0$). With the exception of S-III all scenarios were run with the effect of gravity turned off.*

A.4.4 Synthetic diagnostic scenarios

Table A.14 provides detailed specifications on how the diagnostic scenarios are run in the models.

Scenario I compares the amount of diffusive fractionation (DF) of isotopes in the firn. We model the mole fractions of $[^{12}CO_2]$ and $[^{13}CO_2]$ separately using the relative diffusion coefficients given in Sect. A.3.1.2. For convenience we let our reference atmosphere have the property

$$^{13}R_{\mathrm{std}} = \left.\frac{[^{13}\mathrm{CO_2}]}{[^{12}\mathrm{CO_2}]}\right|_{\mathrm{std}} = 1 \tag{A.34}$$

meaning that at in the atmosphere $[^{12}CO_2] = [^{13}CO_2]$ as we let the mixing ratio increase with time. We use the same atmospheric input file to force both isotopologues. The fractionation with depth is then given as

$$\delta^{13}\mathrm{CO_2}(z) = \left(\frac{[^{13}\mathrm{CO_2}](z)}{[^{12}\mathrm{CO_2}](z)} - 1\right) \times 10^3 \text{ ‰} \tag{A.35}$$

Table A.14: Details on running the diagnostic scenarios.

Gas	Mass ($\mathrm{g\,mol^{-1}}$)	$D/D_{\mathrm{CO_2}}$	Scenario file	Gravity	Run time (yr CE)
Scenario I					
$^{12}CO_2$	43.99	1.000048	Diagnostic_1.txt	OFF	1800-2008.54
$^{13}CO_2$	44.99	0.995613	Diagnostic_1.txt	OFF	1800-2008.54
Scenario II					
CO_2	44.01	1	Diagnostic_2a.txt	OFF	1800-2008.54
CO_2	44.01	1	Diagnostic_2b.txt	OFF	1800-2008.54
Scenario III					
X	$M_{\mathrm{air}}+1$	0.025	Diagnostic_3.txt	ON	1000-2008.54
Scenario IV					
Y	44.01	0	Diagnostic_4.txt	OFF	400-2008.54

Fig. A.9 shows the scenario comparison for the US borehole. We observe similar model differences as on the EU borehole. For scenario I (Fig. A.9a) we see a large discrepancy in modeled diffusive isotopic fractionation between the firn models. The magnitude of the model discrepancy is similar to that of the EU borehole. For scenario II we see that the CSIRO model has no diffusion in the LIZ, contrary to the other models. This is related to the CSIRO reconstructed diffusivity profile, which goes to zero in the LIZ (Fig. A.7b). Scenario IV is identical between the two boreholes, since the advective transport term depends only on the porosity parameterisation and accumulation rate which are the same for both boreholes.

Notation

A	Accumulation rate ($\mathrm{m\,yr^{-1}}$ ice equivalent)
A_{abs}	Absolute ^{14}C abundance (1.1764×10^{-12})
C	Mixing ratio ($\mathrm{mol\,mol^{-1}}$)
D_{eddy}	Eddy diffusion coefficient ($\mathrm{m^2\,s^{-2}}$)
D_X	Diffusion coefficient of gas X ($\mathrm{m^2\,s^{-2}}$)
D_X^0	Free air diffusion coeff. of gas X ($\mathrm{m^2\,s^{-2}}$)
d_i	Data point i
g	Gravitational acceleration (9.82 $\mathrm{m\,s^{-2}}$)
J	Trace gas flux ($\mathrm{mol\,mol^{-1}\,m\,s^{-1}}$)
M_{air}	Molar mass of air ($\mathrm{kg\,mol^{-1}}$)
M_{X}	Molar mass of gas X ($\mathrm{kg\,mol^{-1}}$)
m_i	Modeled value for data point i
p	Air pressure (Pa)
$p\mathrm{H_2O}$	Vapour pressure of water (Pa)
R	Molar gas constant (8.314 $\mathrm{J\,mol^{-1}\,K^{-1}}$)
RMSD	Root Mean Square Deviation
s	Total porosity ($\mathrm{m^3\,m^{-3}}$)
s_{co}	Mean close-off porosity ($\mathrm{m^3\,m^{-3}}$)
$s_{\mathrm{op(cl)}}$	Open (closed) porosity ($\mathrm{m^3\,m^{-3}}$)
s^*_{op}	Effective open porosity ($\mathrm{m^3\,m^{-3}}$)
T	Absolute temperature (K)
u_X	Uncertainty in gas X ($\mathrm{mol\,mol^{-1}}$)
V_{contam}/V	Fraction of contamination ($\mathrm{m^3\,m^{-3}}$)
w_{air}	Downward velocity of air ($\mathrm{m\,s^{-1}}$)
w_{ice}	Downward velocity of ice layers ($\mathrm{m\,s^{-1}}$)
$[X]$	Mixing ratio of gas X ($\mathrm{mol\,mol^{-1}}$)
x_{air}	Air content of ice (mL STP per kg ice)
z	Depth (m)
z_{COD}	Full close-off depth; $s_{\mathrm{op}}(z_{\mathrm{COD}}) = 0$ (m)
z_{LID}	Lock-in depth (m)
γ_X	Diffusion coefficient relative to $\mathrm{CO_2}$
Δage	Ice age-gas age difference (yr)
$\Delta\mathrm{age_{op}}$	Ice age- open pore gas age difference (yr)
ΔM	Molar mass deviation from air ($\mathrm{kg\,mol^{-1}}$)
Δt	Temporal step size (s) or (yr)
Δz	Spatial step size (m)
δ_{grav}	Gravitational fractionation p. unit mass (‰)
Θ	Temperature (° C)
θ	Trapping rate ($\mathrm{s^{-1}}$)
λ_X	Radioactive decay constant of gas X ($\mathrm{s^{-1}}$)
μ	Mean value of a series
ρ	Firn density ($\mathrm{g\,cm^{-3}}$)
ρ_{co}	Mean close-off density ($\mathrm{g\,cm^{-3}}$)
ρ_{COD}	Full close-off density; $\rho(z_{\mathrm{COD}})$ ($\mathrm{g\,cm^{-3}}$)
ρ_{ice}	Solid ice density ($\mathrm{g\,cm^{-3}}$)
σ_i	Assigned uncertainty for data point i
τ	Tortuosity
τ_0	Initial guess for τ in tuning algorithm
$\phi_{\mathrm{op(cl)}}$	Air flux in open (closed) porosity ($\mathrm{m\,s^{-1}}$)

A.5 References

Arnaud, L., Barnola, J. M., and Duval, P. (2000). Physical modeling of the densification of snow/firn and ice in the upper part of polar ice sheets. In Hondoh, T., editor, *Physics of Ice Core Records*, pages 285–305. Hokkaido University Press.

Aydin, M., Montzka, S. A., Battle, M. O., Williams, M. B., De Bruyn, W. J., Butler, J. H., Verhulst, K. R., Tatum, C., Gun, B. K., Plotkin, D. A., Hall, B. D., and Saltzman, E. S. (2010). Post-coring entrapment of modern air in some shallow ice cores collected near the firn-ice transition: evidence from cfc-12 measurements in antarctic firn air and ice cores. *Atmos. Chem. Phys.*, 10(11):5135–5144.

Barr, R. F. and Watts, H. (1972). Diffusion of some organic and inorganic compounds in air. *J. Chem. Eng. Data*, 17(1):45–46.

Blanc, A. (1908). Recherches sur les mobilités des ions dans les gaz. *J. Phys. Theor. Appl.*, 7:825–839.

Buizert, C., Martinerie, P., Petrenko, V. V., Severinghaus, J. P., Trudinger, C. M., Witrant, E., Rosen, J. L., Orsi, A. J., Rubino, M., Etheridge, D. M., Steele, L. P., Hogan, C., Laube, J. C., Sturges, W. T., Levchenko, V. A., Smith, A. M., Levin, I., Conway, T. J., Dlugokencky, E. J., Lang, P. M., Kawamura, K., Jenk, T. M., White, J. W. C., Sowers, T., Schwander, J., and Blunier, T. (2011). Gas transport in firn: multiple-tracer characterisation and model intercomparison for neem, northern greenland. *Atmos. Chem. Phys. Discuss.*, 11:15975–16021.

Bzowski, J., Kestin, J., Mason, E. A., and Uribe, F. (1990). Equilibrium and transport properties of gas mixtures at low density: eleven polyatomic gases and five noble gases. *J. Phys. Chem. Ref. Data*, 19:1179–1232.

Chen, N. H. and Othmer, D. F. (1962). New generalized equation for gas diffusion coefficient. *J. Chem. Eng. Data*, 7(1):37–41.

Cowie, M. and Watts, H. (1971). Diffusion of methane and chloromethanes in air. *Can. J. Chem.*, 49:74–77.

Craig, H. (1957). Isotopic standards for carbon and oxygen and correction factors for mass-spectrometric analysis of carbon dioxide. *Geochim. Cosmochim. Ac.*, 12(1-2):133 – 149.

CRC (2002). *CRC Handbook of Chemistry and Physics, 83rd Edition.* CRC Press, Boca Raton, FL, USA.

Etheridge, D., Steele, L., Francey, R., and Langenfelds, R. (1998). Atmospheric methane between 1000 AD and present: Evidence of anthropogenic emissions and climatic variability. *J. Geophys. Res.-Atm.*, 103(D13):15979–15993.

Etheridge, D. M., Steele, L. P., Langenfelds, R. L., Francey, R. J., Barnola, J. M., and Morgan, V. I. (1996). Natural and anthropogenic changes in atmospheric co_2 over the last 1000 years from air in antarctic ice and firn. *J. Geophys. Res.*, 101(D2):4115–4128.

Fink, D., Hotchkis, M., Hua, Q., Jacobsen, G., Smith, A., Zoppi, U., Child, D., Mifsud, C., van der Gaast, H., Williams, A., and Williams, M. (2004). The ANTARES AMS facility at ANSTO. *Nucl. Instrum. Meth. B*, 223:109–115.

Francey, R., Allison, C., Etheridge, D., Trudinger, C., Enting, I., Leuenberger, M., Langenfelds, R., Michel, E., and Steele, L. (1999). A 1000-year high precision record of delta C-13 in atmospheric CO_2. *Tellus B*, 51(2):170–193.

Fuller, E. N., Schettler, P. D., and Giddings, J. C. (1966). A new method for prediction of binary gas-phase diffusion coefficients. *Ind. Eng. Chem.*, 58:19–27.

Gilliland, E. R. (1934). Diffusion coefficients in gaseous systems. *Ind. Engng. Chem.*, 26:681–685.

Goujon, C., Barnola, J. M., and Ritz, C. (2003). Modeling the densification of polar firn including heat diffusion: Application to close-off characteristics and gas isotopic fractionation for Antarctica and Greenland sites. *J. Geophys. Res.-Atm*, 108(D24):18.

Guzman, M. I., Hoffmann, M. R., and Colussi, A. J. (2007). Photolysis of pyruvic acid in ice: Possible relevance to co and co_2 ice core record anomalies. *J. Geophys. Res.-Atm*, 112(D10):10.

Haupt, R. L. and Haupt, S. E. (1998). *Practical Genetic Algorithms.* John Wiley & Sons, Inc., Hoboken, New Jersey.

Hua, Q. and Barbetti, M. (2004). Review of tropospheric bomb C-14 data for carbon cycle modeling and age calibration purposes. *Radiocarbon*, 46(3):1273–1298.

Karlen, I., Olsson, I. U., Kallburg, P., and Kilici, S. (1968). Absolute determination of the activity of two ^{14}c dating standards. *Arkiv Geofysik*, 4:465–471.

Kawamura, K., Severinghaus, J. P., Ishidoya, S., Sugawara, S., Hashida, G., Motoyama, H., Fujii, Y., Aoki, S., and Nakazawa, T. (2006). Convective mixing of air in firn at four polar sites. *Earth Planet Sc. Lett.*, 244(3-4):672–682.

Lal, D., Jull, A. J. T., Donahue, D. J., Burtner, D., and Nishiizumi, K. (1990). Polar ice ablation rates measured using in-situ cosmogenic c-14. *Nature*, 346(6282):350–352.

Levin, I., Hammer, S., Kromer, B., and Meinhardt, F. (2008). Radiocarbon observations in atmospheric CO_2: Determining fossil fuel CO_2 over Europe using Jungfraujoch observations as background. *Sci. Total Environ.*, 391(2-3):211–216.

Levin, I. and Kromer, B. (2004). The tropospheric (CO_2)-C-14 level in mid-latitudes of the Northern Hemisphere (1959-2003). *Radiocarbon*, 46(3):1261–1272.

Levin, I., Naegler, T., Heinz, R., Osusko, D., Cuevas, E., Engel, A., Ilmberger, J., Langenfelds, R. L., Neininger, B., Rohden, C. v., Steele, L. P., Weller, R., Worthy, D. E., and Zimov, S. A. (2010a). The global sf_6 source inferred from long-term high precision atmospheric measurements and its comparison with emission inventories. *Atmos. Chem. Phys.*, 10(6):2655–2662.

Levin, I., Naegler, T., Kromer, B., Diehl, M., Francey, R. J., Gomez-Pelaez, A. J., Steele, L. P., Wagenbach, D., Weller, R., and Worthy, D. E. (2010b). Observations and modelling of the global distribution and long-term trend of atmospheric (CO_2)-C-14. *Tellus B*, 62(3):207.

Lugg, G. A. (1968). Diffusion coefficients of some organic and other vapors in air. *Anal. Chem.*, 40:1072–1077.

Manning, M. and Melhuish, W. H. (1994). Atmospheric delta 14c record from wellington. In *Trends: A Compendium of Data on Global Change*. Carbon Dioxide Information Analysis Center, Oak Ridge National Laboratory, U.S. Department of Energy, Oak Ridge, Tenn., U.S.A.

Marrero, T. R. and Mason, E. A. (1972). Gaseous diffusion coefficients. *J. Phys. Chem. Ref. Data*, 1:3–118.

Martinerie, P., Lipenkov, V. Y., Raynaud, D., Chappellaz, J., Barkov, N. I., and Lorius, C. (1994). Air content paleo record in the vostok ice core (antarctica): A mixed record of climatic and glaciological parameters. *J. Geophys. Res.*, 99:10565–10576.

Martinerie, P., Nourtier-Mazauric, E., Barnola, J. M., Sturges, W. T., Worton, D. R., Atlas, E., Gohar, L. K., Shine, K. P., and Brasseur, G. P. (2009). Long-lived halocarbon trends and budgets from atmospheric chemistry modelling constrained with measurements in polar firn. *Atmos. Chem. Phys.*, 9(12):3911–3934.

Martinerie, P., Raynaud, D., Etheridge, D. M., Barnola, J. M., and Mazaudier, D. (1992). Physical and climatic parameters which influence the air content in polar ice. *Earth Planet Sc. Lett.*, 112(1-4):1–13.

Massman, W. J. (1998). A review of the molecular diffusivities of h_2o, co_2, ch_4, co, o_3, so_2, nh_3, n_2o, no, and no_2 in air, o_2 and n_2 near stp. *Atmos. Environ.*, 32:1111–1127.

Massman, W. J. (1999). Molecular diffusivities of hg vapor in air, o_2 and n_2 near stp and and the kinematic viscosity and thermal diffusivity of air near stp. *Atmos. Environ.*, 33:453–457.

Matsunaga, N., Hori, M., and Nagashima, A. (1993). Mutual diffusion coefficients of halogenated-hydrocarbon refrigerant-air systems. *High Temp.-High Press.*, 25:185–192.

Matsunaga, N., Hori, M., and Nagashima, A. (1998). Diffusion coefficients of global warming gases into air and its component gases. *High Temp.-High Press.*, 30(1):77–83.

Matsunaga, N., Hori, M., and Nagashima, A. (2002a). Measurements of mutual diffusion coefficients gases by the taylor method: measurements on h_2-air, h_2-n_2, and h_2-o_2 sustems. *Heat Trans. Asian Res.*, 31:182–193.

Matsunaga, N., Hori, M., and Nagashima, A. (2002b). Measurements of the mutual diffusion coefficients of gases by the taylor method (7th report, measurements on the sf_6-air, sf_6-n_2, sf_6-o_2, cfc12-n_2, cfc12-o_2, hcfc22-n_2 and hcfc22-o_2 systems). *Trans. Jpn. Soc. Mech. Eng. B.*, 68:550–555.

Matsunaga, N., Hori, M., and Nagashima, A. (2002c). Measurements of the mutual diffusion coefficients of gases by the taylor method (8th report, measurements on the hfc32-air, hcfc124-air, hcfc125-air, hcfc143a-air, and hfc43-10mee-air systems). *Trans. Jpn. Soc. Mech. Eng. B.*, 68:550–555.

Matsunaga, N., Hori, M., and Nagashima, A. (2003). Measurements of the mutual diffusion coefficients of chloromethanes, chloroethanes and chloroethylenes into air by the taylor dispersion method. *Proc 24th Jpn Symp Therm Props*, 24:306–308.

Matsunaga, N., Hori, M., and Nagashima, A. (2005). Measurements of the mutual diffusion coefficients of carbon tetrafluoride and methyl bromide into air, nitrogen and oxygen. *Proc 26th Jpn Symp Therm Props*, 26:499–501.

Matsunaga, N., Hori, M., and Nagashima, A. (2006). Gaseous diffusion coefficients of dimethyl ether and diethyl ether into air, nitrogen and oxygen. *Netsu Bussei*, 20:83–86.

Matsunaga, N., Hori, M., and Nagashima, A. (2007). Gaseous diffusion coefficients of propane and propylene into air, nitrogen and oxygen. *Netsu Bussei*, 20:83–86.

Matsunaga, N., Hori, M., and Nagashima, A. (2009). Gaseous diffusion coefficients of methyl bromide and methyl iodide into air, nitrogen and oxygen. *Heat Trans. Asian Res.*, 38.

Nydal, R. and Lövseth, K. (1996). Carbon-14 measurements in atmospheric co$_2$ from northern and southern hemisphere sites, 1962-1993. Carbon Dioxide Information Analysis Center, Oak Ridge National Laboratory, Oak Ridge, Tennessee.

Reimer, P., Baillie, M., Bard, E., Bayliss, A., Beck, J., Bertrand, C., Blackwell, P., Buck, C., Burr, G., Cutler, K., Damon, P., Edwards, R., Fairbanks, R., Friedrich, M., Guilderson, T., Hogg, A., Hughen, K., Kromer, B., McCormac, G., Manning, S., Ramsey, C., Reimer, R., Remmele, S., Southon, J., Stuiver, M., Talamo, S., Taylor, F., van der Plicht, J., and Weyhenmeyer, C. (2004). IntCal04 terrestrial radiocarbon age calibration, 0-26 cal kyr BP. *Radiocarbon*, 46(3):1029–1058.

Rommelaere, V., Arnaud, L., and Barnola, J. M. (1997). Reconstructing recent atmospheric trace gas concentrations from polar firn and bubbly ice data by inverse methods. *J. Geophys. Res.-Atm*, 102(D25):30069–30083.

Schwander, J. (1989). The transformation of snow to ice and the occlusion of gases. In Oescher, H. and Langway, C., editors, *The Environmental record in glaciers and ice sheets*, pages 53–67. John Wiley, New York.

Schwander, J., Barnola, J. M., Andrie, C., Leuenberger, M., Ludin, A., Raynaud, D., and Stauffer, B. (1993). The age of the air in the firn and the ice at summit, greenland. *J. Geophys. Res.-Atm*, 98(D2):2831–2838.

Schwander, J., Stauffer, B., and Sigg, A. (1988). Air mixing in firn and the age of the air at pore close-off. In *Ann. Glaciol.*, volume 10, pages 141–145.

Severinghaus, J. P., Albert, M. R., Courville, Z. R., Fahnestock, M. A., Kawamura, K., Montzka, S. A., Muhle, J., Scambos, T. A., Shields, E., Shuman, C. A., Suwa, M., Tans, P., and Weiss, R. F. (2010). Deep air convection in the firn at a zero-accumulation site, central Antarctica. *Earth Planet Sc. Lett.*, 293(3-4):359–367.

Severinghaus, J. P. and Battle, M. O. (2006). Fractionation of gases in polar lee during bubble close-off: New constraints from firn air Ne, Kr and Xe observations. *Earth Planet Sc. Lett.*, 244(1-2):474–500.

Severinghaus, J. P., Grachev, A., and Battle, M. (2001). Thermal fractionation of air in polar firn by seasonal temperature gradients. *Geochem. Geophy. Geosy.*, 2.

Stuiver, M. and Polach, H. A. (1977). Reporting of c-14 data - discussion. *Radiocarbon*, 19(3):355–363.

Trudinger, C. M., Enting, I. G., Etheridge, D. M., Francey, R. J., Levchenko, V. A., Steele, L. P., Raynaud, D., and Arnaud, L. (1997). Modeling air movement and bubble trapping in firn. *J. Geophys. Res.-Atm*, 102(D6):6747–6763.

Trudinger, C. M., Enting, I. G., Rayner, P. J., Etheridge, D. M., Rubino, M., Buizert, C., Martinerie, P., and Blunier, T. (2011). How well do different tracers constrain the firn diffusivity profile? *in preparation.*

Trudinger, C. M., Etheridge, D. M., Rayner, P. J., Enting, I. G., Sturrock, G. A., and Langenfelds, R. L. (2002). Reconstructing atmospheric histories from measurements of air composition in firn. *J. Geophys. Res.-Atm*, 107(D24):13.

Tschumi, J. and Stauffer, B. (2000). Reconstructing past atmospheric CO$_2$ concentration based on ice-core analyses: open questions due to in situ production of CO$_2$ in the ice. *J. Glaciol.*, 46(152):45–53.

Watts, H. (1971). Temperature dependence of the diffusion of carbon tetrachloride, chloroform, and methylene chloride vapors in air by a rate of evaporation method. *Can. J. Chem.*, 49:67–73.

Witrant, E. and Martinerie, P. (2010). A variational approach for optimal diffusivity identification in firns. In *Proc. of the 18th Med. Conf. on Control and Automation*, pages 892–897, Marrakech, Morocco.

Witrant, E., Martinerie, P., Hogan, C., Laube, J. C., Kawamura, K., Capron, E., Montzka, S. A., Dlugokencky, E. J., Etheridge, D., Blunier, T., and Sturges, W. T. (2011). A new multi-gas constrained model of trace gas non-homogeneous transport in firn: evaluation and behavior at eleven polar sites. *Atmos. Chem. Phys. Discuss.*, 11(8):23029–23080.

WMO (2007). *Scientific Assessment of Ozone Depletion: 2006. Global Ozone Research and Monitoring Project - Report No.50.* World Meteorological Organization, Geneva.

Yoshida, N. and Toyoda, S. (2000). Constraining the atmospheric n_2o budget from intramolecular site preference in n_2o isotopomers. *Nature*, 405(6784):330–334.